

Copyright
by
Ki Yeon Kwon
2012

**The Dissertation Committee for Ki Yeon Kwon Certifies that this is the approved
version of the following dissertation:**

Design Recommendations for CIP-PCP Bridge Decks

Committee:

James O. Jirsa, Supervisor

Richard E. Klingner, Co-Supervisor

Oguzhan Bayrak

Wassim Ghannoum

Harovel G. Wheat

Design Recommendations for CIP-PCP Bridge Decks

by

Ki Yeon Kwon, B.E, M.E

Dissertation

Presented to the Faculty of the Graduate School of

The University of Texas at Austin

in Partial Fulfillment

of the Requirements

for the Degree of

Doctor of Philosophy

The University of Texas at Austin

December 2012

Dedication

To my parents

Acknowledgements

I would like to thank the Texas Department of Transportation and the Center for Transportation Research for their generous support of this research.

I would also like to thank Dr. Jirsa, Dr. Klingner, and Dr. Bayrak for their guidance and instruction throughout this research. Their advice kept me motivated; it has been a great privilege to learn from them.

I express my gratitude to the FSEL staff—Andrew Valentine, Eric Schell, Blake Stassney, Dennis Phillip, Mike Wason, Barbara Howard, and Jessica Hanten. Nothing would get done without their help.

I am also very grateful to my research team mates, Umid and Aaron. Their drive and skilled workmanship enabled rapid and accurate progress of this research.

Finally, I would like to thank my family for always supporting and encouraging me throughout my time at the University of Texas at Austin.

October 3, 2012

Design Recommendations for CIP-PCP Bridge Decks

Ki Yeon Kwon, Ph.D.

The University of Texas at Austin, 2012

Supervisor: James O. Jirsa

Co-Supervisor: Richard E. Klingner

Precast, prestressed concrete panels (PCPs) and cast-in-place (CIP) concrete slabs are commonly used in Texas and elsewhere. Because PCPs are placed between bridge girders, and CIP concrete slabs are cast over the PCPs, PCPs act as formwork, cost and time for construction can be reduced. However, current designs may be further optimized if it can be shown that the reinforcement in the CIP deck can be reduced. Another issue involves cracking of PCP during fabrication and transportation to the site. The goal of this dissertation is to recommend changes to the CIP-PCP bridge decks that will lead to more cost-effective bridges.

The first phase of the research is to suggest an optimized reinforcement layout for cast-in-place (CIP) slabs. Because the capacity of these decks is much greater than the design loads, a decrease in top-mat reinforcement will have minimal effect on the margin of capacity over design loads. Two options were selected, reduced deformed-bar reinforcement; and reduced welded-wire reinforcement. These two options are evaluated through restrained-shrinkage tests and field applications.

The second phase of this dissertation is to reduce cracks in precast, prestressed concrete panels (PCPs) which occur during fabrication, handling, and transportation. Most cracks in PCPs are collinear (occur along the strands). They can be reduced in two ways. The first is to reduce initial prestress. The second is to place additional transverse reinforcement at edges.

Table of Contents

CHAPTER 1 INTRODUCTION.....	1
1.1 Background.....	1
1.2 Issues addressed in project.....	3
1.3 Objectives and Contributions of this Research.....	4
CHAPTER 2 LITERATURE REVIEW	6
2.1 Introduction.....	6
2.2 Issues in CIP-PCP bridge decks.....	7
2.2.1 Issues in CIP slabs	8
2.2.1.1 Arching action in bridge decks	8
2.2.1.2 Conservatism in bridge deck design	8
2.2.1.3 Typical cracking in CIP-PCP bridge deck: reflecting cracks	9
2.2.1.4 “Texas poor-boy” joint	11
2.2.1.5 Welded-wire reinforcement	12
2.2.2 Issues in PCPs as used in Texas.....	13
2.2.2.1 Panel rejection in the field	13
2.2.2.2 Collinear cracking in PCPs	13
2.2.2.3 Ageing and creep coefficients.....	18
2.3 Studies conducted under TxDOT projects 0-4098 and 0-6348	19
2.3.1 TxDOT Project 0-4098	19
2.3.2 TxDOT Project 0-6348: Foster (2010)	20
2.3.3 TxDOT Project 0-6348: Foreman (2010) & Azimov (2012).....	24
CHAPTER 3 OPTIMIZATION of Reinforcement in CIP slabs: FIELD APPLICATION	26
3.1 Introduction.....	26
3.2 Wharton-Weems Overpass	26
3.2.1 Description.....	26
3.2.2 Top-mat reinforcement options for Wharton-Weems Overpass.....	29
3.2.3 Splice details	29

3.2.3.1	Longitudinal splices	29
3.2.3.2	Transverse splices	32
3.2.4	Instrumentation of Wharton-Weems Overpass.....	33
3.2.4.1	Vibrating-wire gages.....	33
3.2.4.2	Gage location and identification	34
3.2.4.3	Data-acquisition equipment	36
3.2.5	Field instrumentation of Wharton-Weems Overpass.....	38
3.2.5.1	Installing vibrating-wire gages	38
3.2.5.2	Placing data-acquisition box	39
3.2.5.3	Mounting solar panel	40
3.2.5.4	Casting concrete deck, Wharton-Weems Overpass	40
3.2.6	Results from Field Instrumentation of Wharton-Weems Overpass	42
3.2.6.1	Cracking inspection	42
3.2.6.2	Long-term monitoring, Wharton-Weems Overpass	44
3.2.6.3	Use of P-method to predict cracking in CIP-PCP bridge decks	48
3.3	Lampasas River Bridge.....	57
3.3.1	Description.....	57
3.3.2	Top-mat reinforcement options, Lampasas River Bridge.....	62
3.3.3	Splice details, Lampasas River Bridge	62
3.3.3.1	Longitudinal splices	62
3.3.3.2	Transverse splices	68
3.3.4	Instrumentation of Lampasas River Bridge	72
3.3.4.1	Gage location and identification	72
3.3.4.2	Data-acquisition equipment	74
3.3.5	Placement of top-mat reinforcement, Lampasas River Bridge ...	74
3.3.6	Field instrumentation of Lampasas River Bridge	79
3.3.6.1	Installing vibrating-wire gages	81
3.3.6.2	Placing data-acquisition box, Lampasas River Bridge ...	84
3.3.6.3	Mounting solar panel	86

3.3.6.4 Casting concrete deck, Lampasas River Bridge	89
3.3.7 Results from Field Instrumentation, Lampasas River Bridge.....	91
3.3.7.1 Cracking inspection	91
3.3.7.2 Long-term monitoring, Lampasas River Bridge	92
3.3.7.3 Calculation of restraint moment using P-method, Lampasas River Bridge.....	96
3.4 Calculations of construction cost of various top-mat reinforcement options	98
3.5 Conclusions from Field Instrumentation	99
CHAPTER 4 OPTIMIZATION of Reinforcement in CIP Slabs: RESTRAINED- SHRINKAGE TEST	100
4.1 Introduction.....	100
4.2 Test specimens for restrained-shrinkage test	101
4.2.1 Reinforcement options for restrained-shrinkage test	101
4.2.2 Specimen configurations for restrained-shrinkage test.....	102
4.2.3 Construction of restraining frame for restrained-shrinkage test	103
4.2.4 Construction of restrained shrinkage specimens.....	105
4.2.5 Placing top-mat reinforcement, restrained-shrinkage test	109
4.2.6 Gage instrumentation, restrained-shrinkage test.....	111
4.2.7 Casting of deck concrete, restrained-shrinkage test.....	115
4.2.8 Concrete compressive strength, restrained-shrinkage test	118
4.3 Results and Conclusions, restrained-shrinkage test	119
4.3.1 Results of restrained-shrinkage test	119
4.3.1.1 Long-term monitoring.....	119
4.3.1.2 Calculation of restraint moment.....	121
4.3.2 Conclusions from restrained-shrinkage test.....	125
CHAPTER 5 CONTROL OF CRACKING IN PRECAST, PRESTRESSED CONCRETE PANELS	126
5.1 Introduction.....	126
5.2 Fabrication of panels.....	126

5.3	Monitoring of strains in PCPs.....	131
5.4	Prestress loss monitoring	135
5.4.1	Measured prestress losses	135
5.4.2	Effects of gage type	137
5.4.3	Effects of aggregate type and environmental conditions on prestress loss	138
5.4.4	Estimated prestress loss using design specification.....	140
5.4.4.1	Calculated prestress losses - AASHTO 2004	141
5.4.4.2	Calculated prestress losses - AASHTO 2008	141
5.4.4.3	Calculated prestress losses - TxDOT design specifications	142
5.5	Results from monitoring of panel strains.....	143
5.5.1	Concrete tensile stress and strain during release.....	143
5.5.2	Concrete tensile stress and strain during the first week after release	146
5.5.3	Measured versus predicted prestress losses	149
5.6	Model for prestress loss in PC panels.....	151
5.6.1	Introduction.....	151
5.6.2	Current prediction models for prestress loss.....	152
5.6.2.1	AASHTO 2008	152
5.6.2.2	TxDOT 2004 Design Specification	155
5.6.2.3	PCI Design Handbook, 6th edition	155
5.6.3	Proposed equation for prestress loss in PC panels.....	158
5.6.3.1	Development of basic form for proposed equation.....	160
5.6.3.2	Derivation of constants, proposed equation.....	165
5.6.3.3	Propose new equation for predicting prestress loss in PCPs	167
5.6.3.4	Verification of proposed equation	168
5.6.3.5	Accuracy of proposed equation	172
5.7	Conclusions of study on Control of Cracking in PCPs.....	177

CHAPTER 6 SUMMARY AND CONCLUSIONS.....	179
6.1 Summary.....	179
6.2 Conclusions.....	184
APPENDIX A DEVELOPMENT LENGTH CALCULATION.....	185
A.1 Section A-A (No. 4 bar at 9 in.).....	185
A.2 Section E-E (D 20 wire at 9 in.).....	186
A.3 Section M-M (No. 5 bar at 6 in.)	187
A.4 Section O-O (D 20 wire at 6 in.).....	188
A.5 Section R-R (No. 4 bar at 6 in.)	189
APPENDIX B SAMPLE RESTRAINT MOMENT CALCULATION USING P-METHOD WHARTON-WEEMS OVERPASS.....	190
B.1 Conditions and assumptions for calculation	190
B.2 Calculations of components for longitudinal restraint moment.....	191
B.3 Calculate longitudinal restraint moment.....	193
B.4 Calculations of components for transverse restraint moment.....	195
B.5 Calculate transverse restraint moment	198
APPENDIX C SAMPLE RESTRAINT MOMENT CALCULATION USING P-METHOD RESTRAINED SHRINKAGE TEST	201
C.1 Conditions and assumptions for calculation	201
C.2 Calculations of each component for calculating restraint moment....	202
C.3 Calculate restraint moment	204
REFERENCE.....	206
VITA.....	211

List of Tables

Table 2-1: Summary of survey of state transportation agencies that use CIP-PCP bridge decks (Sneed <i>et al.</i> 2010).....	7
Table 3-1: Properties of top-mat reinforcement, Lampasas River Bridge.....	75
Table 3-2: Material costs of each top-mat option.....	98
Table 4-1: Reinforcement options for restrained-shrinkage test.....	102
Table 4-2: Concrete mixture proportions (by weight), restrained-shrinkage test	116
Table 4-3: Details of top-mat reinforcement for restraint-moment calculation...	123
Table 5-1: Summary of fabrication of panels	127
Table 5-2: Summary of results from prestress-loss monitoring.....	135
Table 5-3: Average environmental conditions of both plants during the first month after casting.....	139
Table 5-4: Calculated prestress losses - AASHTO 2004.....	141
Table 5-5: Calculated prestress losses - AASHTO 2008.....	142
Table 5-6: Typical tensile strengths and corresponding strains using two different tensile test methods	143
Table 5-7: Average measured tensile strain and stress depending on existence of additional transverse edge bar and type of coarse aggregate.....	146
Table 5-8: Resultant values for constants C_{SH} and C_{CR}	167
Table 5-9: Constant values and parameters for Equation 5-45.....	168
Table 5-10: Comparative accuracy by residual method	176
Table 5-11: Summary of statistical analysis results for accuracy.....	176
Table 6-1: Current status, limitations and future studies of this research.....	182

List of Figures

Figure 1-1: CIP-PCP bridge deck (adapted from Buth <i>et al.</i> (1972)).....	2
Figure 1-2: CIP-PCP bridge deck (section view)	2
Figure 1-3: Criteria for rejection of precast panel	4
Figure 2-1: Arching Action in Concrete Slabs (adopted from (Foster 2010)).....	8
Figure 2-2 Reflected cracking in top surface of CIP-PCP bridge deck (Folliard <i>et al.</i> 2003)	9
Figure 2-3: “Poor-boy” Joint (adapted from Roberts <i>et al.</i> 1993)	12
Figure 2-4: Force acting on a strand after release.....	15
Figure 2-5: Gradient of prestress in strand after releasing.....	15
Figure 2-6: The force acting in the surrounding concrete.....	16
Figure 2-7: Poisson’s effect	17
Figure 2-8: Forces on strand due to “wedge” created by Hoyer effect.....	18
Figure 2-9: Restrained-shrinkage test setup of TxDOT Project 0-4098 (Folliard <i>et al.</i> 2003)	20
Figure 2-10: Constant bending moment test setup (Foster 2010).....	21
Figure 2-11: Concentrated-load test setup (Foster 2010)	22
Figure 2-12: Direct tensile test using composite specimen (Foster 2010).....	22
Figure 2-13: Delamination during direct tensile test (Foster 2010).....	23
Figure 2-14: Direct tensile test using non-composite specimen (Foster 2010)	23
Figure 2-15: Long-term monitoring of prestress loss in PCPs	24
Figure 2-16: Knife-edge test (Foreman 2010)	25
Figure 3-1: Plan view, Wharton-Weems Overpass.....	27
Figure 3-2: Section view, Wharton-Weems Overpass.....	28

Figure 3-3: CIP deck reinforcement options, Wharton-Weems Overpass	29
Figure 3-4: Details of longitudinal splices, Wharton-Weems Overpass.....	31
Figure 3-5: Section showing details of longitudinal splices, Wharton-Weems Overpass (Joint 1)	31
Figure 3-6: Section showing details of longitudinal splices, Wharton-Weems Overpass (Joint 2)	31
Figure 3-7: Details of transverse splices, Wharton-Weems Overpass.....	32
Figure 3-8: Details of transverse splices, Wharton-Weems Overpass (Section A-A)	32
Figure 3-9: Details of transverse splices, Wharton-Weems Overpass (Section B-B)	33
Figure 3-10: Details of transverse splices, Wharton-Weems Overpass (Section C-C)	33
Figure 3-11: Typical VWG as installed on the reinforcement.....	34
Figure 3-12: Gage layout for longitudinal bars, Wharton-Weems Overpass	35
Figure 3-13: Gage layout for transverse bars, Wharton-Weems Overpass	35
Figure 3-14: Solar-powered data-acquisition system, Wharton-Weems Overpass	36
Figure 3-15: Location of data-acquisition box, Wharton-Weems Overpass	37
Figure 3-16: Bracket for solar panel, Wharton-Weems Overpass	37
Figure 3-17: Gage instrumentation, Wharton-Weems Overpass	38
Figure 3-18: Threading wires though holes in bedding strip, Wharton-Weems Overpass.....	39
Figure 3-19: Data-acquisition box after connection, Wharton-Weems Overpass	39

Figure 3-20: Mounting solar panel beside bent cap, Wharton-Weems Overpass	40
Figure 3-21: Construction sequence for CIP deck, Wharton-Weems Overpass.....	41
Figure 3-22: Spraying water on bridge deck for cracking inspection, Wharton-Weems Overpass.....	42
Figure 3-23: Results of first cracking inspection, Wharton-Weems Overpass.....	44
Figure 3-24: Results of second cracking inspection, Wharton-Weems Overpass	44
Figure 3-25: Stresses in Current TxDOT Standard Reinforcement, Wharton-Weems Overpass (longitudinal direction)	46
Figure 3-26: Stresses in Reduced Deformed-Bar Reinforcement, Wharton-Weems Overpass (longitudinal direction)	46
Figure 3-27: Stresses in Current TxDOT Standard Reinforcement, Wharton-Weems Overpass (transverse direction).....	47
Figure 3-28: Stresses in Reduced Deformed-Bar Reinforcement, Wharton-Weems Overpass (transverse direction).....	47
Figure 3-29: The area for the calculation of longitudinal restraint moment of Wharton-Weems Overpass	51
Figure 3-30: Simplified Section T-T.....	51
Figure 3-31: Longitudinal restraint moment and cracking moment, Wharton-Weems Overpass.....	53
Figure 3-32: Area for calculation of transverse restraint moment, Wharton-Weems Overpass.....	55
Figure 3-33: Simplified Section L-L, Wharton-Weems Overpass	55

Figure 3-34: Transverse restraint moment and cracking moment, Wharton-Weems Overpass.....	56
Figure 3-35: Plan view of Lampasas River Bridge (Spans 1 to 3)	58
Figure 3-36: Plan view of Lampasas River Bridge (Spans 4 to 5)	59
Figure 3-37: Section view of Lampasas River Bridge (Spans 1 to 3)	60
Figure 3-38: Section view of Lampasas River Bridge (Spans 4 to 5)	61
Figure 3-39: Reinforcement options, Lampasas River Bridge	62
Figure 3-40: Details of longitudinal splices, Lampasas River Bridge (Span 1 and Span 2)	64
Figure 3-41: Details of longitudinal splices, Lampasas River Bridge (Span 4 and Span 5)	64
Figure 3-42: Details of longitudinal splices, Lampasas River Bridge (Sections A-A and G-G)	65
Figure 3-43: Details of longitudinal splices, Lampasas River Bridge (Sections B-B and H-H)	65
Figure 3-44: Details of longitudinal splices, Lampasas River Bridge (Sections C-C and I-I)	65
Figure 3-45: Details of longitudinal splices, Lampasas River Bridge (Section D-D)	66
Figure 3-46: Details of longitudinal splices, Lampasas River Bridge (Section E-E)	66
Figure 3-47: Details of longitudinal splices, Lampasas River Bridge (Section F-F).	66
Figure 3-48: Details of longitudinal splices, Lampasas River Bridge (Section J-J)	67

Figure 3-49: Details of longitudinal splices, Lampasas River Bridge (Section K-K)	67
Figure 3-50: Details of longitudinal splices, Lampasas River Bridge (Section L-L)	67
Figure 3-51: Details of transverse splices, Lampasas River Bridge (Span 1 and Span 2)	68
Figure 3-52: Details of transverse splices, Lampasas River Bridge (Span 4 and Span 5)	69
Figure 3-53: Details of transverse splice, Lampasas River Bridge (Section M-M)	69
Figure 3-54: Details of transverse splice, Lampasas River Bridge (Section N-N)	70
Figure 3-55: Details of transverse splice, Lampasas River Bridge (Section O-O)	70
Figure 3-56: Details of transverse splice, Lampasas River Bridge (Section P-P)	70
Figure 3-57: Details of transverse splice, Lampasas River Bridge (Section Q-Q)	71
Figure 3-58: Details of transverse splice, Lampasas River Bridge (Section R-R)	71
Figure 3-59: Gage layout for longitudinal bars, Lampasas River Bridge	73
Figure 3-60: Gage layout for transverse bars, Lampasas River Bridge	73
Figure 3-61: Location of data-acquisition system, Lampasas River Bridge	74
Figure 3-62: View of top-mat reinforcement from south end, Lampasas River Bridge	75

Figure 3-63: Test area for Current TxDOT Standard Reinforcement, Lampasas River Bridge.....	76
Figure 3-64: Typical placement of Current TxDOT Standard Reinforcement, Lampasas River Bridge.....	76
Figure 3-65: Test area for Reduced Welded-Wire Reinforcement, Lampasas River Bridge.....	77
Figure 3-66: Typical placement of Reduced Welded-Wire Reinforcement, Lampasas River Bridge.....	77
Figure 3-67: Test area for Reduced Deformed-Bar Reinforcement, Lampasas River Bridge.....	78
Figure 3-68: Typical placement of Reduced Deformed-Bar Reinforcement, Lampasas River Bridge.....	78
Figure 3-69: Armor joint between Spans 2 and 3, Lampasas River Bridge	79
Figure 3-70: Side view of Lampasas River Bridge from north end.....	80
Figure 3-71: Side view of Lampasas River Bridge from south end	80
Figure 3-72: Typical field installation of VWG, Lampasas River Bridge	81
Figure 3-73: Making holes in bedding strip, Lampasas River Bridge	82
Figure 3-74: Checking gage before threading wire through the holes in bedding strip, Lampasas River Bridge.....	82
Figure 3-75: Sealing holes in bedding strip (Spans 1 and 2), Lampasas River Bridge	83
Figure 3-76: Split tube covering exposed parts of wires, Lampasas River Bridge	83
Figure 3-77: Data-acquisition box between Spans 1 and 2, Lampasas River Bridge	84

Figure 3-78: Data-acquisition box between Spans 4 and 5, Lampasas River Bridge	85
Figure 3-79: Scaffolding for accessing bent cap between Spans 4 and 5, Lampasas River Bridge.....	85
Figure 3-80: Inside of data-acquisition box placed on the bent between Spans 1 and 2, Lampasas River Bridge.....	86
Figure 3-81: Drilling holes on the side face of the bent caps for anchor bolts, Lampasas River Bridge.....	87
Figure 3-82: Mounting bracket for solar panel, Lampasas River Bridge	87
Figure 3-83: Solar panel mounted on side face of bent between Span 1 and 2, Lampasas River Bridge.....	88
Figure 3-84: Back side of the bracket showing wireless antenna, Lampasas River Bridge.....	88
Figure 3-85: Construction sequence for deck, Lampasas River Bridge	90
Figure 3-86: Result of cracking inspection of Lampasas River Bridge.....	91
Figure 3-87: Exposure of crack former, Lampasas River Bridge.....	92
Figure 3-88: Stresses in Current TxDOT Standard Reinforcement, Lampasas River Bridge (longitudinal direction)	93
Figure 3-89: Stresses in Reduced Deformed-Bar Reinforcement, Lampasas River Bridge (longitudinal direction)	93
Figure 3-90: Stresses in Reduced Welded-Wire Reinforcement, Lampasas River Bridge (longitudinal direction)	94
Figure 3-91: Stresses in Current TxDOT Standard Reinforcement, Lampasas River Bridge (transverse direction).....	94

Figure 3-92: Stresses in Reduced Deformed-Bar Reinforcement, Lampasas River Bridge (transverse direction).....	95
Figure 3-93: Stresses in Reduced Welded-Wire Reinforcement, Lampasas River Bridge (transverse direction).....	95
Figure 3-94: The area for calculation of longitudinal restraint moment, Lampasas River Bridge.....	97
Figure 3-95: The area for calculation of transverse restraint moment, Lampasas River Bridge.....	97
Figure 4-1: Region of the bridge deck simulated in the restrained-shrinkage test	101
Figure 4-2: Dimensions of restrained-shrinkage specimen	102
Figure 4-3: Terminology for restrained-shrinkage specimen	103
Figure 4-4: Mechanism of restrained shrinkage test.....	104
Figure 4-5: Components of restrained-shrinkage specimen	104
Figure 4-6: Attaching steel tube to back-to-back channels.....	105
Figure 4-7: Half-size precast, prestressed concrete panels (strands cut on one side)	106
Figure 4-8: Wooden side forms with anchors, restrained-shrinkage test.....	107
Figure 4-9: Complete assembly of first bay, restrained-shrinkage test	107
Figure 4-10: Space between precast, prestressed panels, restrained-shrinkage test	108
Figure 4-11: Installing restraining rods, restrained-shrinkage test	108
Figure 4-12: Arrangement of Current TxDOT Standard Reinforcement, restrained- shrinkage test	109

Figure 4-13: Arrangement of Reduced Deformed-Bar Reinforcement, restrained-shrinkage test	110
Figure 4-14: Arrangement of Reduced Welded-Wire Reinforcement, restrained-shrinkage test	110
Figure 4-15: Gage layout for restrained-shrinkage test	111
Figure 4-16: Location of outlets for gage wires, restrained-shrinkage test	112
Figure 4-17: Complete gage installation for one bay of restrained-shrinkage test	112
Figure 4-18: Installation sequence for foil gages, restrained-shrinkage test	114
Figure 4-19: Gage instrumentation (foil gage and vibrating-wire gage)	115
Figure 4-20: Deck-construction sequence, restrained-shrinkage test	117
Figure 4-21: Compressive strength from 4- \times 8-in. cylinder tests, restrained-shrinkage specimen	118
Figure 4-22: Long-term monitoring results from vibrating-wire gage, restrained-shrinkage test	120
Figure 4-23: Long-term monitoring results from foil gage, restrained-shrinkage test	120
Figure 4-24: Dimensions of the specimen for calculation	122
Figure 4-25: Restraint moment and cracking moment of the test frame	124
Figure 5-1: Gage layout for Current TxDOT initial prestressed panel from Plant A (Foreman 2010).....	128
Figure 5-2: Gage layout for Current TxDOT initial prestressed panel from Plant B (Foreman 2010).....	129
Figure 5-3: Gage layout for Reduced initial prestressed panel from Plants A and B (Azimov 2012).....	130

Figure 5-4: Stacking panels at Ferguson Laboratory (Azimov 2012)	131
Figure 5-5: Stacked panels at Ferguson Laboratory	132
Figure 5-6: Campbell Scientific CR 5000 data logger.....	132
Figure 5-7: Steel box for data logger	133
Figure 5-8: Wooden box for data logger.....	133
Figure 5-9: Hand-held reader for VWGs (Model GK-404, Geokon)	134
Figure 5-10: Long-term monitoring results, Current TxDOT initial prestress	136
Figure 5-11: Long-term monitoring results, Reduced initial prestress	137
Figure 5-12: Typical long-term monitoring data	138
Figure 5-13: Prestress losses during first month after casting	140
Figure 5-14: Calculations of prestress losses using AASHTO and TxDOT procedures	142
Figure 5-15: Measured tensile strains in all test panels in transverse direction (Foreman 2010, Azimov 2012).....	145
Figure 5-16: Strain variation in Current TxDOT initial prestressed panel during first week after release.....	148
Figure 5-17: Strain variation in Reduced initial prestressed panel during first week after release	148
Figure 5-18: Long-term prestress in the Current TxDOT initial prestressed panels	149
Figure 5-19: Long-term prestress losses in the Reduced initial prestressed panels	150
Figure 5-20: Long-term monitoring results of the Current TxDOT and the Reduced initial prestressed panels	150

Figure 5-21: Flow chart for proposing new equation for predicting prestress loss in PCPs.....	160
Figure 5-22: Curve fitting result for Plant A	166
Figure 5-23: Curve fitting result for Plant B.....	166
Figure 5-24: Measured and predicted prestress losses, Current TxDOT initial prestress, Plant A	170
Figure 5-25: Measured and predicted prestress losses, Current TxDOT initial prestress, Plant B.....	170
Figure 5-26: Measured and predicted prestress losses, Reduced initial prestress, Plant A	171
Figure 5-27: Measured and predicted prestress losses, Reduced initial prestress, Plant B.....	171
Figure B-1: Longitudinal restraint moment due to M_s	194
Figure B-2: Longitudinal restraint moment due to M_d	194
Figure B-3: Transverse restraint moment due to M_p	198
Figure B-4: Transverse restraint moment due to M_s	199
Figure B-5: Transverse restraint moment due to M_d	199

CHAPTER 1

INTRODUCTION

1.1 BACKGROUND

Since the Cast-In-Place (CIP)-Precast, prestressed Concrete Panel (PCP) bridge deck system was first used in a bridge on the Illinois Tollway project in the 1950s (Barker 1975), this system has been used all over the world (Goldberg 1987). The Texas Department of Transportation (TxDOT) uses the CIP-PCP concrete slab system for approximately 85% of all bridges built in Texas (Merrill 2002).

Precast, prestressed Concrete Panels (PCPs) span between the adjacent girders and serve as stay-in-place forms for the cast-in-place (CIP) concrete slabs. Panels, 4-in. thick and 8-ft wide with lengths that vary according to girder spacing are commonly used in Texas. Dimensions of the panels differ from state to state (Sneed *et al.* 2010). In Texas, PCPs have 16 strands spaced at 6 in. on-centers and located at mid-depth of the panels. After the PCPs are placed on the top flange of adjoining girders, the top mat reinforcement is placed and a cast-in-place concrete slab is cast to produce an 8-in. thick deck.

CIP-PCP bridge decks have many advantages compared to previous construction methods which used only cast-in-place concrete. The CIP-PCP system requires significantly less formwork, which reduces the cost and time for construction. Increasing construction speed reduces the time that workers are exposed to construction hazards. Moreover, CIP-PCP bridge decks are suitable for bridges constructed in sensitive sites such as sites over water or sites with limited construction access.

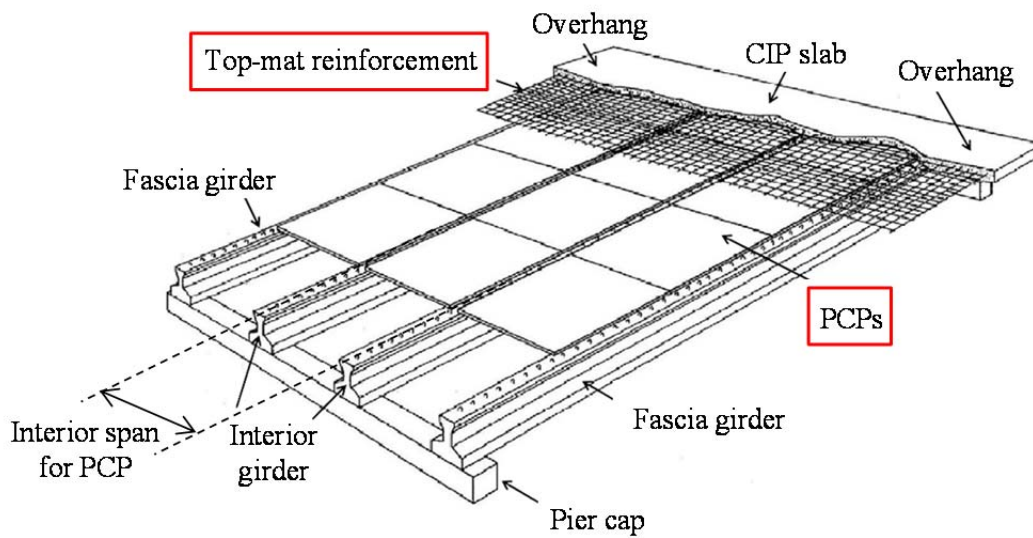


Figure 1-1: CIP-PCP bridge deck (adapted from Buth et al. (1972))

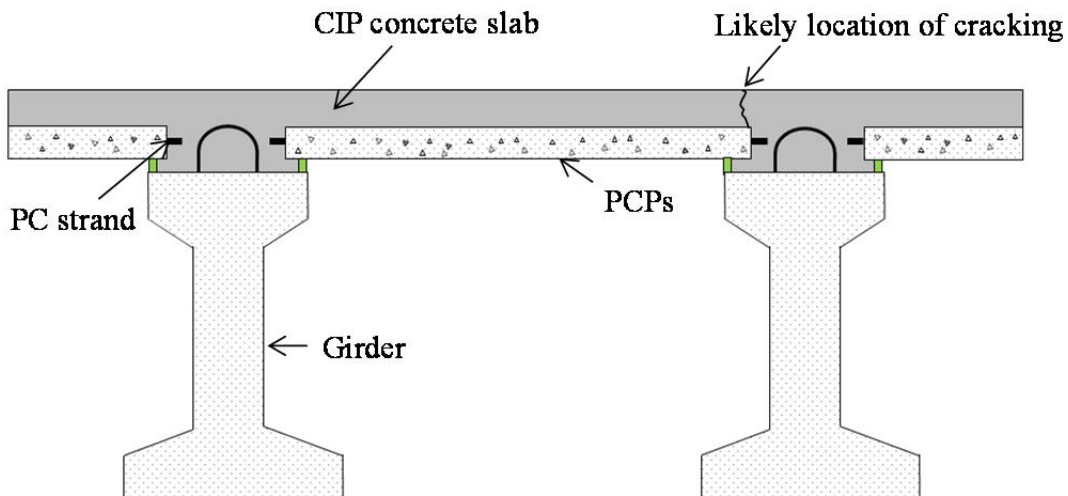


Figure 1-2: CIP-PCP bridge deck (section view)

1.2 ISSUES ADDRESSED IN PROJECT

Cracking in bridge decks tends to be at the interface between PCPs or at the PCP-to-CIP transition over the girder (Figure 1-2). The cracks at panel joints are caused by shrinkage in the CIP portion of the deck and creep in the PCPs (Merrill 2002). The cracks do not affect the strength of the bridge decks, but can cause serviceability problems such as corrosion of reinforcement due to ingress of deicing agents or damage due to freeze-thaw cycles (Sprinkel 1985; Goldberg 1987). To eliminate serviceability problems in CIP concrete slabs, TxDOT requires a minimum amount of reinforcement in both directions. Coselli (2004) indicates that current CIP slabs, especially for interior span, have much higher strength due to arching action than the strength determined in the design stage. No serious serviceability problems should develop under service loads. Therefore, it is possible that current reinforcement details can be optimized by reducing the amount of reinforcing steel in the CIP slabs (Coselli 2004). Current reinforcement requirements in Texas for CIP slabs are No. 4 bars spaced 9 in. on center in the longitudinal direction and No. 5 bars spaced 6 in. on center in the transverse direction.

Another issue is that significant numbers of PCPs are rejected due to cracking that occurs during fabrication and transportation. The cracks usually form as shown in Figure 1-3. To be accepted by TxDOT, the following conditions should be satisfied (TxDOT 2004):

- i) any cracks parallel to strands should not occur within 1 in. of the strand and their length should be less than 1/3 of the total length of the embedded strands
- ii) any transverse cracks should not cross two adjacent strands

If the rejection rate of PCPs is reduced, construction cost and time for fabricating additional PCPs can be reduced.

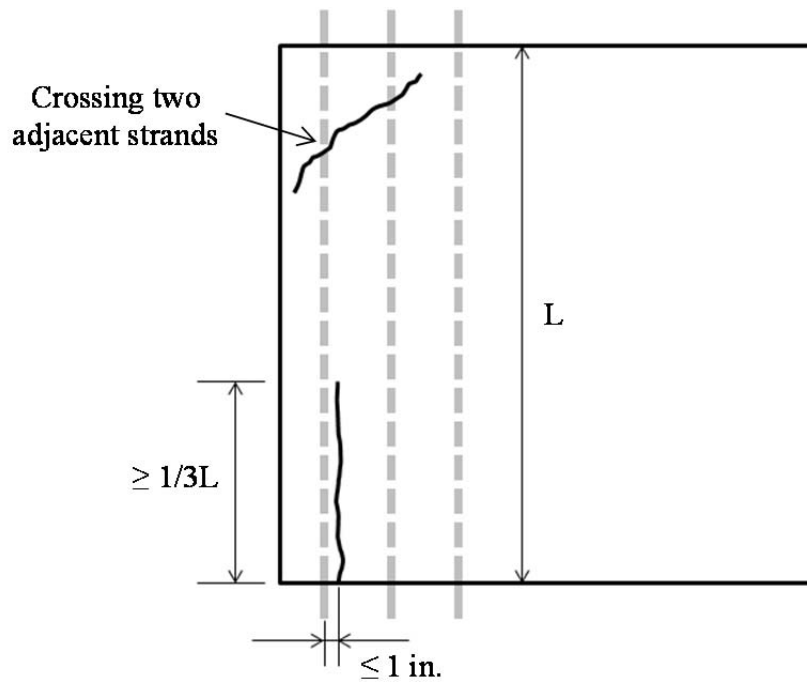


Figure 1-3: Criteria for rejection of precast panel

1.3 OBJECTIVES AND CONTRIBUTIONS OF THIS RESEARCH

The goal of this research is to propose more cost-effective design guidelines for CIP-PCP bridge deck systems. To achieve the goal, this study focuses on the following issues: i) optimization of top-mat reinforcement; and control of cracking in PCPs.

The first objective of this dissertation is to recommend optimized top-mat reinforcement layouts for CIP concrete slabs. In a previous study (Foster 2010), the following issues are verified: i) the longitudinal reinforcement currently required by TxDOT cannot be reduced; ii) transverse reinforcement can be further optimized; and iii) to determine an optimized reinforcement detail in the transverse direction, CIP-PCP interaction must simulate as closely as possible the boundary conditions in actual bridges.

To optimize reinforcement details in the transverse direction considering CIP-PCP interaction, bridge decks under construction were instrumented and large-scale restrained-shrinkage tests were conducted. Several reinforcement options, including

welded-wire reinforcement (WWR), were selected based on the test results from the previous study (Foster 2010). The selected options were installed in bridges near Houston and Belton. Their behavior after construction was monitored, and was evaluated by comparing observed strains to calculated cracking strains. The width and pattern of cracking in the instrumented bridges were inspected periodically. To evaluate the behavior of various reinforcement options, large-scale restrained-shrinkage tests were also conducted.

The second aim of this study was to reduce cracking in PCPs. In previous research studies (Foreman 2010; Azimov 2012), design options were suggested to control cracking in PCPs. One option was to reduce initial prestress force, and the other was to place additional transverse reinforcement at the edges of the panels. In this dissertation, only control of cracking along strands through reduction of prestress force is discussed.

Long-term prestress loss in PCPs with different levels of initial prestress was measured and the results were compared with losses predicted using models that were developed based on the test results of prestressed beams and girders. Some of the equations in codes may give reasonable results for PCPs because they were developed from the test results that exhibited wide scatter. However, they do not consider characteristics of PCPs, so they may not be accurate for all cases. Therefore, the available data on PCPs was analyzed and a model for losses in PCPs was developed.

The design recommendations of this study are intended to contribute to more cost-effective design of CIP-PCP bridge decks by reducing the amount of steel in CIP concrete, and by decreasing the number of rejected panels.

CHAPTER 2

LITERATURE REVIEW

2.1 INTRODUCTION

A CIP-PCP bridge deck consists of precast, prestressed concrete panels (PCPs) and a cast-in-place (CIP) concrete deck. As shown in Table 2-1, it has been used in many states (Sneed *et al.* 2010).

The thickness of PCPs ranges from 3 to 6 in., with the most common thickness being 3.5 in. Specified compressive strengths of concrete for PCPs are generally greater than those of the CIP topping. Specified concrete strengths of PCPs range from 4,000 to 10,000 psi, and those of CIP topping range from 3,500 to 5,800 psi. The trend for PCPs is towards higher compressive strength and reduced panel thickness.

Six states have been using CIP-PCP bridge decks for fewer than 20 years; three states have been using the system for 20 to 30 years; and three states have been using the system for 30 to 40 years.

The CIP-PCP bridge decks have following advantages:

- i) Fast construction;
- ii) Less formwork;
- iii) Easy construction at sensitive sites; and
- iv) Better durability

Table 2-1: Summary of survey of state transportation agencies that use CIP-PCP bridge decks (Sneed et al. 2010)

State	PCPs			CIP topping		Ages (year)
	Thickness (in.)	Reinforcement type	f'_c (psi)	Curing method	f'_c (psi)	
Arkansas	-	EC	5,800	MC	5,800	-
Colorado	-	PR, MR	5,000	LM, WC	5,000	16
Florida	-	PR, EC	-	-	-	40
Georgia	6	PR, MR	5,000	MC, WC	3,500	28
Hawaii	3.5	PR, MR	6,000	MC, LM	4,000	14
Iowa	3.5	PR, EC, MR	10,000	WC	3,500	25
Kansas	3-3.5	PR, EC	4,000	MC	4,000	20
Kentucky	-	PR, EC		MC	5,000	10
Michigan	-	EC	4,000	MC	4,000	-
Minnesota	3.5	PR, EC, WWR	6,000	MC	4,000	8
Missouri	3	PR	6,000	MC, LM	4,000	35
Oklahoma	4	PR	5,000	MC	4,000	15
Tennessee	3.5-4	PR	4,000	MC, LM	4,000	33
Texas	4	PR	5,000	MC, WC	4,000	25

PR=Prestressing reinforcement, EC=Epoxy-coated reinforcement, WWR=Welded-wire reinforcement, MR=Uncoated mild reinforcement, MC=Moisture curing, WC=Water-proof curing, LM=Liquid membrane curing

2.2 ISSUES IN CIP-PCP BRIDGE DECKS

To identify key aspects of the behavior of CIP-PCP bridge decks, an in-depth literature review was conducted. Similar reviews were conducted in theses by Foster (2010), Forman (2010) and Azimov (2012). These theses dealt with different aspects of the research project TxDOT 0-6348. The content of this chapter includes the reviews in those theses as well as additional literature.

2.2.1 Issues in CIP slabs

2.2.1.1 Arching action in bridge decks

Most bridge decks have greater flexural strength than is customarily assumed in design, because of arching action. Arching action increases strength because of the in-plane restraint in a deck from surrounding portions of the deck. This horizontal restraint results in compressive membrane action. This phenomenon was defined by Ockleston (1958), and has been studied by many researchers. The effects of the compressive membrane forces on flexural strength of deck are negligible before cracking, but the compressive membrane force could cause considerable increase of flexural strength of the deck after cracking (Fang *et al.* 1986; Fang *et al.* 1990; Klingner *et al.* 1990; Kim *et al.* 1994; Graddy *et al.* 1995; Graddy *et al.* 2002). Figure 2-1 shows arching action in concrete slabs.

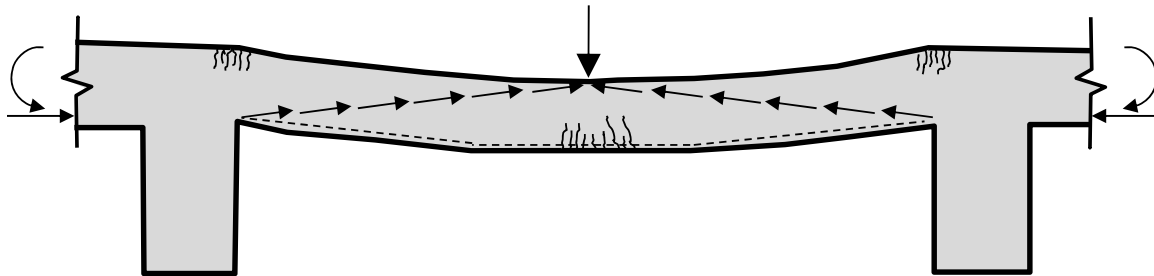


Figure 2-1: Arching Action in Concrete Slabs (adopted from (Foster 2010))

2.2.1.2 Conservatism in bridge deck design

Significant reserve strength of bridge decks has been confirmed by recent studies (Coselli 2004; Coselli, Griffith *et al.* 2006). Through tests conducted by Coselli in 2004 using a full-scale CIP-PCP bridge deck, it was observed that decks tested could carry 3 times the HS-25 design load on an overhang and more than 5 times the design load on interior spans. This reserve strength is due partially to arching action of the bridge deck and also to the conservative nature of design standards. As a result, it may be possible to

reduce reinforcement in some bridge decks. A deck without any reinforcement can resist twice its design load (Batchelor and Hewitt 1976).

2.2.1.3 Typical cracking in CIP-PCP bridge deck: reflecting cracks

To optimize top-mat reinforcement, it is important to understand the cracking pattern in CIP-PCP bridge decks. The main role of top-mat reinforcement is to control the widths of cracks in a bridge deck.

Figure 2-2 shows typical cracking in a CIP-PCP bridge deck. The cracks lie along the edges of the panels, and reflect the discontinuity between the PCPs and between the PCPs and CIP concrete. The cracks that run parallel to the direction of traffic are labeled longitudinal cracks, and the cracks perpendicular to the direction of traffic are labeled transverse cracks.

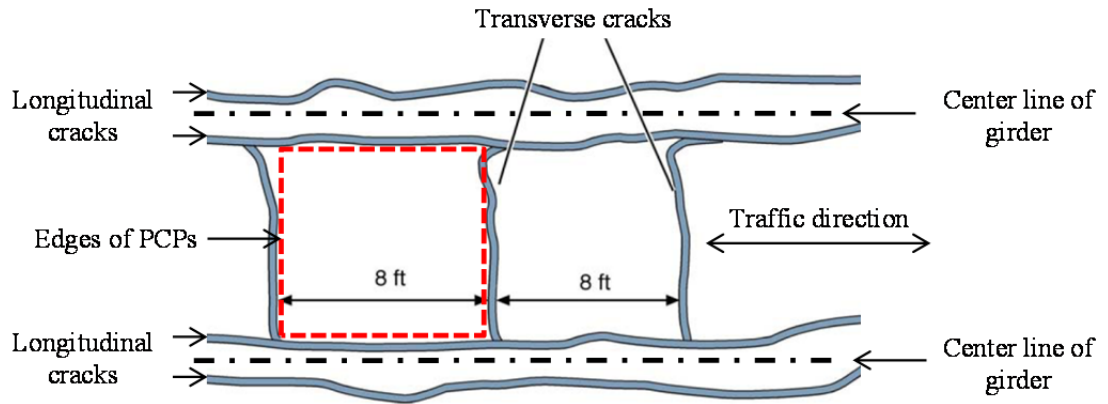


Figure 2-2 Reflected cracking in top surface of CIP-PCP bridge deck

(Folliard et al. 2003)

Transverse cracking in bridge decks is caused by creep and shrinkage deformations in CIP slabs and PCPs. In most case, the deformations in the PCPs are smaller than that in the CIP slabs, because old PCPs are generally used, in which most deformation due to creep and shrinkage has already occurred. Shrinkage deformation in the CIP slabs is restrained at the supports, and causes tensile stress throughout the CIP

deck. Because old PCPs experience less shrinkage than the deck overlying the panels, they restrain the shrinkage of that deck. Because of the discontinuities at panel edges, cracks tend to form along the joints. If new PCPs are used, their shrinkage and creep produce tensile stresses in the deck at panel edges, exacerbating deck cracking. Because most transverse cracks develop before the bridge deck is opened to traffic, traffic load is not a main cause of transverse cracking. However, it can widen existing cracks. The type of girder supporting the panels does not affect cracking in the transverse direction (Krauss and Rogalla 1996).

Longitudinal cracks develop in the negative-moment regions of the CIP deck, over the girder. Their occurrence is affected by the type of girder. A bridge with steel girders is more susceptible to longitudinal cracking than a bridge with concrete girders because of smaller stiffness of steel girders (Krauss and Rogalla 1996). Longitudinal cracks usually do not occur before a bridge is opened to traffic. Loads on the bridge before opening the bridge to traffic are not large enough to crack the concrete. The main causes of longitudinal cracks are shrinkage deformation of the CIP deck and (with new PCPs) shrinkage and creep deformations of PCPs. Although the stress induced by creep and shrinkage may be large enough to crack the deck, the cracks will generally be quite narrow.

Restrained thermal deformation of concrete may cause cracking in both directions in the deck. Because the level of restraint is generally higher in the longitudinal direction than the transverse direction of a bridge deck, cracking due to restrained thermal deformations is more likely to occur in the transverse direction than in the longitudinal direction of the deck.

The coefficient of thermal expansion (CTE) is usually a function of the coarse aggregate type; river gravel has a higher CTE than limestone (Lukefahr and Du 2010). In studying means of controlling thermal cracking in concrete at early ages, Riding *et al.* (2009) conclude that thermal cracking can be reduced by replacing aggregates with a high CTE by aggregates with a low CTE, and by casting the deck at cooler times of the day.

2.2.1.4 “Texas poor-boy” joint

The “Texas poor-boy joint,” commonly used in Texas, is made by casting a continuous concrete slab over the girders, with reinforcement placed in the continuous slab to control crack widths over the joint (Figure 2-3).

No closure strip is cast and no construction joints are used at the ends of the girders. Cracks form in the deck at the ends of the girders due to negative moment and long-term shrinkage of the deck. Because no special attention is given to the slabs over the ends of the girders, the cost of construction and maintenance of joints between girders can be reduced.

Roberts *et al.* (1993) note that the poor-boy joint behaves very similarly to a joint where the space between the girders is filled with concrete. In bridge design, however, the poor-boy joint region is treated as simply supported, implicitly accounting for possible yielding over time of the reinforcement crossing the joint.

The bridges instrumented in this study (Chapter 3) included the “Texas poor-boy joint.” Tests were conducted to determine whether the amount of top-mat reinforcement crossing the poor-boy joint could be reduced. In addition, the bridges were instrumented with gages to monitor cracking at the poor-boy joint and cracks were monitored following completion of the bridge decks.

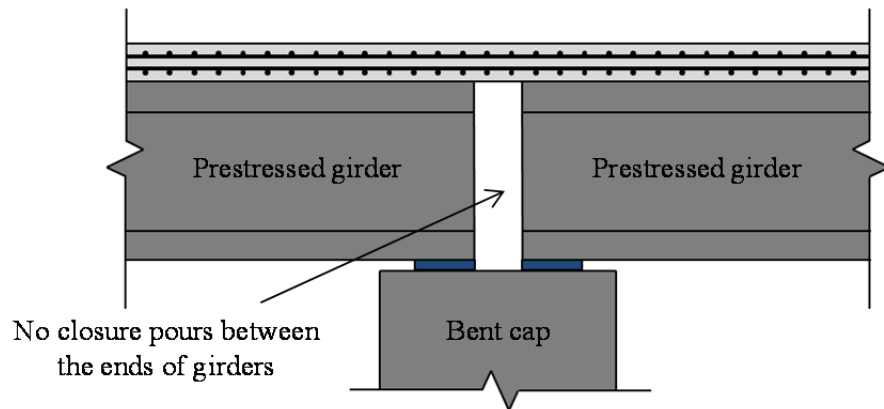


Figure 2-3: “Poor-boy” Joint (adapted from Roberts et al. 1993)

2.2.1.5 Welded-wire reinforcement

Welded-wire reinforcement is a possible design option for top-mat reinforcement of bridge decks due to its high strength, bonding characteristics, and ease of placement. Welded-wire reinforcement is prefabricated, so construction time, labor and field errors can be reduced (Bernold *et al.* 1989).

Ayyub *et al.* (1994) tested ultimate strength and ductility of various types of welded-wire reinforcement from different countries (United States, Germany, and Canada) to encourage engineers to use welded-wire reinforcement in field. They conclude that US welded-wire reinforcement has mechanical properties appropriate for use in bridge decks. They note that tempering wire and coating it with epoxy might decrease its strength, but also increase its ductility (Ayyub *et al.* 1994).

Russo (1999) focused on differences in behavior of concrete slabs depending on ductility of welded-wire reinforcement. Two prestressed double-T concrete slabs were tested; one was reinforced with high-ductility welded-wire reinforcement, and the other with normal welded-wire reinforcement. The slab reinforced with high-ductility welded-wire reinforcement had higher maximum moment and larger curvature at failure (Russo 1999).

Soltani *et al.* (2004) studied effects of arrangement of wire on ductility, cracking, and post-cracking performance, using RC membrane elements subjected to in-plane stress. They observed that specimens reinforced with welded-wire reinforcement have smaller crack spacing and narrower crack width than specimens reinforced with standard deformed bars, because welded-wire reinforcement has higher anchorage strength than normal deformed bars. They also found that crack spacing was not determined by the spacing of wire when that spacing is less than 20 times the wire diameter. The effect of tension stiffening was much greater with welded-wire reinforcement than with conventional deformed bars (Soltani *et al.* 2004).

Gilbert and Sakka (2007) studied failures of concrete slabs reinforced with low-ductility, welded-wire reinforcement. The slabs failed in a brittle manner with little plastic deformation and little stress redistribution. Based on the test results, they suggest that strength reduction should be considered when engineers design the slab with low-ductility welded-wire reinforcement (Gilbert and Sakka 2007).

2.2.2 Issues in PCPs as used in Texas

2.2.2.1 Panel rejection in the field

In Texas, about 200,000 square feet of PCPs for bridge decks are rejected every year, amounting to about 5 percent of the annual production of PCPs. There is concern that cracks collinear with the prestressing strand may lead to significant prestress loss and corrosion. This concern may not be entirely justified. As noted by Foreman (2010), strands do not lose prestress even in the presence of wide collinear cracks. Also, because CIP concrete slabs are cast over the PCPs, cracks in the top surface of PCPs would not appear to be a problem provided that the CIP topping is sound. Collinear cracks, if present in the bottom surface, could raise some durability issues.

2.2.2.2 Collinear cracking in PCPs

Figure 2-4 shows the forces acting on a prestressing strand in a PCP after release. An unrestrained strand would shorten; because the strand is restrained by the surrounding

concrete, forces are created that act inward on the concrete, away from the ends of the member, and outward on the strand, toward the ends of the member. The bond force acts on the circumferential surface of the strand. The magnitude of the bond force increases toward the ends of the strand. The reason is that bond force is proportional to the gradient of stress in the strand. The maximum gradient of the prestress occurs at the ends, and the value decreases as the distance from the ends increases (Figure 2-5).

The strand has reduced diameter before release due to initial applied prestress. After release, the strand at the ends tends to regain its original diameter and expand circumferentially because the prestress force is zero at the ends (Figure 2-5). This radial expansion is due to Poisson's effect and this expansion is restrained by surrounding concrete. Therefore, radial force toward the strand develops and acts on the strand. The magnitude of the radial force at the ends is larger than that at the center, because radial deformation of the strand at the ends is bigger than that at the center. These two forces in the axial and radial directions result inclined force acting toward the strand.

Figure 2-6 shows the force acting in the surrounding concrete when the strand is released. To resist the force acting on the strand shown in Figure 2-4, an inclined force acts on the concrete. The direction of the inclined force in concrete is opposite to the direction of the force acting on the strand. The inclined force in the concrete produces circumference tensile stress and if its value is greater than the tensile strength of concrete, crack forms along the strand. This crack is called a collinear crack.

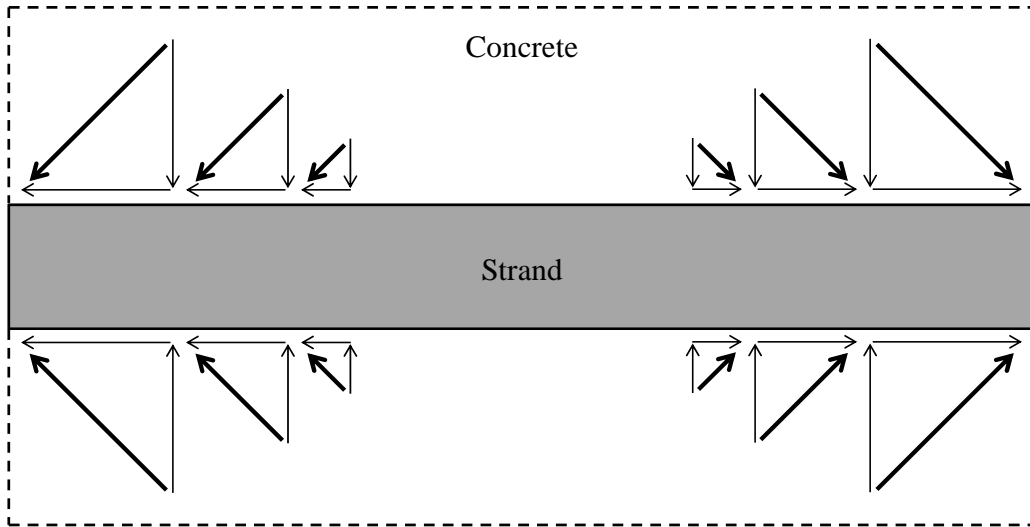


Figure 2-4: Force acting on a strand after release

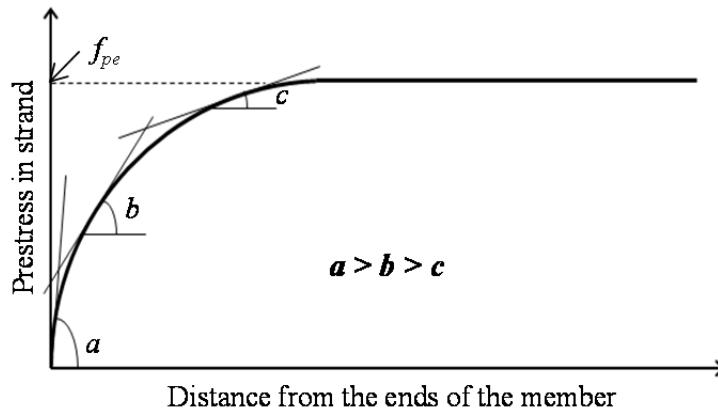


Figure 2-5: Gradient of prestress in strand after releasing

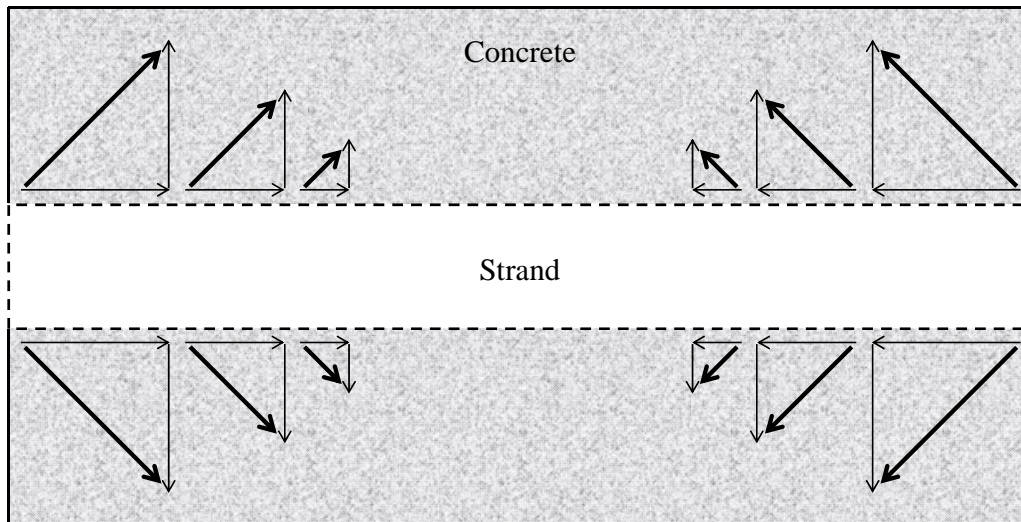


Figure 2-6: The force acting in the surrounding concrete

Collinear cracking usually starts at the edge of the panels and extends toward the center. The potential for collinear cracking increases if prestress force in the strand is released suddenly, or if the strand has insufficient transfer length (Sneed *et al.* 2010).

Circumferential stresses are also created in the concrete surrounding the strand due to Poisson's effect (Figure 2-7). In the figure, the red block represents the original shape before applying loading. The blue block represents the deformed shape after loading. When a material is loaded in one direction, the material usually deforms perpendicular to the loading direction. This phenomenon is called Poisson's effect. Poisson's effect can be quantified by calculating Poisson's ratio. Poisson's ratio is obtained by dividing the strain in loading direction by the strain normal to the loading direction. The ratio ranges from 0.0 to 0.5. Generally, Poisson's ratio for steel is 0.3 before yield and 0.5 after yield.

When releasing the strands, the stress at both ends of the strands becomes zero. Due to the zero stress at both ends after release, the length of the strands is reduced, and the diameter of the strands increases due to Poisson's effect. This radial expansion causes circumferential tensile stress in the surrounding concrete (Hoyer effect). If the tensile stress is larger than the tensile strength of the surrounding concrete, it may cause

cracks in PCPs. However, if the strength of concrete and depth of clear cover are large enough to resist this expansion, a wedge may be created by the Hoyer effect as shown in Figure 2-8 (Collins and Mitchell 1991). This wedge effect helps transfer prestress from strand to concrete (Krishnamurthy 1971; Krishnamurthy 1973).

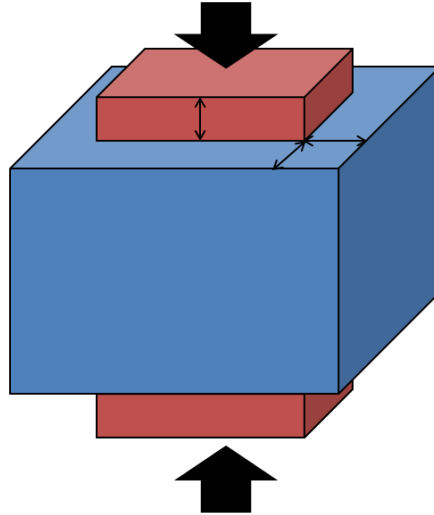


Figure 2-7: Poisson's effect

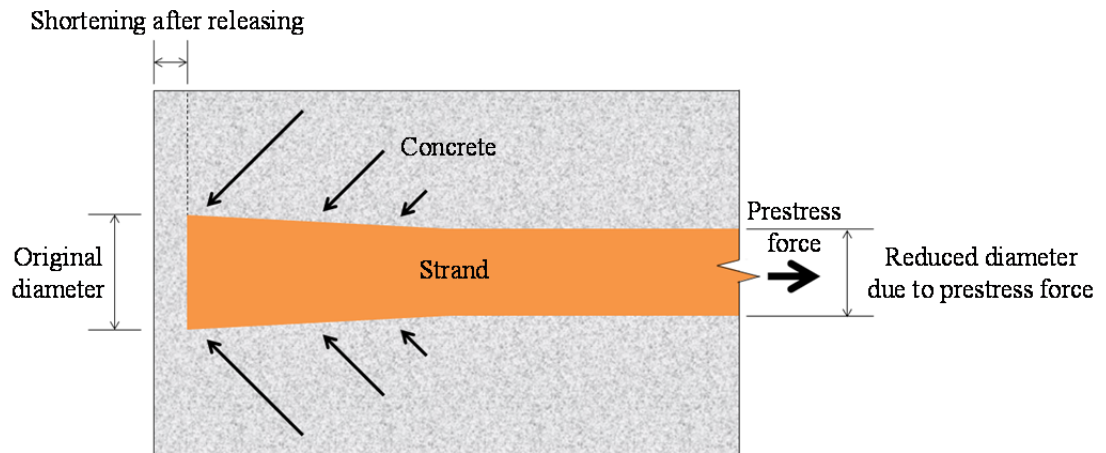


Figure 2-8: Forces on strand due to “wedge” created by Hoyer effect

2.2.2.3 Ageing and creep coefficients

To determine the rate of loss initial prestress, the first step is to evaluate time-dependent deformation, using reliable creep and ageing coefficients. The creep coefficient is the ratio of creep strain to elastic strain under constant load, and is designated as ‘ ϕ ’ in most references. The ageing coefficient, developed to account for changes in load over time, is generally expressed as ‘ χ ’. For example, if the specimen is subjected to constant stress from time t' to time t , the creep deformation can be calculated by multiplying elastic strain by $\phi(t, t')$. However, if the load changes with time, the creep deformation can be calculated by multiplying elastic strain by $\chi(t, t')$ and $\phi(t, t')$ (Neville *et al.* 1983).

Several researchers (Bazant 1972; Tadros, Ghali *et al.* 1975; Dilger 1982) suggest that a reasonable range for the creep coefficient is 0.6 to 0.8. Creep and ageing coefficients under specific environmental conditions have been studied by Shrestha and Chen (2011).

ACI 209 provides options for determining creep and shrinkage effects. In Chapter 5, prestress losses are discussed in more detail.

2.3 STUDIES CONDUCTED UNDER TxDOT PROJECTS 0-4098 AND 0-6348

In TxDOT 0-4098, restrained creep and shrinkage were studied and the procedure used was adopted in this study (Chapter 4). Foster (2010), Foreman (2010), and Azimov (2012) reported on studies conducted under project TxDOT 0-6348 and their data was used in this dissertation. Therefore, those studies are summarized here.

2.3.1 TxDOT Project 0-4098

The objective of TxDOT Project 0-4908 was to find the most promising concrete mixtures for preventing or minimizing cracking due to drying shrinkage. Based on a literature review, the researchers selected several concrete mixtures and tested them using small- and large-scale laboratory tests. Several inspections of cracking in bridge decks were also conducted to evaluate characteristics of drying-shrinkage cracks in the field. In Figure 2-9, the test setup for the large-scale laboratory tests in Project 0-4098 is shown.

Shear studs and threaded reinforcing bars were firmly attached to the restraining frame and two PC panels were used for each specimen. Shear studs, reinforcing bars at end regions and PC panels restrain the CIP portion and result in cracking at the middle of the specimens. To force a crack to form at the middle of the CIP slab, no reinforcement was placed in the CIP slab across the joint between precast panels. No shear stud was installed in middle portion of the frame.

Based on test results from project 0-4098, it was concluded that drying-shrinkage cracking can be controlled by adding shrinkage-reducing admixture, fibers, calcium-sulfoaluminate admixture, or a high volume of fly ash to the concrete mixture.

The test setup for the restrained-shrinkage test in Chapter 4 was built using the test setup of the large-scale laboratory tests in Project 0-4098.

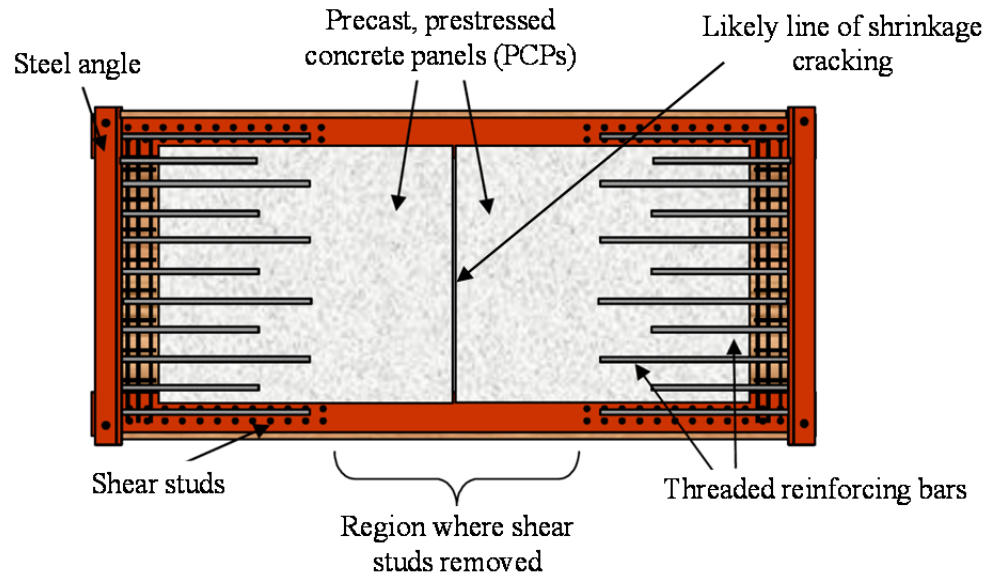


Figure 2-9: Restrained-shrinkage test setup of TxDOT Project 0-4098
(Folliard et al. 2003)

2.3.2 TxDOT Project 0-6348: Foster (2010)

The objectives of this research were to optimize top-mat reinforcement in a CIP-PCP bridge deck considering the effects of PC panels on cracking in CIP slabs. Foster reviewed several different formulas for crack width calculations and suggested possible design options for top-mat reinforcement (Foster 2010). The selected reinforcement options were tested in the lab using bending tests and direct tensile tests.

Figure 2-10 and Figure 2-11 show two different bending test setups. In the bending moment tests, composite specimens consisting of CIP slab and PCPs were used to consider the effects of the PC panel on cracking in CIP slabs. However, the cracking pattern of the test specimens did not match the pattern shown in Figure 2-2. In the bending tests, multiple cracks occurred in the uniform moment region and delamination between the CIP deck and the PCPs was observed. The loading condition in the tests did not simulate the shrinkage conditions in a real bridge deck.

To overcome these problems, Foster applied direct tension to composite specimens (Figure 2-12). Tensile load was applied through the reinforcement in the CIP

portion. In this test, delamination was still observed due to eccentricities of geometry between the geometry of the specimen and the loading (Figure 2-13).

Finally, Foster used a direct tensile test of the CIP portion of the bridge deck (Figure 2-14). To force the first crack to form at the mid-height of the specimen and to minimize geometrical eccentricity of the specimen, a saw cut was made on both sides of the specimens. While the test provided information on the relationship between crack width and steel stress, CIP-PCP interaction was not included. Longitudinal cracks, which are controlled by transverse reinforcement, occur due to restrained shrinkage of CIP slabs and creep of PC panels neither of which was reflected in the test specimens.

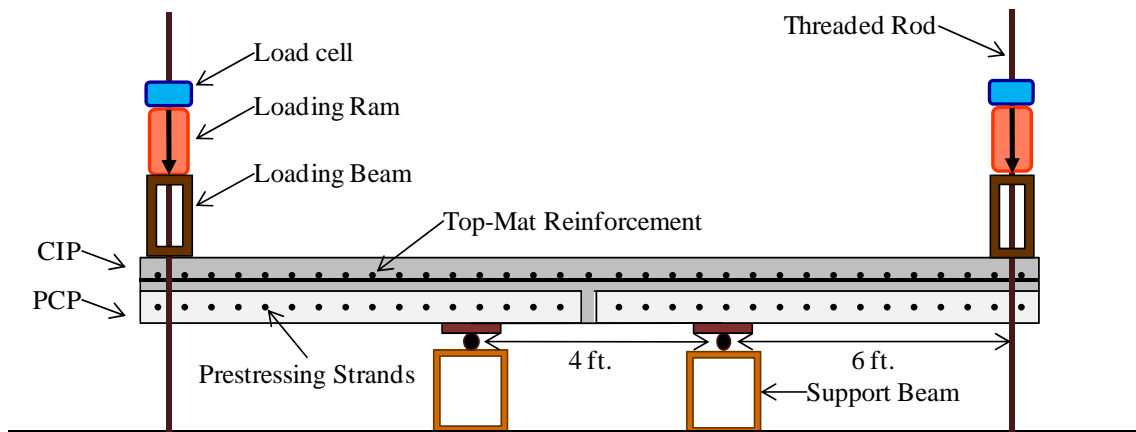


Figure 2-10: Constant bending moment test setup (Foster 2010)

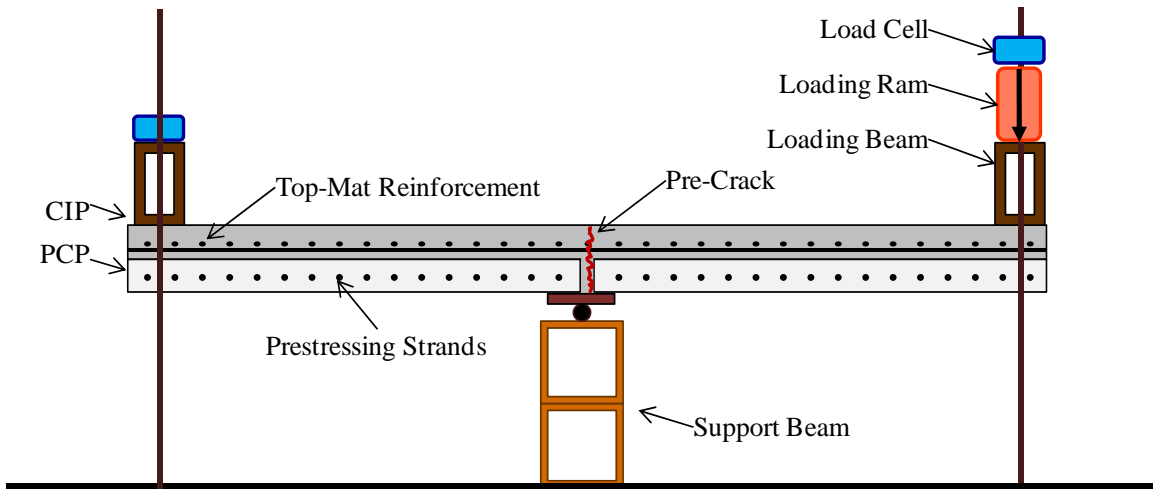


Figure 2-11: Concentrated-load test setup (Foster 2010)

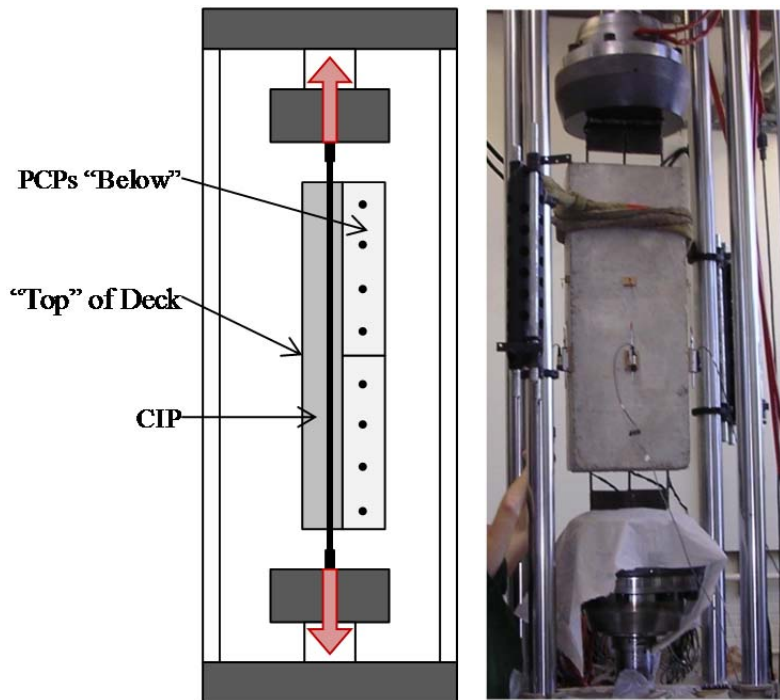


Figure 2-12: Direct tensile test using composite specimen (Foster 2010)



Figure 2-13: Delamination during direct tensile test (Foster 2010)

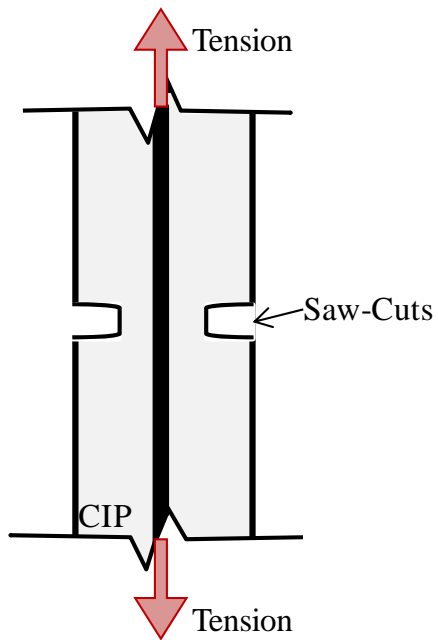


Figure 2-14: Direct tensile test using non-composite specimen (Foster 2010)

Based on the test results, Foster found that current top-mat reinforcement in the longitudinal direction (No. 4 bar @ 9 in.) is already optimized, but further reduction may be possible for the reinforcement in the transverse direction. Smaller-diameter

reinforcement or welded-wire reinforcement were recommended as possible design options for the transverse direction.

2.3.3 TxDOT Project 0-6348: Foreman (2010) & Azimov (2012)

The goal of both studies was to reduce collinear cracking in PCPs. Two possible design approaches were proposed. The first is to reduce the initial prestress force from 16.1 kips per strand to 14.4 kips per strand. The second is to place additional transverse reinforcement at the ends of the panel perpendicular to prestressing strands. To verify effects of both recommendations, long-term prestress loss was monitored using PCPs with different levels of initial prestress (Figure 2-15), and knife-edge tests were conducted (Figure 2-16). Detailed information about the long-term monitoring is given in Chapter 5.



Figure 2-15: Long-term monitoring of prestress loss in PCPs

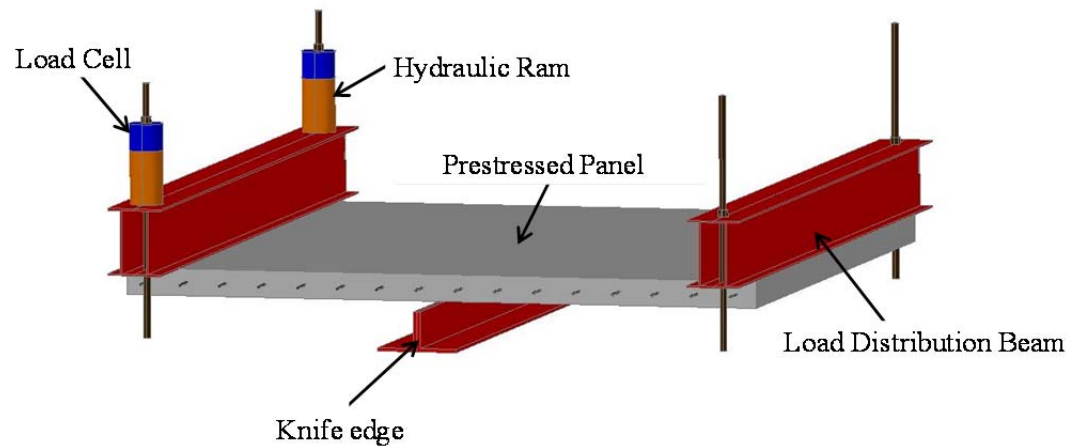


Figure 2-16: Knife-edge test (Foreman 2010)

The objectives of the knife-edge test (Figure 2-16) were to find the effects of additional transverse bars on control of collinear cracking, and the relation between prestress loss and crack width. The test panel was positioned so that a prestressing strand was located directly over the knife edge. All strands were parallel to the knife edge. Negative bending moment was applied on the panel using two hydraulic rams. The highest bending moment occurred along the knife edge, and cracks formed along the strands. Through the knife-edge test, two conclusions were derived:

- i) Placing additional transverse bars at ends of PC panels helped control collinear cracking in the panels; and
- ii) Slip of prestressing strands did not start until collinear cracks become very wide.

CHAPTER 3

OPTIMIZATION OF REINFORCEMENT IN CIP SLABS: FIELD APPLICATION

3.1 INTRODUCTION

The objective of the field studies is to compare the behavior of selected top-mat reinforcement options and to suggest optimized reinforcement layouts for CIP slabs. Field instrumentation provides a means of obtaining data that cannot be obtained in the laboratory, where the CIP-PCP interface and boundary conditions of CIP-PCP bridge decks are difficult to simulate. Two structures were investigated: the Wharton-Weems Overpass near Houston (Texas), and the Lampasas River Bridge near Waco (Texas).

3.2 WHARTON-WEEMS OVERPASS

3.2.1 Description

The Wharton-Weems Overpass is located in the Houston District, at the intersection of Choate Road and Shoreacres Boulevard. The overpass consists of three identical spans, each of which has 9 girders. The overpass has a very slight skew. The CIP concrete slabs and the PCPs are both 4-in. thick, producing an 8-in. composite deck slab. In Figure 3-1 and Figure 3-2, overall views of the Wharton-Weems Overpass are presented.

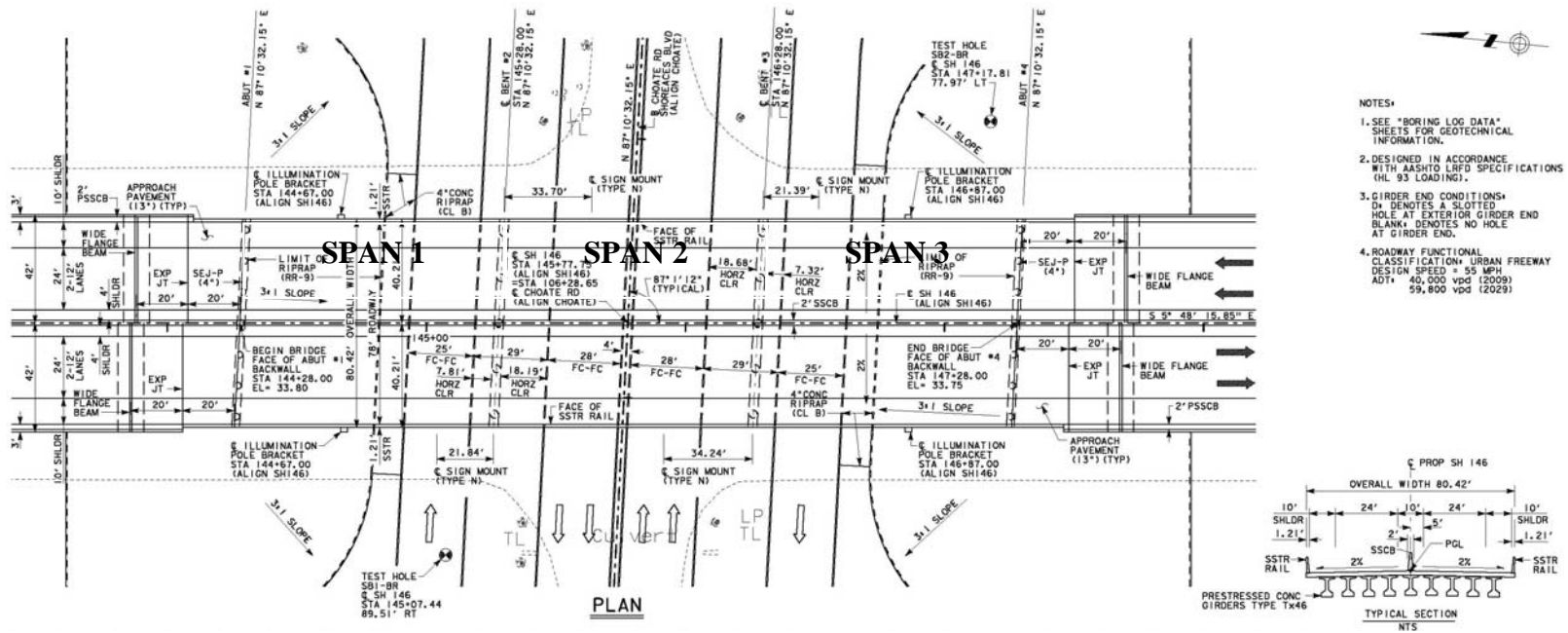


Figure 3-1: Plan view, Wharton-Weems Overpass

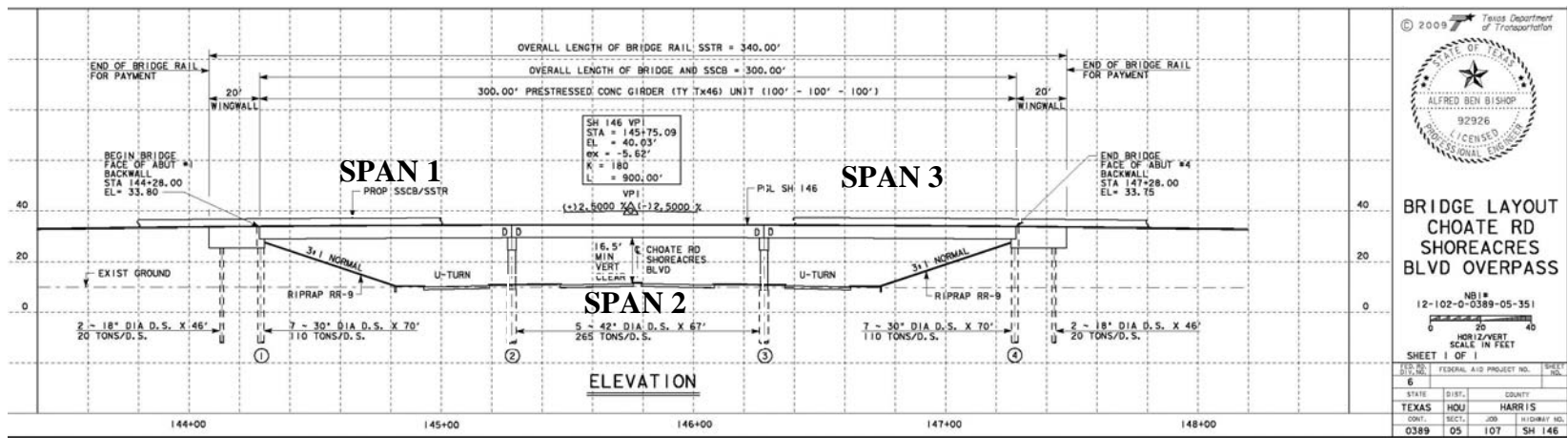


Figure 3-2: Section view, Wharton-Weems Overpass

3.2.2 Top-mat reinforcement options for Wharton-Weems Overpass

The top-mat reinforcement options for the Wharton-Weems Overpass are shown in Figure 3-3. As shown in the figure, two spans contained Current TxDOT Standard Reinforcement and one span contained Reduced Deformed-Bar Reinforcement. In the Reduced Deformed-Bar Reinforcement option, the reinforcement layout for the longitudinal direction is the same as the Current TxDOT Standard Design (No. 4 @ 9 in.); for the transverse direction, however, the diameter of the bar is reduced.

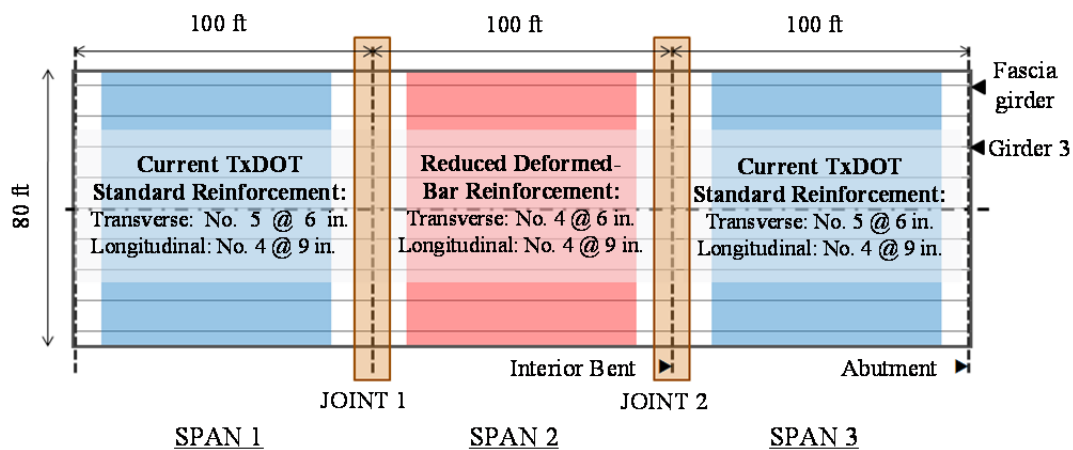


Figure 3-3: CIP deck reinforcement options, Wharton-Weems Overpass

3.2.3 Splice details

3.2.3.1 Longitudinal splices

Details of the longitudinal splices are shown in Figure 3-4 to Figure 3-6. Splices were located away from joints, and the longitudinal splice length was calculated using Equation 3-1 (Equation 12-1 of ACI 318 (2011)). Red lines represent the reinforcement in the Reduced Deformed-Bar Reinforcement option and blue lines represent the reinforcement in the Current TxDOT Standard Design. Detailed calculations of splice length are shown in Appendix A.

$$\frac{l_d}{d_b} = \frac{3}{40} \frac{f_y}{\lambda \times \sqrt{f'_c}} \frac{\psi_t \times \psi_e \times \psi_s}{\left(\frac{c_b + K_{tr}}{d_b}\right)} \quad \text{Equation 3-1}$$

(Eq. 12-1, ACI 318-11)

- Where,
- l_d = development length in tension, in.
 - d_b = nominal diameter of bar, in.
 - f_y = specified yield strength of reinforcement, psi
 - f'_c = specified compressive strength of concrete, psi
 - ψ_t = factor used to modify development length based on reinforcement location
 - ψ_e = factor used to modify development length based on reinforcement coating
 - ψ_s = factor used to modify development length based on reinforcement size
 - λ = modification factor related to unit weight of concrete
 - c_b = smaller of (a) the distance from center of bar to nearest concrete surface, and (b) one-half the concrete center-to-center spacing of bars or wires being developed, in.
 - K_{tr} = transverse reinforcement index

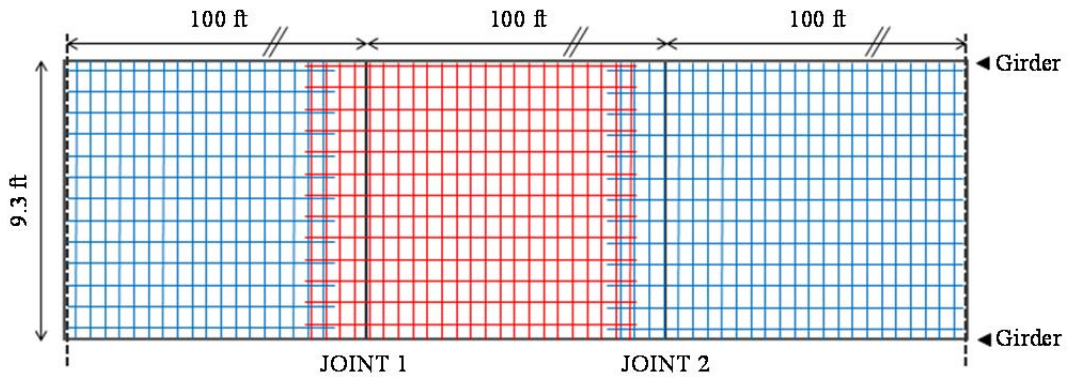


Figure 3-4: Details of longitudinal splices, Wharton-Weems Overpass

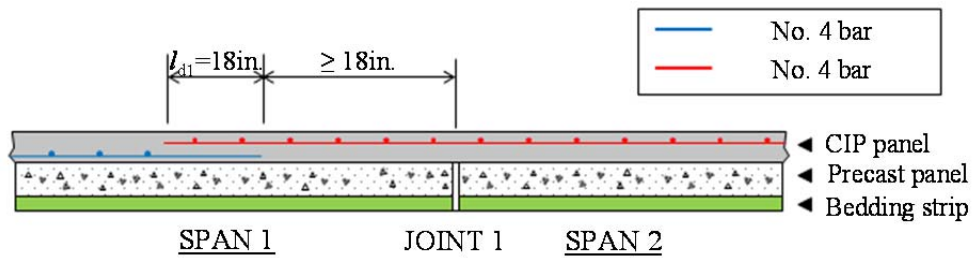


Figure 3-5: Section showing details of longitudinal splices, Wharton-Weems Overpass (Joint 1)

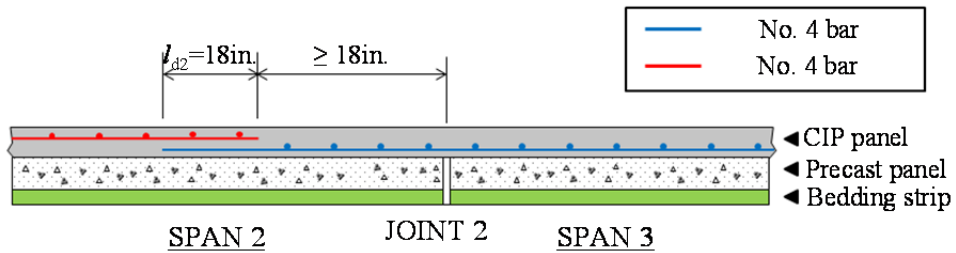


Figure 3-6: Section showing details of longitudinal splices, Wharton-Weems Overpass (Joint 2)

3.2.3.2 Transverse splices

Details of transverse splices are shown in Figure 3-7 to Figure 3-10. Splice lengths are calculated using the same equation used in the longitudinal direction (Equation 3-1), and detailed calculations are shown in Appendix A.

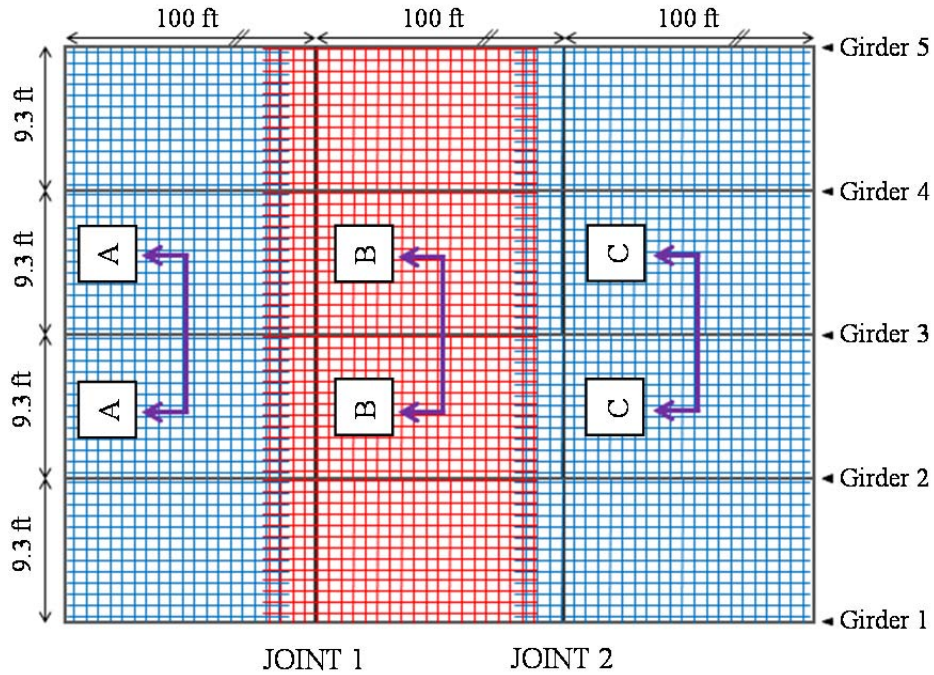


Figure 3-7: Details of transverse splices, Wharton-Weems Overpass

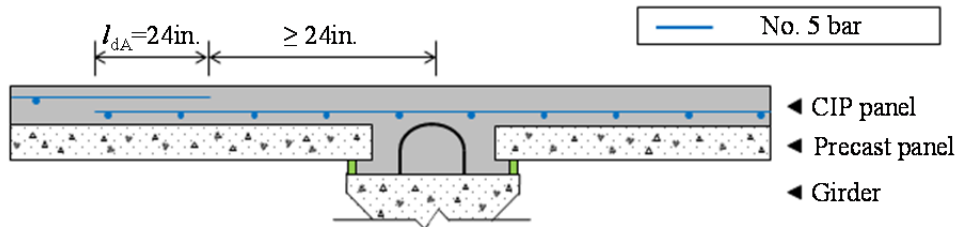


Figure 3-8: Details of transverse splices, Wharton-Weems Overpass (Section A-A)

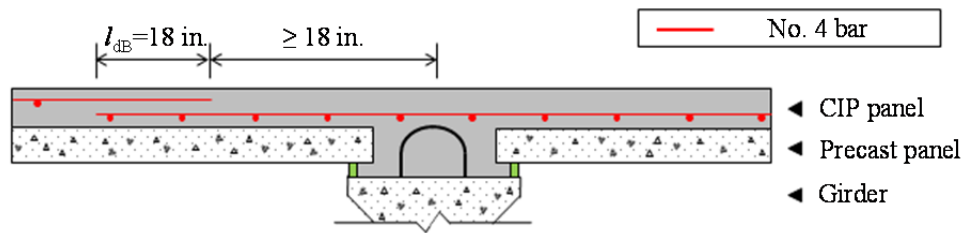


Figure 3-9: Details of transverse splices, Wharton-Weems Overpass (Section B-B)

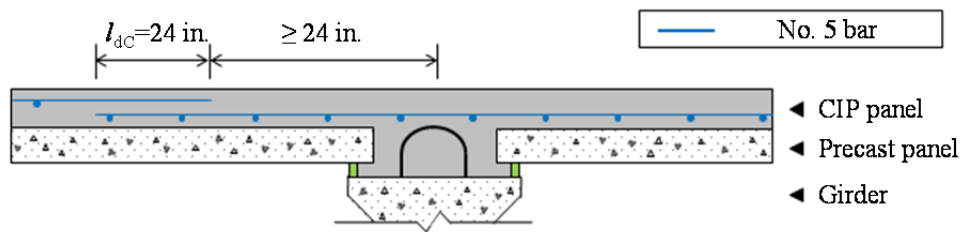


Figure 3-10: Details of transverse splices, Wharton-Weems Overpass (Section C-C)

3.2.4 Instrumentation of Wharton-Weems Overpass

3.2.4.1 Vibrating-wire gages

Geokon Vibrating-Wire Gages (VWGs), Model VCE-4200, were installed to measure strains in the CIP deck of the Wharton-Weems Overpass. VWGs were attached to top mat reinforcement. The strain values from VWGs represent the strain in the concrete at the same level as that of the bars, assuming perfect bond between reinforcement and concrete. Field installation of a typical VWG is illustrated in Figure 3-11. Each gage was attached to the reinforcement using two wood blocks and plastic zip-ties. The gages should be aligned with the reinforcement, and this orientation should not change during casting. It is also important not to apply bending moment to the gages during installation because it can cause inaccurate measurement. Bending moment can be applied to the gages during installation when the heights of wood blocks are not the same or the two plastic zip-ties have different tensions.

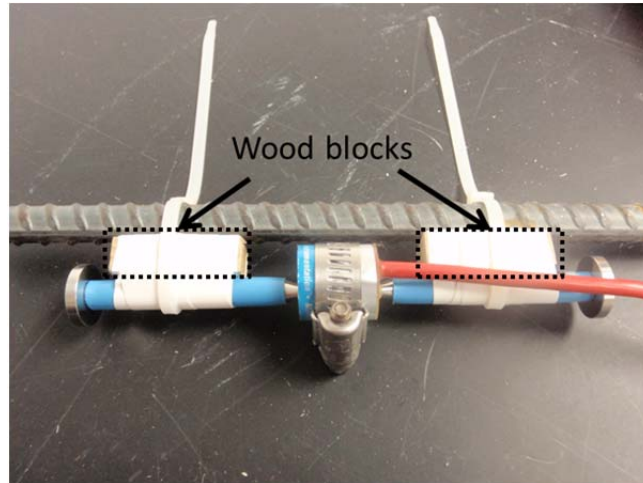


Figure 3-11: Typical VWG as installed on the reinforcement

3.2.4.2 Gage location and identification

The gage designations are as follows:

- i) Longitudinal gages are denoted as “Lxx”. Odd-numbered gages are located over the fascia girder. Even-numbered gages are placed over Girder 3.
- ii) Transverse gages are denoted as “Txx”. Gages T03 to T06 are located at 25 feet from Joint 2, and T01, T02 and T07, T08 are located 75-ft away from Joint 2. Odd-numbered gages are placed along Girder 2, and even-numbered gages are placed along the centerline of the bridge.

Figure 3-12 and Figure 3-13 show the gage layout for longitudinal bars and for transverse bars, respectively. The brown star in these figures indicates the location of data-acquisition equipment.

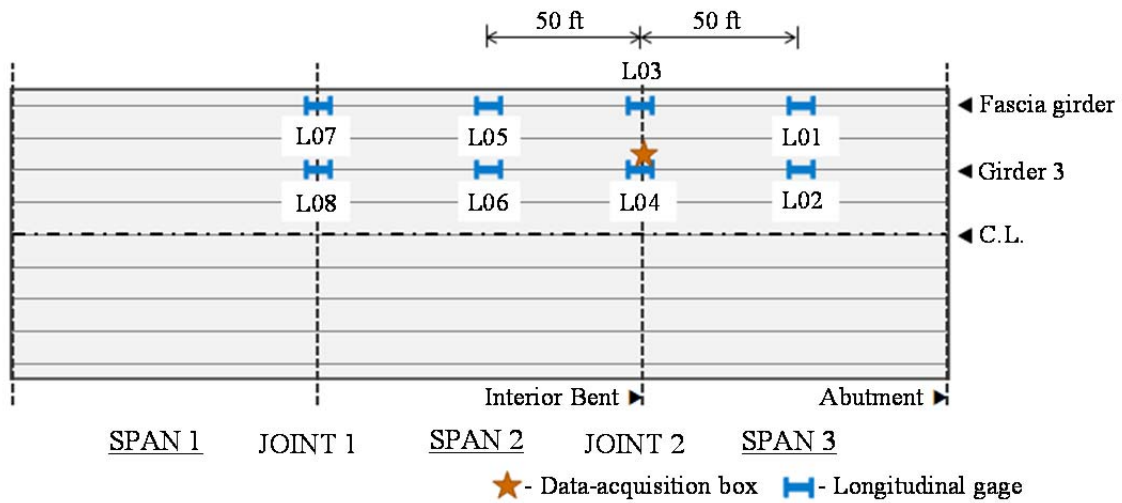


Figure 3-12: Gage layout for longitudinal bars, Wharton-Weems Overpass

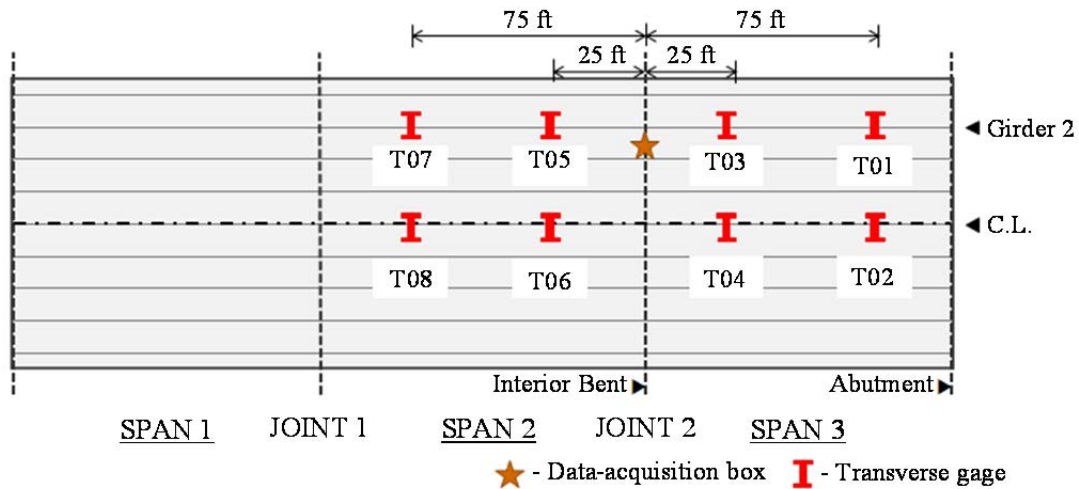


Figure 3-13: Gage layout for transverse bars, Wharton-Weems Overpass

3.2.4.3 Data-acquisition equipment

Data are recorded automatically and monitored using a wireless connection. Data-acquisition system for the Wharton-Weems Overpass is shown in Figure 3-14, consists of a data logger, a multiplexer, an analyzer, a modem, a battery and a charge regulator. All components were placed in a stainless-steel box fastened to the bent between Girder 2 and 3 (Figure 3-15), because several wood braces were still in place between Girder 1 and 2.

The data-acquisition system is powered by a solar panel whose size was determined based on the number of vibrating-wire gages and the highest designed scanning rate. The south-facing solar panel was installed on the side face of the bent cap using anchor bolts. If the voltage from the solar panel exceeds a set level, the charge regulator makes an adjustment to avoid malfunction of the system. The battery provides a secondary power source when sunlight is insufficient to operate the system.

Before going to the field, all components of the instrumentation system were tested in the laboratory. The bracket for the solar panel, shown in Figure 3-16, was fabricated to permit the solar panel to face south and to prevent shading from the deck.

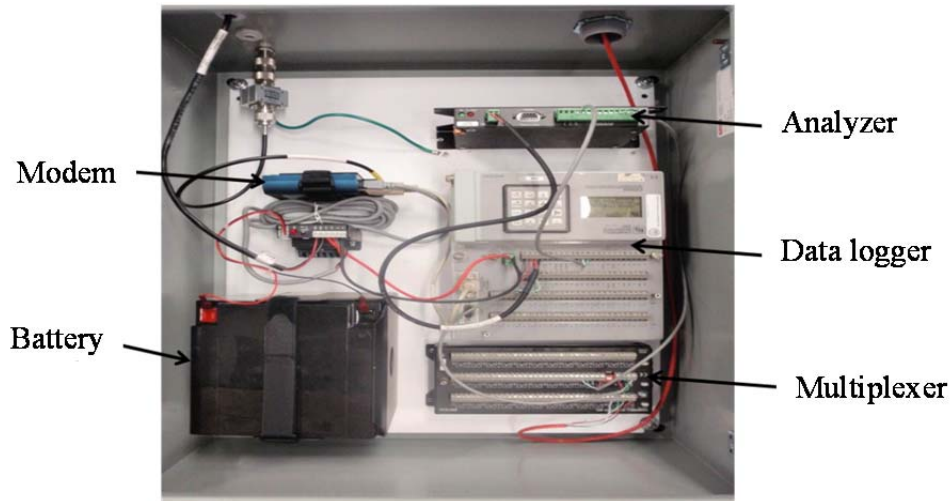


Figure 3-14: Solar-powered data-acquisition system, Wharton-Weems Overpass

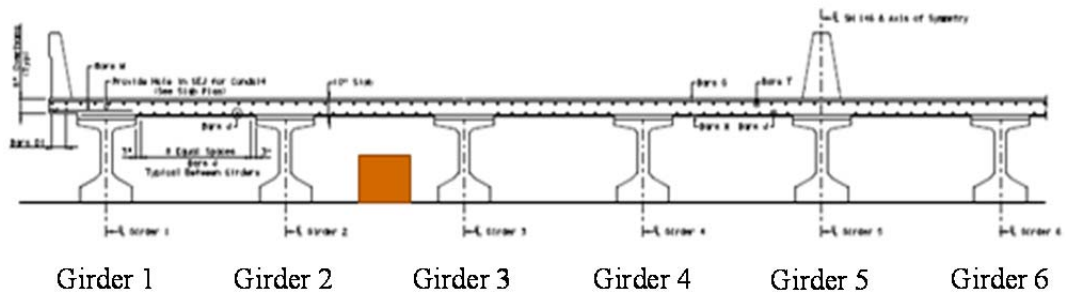


Figure 3-15: Location of data-acquisition box, Wharton-Weems Overpass



Figure 3-16: Bracket for solar panel, Wharton-Weems Overpass

3.2.5 Field instrumentation of Wharton-Weems Overpass

The Wharton-Weems Overpass was instrumented on July 25, 2011 after the contractor had placed all PCPs and the reinforcement for the CIP slab.

3.2.5.1 *Installing vibrating-wire gages*

Sixteen vibrating-wire gages were located as shown in Figure 3-17 and Figure 3-18. To identify the locations for gage installation easily, orange and yellow paint were sprayed over reinforcement at gage locations (Figure 3-17). Orange paint was used to mark locations for longitudinal gages, and yellow paint was used for transverse gages. All gage wires were routed under top-mat reinforcement to holes in the bedding strip under the PCPs (Figure 3-18). Before threading wires through the holes, gages were checked using a hand-held reader. After confirming proper connection between data logger and gages, gage wires were neatly arranged with zip-ties, and the holes in bedding strip were sealed with spray foam. During installation, the detection interval of the gages was 2 min. to make sure that connection between the data logger and the gages was maintained. Before casting, the interval was changed to 30 min. to save power and memory space in the data logger. The 30-min. interval was maintained for the next three months.



Figure 3-17: Gage instrumentation, Wharton-Weems Overpass



Figure 3-18: Threading wires through holes in bedding strip, Wharton-Weems Overpass

3.2.5.2 Placing data-acquisition box

The data acquisition-box was placed between Girder 2 and 3 on an interior bent. The box was anchored to the bent. Two bags of desiccant were placed in the box to protect the equipment from moisture. After connection, the hole for gage wires into the box was sealed using spray foam.

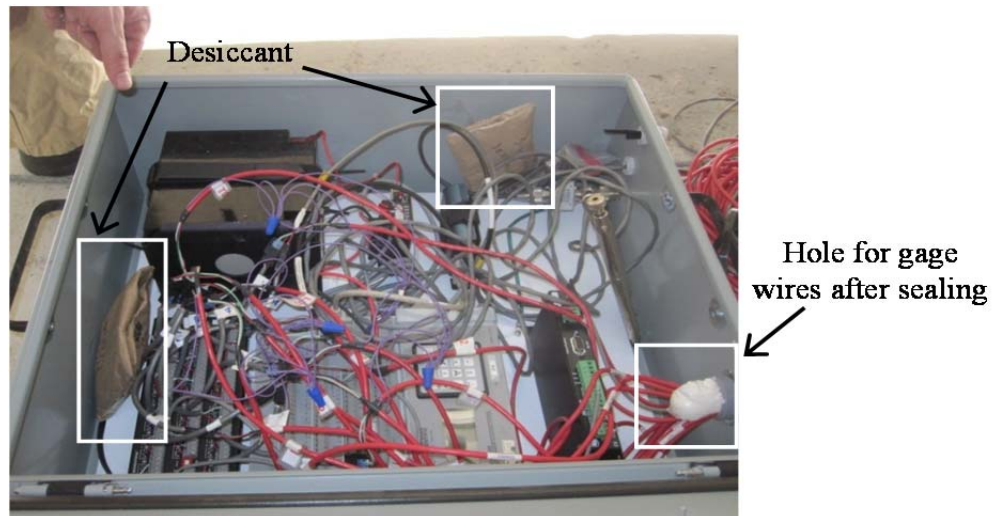


Figure 3-19: Data-acquisition box after connection, Wharton-Weems Overpass

3.2.5.3 Mounting solar panel

After mounting the solar panel and antenna to the bracket, the pre-fabricated bracket was installed on the side face of bent cap between Spans 2 and 3 after mounting the solar panel and antenna to the bracket. Power cables for the solar panel and antenna were routed to the data-acquisition box.



Figure 3-20: Mounting solar panel beside bent cap, Wharton-Weems Overpass

3.2.5.4 Casting concrete deck, Wharton-Weems Overpass

The concrete deck was cast on July 28, 2011 during a 9-hour period, using concrete with a specified compressive strength of 4000 psi. Two concrete pump trucks were used. The casting sequence is shown in chronologically in Figure 3-21. Water was sprayed on the surface of the precast panels (Figure 3-21 a) to avoid excessive early-age shrinkage of the CIP portion. The concrete was distributed over the deck by moving the hose from the concrete pump truck (Figure 3-21 b). The distributed concrete was consolidated with hand-held vibrators (Figure 3-21 c) and the surface was finished smoothly using a motorized trowel after screeding (Figure 3-21 d). Crack formers (“zip-strips”) were inserted along the transverse joints between spans (Figure 3-21 e) and curing compound was sprayed on the surface after bleed water had evaporated (Figure 3-21 f).



(a) Spraying water on panels



(b) Placing concrete



(c) Consolidating concrete



(d) Finishing surface



(e) Inserting crack former



(f) Spraying curing compound on deck surface

Figure 3-21: Construction sequence for CIP deck, Wharton-Weems Overpass

3.2.6 Results from Field Instrumentation of Wharton-Weems Overpass

3.2.6.1 Cracking inspection

The Wharton-Weems Overpass was inspected twice before it was opened to traffic on April 21, 2012. To observe cracks more clearly, water was sprayed on the surface. Because water in cracks evaporates more slowly than water on a sound surface, this procedure highlights cracks (Figure 3-22).



Figure 3-22: Spraying water on bridge deck for cracking inspection, Wharton-Weems Overpass

The first cracking inspection was conducted on September 12, 2011, and the result is shown in Figure 3-23. Yellow boxes in the figure refer to expected cracking locations based on readings from the vibrating-wire gages. Two transverse cracks along panel joints were expected, because strains measured by the gages which were

instrumented along the joints were much higher than the theoretical cracking strain. The theoretical cracking strain was calculated by dividing the expected cracking stress of the topping slab concrete by the elastic modulus of the concrete.

Two transverse cracks were located at the construction joints over the bents. The average crack width over Joint 1 was 0.013 in., and the average crack width over Joint 2 was 0.007 in. No longitudinal cracks were observed.

The second cracking inspection was conducted on April 5, 2012, and the result is shown in Figure 3-24. Middle and side barriers were installed one to two weeks before the second cracking inspection. Cracking was inspected only in the half-width of the bridge where gages had been installed.

The center line of the bridge is highly susceptible to longitudinal cracking due to negative moment from self-weight and traffic loads. However, any cracking along the center line of the bridge could not be seen because the middle barrier was on the centerline of the bridge. As in the first cracking inspection, two transverse cracks located along construction joints were observed, and no longitudinal cracks were found. The average crack widths along Joint 1 and Joint 2 were 0.010 in. Crack-width values at the locations where plastic crack formers were exposed were not considered for calculating average crack width. The reason is that in those locations, the concrete over the plastic crack former spalled off and accurate crack widths could not be obtained. The measured widths of both cracks do not show significant changes from the first to the second inspection.

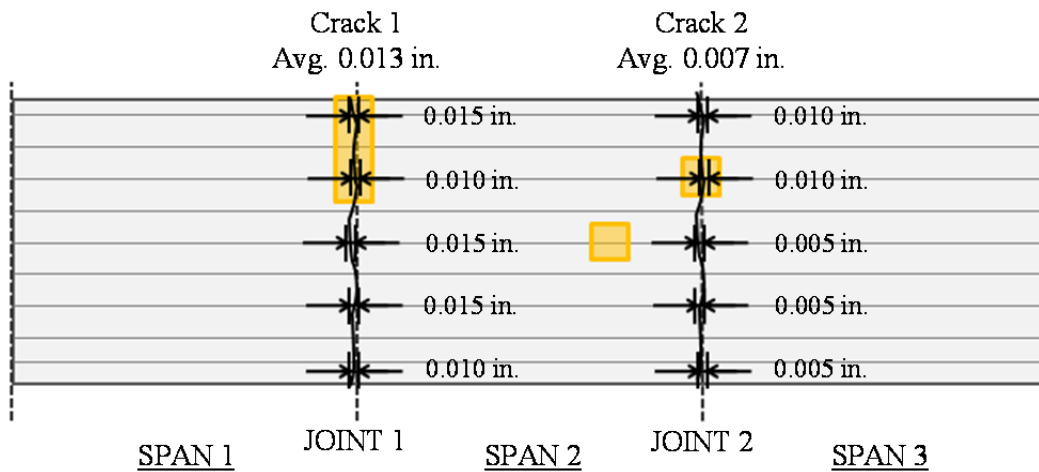


Figure 3-23: Results of first cracking inspection, Wharton-Weems Overpass

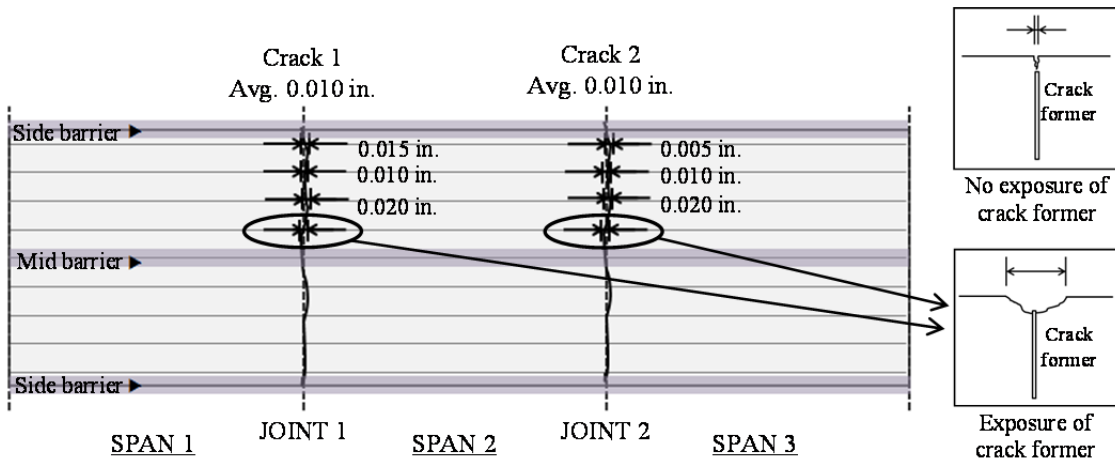


Figure 3-24: Results of second cracking inspection, Wharton-Weems Overpass

3.2.6.2 Long-term monitoring, Wharton-Weems Overpass

About a year's worth of data has been collected since the casting date (July 28, 2011), and the results are shown in Figures 3-25 to 3-28. In the figures, the x-axis represents the age of the deck from the casting date, and the y-axis represents stress in the

concrete. Positive y-axis values indicate tensile stress, and negative values indicate compressive stress.

Figure 3-25 and Figure 3-26 show the results of long-term monitoring in the longitudinal direction of two testing areas in the Wharton-Weems Overpass. In both figures, the readings from the gages along the construction joints increased rapidly and reached the theoretical cracking value within a week after casting. The values started to stabilize about a month after casting. Other gages, located 50 ft from each joint, did not show significant changes in their readings during the entire monitoring period and their highest values were close to theoretical cracking stress.

The Wharton-Weems Overpass was opened to traffic on April 21, 2012, about 270 days after casting. That date is indicated by the black dashed vertical lines in Figure 3-25 to Figure 3-28. In the longitudinal direction, significant increases in steel stresses at the construction joints were observed. The largest measured strains in two testing areas were near the specified yield stress of the top-mat reinforcement. Other longitudinal gages did not show any significant changes.

All gages in the transverse direction showed similar behavior during the monitoring period, as shown in Figure 3-27 and Figure 3-28. High stress values are monitored during cold weather and low stress values are measured during hot weather. The concrete deck expands when the temperature increases, but this expansion is restrained by girders or adjacent decks; compressive stress occurred in bridge deck and it offsets tensile stress in the decks due to restrained creep and shrinkage. Therefore, the tensile stress values measured in hot weather are smaller than the values measured in cold weather. In Figure 3-28, the reading values of T08 are not included. Unrealistic values of strain were monitored in T08 on March 28, 2012, 245 days after casting. The date coincided with installation of the middle barrier. There are two possible reasons for this change in T08. First, a drill bit may have hit the gage while drilling the holes for the barrier. Second, heavy trucks or equipment used during installation of the middle barrier might have caused cracking and large strain measurement.

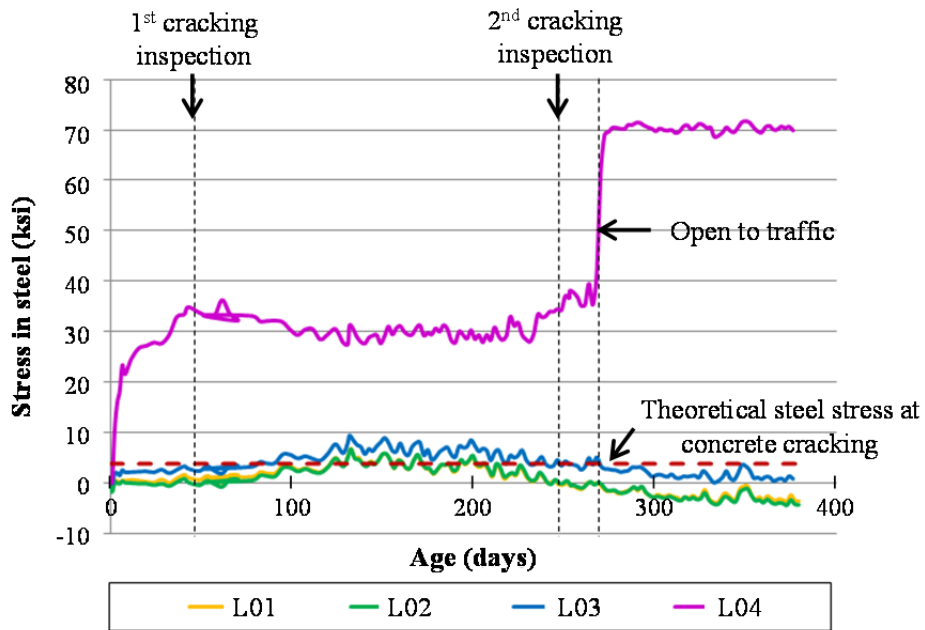


Figure 3-25: Stresses in Current TxDOT Standard Reinforcement, Wharton-Weems Overpass (longitudinal direction)

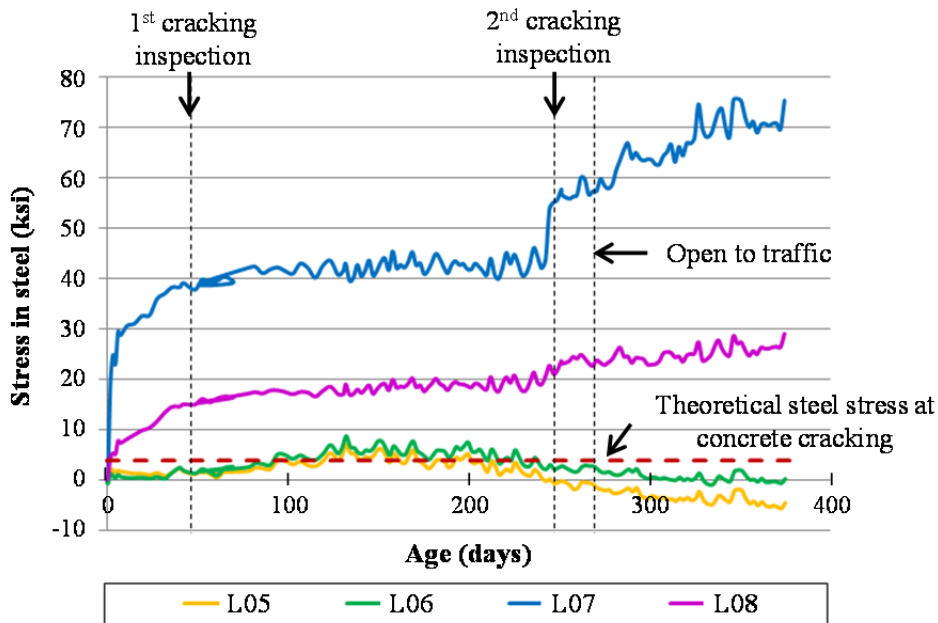


Figure 3-26: Stresses in Reduced Deformed-Bar Reinforcement, Wharton-Weems Overpass (longitudinal direction)

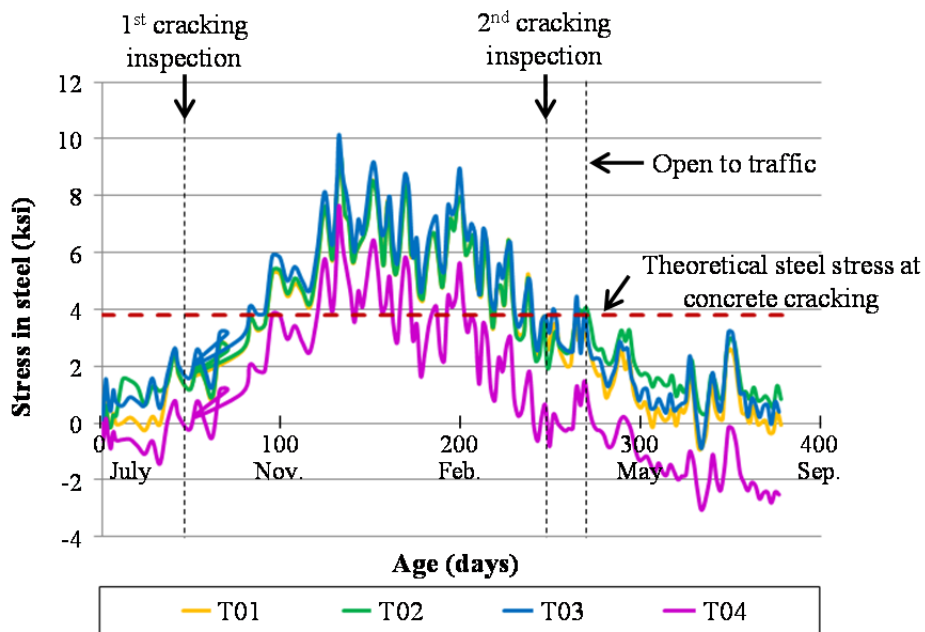


Figure 3-27: Stresses in Current TxDOT Standard Reinforcement, Wharton-Weems Overpass (transverse direction)

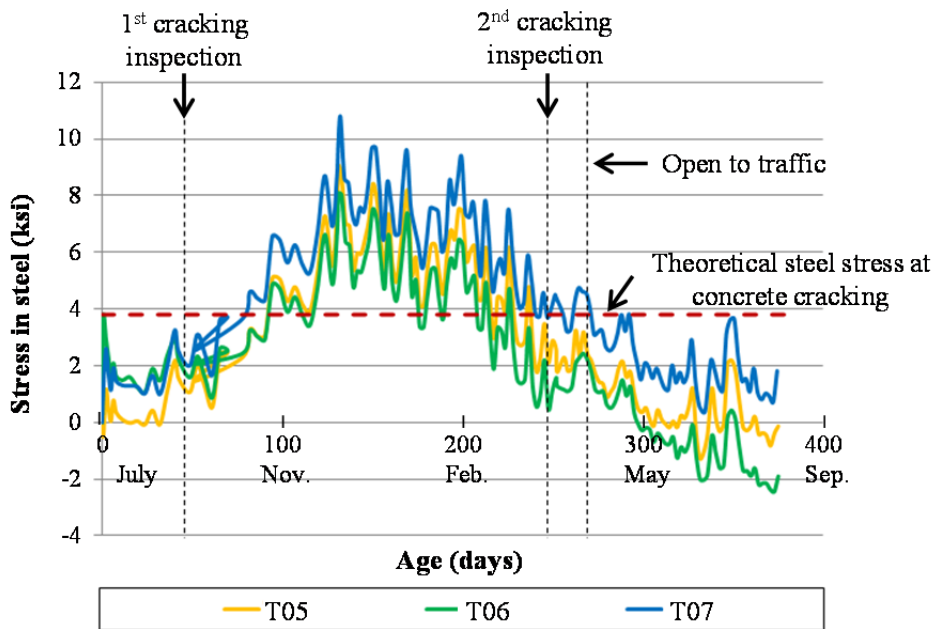


Figure 3-28: Stresses in Reduced Deformed-Bar Reinforcement, Wharton-Weems Overpass (transverse direction)

3.2.6.3 Use of P-method to predict cracking in CIP-PCP bridge decks

3.2.6.3.1 Description of P-method

Peterman and Ramirez (1998) propose a technique, called the “P-method,” to determine when cracks are likely to form in CIP-PCP bridge decks. The P-method takes into account the following items: i) the length and stiffness of diaphragm region; ii) the different initiation time for creep of PCPs and CIP slabs; and iii) restraining effects of PCPs and top-mat reinforcement in CIP slabs on shrinkage of CIP slabs. In the P-method, the diaphragm region indicates the area between interior supports subjected to negative moment, and it is assumed that the cracks due to restraint moment will form on the top surface of the diaphragm region and these cracks will reduce the stiffness of the diaphragm region. Moreover, it is also assumed that the cracks due to restraint moment will not form in the main span regions, so the stiffness of the main span does not change after cracking.

Using the P-method, the restraint moment (M_r) at a critical section of the deck can be calculated using Equation 3-2.

$$M_r = \left[\frac{3}{2} \alpha M_p - \alpha (M_d)_{precast} \right] \times [\Delta(1 - e^{-\phi_1})] - \alpha (M_d)_{CIP} \times (1 - e^{-\phi_2}) - \frac{3}{2} \alpha M_s \left(\frac{1 - e^{-\phi_2}}{\phi_2} \right) \quad \text{Equation 3-2}$$

Where, α = coefficient that accounts for the relative stiffness of the diaphragm region and main spans

M_p = moment caused by prestressing force about centroid of composite member

- M_s = differential shrinkage moment, adjusted for restraint of precast panels and steel reinforcement
- $(M_d)_{precast}$ = mid-span moment due to dead load of precast panels
- $(M_d)_{CIP}$ = mid-span moment due to dead load of CIP topping
- φ_1 = creep coefficient for creep effects initiating when prestress force is transferred to precast panels
- φ_2 = creep coefficient for creep effects initiating when CIP topping is cast
- $\Delta(1-e^{-\varphi_1})$ = change in expression $(1-e^{-\varphi_1})$ occurring from time CIP topping is cast to time corresponding to restraint moment calculation

In Equation 3-2, the coefficient α was obtained using moment distribution method. M_p , M_s , $(M_d)_{precast}$, and $(M_d)_{CIP}$ can be assumed to act uniformly over the length of members. If uniform moment is applied over entire length of the member with fixed ends, fixed-end moments occur at both ends, equal in magnitude to the applied uniform moment. Therefore, the restraint moment due to uniform moment can be calculated by applying the fixed-end moment at the ends and distributing them according to the stiffness of the member by moment distribution method (Peterman and Ramirez 1998). Moreover, the different shrinkage moment (M_s) in Equation 3-2 was estimated by Equation 3-3.

$$M_s = \epsilon_s E_d A_d \left(e_c + \frac{h}{2} \right) \left[\frac{I}{1 + \frac{E_p A_p}{E_d A_d}} \right] \left[\frac{I}{1 + \frac{E_s A_s}{E_d A_d}} \right] \quad \text{Equation 3-3}$$

Where,

E_p	=	modulus of elasticity of precast panels
A_p	=	area of precast panels
E_s	=	modulus of elasticity of steel reinforcement in CIP deck
A_s	=	area of steel reinforcement in CIP deck
E_d	=	modulus of elasticity of CIP deck
A_d	=	area of CIP deck

3.2.6.3.2 Application of P-method to Wharton-Weems Overpass

In this section, the restraint moments in the Wharton-Weems Overpass were calculated using the P-method to estimate the likelihood of deck cracking, and the probable time for the development of that cracking. The results of the calculation are also compared with the results of the cracking inspection to determine whether or not the P-method can accurately predict bridge-deck cracking.

3.2.6.3.2.1 Longitudinal restraint moment - Transverse crack

Figure 3-29 shows the area considered in the calculation for longitudinal restraint moment in the Wharton-Weems Overpass. The width of the section was 9.3 ft, equal to the space between two adjacent girders. The section consisted of PCPs and CIP slabs, with a thickness of 4 in.; therefore, the entire thickness of the section was 8 in. Section T-T in Figure 3-29 can be simplified as in Figure 3-30. The length of the main-span region (L_m) was 600 in., and the length of diaphragm (L_d) was 1 in., a space between PCPs in the bridge.

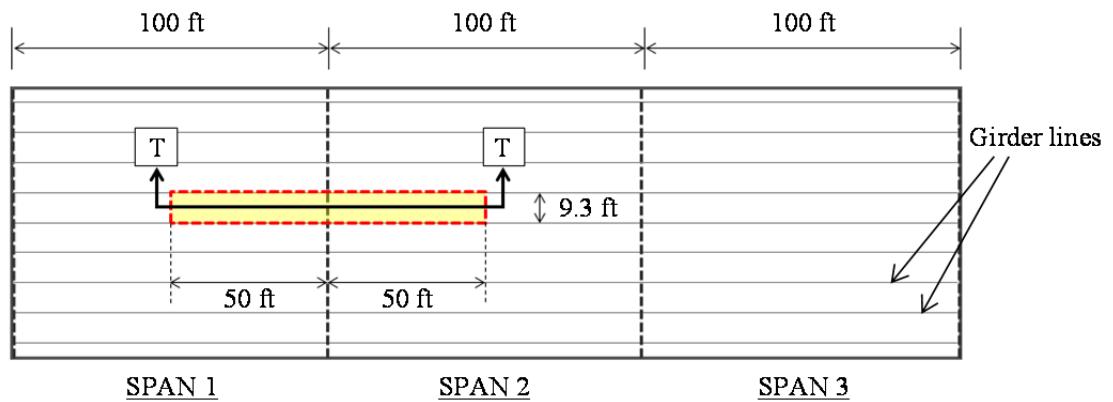


Figure 3-29: The area for the calculation of longitudinal restraint moment of Wharton-Weems Overpass

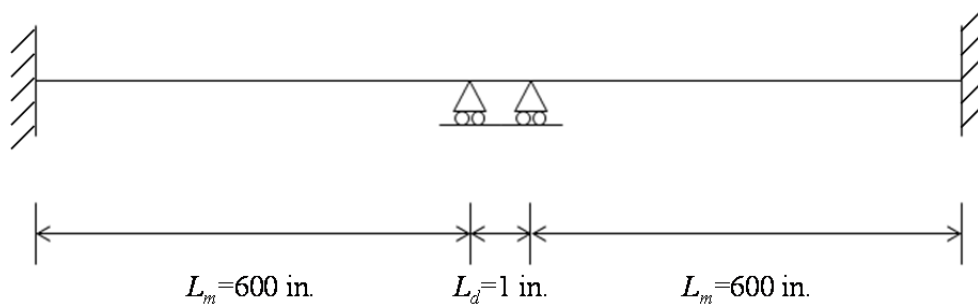


Figure 3-30: Simplified Section T-T

The moment due to prestressing strand was ignored because the strands were placed perpendicular to the girder lines. Much of information required for the calculation was unknown, so the following values were assumed. Only the Current TxDOT Standard Reinforcement was considered as top-mat reinforcement, because the change of the top-mat reinforcement in this study is not big enough to change the calculations using the P-method.

- i) Specified concrete strength of PCPs: 9,000 psi
- ii) specified concrete strength of CIP slabs: 4,000 psi

- iii) Age of PCPs when CIP topping was cast: 55 days
- iv) Average humidity: 60%
- v) Prestressing strands of PCPs: 3/8 in. seven-wire strands at 6 in.
- vi) Remaining prestress in strand during first month after the casting: 175 ksi
- vii) Elastic modulus of reinforcement: 29,000 ksi.
- viii) Top-mat reinforcement
 - No. 4 bar at 9 in. (longitudinal direction)
 - No. 5 bar at 6 in. (transverse direction)

Using the assumed information and ACI 209, ultimate creep coefficients and shrinkage strains of PCPs and CIP slabs were calculated and the resultant values are shown in below:

- i) Ultimate creep coefficient of PCPs: 3.42
- ii) Ultimate creep coefficient of CIP slabs: 3.40
- iii) Ultimate shrinkage strain of PCPs: 600×10^{-6}
- iv) Ultimate shrinkage strain of CIP slabs: 613×10^{-6}

Creep and shrinkage strain at time t can be obtained by multiplying their ultimate values by R (Equation 3-4), a time-dependent creep and shrinkage coefficient (Corley and Sozen, 1966):

$$R = 0.13 \times \ln(t+1)$$

Equation 3-4

Section properties were also evaluated by transforming the PCP section into a section which has the same compressive strength as the CIP slabs. The compressive strength of the PCPs was taken as 9,000 psi regardless of age, because the compressive strength of concrete does not changed significantly 28 days after casting. The

compressive strength of the CIP slabs did change with time, and was expressed as Equation 3-5 adapted from ACI 209. The detailed procedure for calculating restraint moment is shown in Appendix B.

$$f_c(t) = f_c(28) \times \left(\frac{t}{2.3 + 0.92 \times t} \right) \quad \text{Equation 3-5}$$

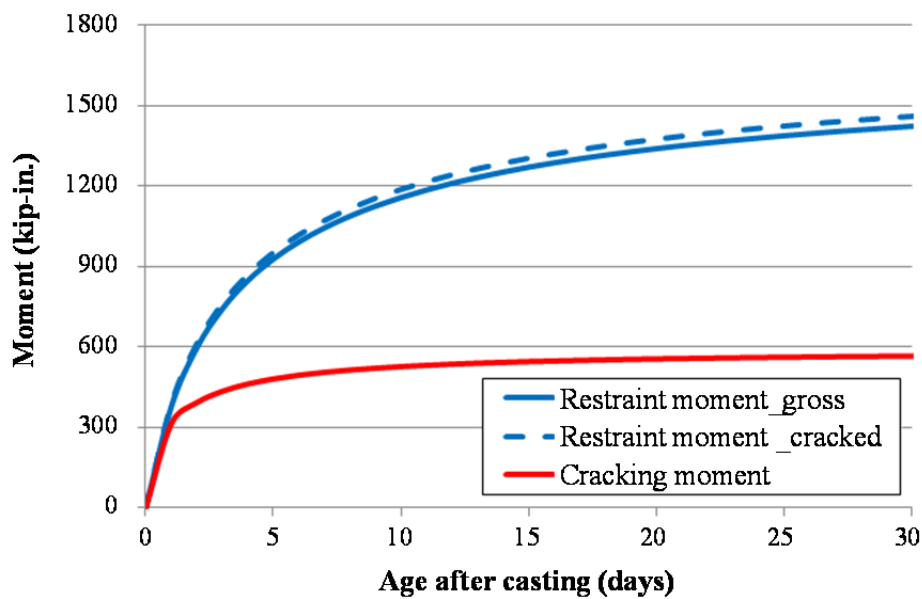


Figure 3-31: Longitudinal restraint moment and cracking moment, Wharton-Weems Overpass

In Figure 3-31, restraint moments calculated using the P-method, and calculated cracking moment using modulus of rupture of the CIP topping concrete are plotted together. In the calculation for the longitudinal restraint moment, M_p is zero because the strands were placed perpendicular to girder lines, so the effect of the prestressing force on the longitudinal restraint moment can be ignored.

In that figure, the blue solid line represents the calculated restraint moment of the uncracked section, and the blue dashed line represents the calculated restraint moment of cracked section. The same values of gross section moment of inertias were used for the diaphragm and main span region for the calculation of un-cracked section. In calculating restraint moment in a cracked specimen, however, the cracked moment of inertia was used for the diaphragm region, and the gross moment of inertia for the main-span region. The red line represents cracking moment calculated using the modulus of rupture of the CIP concrete. If the restraint moment is greater than the cracking moment, it may be concluded that cracks have developed in the specimen.

As shown in Figure 3-31, the restraint moment of the uncracked and the cracked section were almost same in this case, because the length of the diaphragm region was very small compared to the length of the main-span region. Moreover, the restraint moment became greater than the cracking moment within a day after CIP slab casting implying that the bridge may have transverse cracks on the deck within a day after casting. Actually, transverse cracks are expected to occur around 2-3 days after casting based on the measured strain values.

3.2.6.3.2.2 Transverse restraint moment - Longitudinal crack

The area considered in the calculation for transverse restraint moment of Wharton-Weems Overpass is shown in Figure 3-32. Transverse restraint moment can cause longitudinal cracks on the bridge deck. Section L-L in Figure 3-32 can be simplified as shown in Figure 3-33. The width of the section was 100 ft, equal to the span length of the bridge. The length of main span region (L_m) was 92 in., and the length of the diaphragm region (L_d) was 36 in., equal to the length of top flange of a Tx 46 I-girder used in Wharton-Weems Overpass. The material properties and construction conditions were assumed the same as in Section 3.2.6.3.2.1.

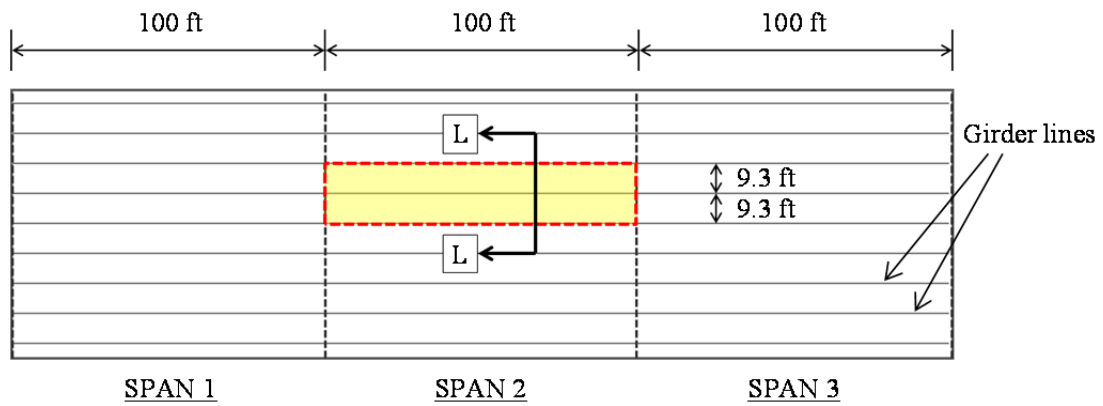


Figure 3-32: Area for calculation of transverse restraint moment, Wharton-Weems Overpass

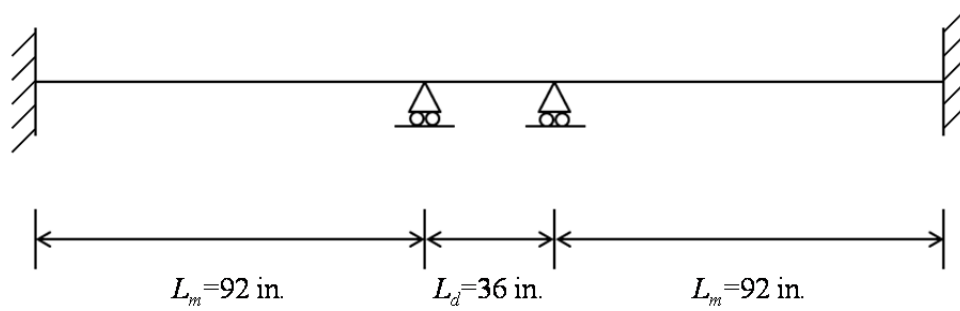


Figure 3-33: Simplified Section L-L, Wharton-Weems Overpass

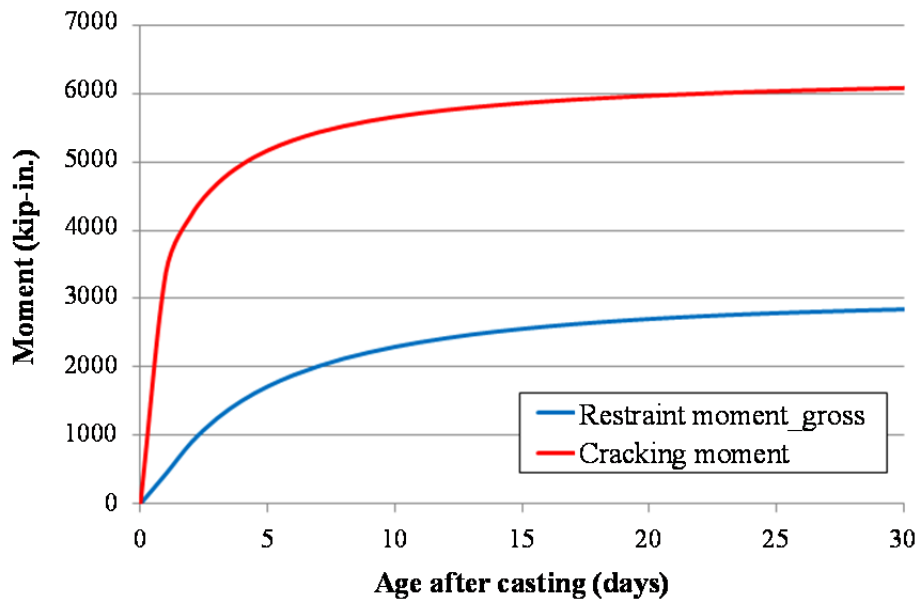


Figure 3-34: Transverse restraint moment and cracking moment, Wharton-Weems Overpass

In Figure 3-34, calculated transverse restraint moments using the P-method, and calculated cracking moment using the modulus of rupture of the CIP topping concrete are shown. In the figure, the blue line represents the calculated restraint moment by P-method assuming that the specimen is not cracked. The values on this blue line were obtained by using the same moment of inertia for diaphragm and main-span regions as stated in previous section. The red represents the cracking, calculated using the modulus of rupture of the CIP concrete.

As shown in Figure 3-34, the values on the blue line are smaller than the value on the red line at the same age. It means that the restraint moment in the bridge was not large enough to cause cracking in the longitudinal direction. This result matches well with the result of cracking inspection

3.3 LAMPASAS RIVER BRIDGE

3.3.1 Description

The Lampasas River Bridge is, located near Belton on US IH-35. The bridge consists of 5 spans with different lengths and different numbers of girders. Spans 1 and 2 are 100-ft long and have 4 girders. Span 3 is 120-ft long and has 5 girders. Spans 4 and 5 are 80 ft. long and have 4 girders. The bridge has a 15-degree skew. The bridge was constructed using the CIP-PCP bridge deck system. The CIP concrete slabs and PCPs are 4-in. thick. In Figure 3-35 to Figure 3-38, plan and section views of the Lampasas River Bridge are shown.

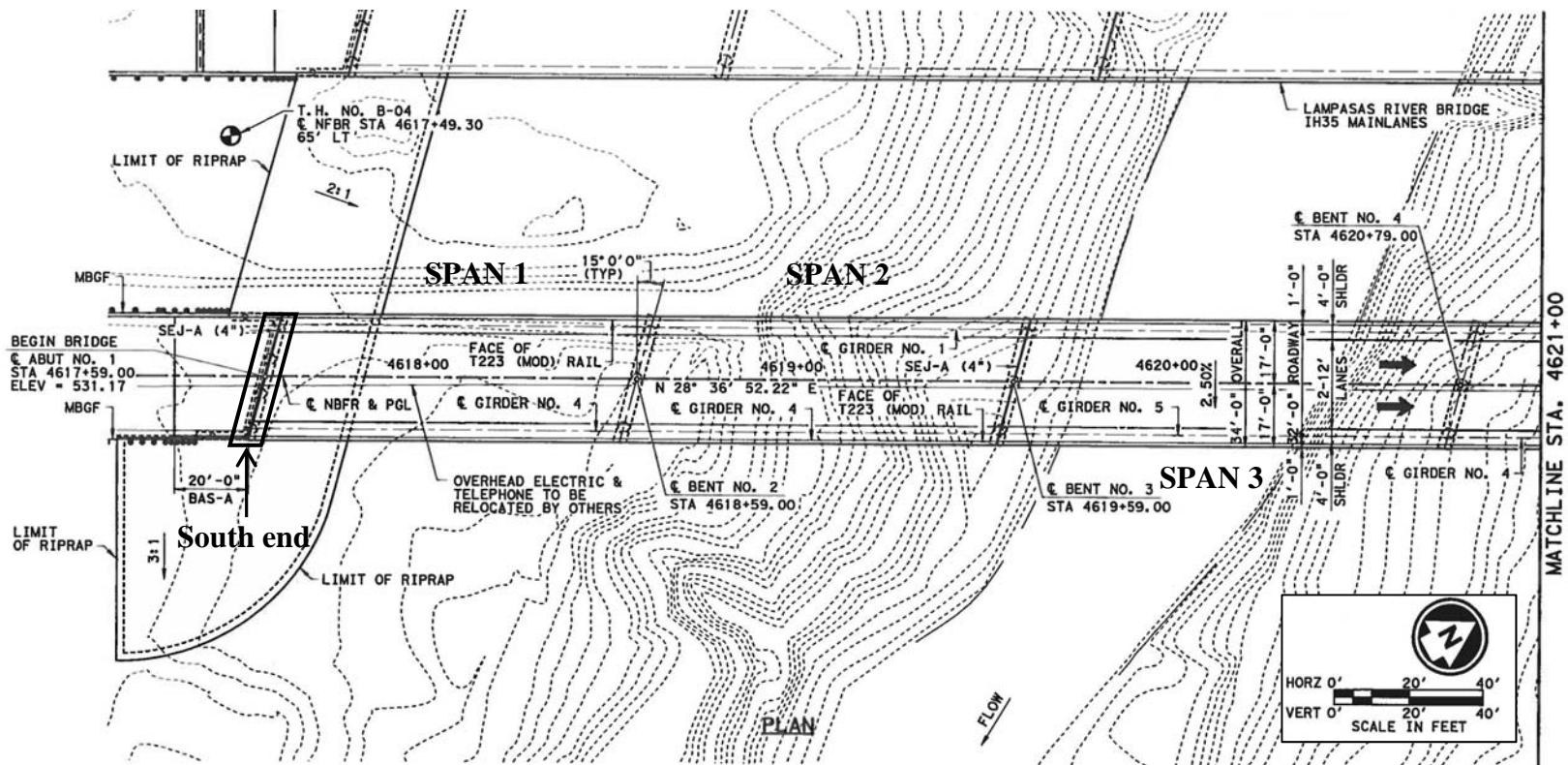


Figure 3-35: Plan view of Lampasas River Bridge (Spans 1 to 3)

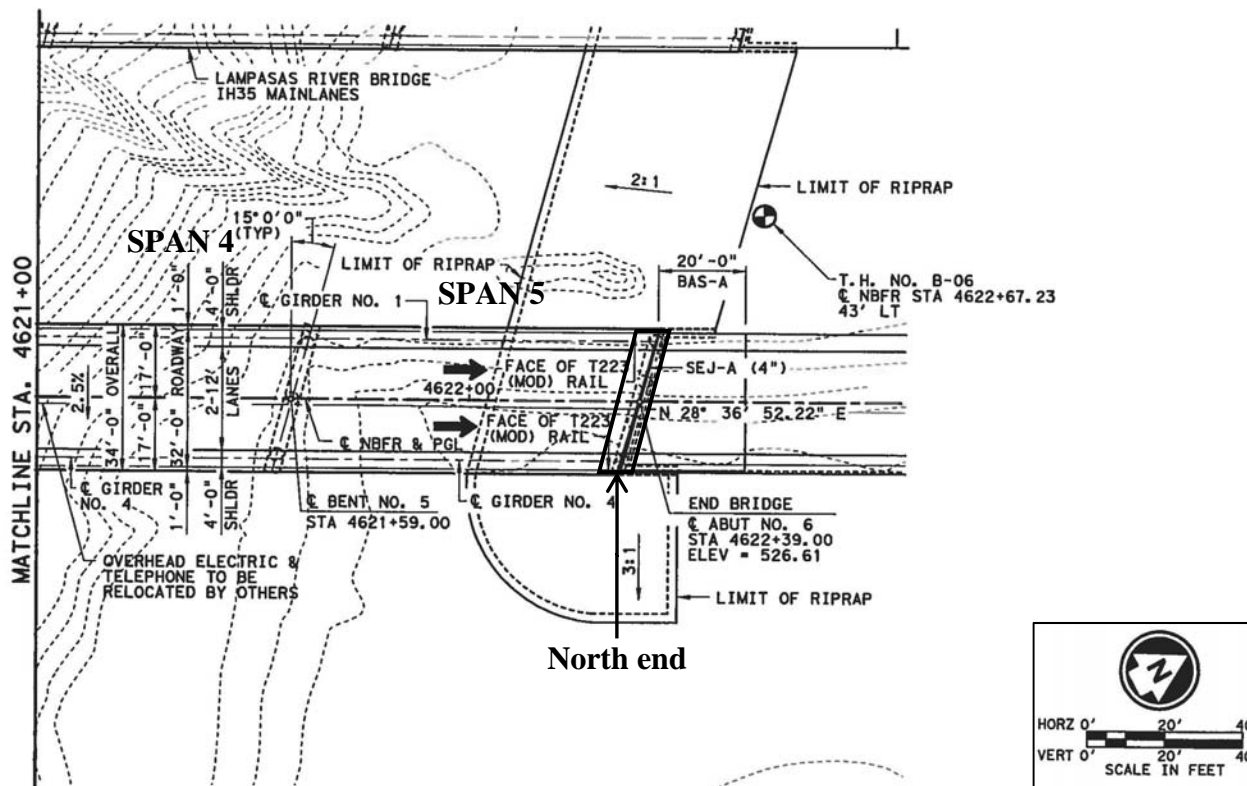


Figure 3-36: Plan view of Lampasas River Bridge (Spans 4 to 5)

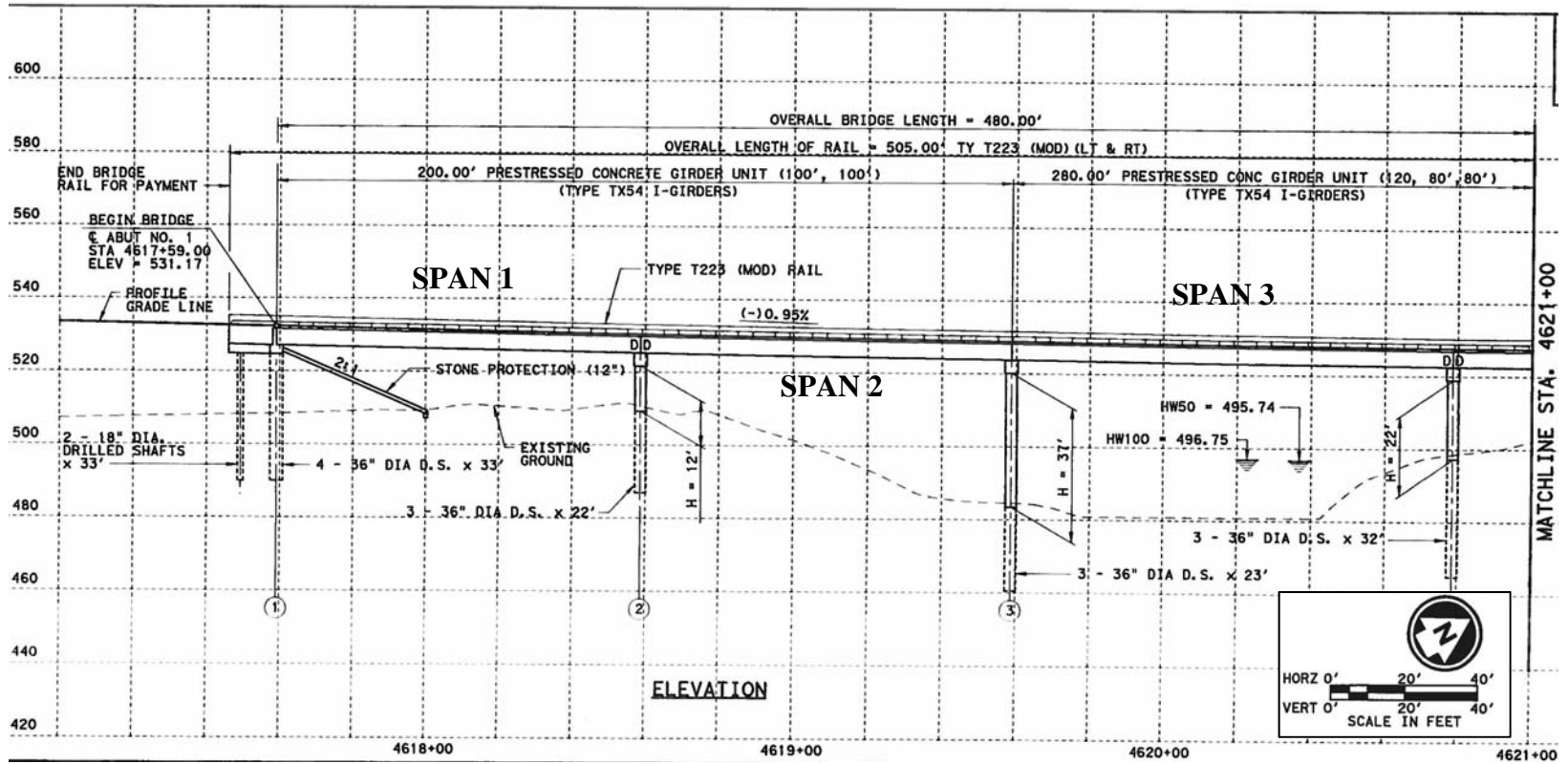


Figure 3-37: Section view of Lampasas River Bridge (Spans 1 to 3)

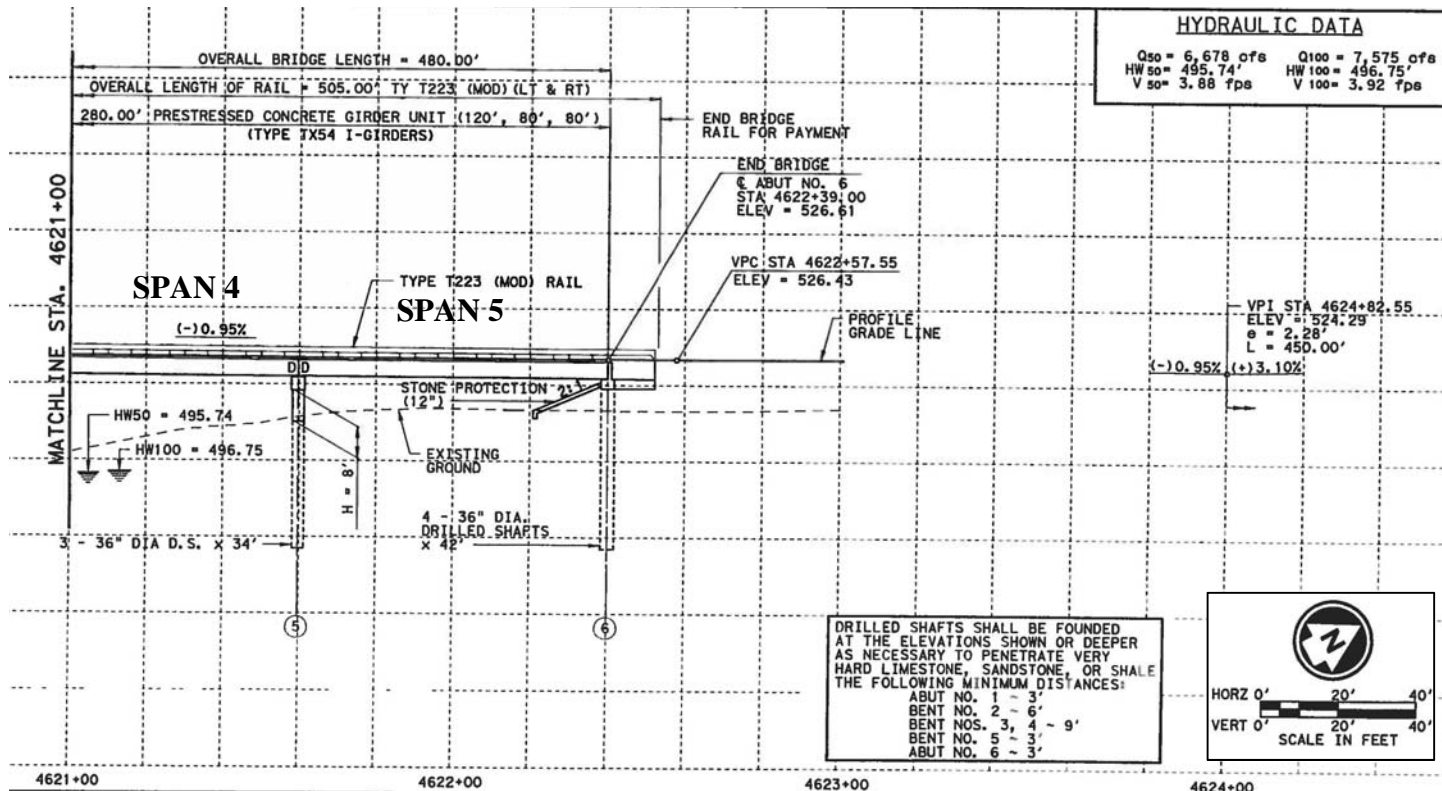


Figure 3-38: Section view of Lampasas River Bridge (Spans 4 to 5)

3.3.2 Top-mat reinforcement options, Lampasas River Bridge

In Figure 3-39 are shown the top-mat transverse reinforcement options for the Lampasas River Bridge. Three reinforcement options were included; Current TxDOT Standard Design (No. 5 bars at 6 in.); Reduced Deformed-Bar Reinforcement (No. 4 bars at 6 in.); and Reduced Welded-Wire Reinforcement (D20 wires at 6 in.). To obtain similar testing areas for each option, the testing areas are divided as shown in Figure 3-39. SPAN 3 has a different number of girders compared to other spans, so SPAN 3 was not instrumented. A D20 wire has the same area as a No. 4 bar.

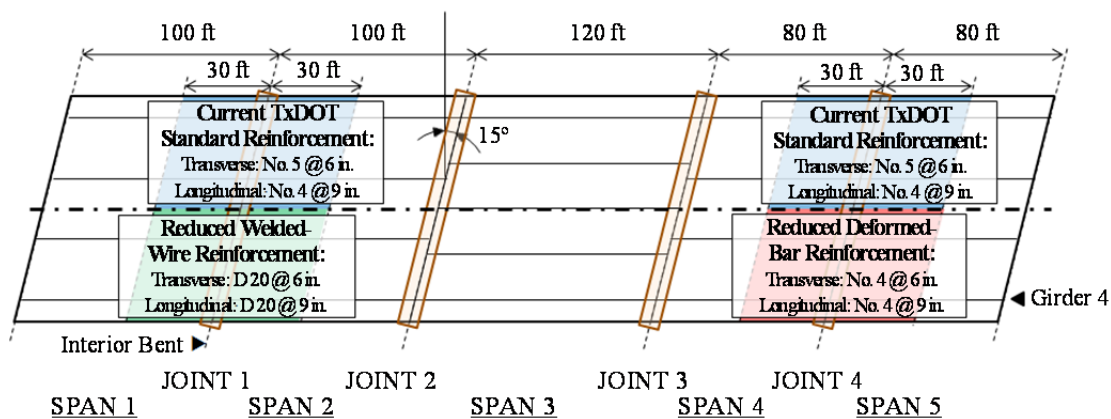


Figure 3-39: Reinforcement options, Lampasas River Bridge

3.3.3 Splice details, Lampasas River Bridge

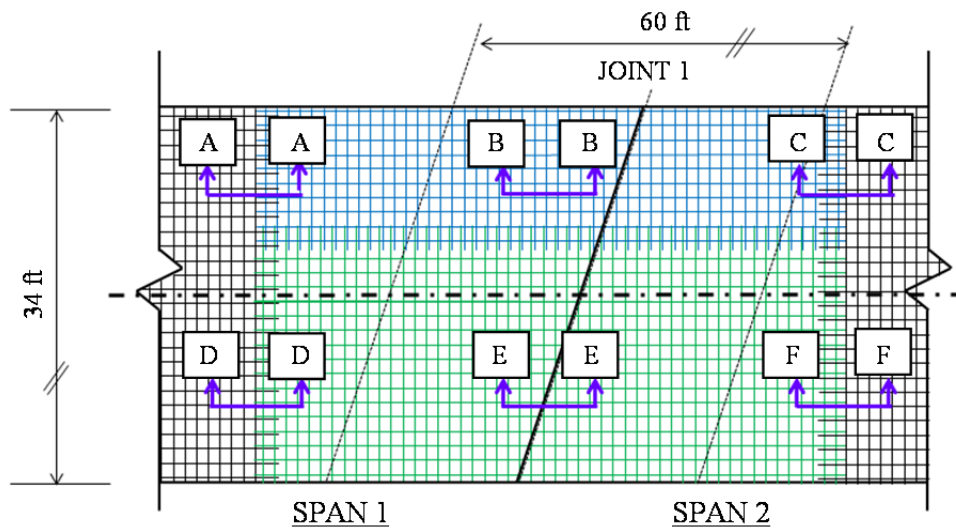
3.3.3.1 Longitudinal splices

Figure 3-40 to Figure 3-50 shows the details of the longitudinal bar splices. As with the Wharton-Weems Overpass, splices were located away from joints. Reinforcement splice lengths for standard deformed bars were calculated using Equation 3-1 (Equation 12-1 of ACI 318 (2011)); and splice lengths for welded wire reinforcement using Equation 3-6. The welded deformed-wire factor (ψ_w) in Equation 3-6 was adopted from Section 12.7.2 of ACI 318 (2011). Blue lines refer to the Current TxDOT Standard Design option; green lines refer to the Reduced Welded-Wire Reinforcement option; and

red lines indicate the Reduced Deformed-Bar Reinforcement option. Black lines represent the reinforcement in non-test areas. Detailed calculations for required splice length are shown in Appendix A.

$$\frac{l_d}{d_b} = \psi_w \times \frac{3}{40} \times \frac{f_y}{\lambda \times \sqrt{f'_c}} \times \frac{\psi_t \times \psi_e \times \psi_s}{\left(\frac{c_b + K_{tr}}{d_b}\right)} \quad \text{Equation 3-6}$$

- Where,
- ψ_w = welded deformed-wire reinforcement factor, Section 12.7.2 in ACI 318-11
 - l_d = development length in tension, in.
 - d_b = nominal diameter of bar, in.
 - f_y = specified yield strength of reinforcement, psi
 - λ = modification factor related to unit weight of concrete
 - f'_c = specified compressive strength of concrete, psi
 - ψ_t = factor used to modify development length based on reinforcement location
 - ψ_e = factor used to modify development length based on reinforcement coating
 - ψ_s = factor used to modify development length based on reinforcement size
 - c_b = smaller of (a) the distance from center of bar or wire to nearest concrete surface, and (b) one-half the concrete center-to-center spacing of bars or wires being developed, in.
 - K_{tr} = transverse reinforcement index



**Figure 3-40: Details of longitudinal splices, Lampasas River Bridge
(Span 1 and Span 2)**

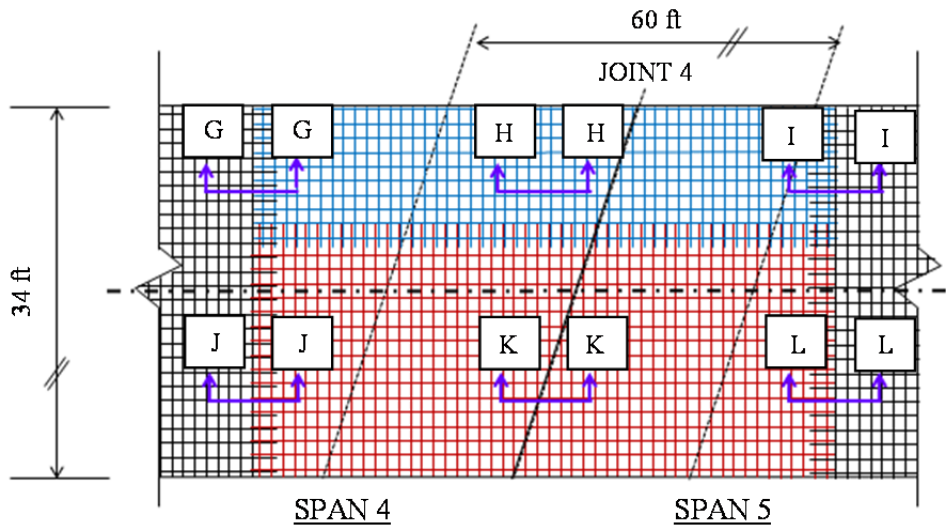


**Figure 3-41: Details of longitudinal splices, Lampasas River Bridge
(Span 4 and Span 5)**

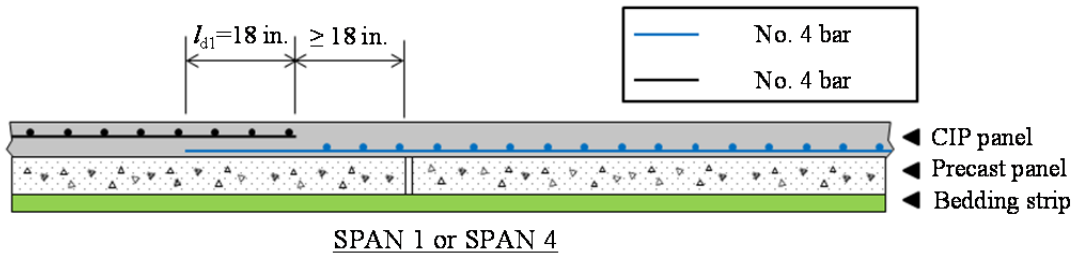


**Figure 3-42: Details of longitudinal splices, Lampasas River Bridge
(Sections A-A and G-G)**

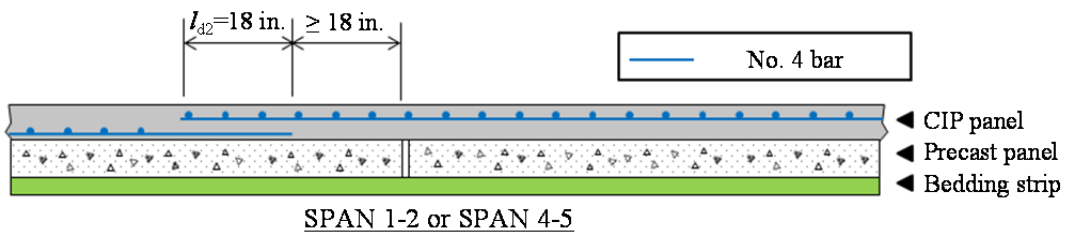


**Figure 3-43: Details of longitudinal splices, Lampasas River Bridge
(Sections B-B and H-H)**

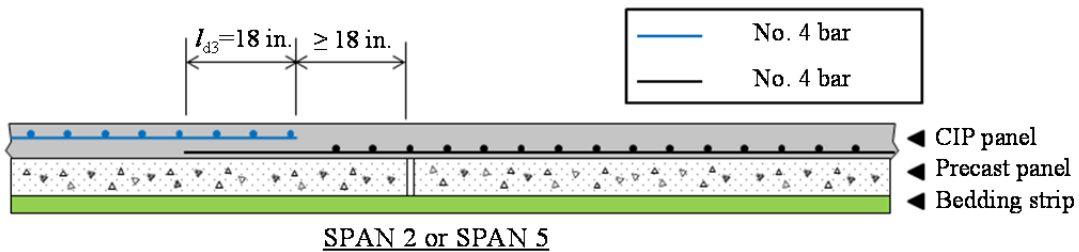


**Figure 3-44: Details of longitudinal splices, Lampasas River Bridge
(Sections C-C and I-I)**

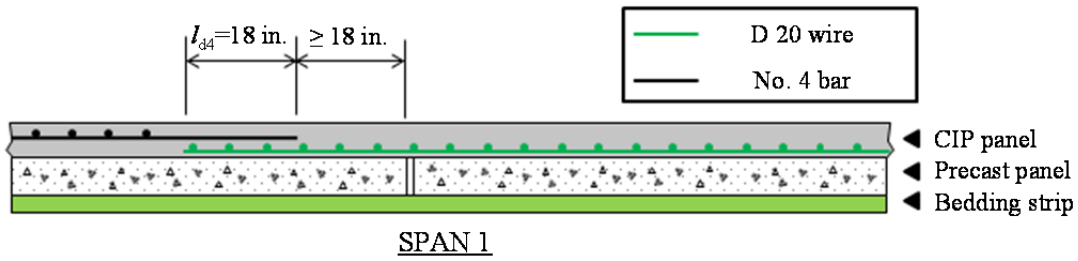


Figure 3-45: Details of longitudinal splices, Lampasas River Bridge (Section D-D)

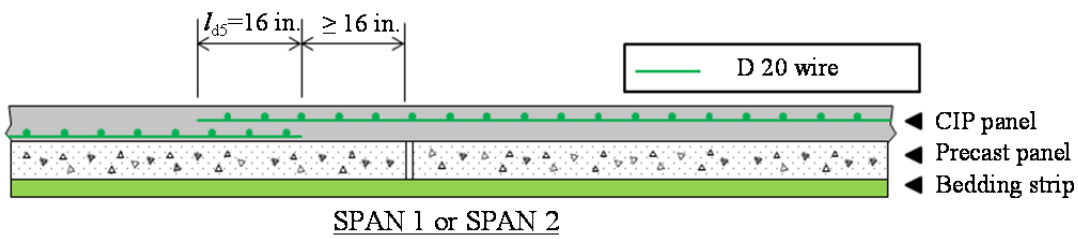


Figure 3-46: Details of longitudinal splices, Lampasas River Bridge (Section E-E)

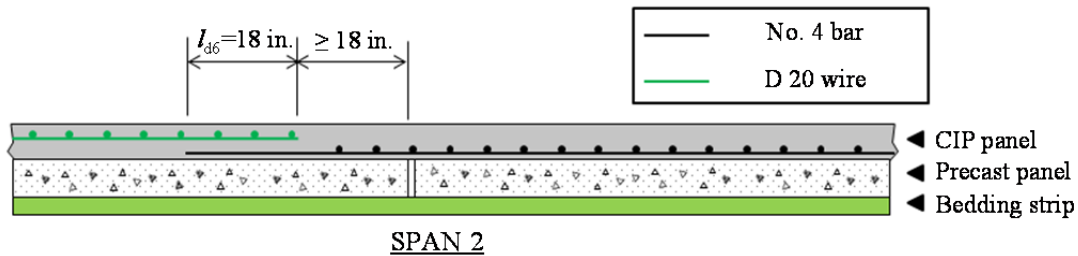


Figure 3-47: Details of longitudinal splices, Lampasas River Bridge (Section F-F)

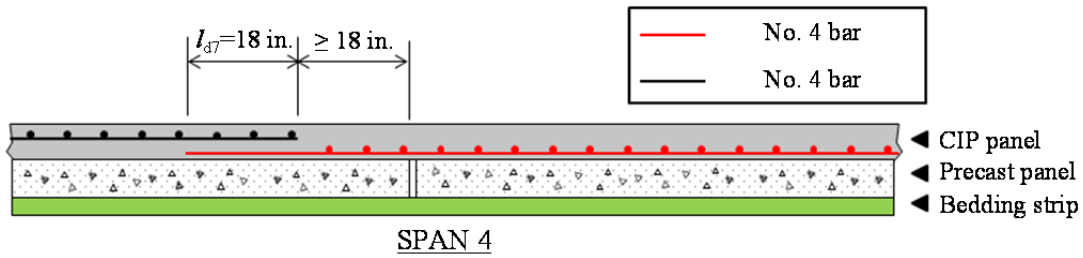


Figure 3-48: Details of longitudinal splices, Lampasas River Bridge (Section J-J)

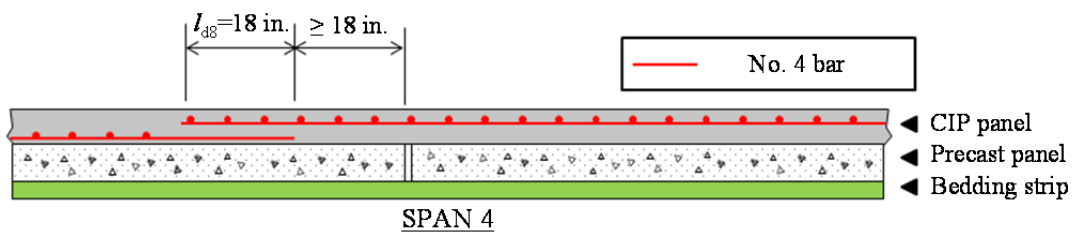


Figure 3-49: Details of longitudinal splices, Lampasas River Bridge (Section K-K)

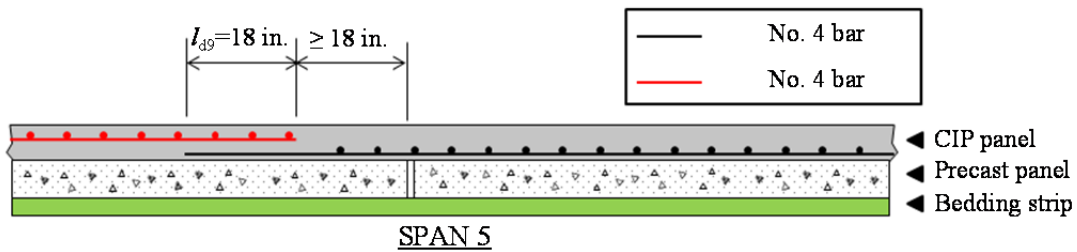
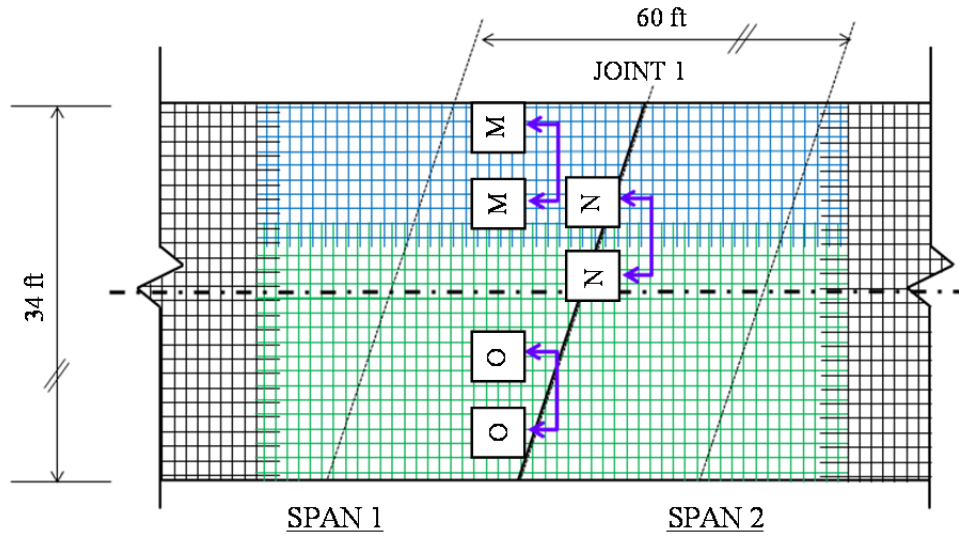


Figure 3-50: Details of longitudinal splices, Lampasas River Bridge (Section L-L)

3.3.3.2 Transverse splices

In Figure 3-51 to Figure 3-58 are shown details of the transverse bar splices. The calculations are shown in Appendix A.



**Figure 3-51: Details of transverse splices, Lampasas River Bridge
(Span 1 and Span 2)**

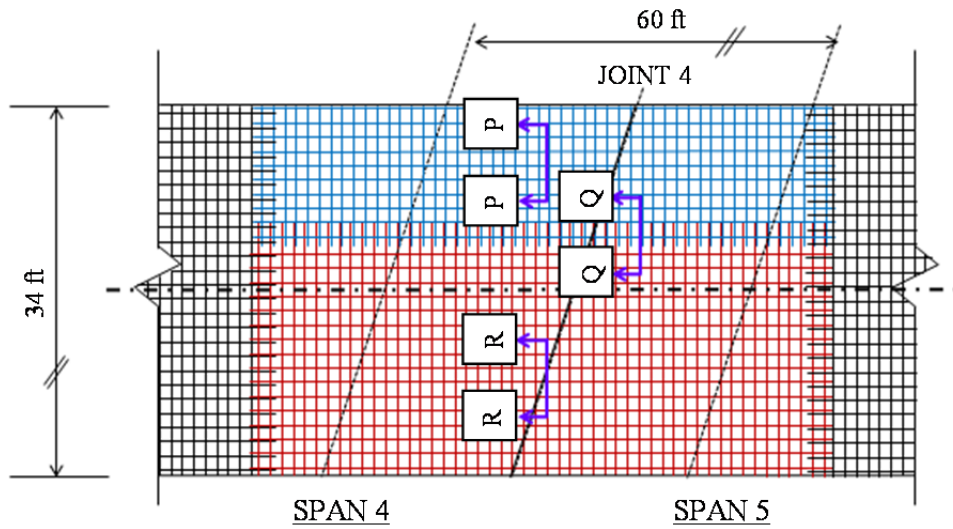


Figure 3-52: Details of transverse splices, Lampasas River Bridge (Span 4 and Span 5)

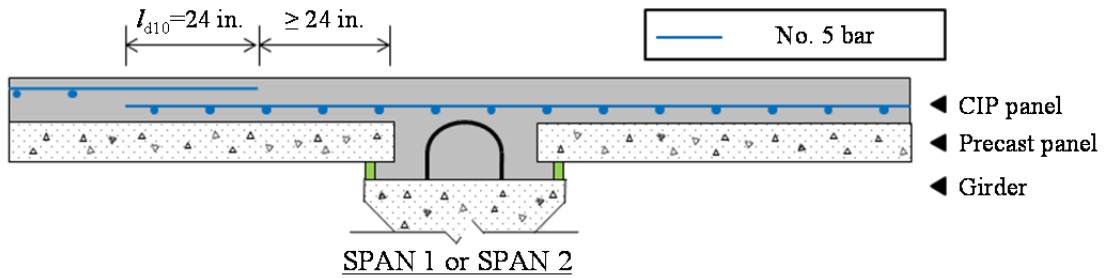


Figure 3-53: Details of transverse splice, Lampasas River Bridge (Section M-M)

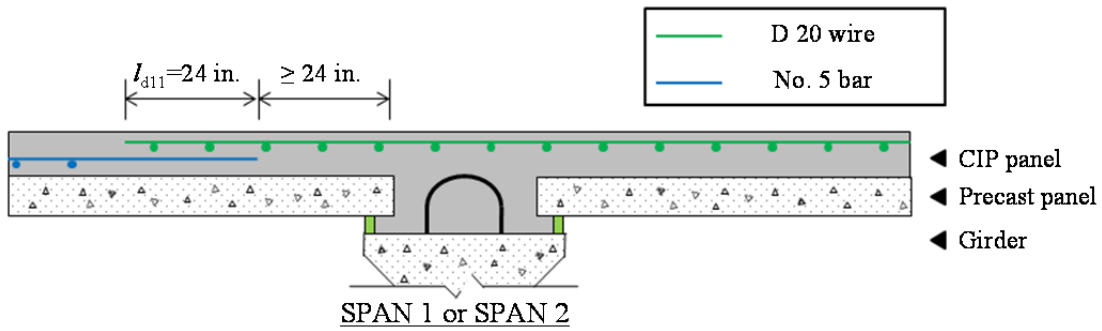


Figure 3-54: Details of transverse splice, Lampasas River Bridge (Section N-N)

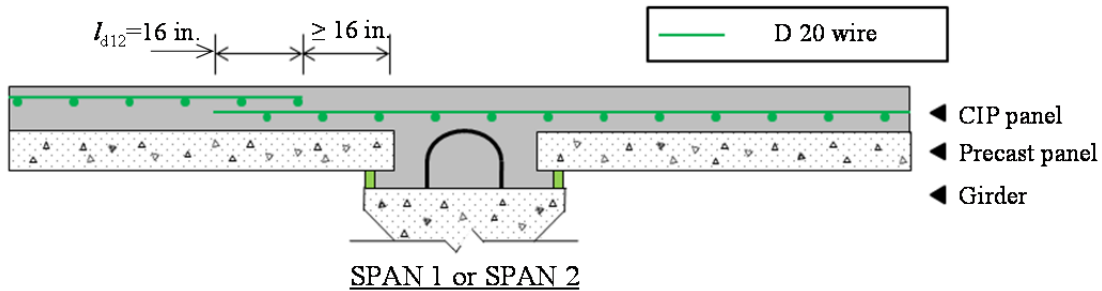


Figure 3-55: Details of transverse splice, Lampasas River Bridge (Section O-O)

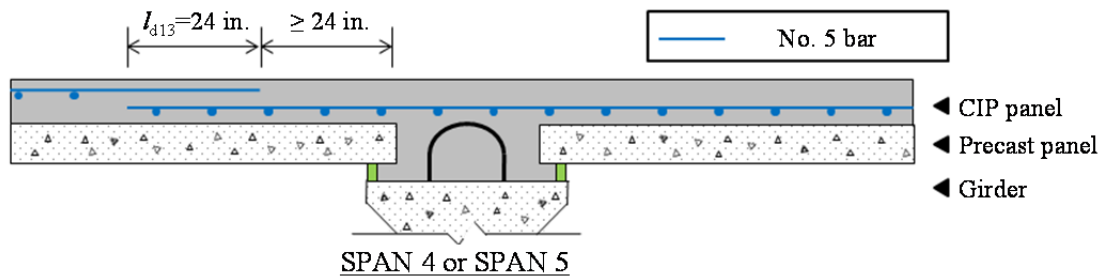


Figure 3-56: Details of transverse splice, Lampasas River Bridge (Section P-P)

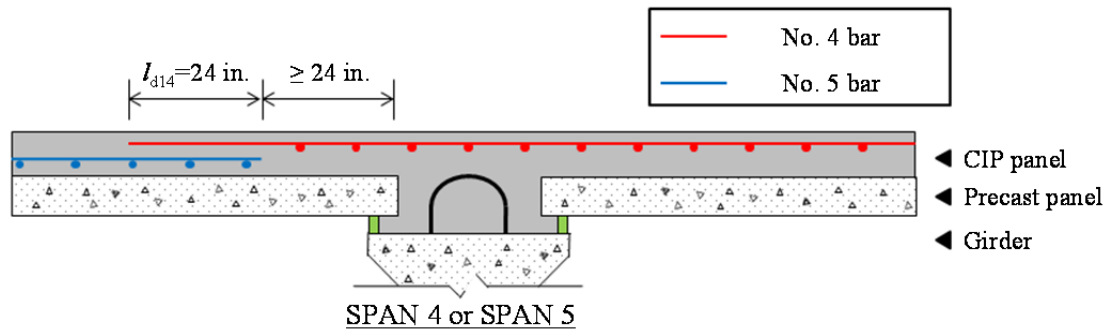


Figure 3-57: Details of transverse splice, Lampasas River Bridge (Section Q-Q)

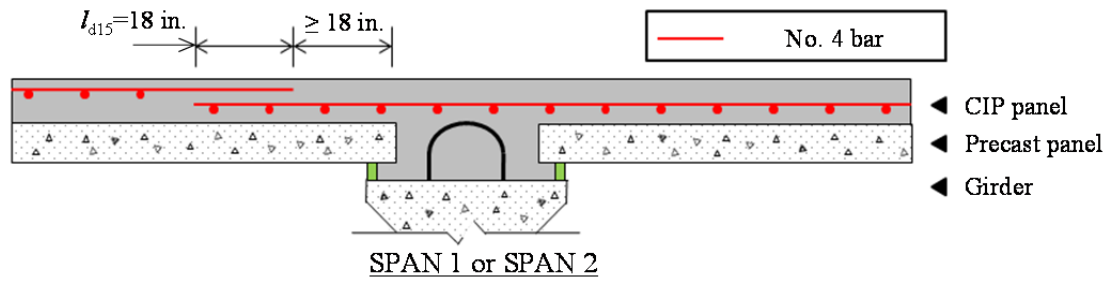


Figure 3-58: Details of transverse splice, Lampasas River Bridge (Section R-R)

3.3.4 Instrumentation of Lampasas River Bridge

3.3.4.1 Gage location and identification

The gages used in the Lampasas River Bridge are the same as the gages used in the Wharton-Weems Overpass (Section 3.2.4).

Figure 3-59 and Figure 3-60 indicate gage layouts for longitudinal bars and for transverse bars. Brown stars indicate the location of the data-acquisition equipment. Because the number of girders in Span 3 is not equal to the number of girders in other spans, Span 3 was not used as a test area. The following designation system is used:

- i) Longitudinal gages are denoted as “Lxx.” Odd-numbered gages are located over Girder 1 or 4, and even-numbered gages over Girder 2 or 3. Gages on the longitudinal bars are located at the joint and at 25 ft on each side of the joint.
- ii) Transverse gages are denoted as “Txx.” Odd-numbered gages are located over Girder 1 or 4, and even-numbered gages over Girder 2 or 3. All transverse gages are located 20 ft from Joint 1 or Joint 4

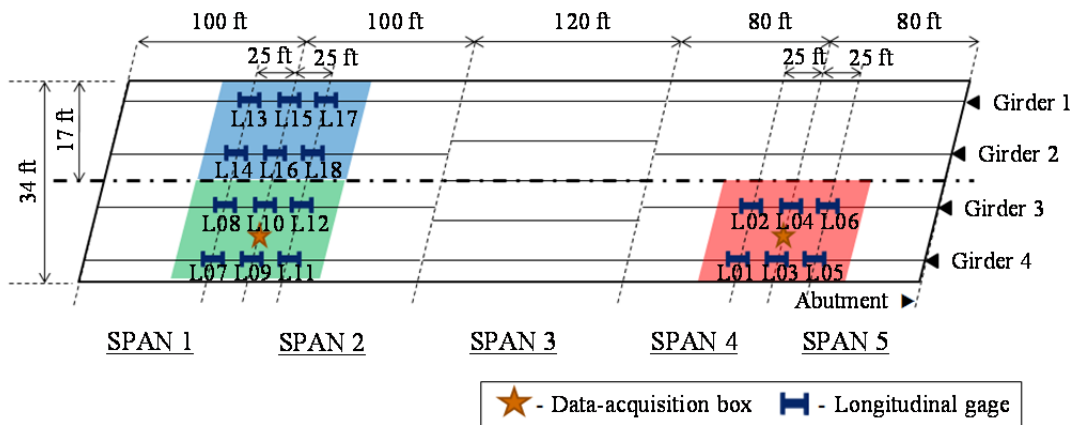


Figure 3-59: Gage layout for longitudinal bars, Lampasas River Bridge

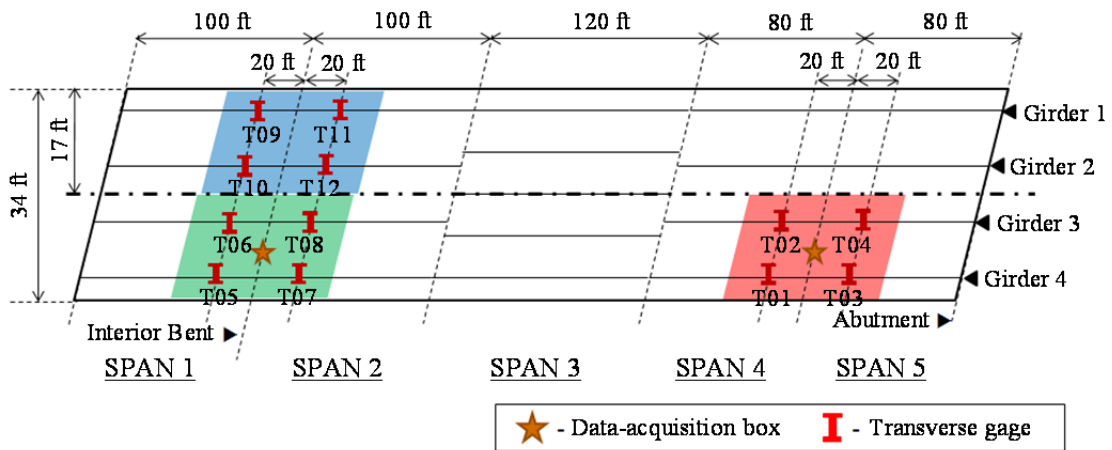


Figure 3-60: Gage layout for transverse bars, Lampasas River Bridge

3.3.4.2 Data-acquisition equipment

Because the testing areas for the Reduced Welded-Wire Reinforcement and the Reduced Deformed-Bar Reinforcement are 300 ft apart, two data-acquisition boxes were installed. The first box consists of one data logger, two multiplexers, one analyzer, one modem, one battery and one charge regulator. The boxes were mounted on the interior bents between Girder 3 and 4. The first box was located at Joint 1 and the second box was located at Joint 4. The solar panel was installed on the side of the bent cap at Joint 1, as shown in Figure 3-61.

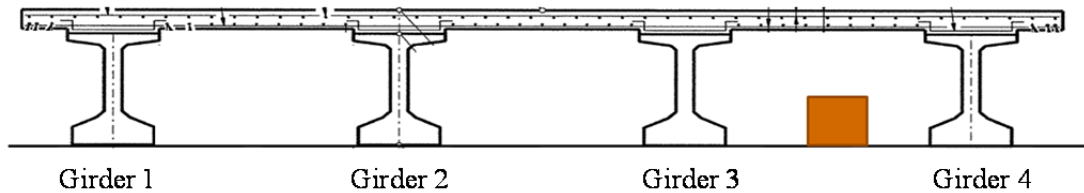


Figure 3-61: Location of data-acquisition system, Lampasas River Bridge

3.3.5 Placement of top-mat reinforcement, Lampasas River Bridge

Top-mat reinforcement was placed over the precast, prestressed concrete panels on May 7 and May 8, 2012. In Figure 3-63 to Figure 3-68 are shown details of the test area and placement of reinforcement for each top-mat option. The test area for Current TxDOT Standard Reinforcement is located on the east side of the bridge over Spans 1 and 2 (Figure 3-63); and the test area for Reduced Welded-Wire Reinforcement is located on the west side over Spans 1 and 2 (Figure 3-64). The test area for Reduced Deformed-Bar Reinforcement is located on the west side of the bridge over Spans 4 and 5 (Figure 3-67). The location of all bars and splices was checked. An armor joint was located between Spans 2 and 3, shown in Figure 3-69. Properties of top-mat reinforcement are presented in Table 3-1.

Table 3-1: Properties of top-mat reinforcement, Lampasas River Bridge

	Yield strength	Tensile strength
No. 4	63.8 ksi	104.5 ksi
No. 5	64.4 ksi	104.6 ksi
D 20	-	94.9 ksi



Figure 3-62: View of top-mat reinforcement from south end, Lampasas River Bridge

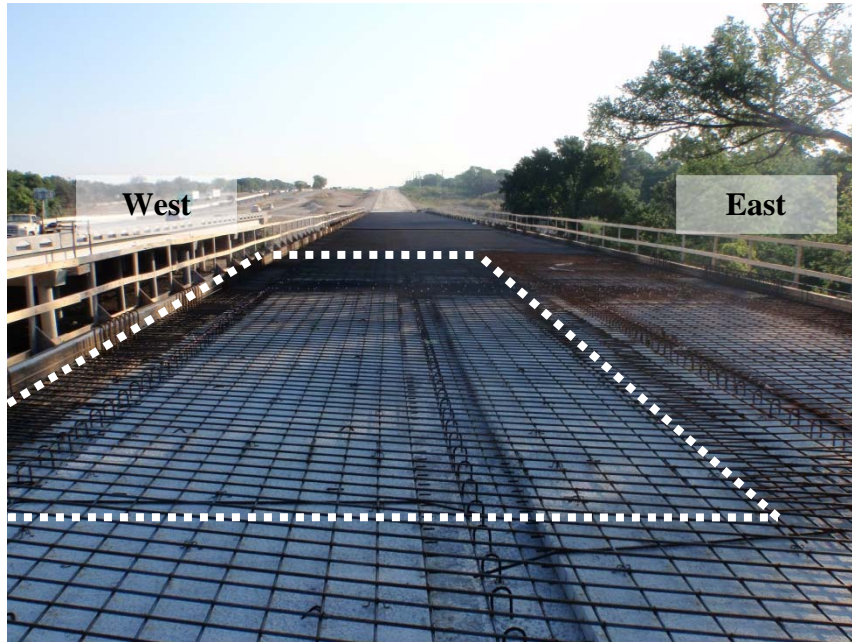


Figure 3-63: Test area for Current TxDOT Standard Reinforcement, Lampasas River Bridge

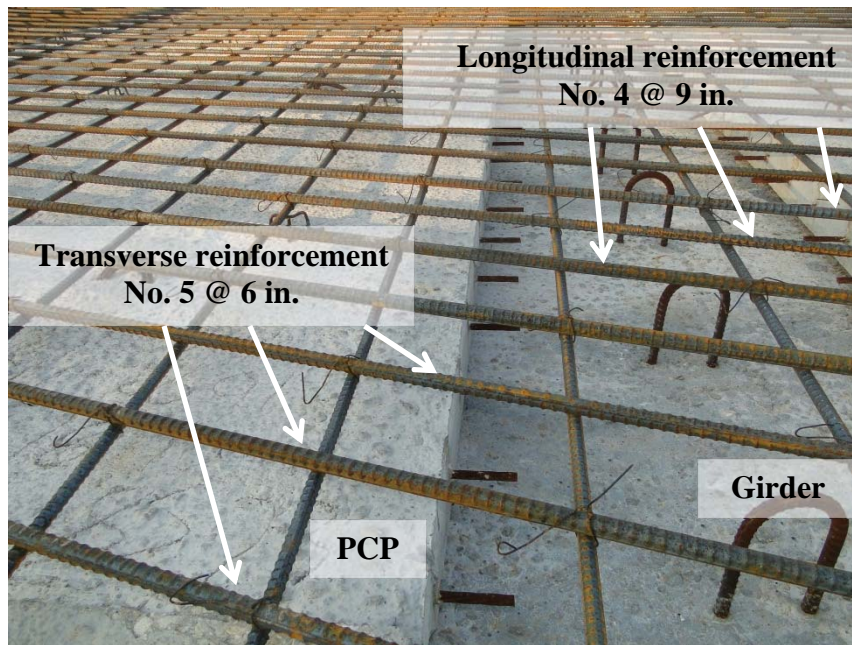


Figure 3-64: Typical placement of Current TxDOT Standard Reinforcement, Lampasas River Bridge



Figure 3-65: Test area for Reduced Welded-Wire Reinforcement, Lampasas River Bridge

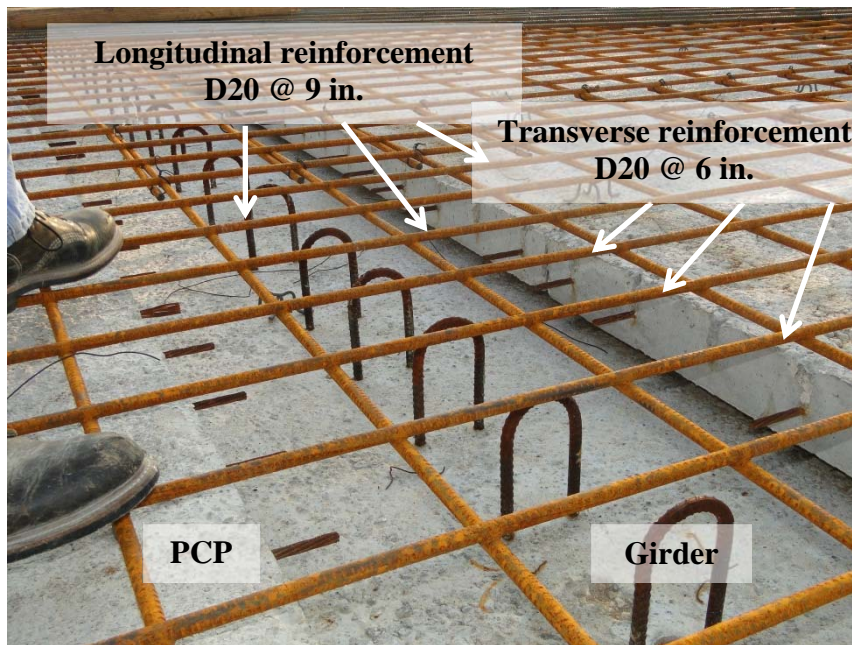


Figure 3-66: Typical placement of Reduced Welded-Wire Reinforcement, Lampasas River Bridge

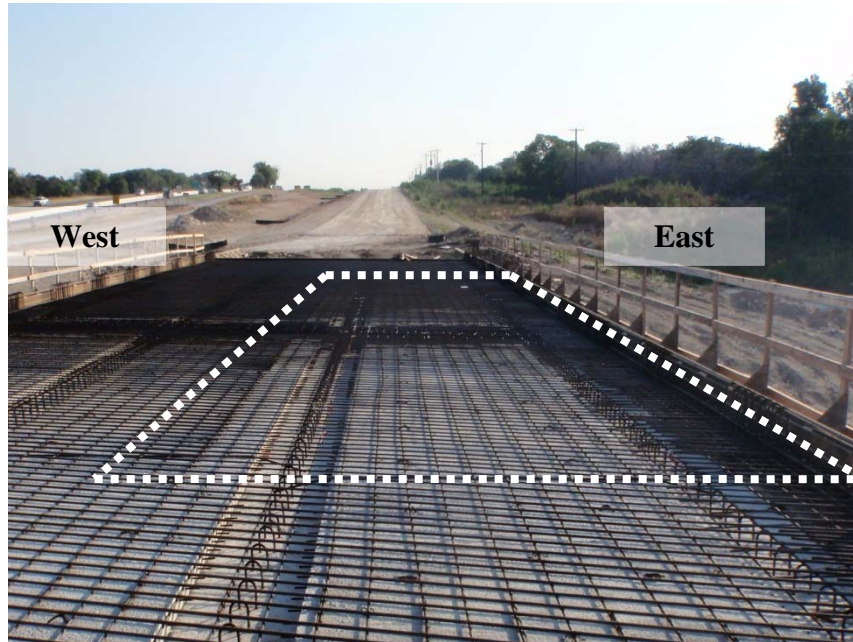


Figure 3-67: Test area for Reduced Deformed-Bar Reinforcement, Lampasas River Bridge

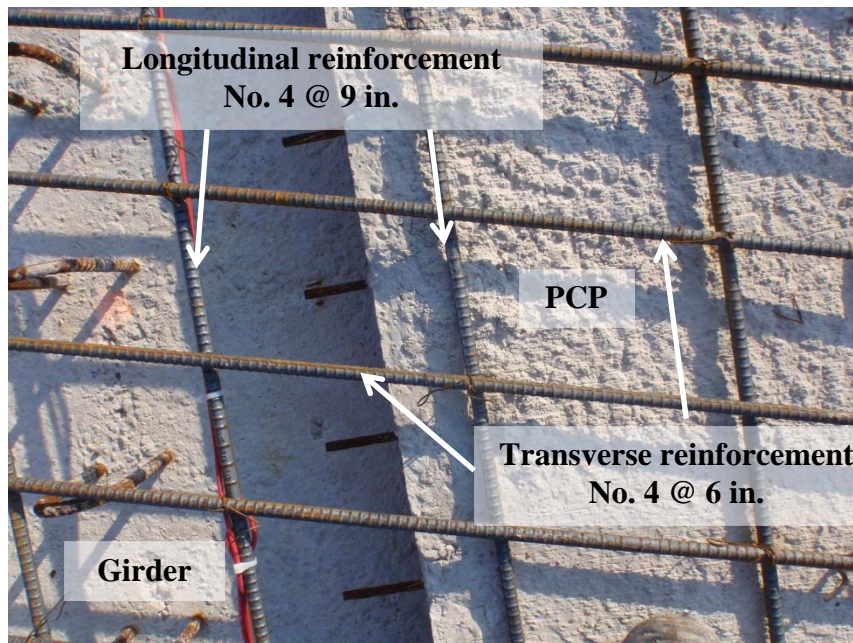


Figure 3-68: Typical placement of Reduced Deformed-Bar Reinforcement, Lampasas River Bridge

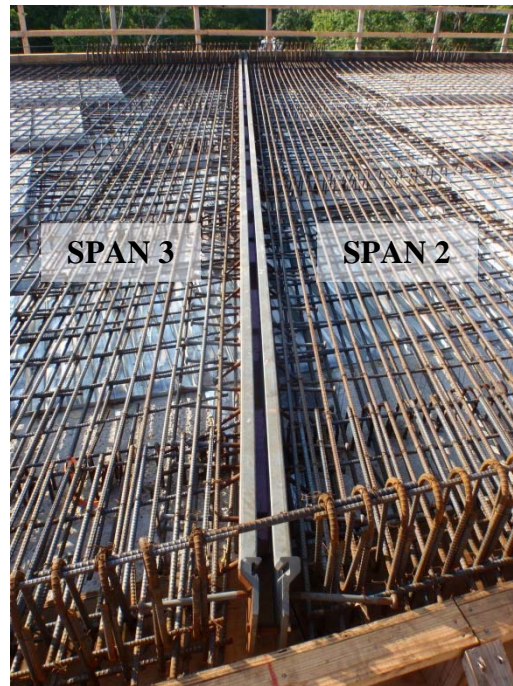


Figure 3-69: Armor joint between Spans 2 and 3, Lampasas River Bridge

3.3.6 Field instrumentation of Lampasas River Bridge

The first day for field installation of the instrumentation for the Lampasas River Bridge was May 10, 2012. Work started at 7:30 A.M. and stopped at 1:00 P.M. because of rain. During the first day, all gages were placed and wires located on the deck. The two data-acquisition boxes were placed on bent caps. The solar panel was attached to the pre-fabricated bracket, and the assembly was installed on the east face of the bent cap between Spans 1 and 2.

Field installation was completed on May 17, 2012. Wires for gages were fastened to reinforcement with plastic zip-ties, and electrical connections were finished. Each gage was connected to a port in the data-acquisition boxes, and the antenna was also connected for wireless monitoring. In Figure 3-70 and Figure 3-71 are shown side views of the bridge from both ends.



Figure 3-70: Side view of Lampasas River Bridge from north end



Figure 3-71: Side view of Lampasas River Bridge from south end

3.3.6.1 Installing vibrating-wire gages

Thirty vibrating-wire gages were installed as shown in Figure 3-72. Yellow and orange paint were used to mark gage locations. All gage wires were routed to holes made in the bedding strip, using an electric drill with a long bit (Figure 3-73). Before feeding wires in the holes, gages were tested using hand-held reader (Figure 3-74). After checking connections between the data logger and the gages, all wires were arranged neatly with plastic zip-ties. Holes in bedding strips and on data-acquisition boxes were sealed with spray foam as shown in Figure 3-75. The exposed portions of the wires were further protected with split tubing (Figure 3-76).



Figure 3-72: Typical field installation of VWG, Lampasas River Bridge

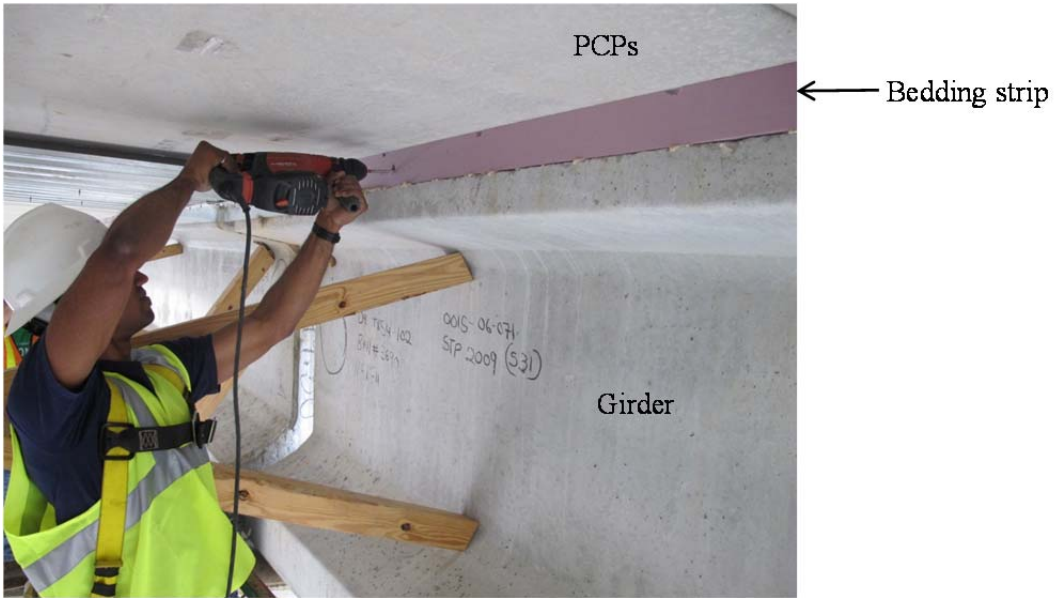


Figure 3-73: Making holes in bedding strip, Lampasas River Bridge

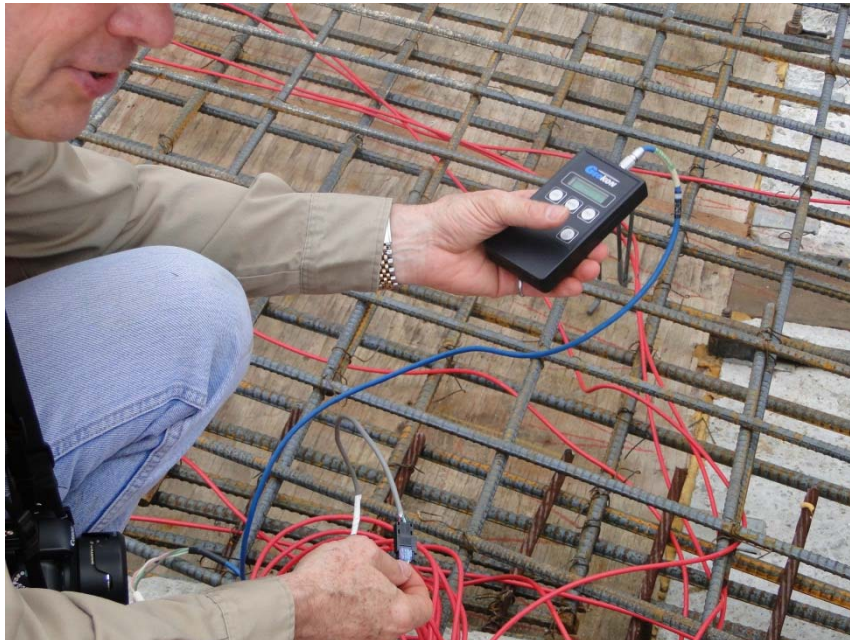


Figure 3-74: Checking gage before threading wire through the holes in bedding strip, Lampasas River Bridge

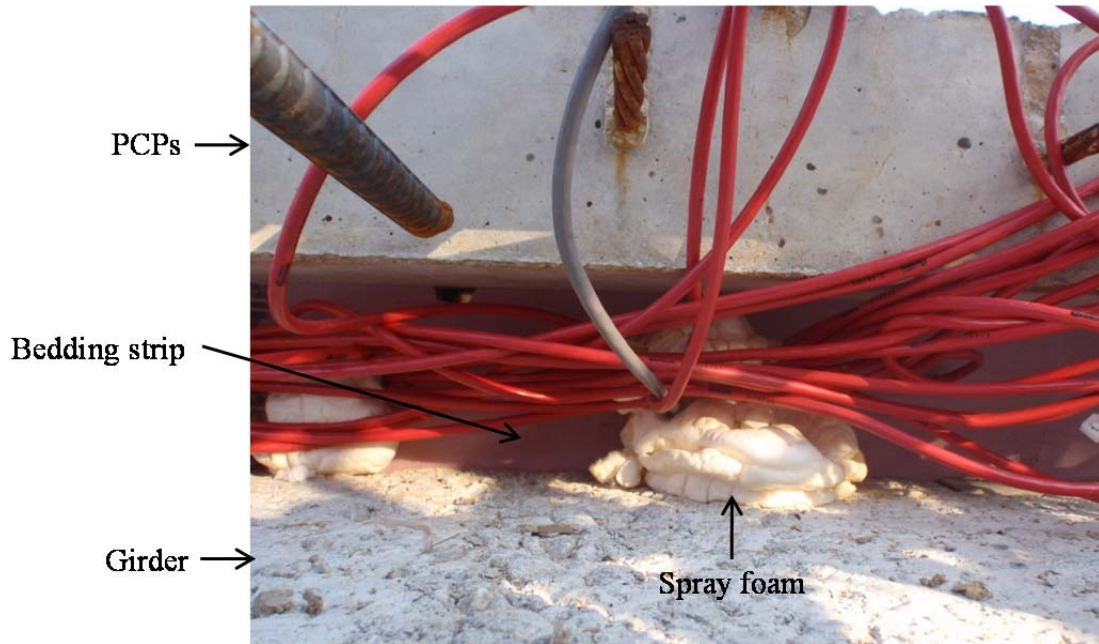


Figure 3-75: Sealing holes in bedding strip (Spans 1 and 2), Lampasas River Bridge

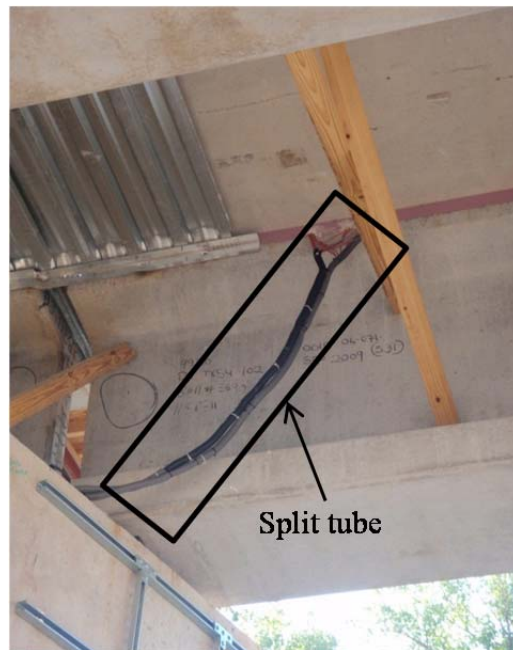


Figure 3-76: Split tube covering exposed parts of wires, Lampasas River Bridge

3.3.6.2 Placing data-acquisition box, Lampasas River Bridge

Two data-acquisition boxes were attached on the bent cap between Girder 3 and 4. The large data-acquisition box was placed on the bent between Spans 1 and 2 (Figure 3-77), and the small data-acquisition box was placed on the bent between Spans 4 and 5 (Figure 3-78). Both boxes were anchored to the bent caps, and one or two bags of desiccant were placed in each box. Because the top face of the bent cap between Spans 4 and 5 is about 8 feet above ground, two layers of scaffolding were used to access the bent cap (Figure 3-79). The height of the bent cap between Spans 1 and 2 is almost 20 feet, so a man-lift was used.

As with the Wharton-Weems Overpass, all holes of the boxes for wires were sealed with spray foam, and the boxes were locked after finishing electrical connection. Figure 3-80 shows the inside of the data-acquisition box placed on the bent between Spans 1 and 2.



Figure 3-77: Data-acquisition box between Spans 1 and 2, Lampasas River Bridge



Figure 3-78: Data-acquisition box between Spans 4 and 5, Lampasas River Bridge



Figure 3-79: Scaffolding for accessing bent cap between Spans 4 and 5, Lampasas River Bridge

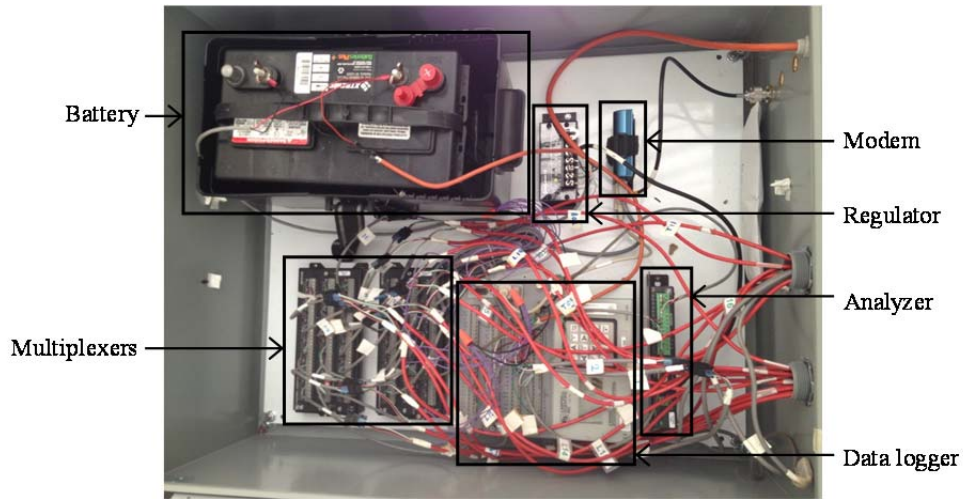


Figure 3-80: Inside of data-acquisition box placed on the bent between Spans 1 and 2, Lampasas River Bridge

3.3.6.3 Mounting solar panel

The solar panel and bracket were installed on side of the bent cap between Spans 1 and 2. Figure 3-81 and Figure 3-82 show the mounting procedure, and Figure 3-83 shows the bracket and the solar panel after mounting. An antenna was attached to the back side of the bracket (Figure 3-84), and power cables for the antenna and the solar panel were routed to the data-acquisition box. For optimum performance, the south-facing solar panel was tilted 30° from the horizontal (Figure 3-84).



Figure 3-81: Drilling holes on the side face of the bent caps for anchor bolts, Lampasas River Bridge



Figure 3-82: Mounting bracket for solar panel, Lampasas River Bridge



Figure 3-83: Solar panel mounted on side face of bent between Span 1 and 2, Lampasas River Bridge

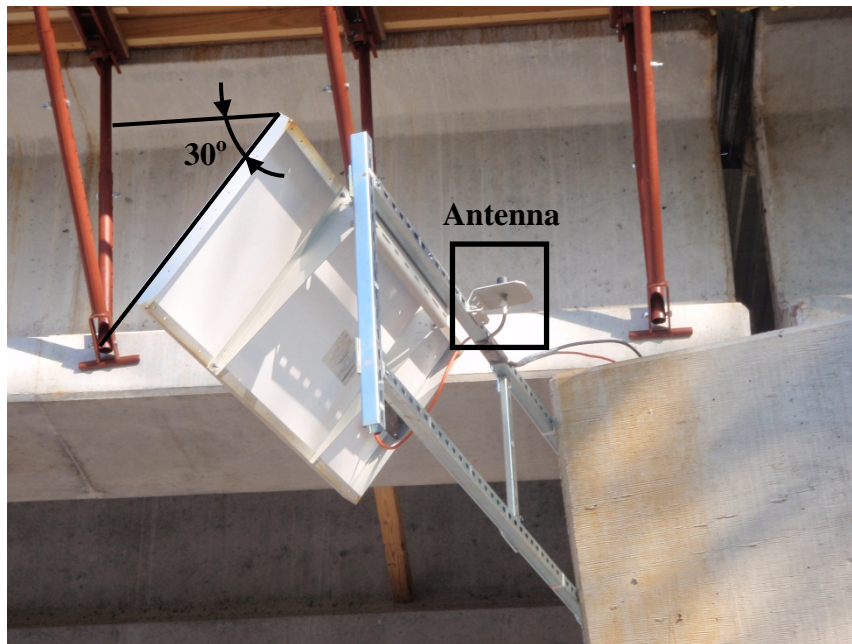


Figure 3-84: Back side of the bracket showing wireless antenna, Lampasas River Bridge

3.3.6.4 Casting concrete deck, Lampasas River Bridge

The deck was cast on June 1, 2012 starting at 1:30 A.M., and took about 6 hours to complete. The casting time was chosen to avoid high temperature the following day and thereby reduce plastic shrinkage cracking. Two concrete pump trucks were used. Class S concrete mix was used, with specified compressive strength of 4,000 psi. The mixture proportions of the concrete were as follows:

- 413 lb of cement (Type I/II)
- 138 lb of fly ash (Class F)
- 1,851 lb of coarse aggregates (limestone)
- 1,271 lb of fine aggregates (natural sand)
- 247.4 lb of water
- 78.4 – 784.1 oz of water reducer (Type A&F)
- 19.6 – 117.6 oz of air entrainment (ASTM C260)
- 78.4 – 313.6 oz of retarder (Type B&D)

The casting sequence of the Lampasas River Bridge is the same as for the Wharton-Weems Overpass, and is shown chronological order in Figure 3-85. Before concrete is placed over the precast panels, water was sprayed on the surface (Figure 3-85 a). One or two workers hold the hose of the concrete pump truck to distribute concrete (Figure 3-85 b), and then the concrete was consolidated with hand-held vibrators (Figure 3-85 c). Uneven surfaces were raked (Figure 3-85 d), and the surface was finished using a screeding machine and hand tools. After that, crack formers were inserted over the joints (Figure 3-85 e).

The portions of the deck, where the screeding machine could not reach, were finished using a wood screed (Figure 3-85 g). Curing compound was sprayed on the surface of the deck right after removing moisture from the surface.



(a) Spraying water on panels



(b) Placing concrete



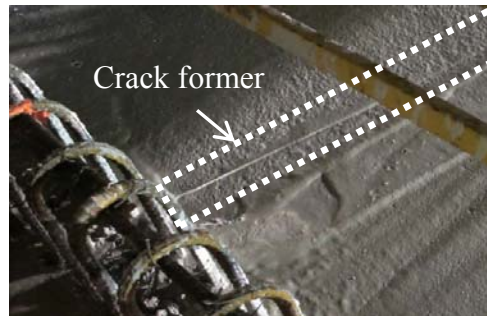
(c) Consolidating concrete



(d) Raking concrete



(e) Finishing surface



(f) Inserting crack former



(g) Hand screeding of portion of deck

Figure 3-85: Construction sequence for deck, Lampasas River Bridge

3.3.7 Results from Field Instrumentation, Lampasas River Bridge

3.3.7.1 Cracking inspection

The deck of the Lampasas River Bridge was inspected for cracking on August 16, 2012 (75 days after casting). The result of the inspection is shown in Figure 3-86. Two transverse cracks were expected because the gages installed along joints indicated much higher stresses than the theoretical cracking value.

The two transverse cracks, located at Joint 1 and Joint 4 had an average widths of 0.008 in. At some locations, part of the crack former was exposed as shown in Figure 3-87. The width at those locations was 0.050 in., but could not be accurately read, so the value was not used for calculating average width of crack. No longitudinal cracks were found.

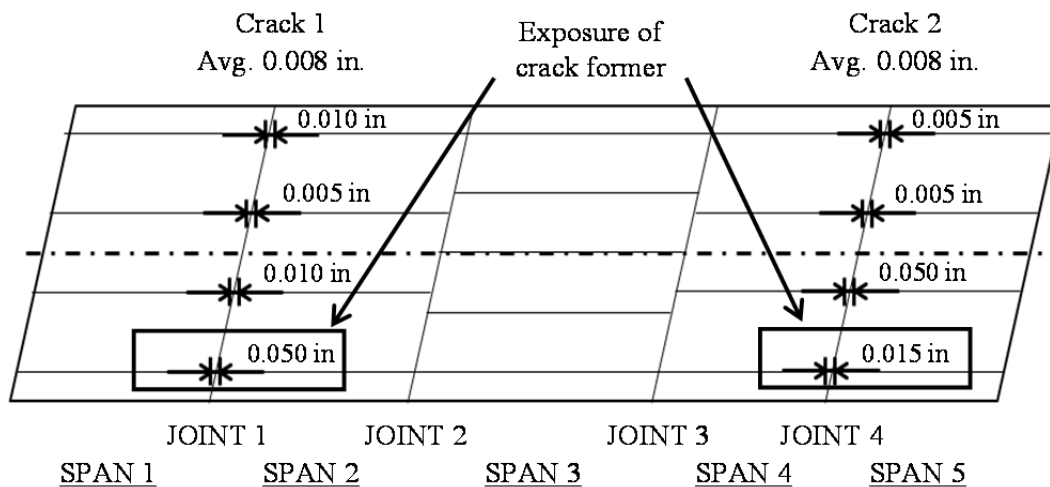


Figure 3-86: Result of cracking inspection of Lampasas River Bridge



Figure 3-87: Exposure of crack former, Lampasas River Bridge

3.3.7.2 Long-term monitoring, Lampasas River Bridge

Long-term monitoring data from the Lampasas River Bridge is quite similar to that of the Wharton-Weems Overpass. The entire monitoring period to date is about two months, and the data logger did not work well during the second month because of problems with the cables between two data acquisition boxes. The long-term monitoring results in both directions are shown in Figure 3-88 through Figure 3-93. In the figures, positive sign indicates tensile stress, and negative sign indicates compressive stress.

In the longitudinal direction (Figure 3-88 to Figure 3-90), the stresses in reinforcement based on strains from gages located over the construction joints increased rapidly, and reached values corresponding to cracking of concrete within a week after casting. Other longitudinal gages away from the joints showed strain values less than the cracking value during entire monitoring period.

In the transverse direction (Figure 3-91 to Figure 3-93), the steel stresses based on strains from gages did not change much and were smaller than the theoretical concrete cracking values. The low stresses may be the result of high temperature, because the compressive stress due to restrained thermal expansion of concrete would be greater in hot weather. The similar patterns can be found in long-term monitoring results from the Wharton-Weems Overpass. The measured tensile strains in the transverse direction of the Wharton-Weems Overpass decreased as ambient temperature increased. The data from all three testing areas were similar. The bridge has not been opened to traffic. The crossing marks in Figure 3-89 and Figure 3-92 represent the stresses measured by hand-held reader.

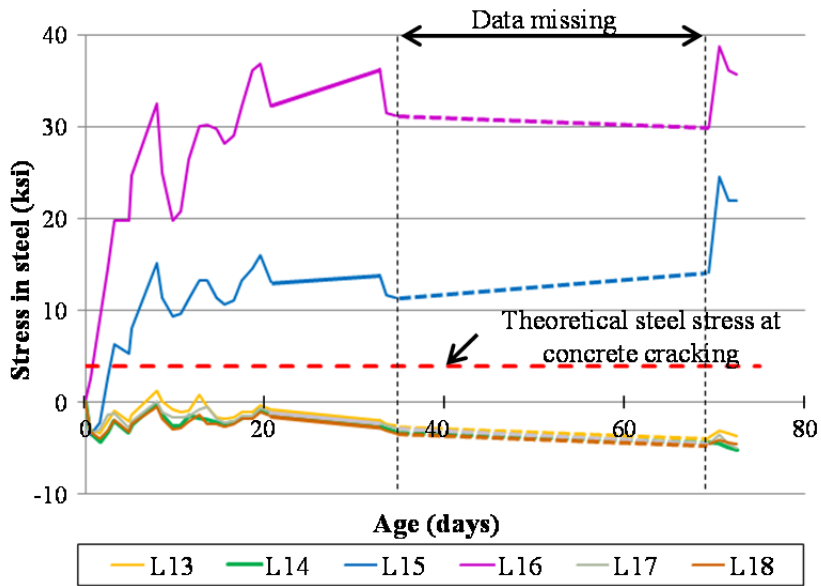


Figure 3-88: Stresses in Current TxDOT Standard Reinforcement, Lampasas River Bridge (longitudinal direction)

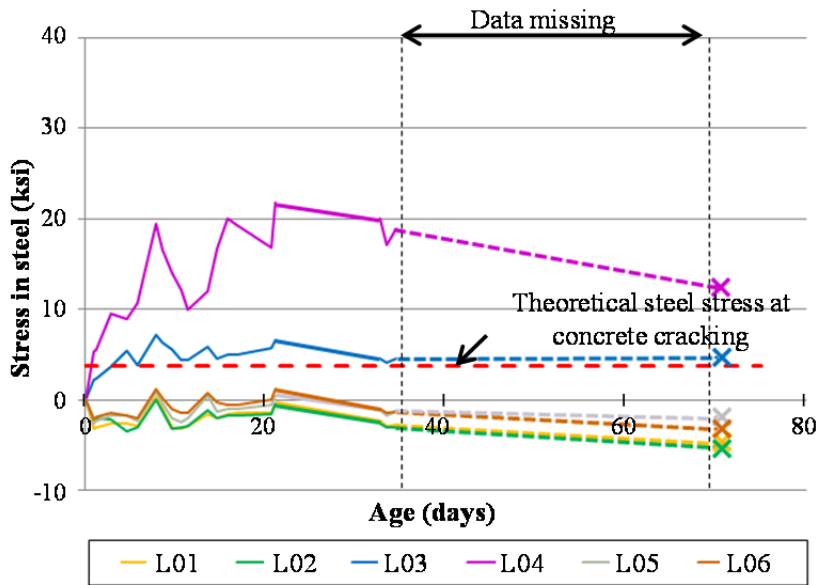


Figure 3-89: Stresses in Reduced Deformed-Bar Reinforcement, Lampasas River Bridge (longitudinal direction)

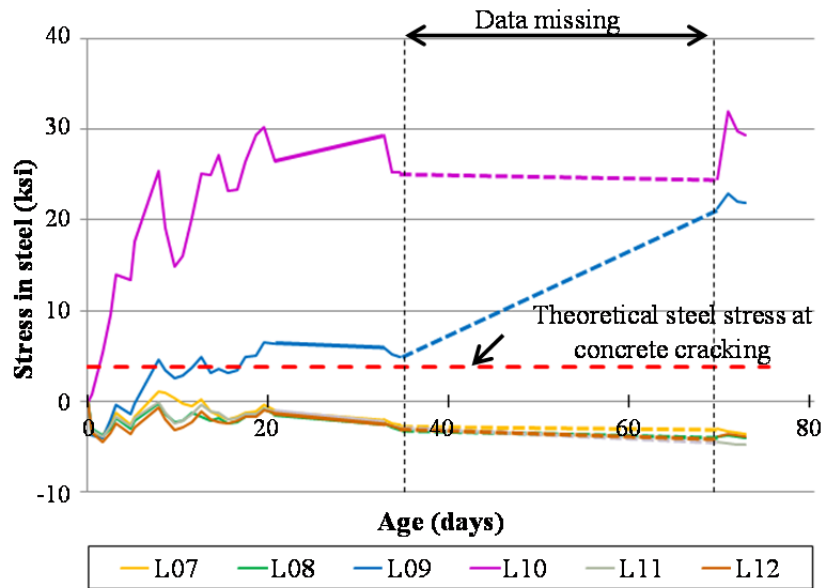


Figure 3-90: Stresses in Reduced Welded-Wire Reinforcement, Lampasas River Bridge (longitudinal direction)

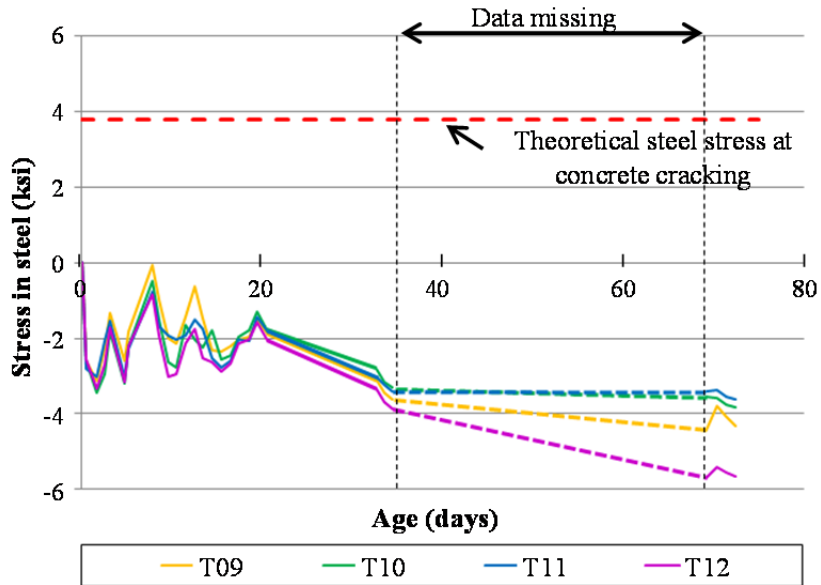


Figure 3-91: Stresses in Current TxDOT Standard Reinforcement, Lampasas River Bridge (transverse direction)

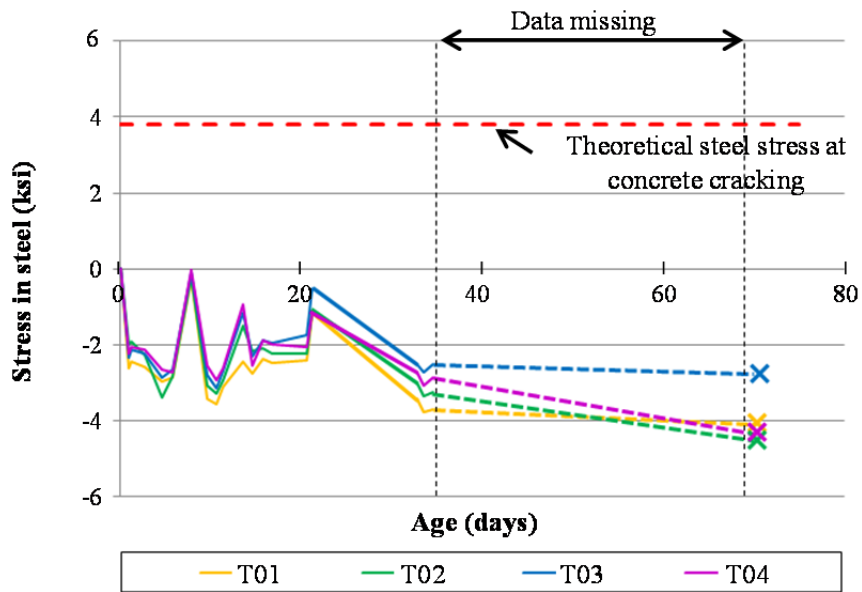


Figure 3-92: Stresses in Reduced Deformed-Bar Reinforcement, Lampasas River Bridge (transverse direction)

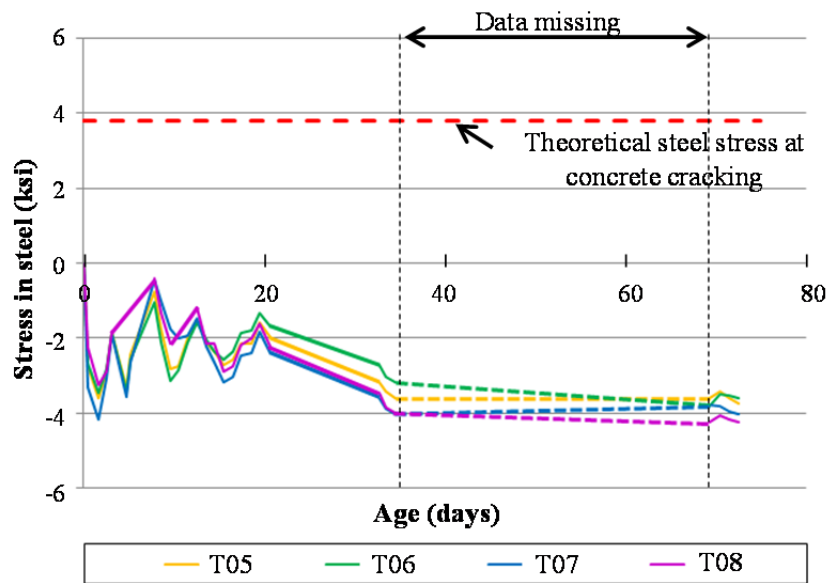


Figure 3-93: Stresses in Reduced Welded-Wire Reinforcement, Lampasas River Bridge (transverse direction)

3.3.7.3 Calculation of restraint moment using P-method, Lampasas River Bridge

Restraint moment of the Lampasas River Bridge can be calculated using the P-method introduced in Section 3.2.6.3 for the same reasons stated in Section 3.2.6.3.2. The areas for the calculation of restraint moment of Lampasas River Bridge in both directions are shown in Figure 3-94 and Figure 3-95. Span 1- 2 and Span 4-5 were the testing areas of the Lampasas River Bridge, but only span 1-2 was used for the calculation because it was the worst case; so the worst case was considered. Restraint moment increases as length of span increases

The dimensions and conditions of those areas of the Lampasas River Bridge are very similar to those of the Wharton-Weems Overpass (Figure 3-29 and Figure 3-32) except that there was a slight skew in the Lampasas River Bridge. In the P-method, there is no term to address skew; therefore the calculation results of the Lampasas River Bridge will be the same as the calculation results of the Wharton-Weems Overpass (Figure 3-31 and Figure 3-34). Similar to the Wharton-Weems Overpass, transverse cracks opened over the joints within a week after CIP slab casting, and no longitudinal crack occurred in the Lampasas River Bridge based on the first month of measured strain values. Therefore, it can be concluded the calculated and the measured results match well in the Lampasas River Bridge also.

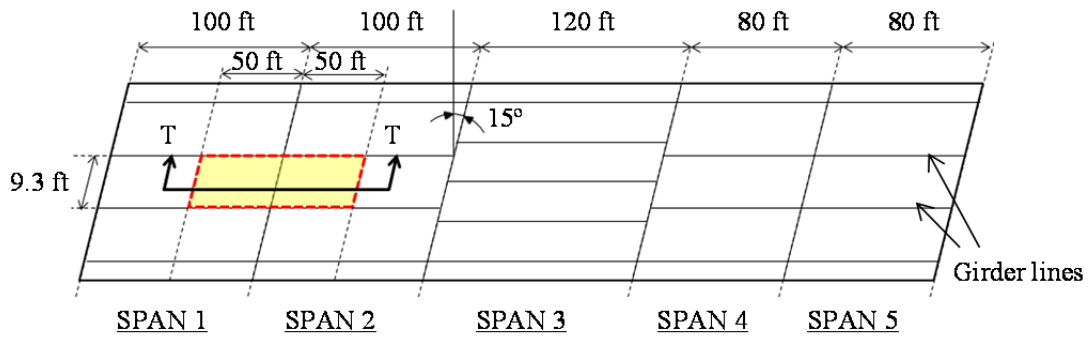


Figure 3-94: The area for calculation of longitudinal restraint moment, Lampasas River Bridge

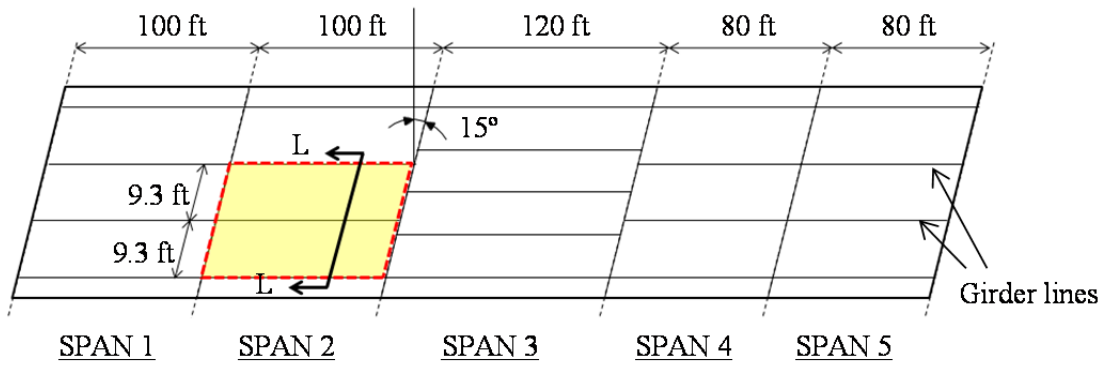


Figure 3-95: The area for calculation of transverse restraint moment, Lampasas River Bridge

3.4 CALCULATIONS OF CONSTRUCTION COST OF VARIOUS TOP-MAT REINFORCEMENT OPTIONS

Table 3-2: Material costs of each top-mat option

	Current TxDOT Standard Reinforcement	Reduced Deformed-Bar Reinforcement	Reduced Welded-Wire Reinforcement
Cost per unit weight of reinforcement	\$0.30/lb	\$0.30/lb	\$0.38/lb
Weight per unit area of deck	2.977 lb/ft ²	2.227 lb/ft ²	2.227 lb/ft ²
Cost per unit area of deck	\$0.89/ft ²	\$0.67/ft ²	\$0.85/ft ²

The material costs of each top-mat reinforcement option were calculated, and the results are listed in Table 3-2. The values in the second row (cost per unit weight of reinforcement) are taken from the web site of Purdue University (<http://rebar.ecn.purdue.edu/wwr/resDesign.aspx>), and the values in the fourth row (cost per unit area of deck) were calculated as the product of the values in the second row and the third row.

According to the results in Table 3-2, material cost can be reduced by 25% by changing the top-mat option from the Current TxDOT Standard Reinforcement to the Reduced Deformed-Bar Reinforcement option. Material cost can be reduced by 5% by changing to the Reduced Welded-Wire Reinforcement option.

By using welded-wire reinforcement, further savings in construction cost can be realized due to savings in labor. Welded-wire reinforcement can be placed more quickly and economically than deformed-bar reinforcement, arranging and tying top-mat reinforcement is eliminated. Based on the comparison of estimated construction cost (considering labor, time, and handling) between welded-wire reinforcement and standard deformed bar shown in the Purdue web site, an average reduction in construction cost of 20% can be realized if welded-wire reinforcement is used. In this regard, the contractor

of the Lampasas River Bridge told study researchers that he preferred to welded-wire reinforcement due to a considerable saving in construction time.

3.5 CONCLUSIONS FROM FIELD INSTRUMENTATION

Two bridge decks were instrumented to monitor optimized top-mat reinforcement layouts for the cast-in-place (CIP) concrete slabs. The field applications provide data based on actual CIP-PCP interaction, boundary conditions, environmental conditions, and loading conditions.

During the monitoring period, the selected top-mat options behaved similarly. The longitudinal reinforcement placed according to current design specifications almost reached yield strain at crack locations over the joints between spans, and the cracks were very narrow. Based on the monitoring results, top-mat reinforcement in the longitudinal direction cannot be reduced. Transverse reinforcement, in contrast, exhibited very low strains, even though the sectional area of the transverse reinforcement was reduced. Because the strains in the transverse direction are nearly the same for all reinforcement options, the data are not conclusive. However, it is highly likely that the Reduced Deformed-Bar Reinforcement (No. 4 @ 6 in.), and the Reduced Welded-Wire Reinforcement (D 20 @ 6 in.) will be acceptable design alternatives for the transverse top-mat reinforcement. Continued monitoring of these bridge decks is needed to confirm the performance of the selected top-mat options.

CHAPTER 4

OPTIMIZATION OF REINFORCEMENT IN CIP SLABS: RESTRAINED-SHRINKAGE TEST

4.1 INTRODUCTION

The large-scale restrained shrinkage test was planned to provide additional data regarding the comparative behavior of the top-mat reinforcement options, and to supplement data from field studies. Because access to construction sites that would permit installation of instrumentation was limited, it was decided to study the design options, especially welded-wire reinforcement, in a controlled laboratory setting. The intent was to simulate the CIP-PCP interface in the transverse direction of a bridge deck more closely than had been possible in the small-scale lab tests conducted early in the project (the direct tensile tests and the deck segments loaded in flexure).

In Figure 4-1 is shown the region of a bridge that was simulated in the restrained-shrinkage test. Because longitudinal reinforcement has already been optimized through previous tests (Foster 2010), the restrained-shrinkage tests in this chapter are focused on transverse reinforcement, which acts to control crack widths in the longitudinal direction (parallel to girder lines in the bridge).

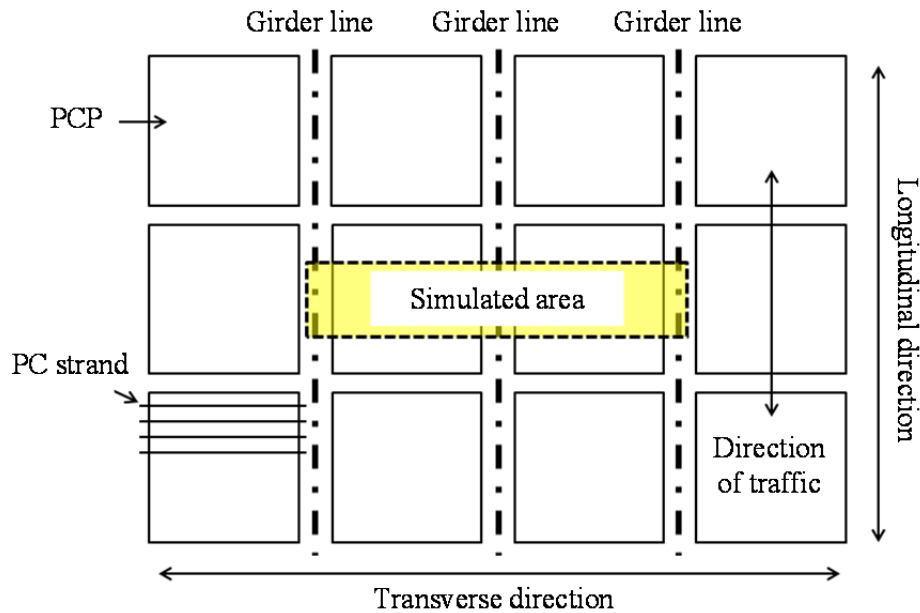


Figure 4-1: Region of the bridge deck simulated in the restrained-shrinkage test

The specimens developed in TxDOT Project 0-4098 (Figure 2-9) were used to establish the test programs described in the next section.

4.2 TEST SPECIMENS FOR RESTRAINED-SHRINKAGE TEST

4.2.1 Reinforcement options for restrained-shrinkage test

The three reinforcement options for the restrained-shrinkage test are listed in Table 4-1. All options have the same reinforcement ratio in the longitudinal direction, but the ratio in the transverse direction for the Reduced Deformed-Bar Reinforcement and the Reduced Welded-Wire Reinforcement is 35% smaller than the ratio for the Current TxDOT Standard Reinforcement. A No. 4 bar and a D 20 wire have the same cross-sectional area.

Table 4-1: Reinforcement options for restrained-shrinkage test

	Current TxDOT Standard Reinforcement		Reduced Deformed-Bar Reinforcement		Reduced Welded-Wire Reinforcement	
	size & spacing	ratio	size & spacing	ratio	size & spacing	ratio
Transverse	No. 5 @ 6 in.	0.0086	No. 4 @ 6 in.	0.0056	D 20 @ 6 in.	0.0056
Longitudinal	No. 4 @ 9 in.	0.0028	No. 4 @ 9 in.	0.0028	D 20 @ 9 in.	0.0028

4.2.2 Specimen configurations for restrained-shrinkage test

Six test specimens were constructed, each 18-ft long and 4-ft wide. The specimens were cast in a stiff steel frame that was designed to provide end restraint (to not shorten in-plane under the loads associated with restrained shrinkage of the concrete). The short direction of the specimens represents the longitudinal direction in a bridge deck, and the long direction of the specimens represents the transverse direction.

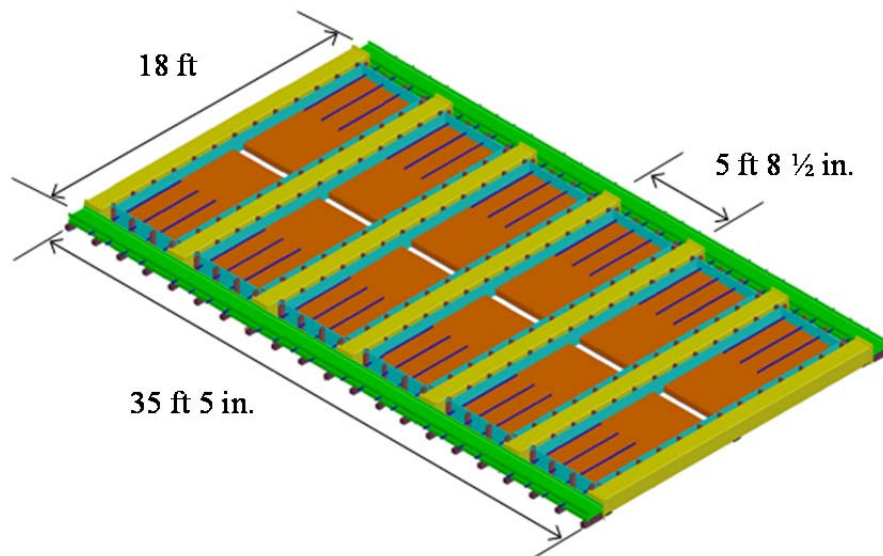


Figure 4-2: Dimensions of restrained-shrinkage specimen

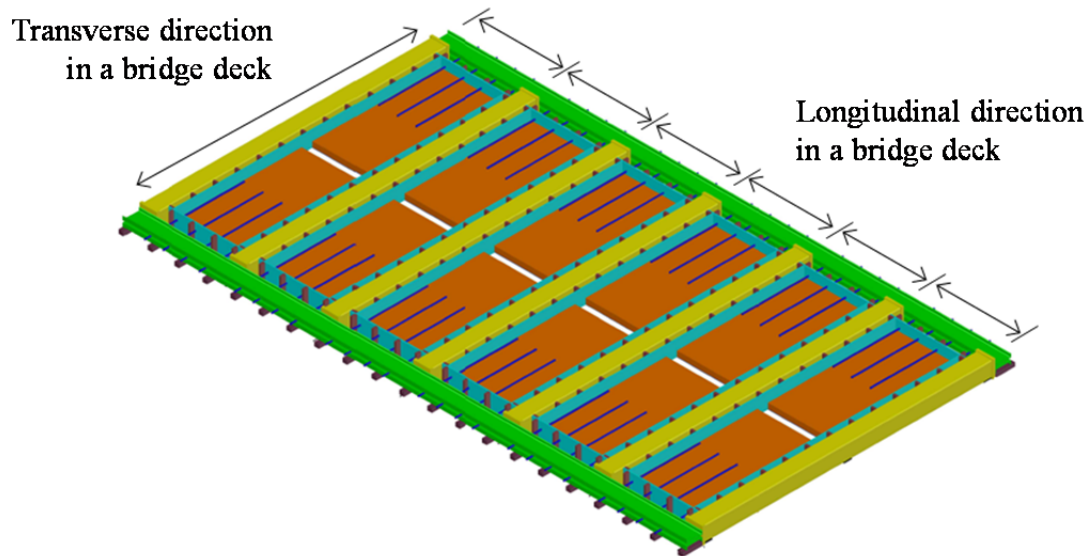


Figure 4-3: Terminology for restrained-shrinkage specimen

4.2.3 Construction of restraining frame for restrained-shrinkage test

In the test setup, the concrete specimen was cast in the restraining frame so that shrinkage of the CIP deck and creep of the PCPs was restrained by bars inserted at both ends of the specimens. This restraint should result in tensile stress in the CIP concrete and cracking in the middle of the specimen where the PCPs are supported on a girder. The cracks usually start at the boundary between the PCP and the CIP concrete (Figure 4-4). The cracking pattern is similar to longitudinal cracking of an actual bridge which generally follows girder lines. Therefore, the behavior of top-mat reinforcement options can be compared. The components of the frame are shown in Figure 4-5.

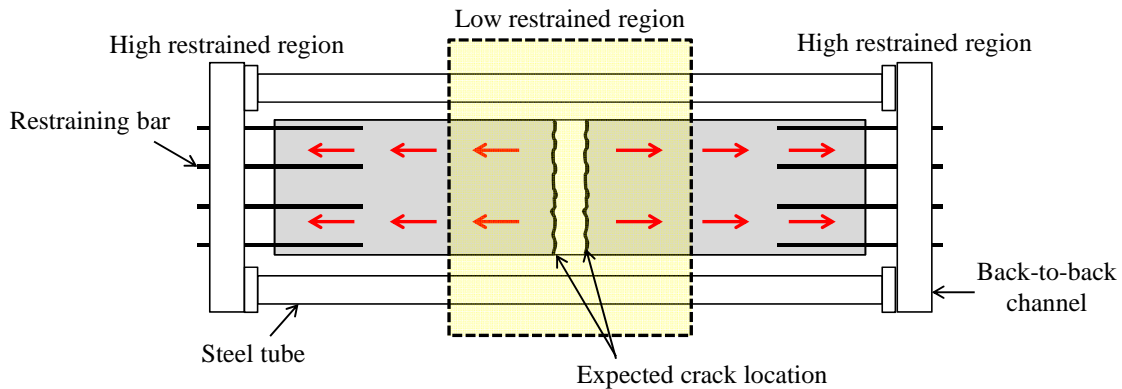


Figure 4-4: Mechanism of restrained shrinkage test

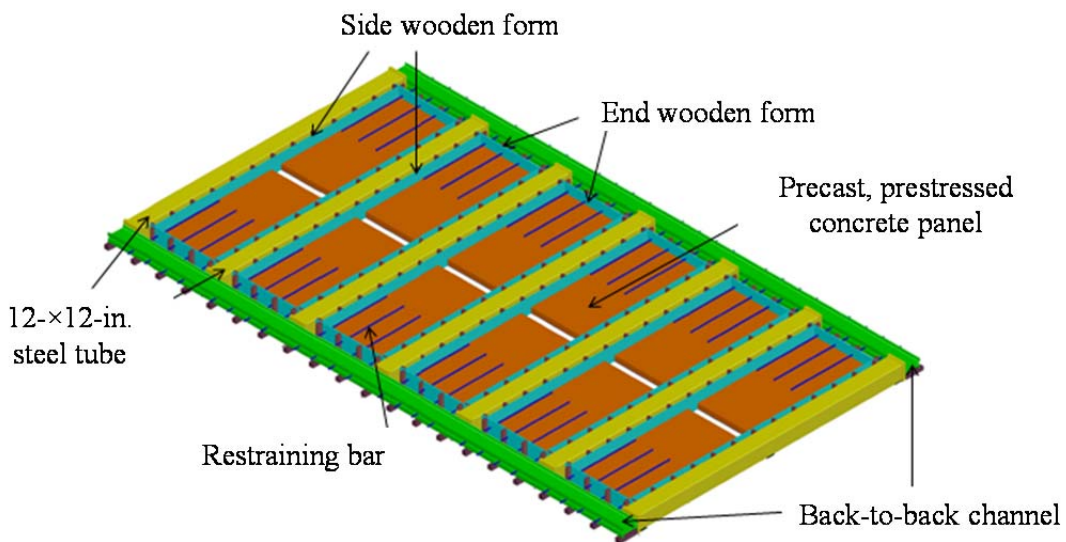


Figure 4-5: Components of restrained-shrinkage specimen

Two back-to-back channels were made using four C10×20 channels, 40-ft long. Small steel plates were welded about 14-in. apart to keep the spacing between two C10×20 channels constant at 1.5 in. The channels were supported on wooden blocks.

Seven 12-×12-in. steel tubes 17.5-ft long were placed between the test specimens to restrain the channels attached to the ends of the specimens. Plates were welded at both

ends. Holes in the steel tubes and plates were used to attach the tubes to the back-to-back channels as shown in Figure 4-6.



Figure 4-6: Attaching steel tube to back-to-back channels

4.2.4 Construction of restrained shrinkage specimens

Four PCPs were cast on September 13, 2011 and were shipped to FSEL on September 27, 2011. Each panel had 8 strands, which protruded from both ends of the panels when they were delivered. The projecting strands on one end were cut using a saw (Figure 4-7) to create a smooth face so that the panels could be placed against the wooden end forms. The panels were cut in half to form 4 × 8-ft panels that constituted the base for the CIP deck.

Wooden forms were used to contain the deck concrete. The side form (Figure 4-8) was shimmed against the steel tubes so that they were in contact with the PCPs. The end forms were placed between the back-to-back channels and the PCP ends where the protruding strands had been removed. In Figure 4-9 are shown the PCP and the side and end forms in place. A space was left between the PCPs (Figure 4-10) to simulate the deck over a girder where the cast-in-place concrete would be used to complete the deck.

The end wooden forms had four 1 ¼ in. diameter holes, placed 12-in. apart to position the restraining bars (Figure 4-5) at the middle depth of the CIP deck.

The restraining bars are used to create large tensile forces in the concrete panels of the specimen by resisting the shrinkage deformation of the panels.. The restraining bars were No. 9 Dywidag bars meeting the requirements of A615 Grade 75. Their yield and ultimate strength were 87.1 ksi and 121.8 ksi, respectively. Each bar was inserted through the space between the back-to-back channels and holes in the wooden end forms (Figure 4-11). All bars protruded about 4 ft over the precast, prestressed concrete panels. Using hex nuts, each bar was attached firmly to the channel, and chair supports were used to position the bars.



Figure 4-7: Half-size precast, prestressed concrete panels (strands cut on one side)



Figure 4-8: Wooden side forms with anchors, restrained-shrinkage test



Figure 4-9: Complete assembly of first bay, restrained-shrinkage test



Figure 4-10: Space between precast, prestressed panels, restrained-shrinkage test

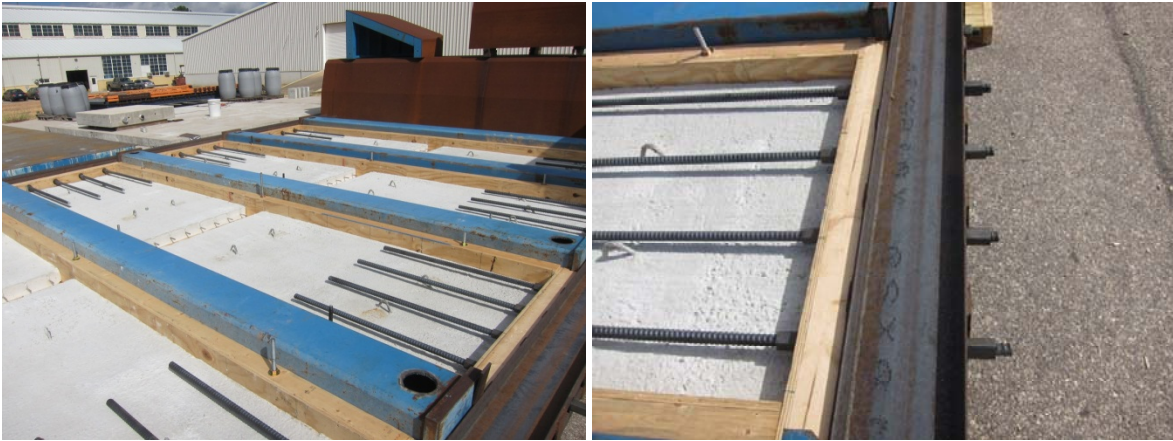


Figure 4-11: Installing restraining rods, restrained-shrinkage test

4.2.5 Placing top-mat reinforcement, restrained-shrinkage test

Standard deformed-bars and welded-wire reinforcement were placed on the PCPs and supported on steel chairs as shown in Figure 4-12 to Figure 4-14. Reinforcement in the longitudinal direction of the bridge was supported on the chairs, and reinforcement in the transverse direction was placed over the longitudinal reinforcement. The bars were tied with steel wires to form a mat of reinforcement. As shown in Figure 4-12 and Figure 4-13, two transverse bars were omitted because those bars were instrumented with foil gages and placed before the deck was cast.

Welded-wire mats were cut to size when fabricated. The time for placing the welded-wire reinforcement was about one-fifth of that for standard deformed-bar reinforcement.

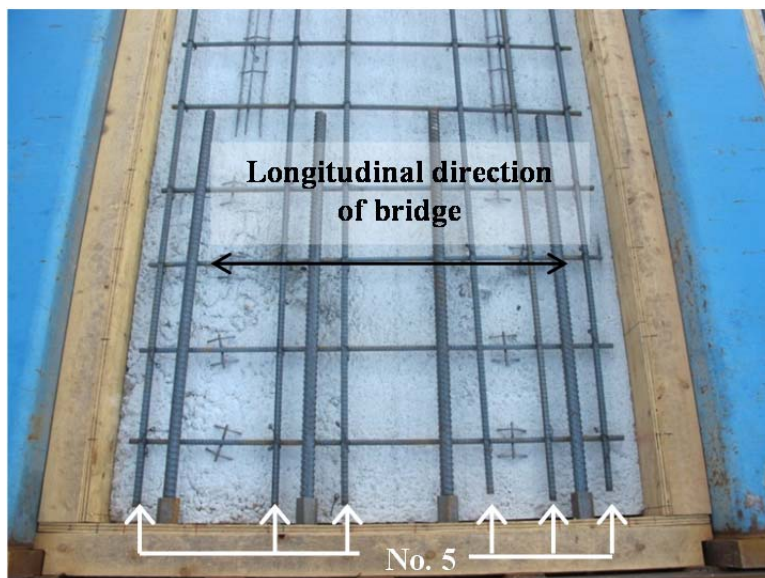


Figure 4-12: Arrangement of Current TxDOT Standard Reinforcement, restrained-shrinkage test

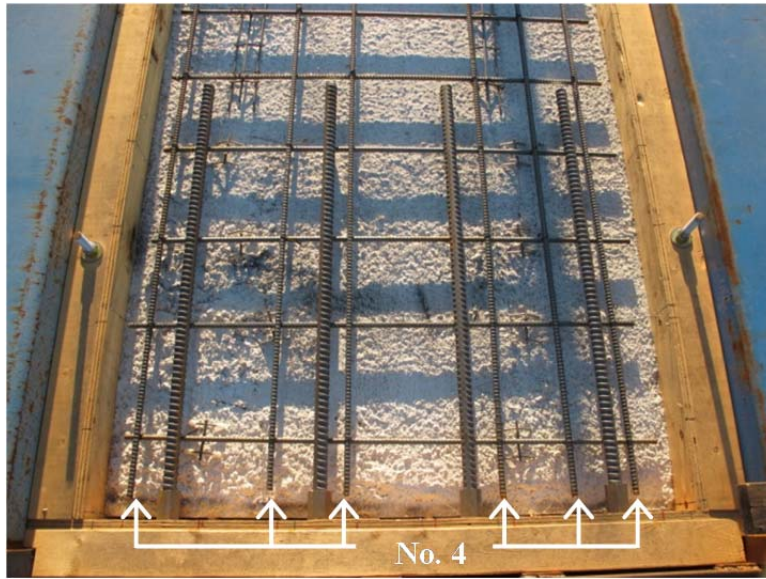


Figure 4-13: Arrangement of Reduced Deformed-Bar Reinforcement, restrained-shrinkage test

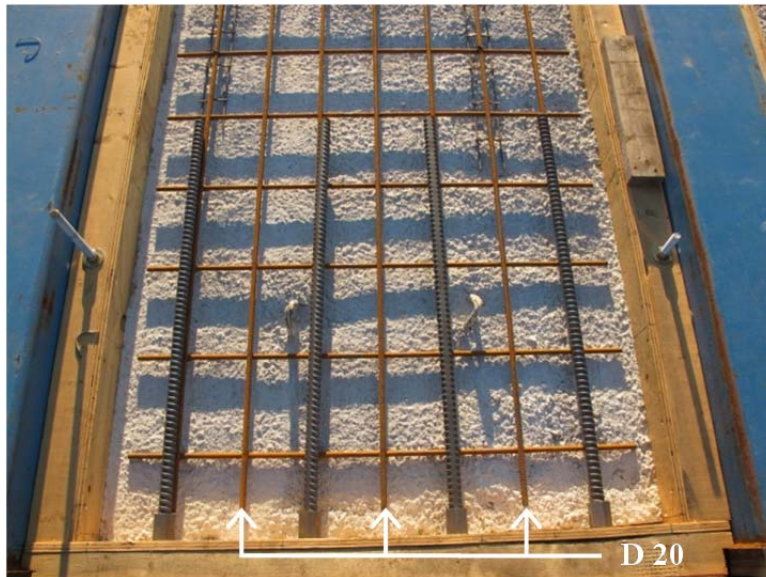


Figure 4-14: Arrangement of Reduced Welded-Wire Reinforcement, restrained-shrinkage test

4.2.6 Gage instrumentation, restrained-shrinkage test

Twenty-four foil gage and twenty-four vibrating-wire gages were installed in the restrained-shrinkage specimen. Four foil gage and four vibrating-wire gage were instrumented in each bay. Figure 4-15 shows gage layout and gage numbering; with F designates a foil gage and V a vibrating-wire gages. Gage wires were arranged neatly using zip-ties and routed to a common point in each test specimen (Figure 4-16).

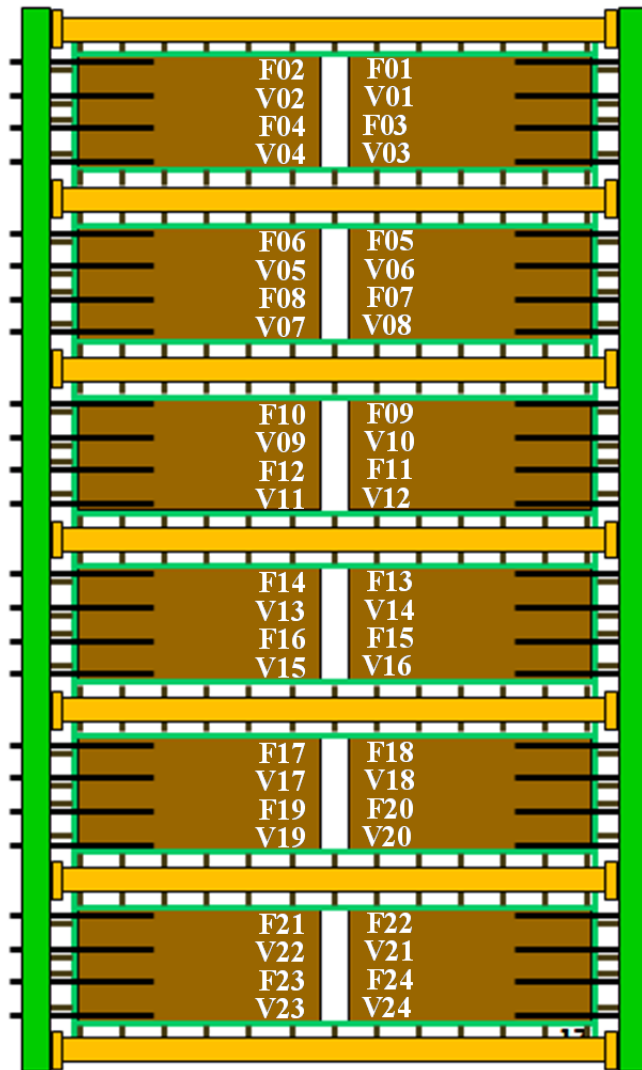


Figure 4-15: Gage layout for restrained-shrinkage test

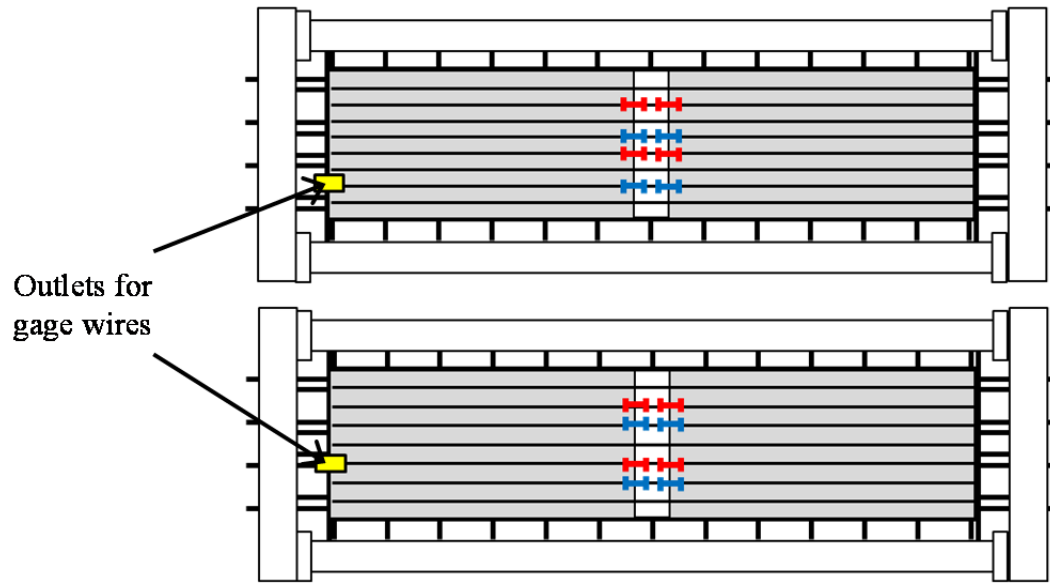


Figure 4-16: Location of outlets for gage wires, restrained-shrinkage test

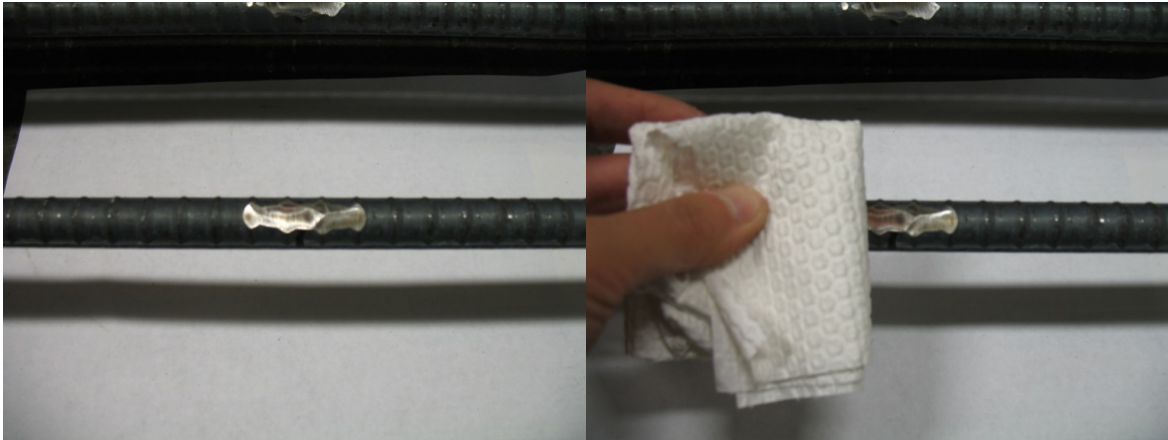


Figure 4-17: Complete gage installation for one bay of restrained-shrinkage test

Both types of gages were instrumented along the edge line of the PCPs, because it was expected that cracks would form at the PCP edge over the simulated girder region (Figure 4-17). Both edges were instrumented since there was no way to determine which edge would crack first.

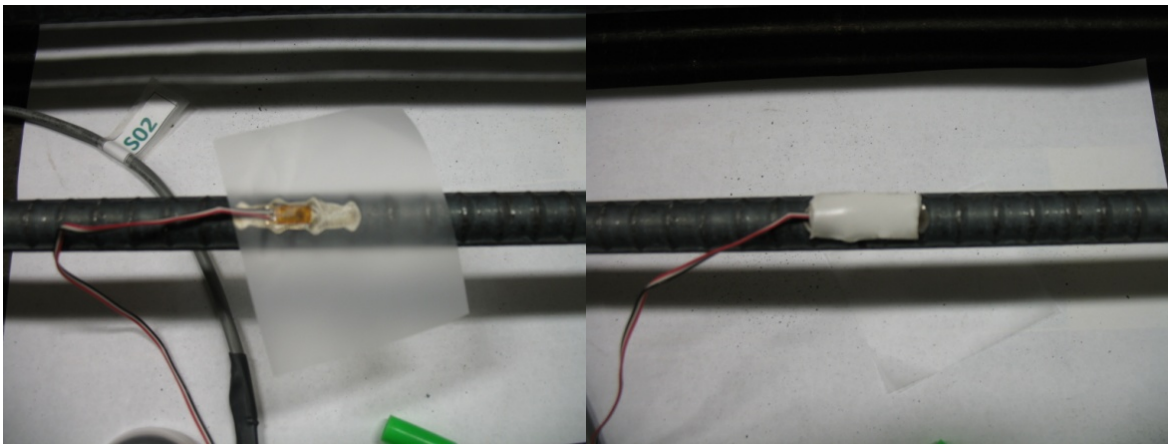
The foil gages for the specimen with Current TxDOT Standard Reinforcement and the Reduced Deformed-Bar Reinforcement options were installed before the bars were tied in mats and placed in the forms. The gages on the welded-wire mats were installed after the mats were placed in the forms. The adhesive for foil gage is cyanoacrylate, and it requires 20~60 second for curing under room temperature. The mounting procedure for foil gages is described in Figure 4-18 a-f and summarized below:

- a) Grind a 7/8 inch long portion of the surfaces of the standard deformed bars
- b) Clean the region using acetone
- c) Apply adhesive and place the gage
- d) Attach waterproof mastic sealing tape on the gage
- e) Wrap gage position with foil tape to protect against abrasion during casting
- f) Installation completed on deformed bars



(a) Grind surface of reinforcing bar

(b) Polish with acetone



(c) Place foil gage

(d) Attach waterproof sealing mastic tape



(e) Wrap with foil tape

(f) Completed installation

Figure 4-18: Installation sequence for foil gages, restrained-shrinkage test

A typical foil gage as installed is shown in Figure 4-19 a. The vibrating-wire gages were tied to the sides of the transverse reinforcing bars with plastic zip-ties and Styrofoam spacers as shown in Figure 4-19 b. The gages should be tied firmly so as not to change their orientation during casting. Care was also taken to avoid damage of the vibrating-wire gages during installation.



(a) foil gage

(b) vibrating-wire gage

Figure 4-19: Gage instrumentation (foil gage and vibrating-wire gage)

4.2.7 Casting of deck concrete, restrained-shrinkage test

Concrete for the CIP slab of the restrained-shrinkage test was cast on November 7, 2011. The specified compressive strength was 4,000 psi and the concrete mixture proportions are shown in Table 4-2. The mixture used a maximum coarse aggregate size of 1.0 in., and Class F-Fly-Ash, 9.20 oz/yd³ of retarder, and 30.93 oz/yd³ of water reducer.

Table 4-2: Concrete mixture proportions (by weight), restrained-shrinkage test

Cement	Water	Coarse agg.	Fine agg.	Fly Ash	Total
1.00	0.38	4.44	2.74	0.39	8.95

A slump test was conducted before casting, and water was added to reach the required slump of 6 in. The added water is included in the concrete mixture proportions shown in Table 4-2.

In Figure 4-20 a-f is shown the casting sequence for the restrained-shrinkage specimens. Each step is explained below:

- a) To prevent plastic shrinkage cracking and delamination of the CIP deck, water was sprayed on the precast, prestressed concrete panels
- b) About one cubic yard of concrete was placed in the center of each specimen, and spread using shovels.
- c) The concrete was consolidated using two hand-held vibrators.
- d) The surface was screeded with 2 × 4 boards.
- e) Curing compound was sprayed on the surface to simulate field curing conditions. It was applied to the surface as soon as the bleed water disappeared.
- f) One side form was removed in each bay, so that the specimen was not restrained by the forms.



(a) Spray water on panels



(b) Place concrete



(c) Consolidate with hand-held vibrator



(d) Screenshot



(e) Spray curing compound



(f) Strip wooden form on one side

Figure 4-20: Deck-construction sequence, restrained-shrinkage test

4.2.8 Concrete compressive strength, restrained-shrinkage test

Sixteen 4-×8-in. cylinders were tested to determine concrete compressive strength at 3, 7 and 28 days. Plastic molds were stripped 1 day after casting and all cylinders were placed near the specimens. No moisture curing or curing compounds were used. Figure 4-21 shows compressive strength with age. Measured compressive strength was equal to design strength. It is expected that the actual compressive strength of the specimen might be greater than the cylinder strength, because the specimen has a smaller surface to volume ratio than the cylinder and the surface of concrete of the specimen was covered with curing compound to minimize loss of water from the surface.

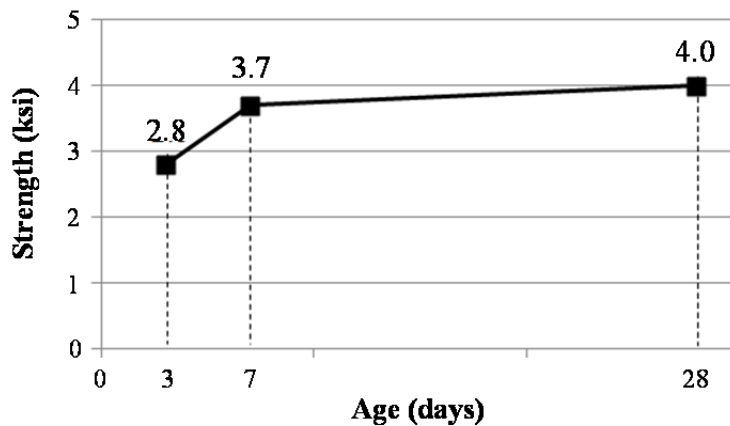


Figure 4-21: Compressive strength from 4-×8-in. cylinder tests, restrained-shrinkage specimen

4.3 RESULTS AND CONCLUSIONS, RESTRAINED-SHRINKAGE TEST

4.3.1 Results of restrained-shrinkage test

4.3.1.1 Long-term monitoring

Figure 4-22 and Figure 4-23 show long-term monitoring results from the restrained-shrinkage test. Figure 4-22 shows the results from vibrating-wire gage, and Figure 4-23 shows the results from foil gages. Detection intervals are 10 minutes for the first week, 30 minutes for the next 4 months, and 4 hours thereafter. The data from only one gage on each reinforcement option was plotted because other gages gave the same results. Moreover, strains at different gages at the same PCP and CIP edges were essentially the same.

Both gage types gave consistent results, and all design options showed similar behavior during the entire monitoring period. No cracks have been detected.

The stress increased during the first month, because most deformation due to shrinkage and creep usually occurs at early ages. After that, the values stabilized for about 3 months at strains that would indicate the concrete is near cracking. About 4 months after casting the tensile strain readings decreased slowly because outside temperature increased and specimens expanded.

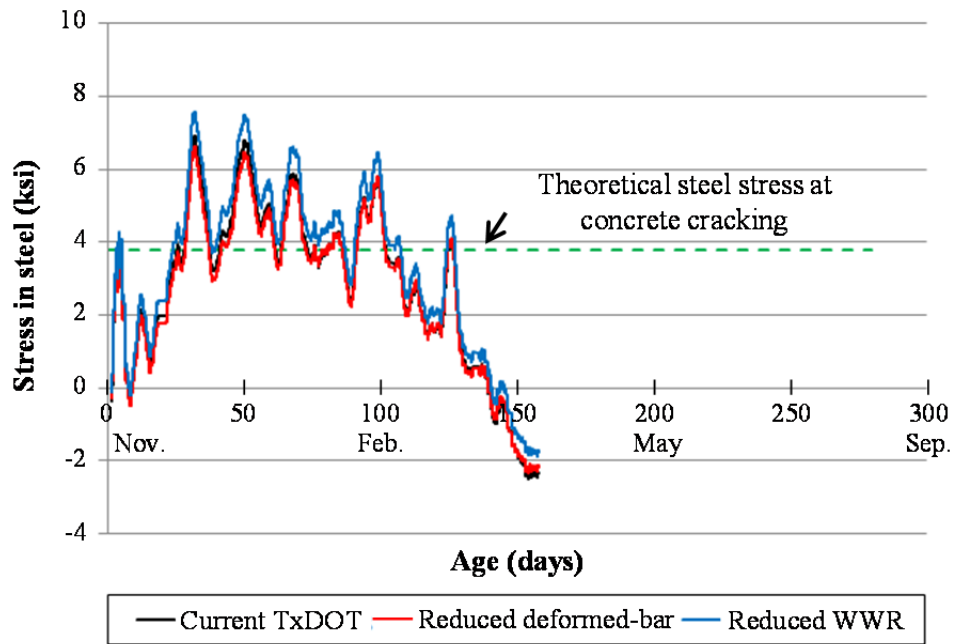


Figure 4-22: Long-term monitoring results from vibrating-wire gage, restrained-shrinkage test

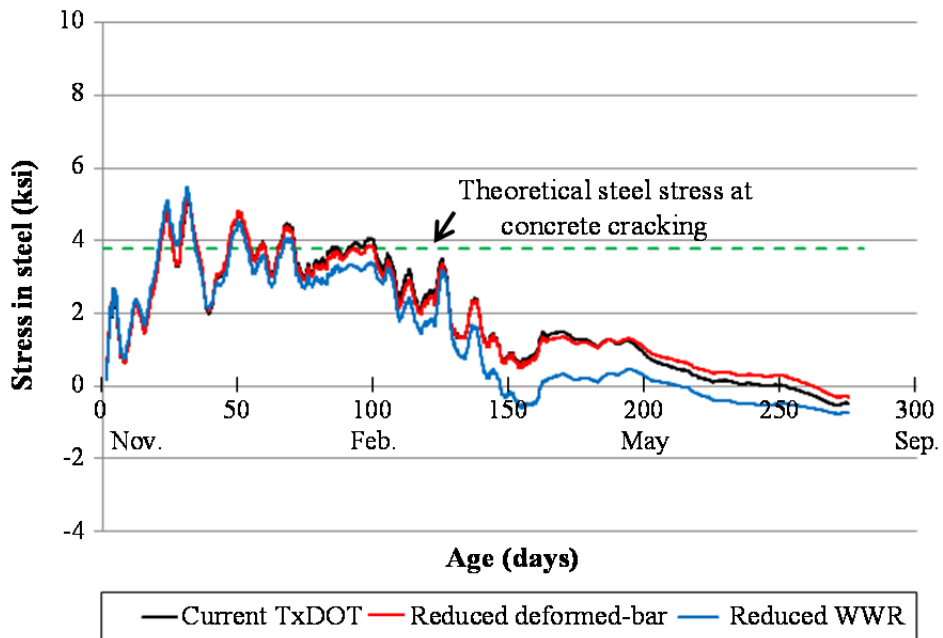


Figure 4-23: Long-term monitoring results from foil gage, restrained-shrinkage test

4.3.1.2 Calculation of restraint moment

The restraint moments of the restrained-shrinkage test were calculated using the P-method. The calculation results were used to predict the likelihood of cracking and time of occurrence of cracks in the restrained-shrinkage specimen. The calculation results were also compared with the monitoring results to determine whether or not the P-method could be used for predicting cracking in the restrained-shrinkage specimen.

The differences in length and stiffness between diaphragm region and main span were considered using a coefficient α and it was calculated using the Equation 4-1 for this case. The result obtained by Equation 4-1 is the same to the result by moment distribution method used in Chapter 3 for two-span continuous beam with the same span length. Before cracking, I_d and I_m in Equation 4-1 have the same values and their values are gross section moment of inertia. After cracking, I_m is changed to cracked section moment of inertia to consider reduced stiffness of diaphragm region, but I_d is not changed keeping its value as gross section moment of inertia.

$$\alpha = \frac{\frac{2I_d}{L_d}}{\frac{2I_d}{L_d} + \frac{3I_m}{L_m}} \quad \text{Equation 4-1}$$

Where, I_d = moment of inertia of diaphragm region
 L_d = length of diaphragm region
 I_m = moment of inertia of main spans
 L_m = length of main spans

One bay of the test specimen can be assumed as a two-span continuous bridge as shown in Figure 4-24. Each span consisted of one precast panel 8-ft long, 4-ft wide and 4-in. thick topped with 4-in. thick CIP slab. Two precast panels were used for one bay of

test specimen and the spacing between the panels was 10 in (Figure 4-10). This spacing was used as a length of the diaphragm region of the test specimen.

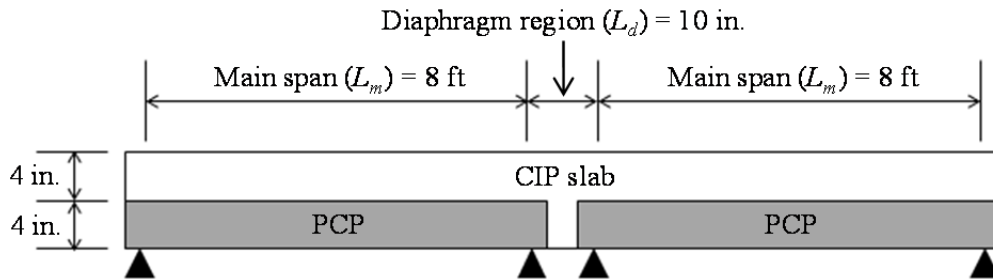


Figure 4-24: Dimensions of the specimen for calculation

Material properties, construction conditions were explained in following several paragraphs, and they were almost the same that in Section 3.2.6.3.

The design strength of concrete for the PCPs was 9,000 psi and the strength of the CIP slabs was 4,000 psi. The design strength for PCPs was determined based on the material test reports from fabrication plant, and the strength for CIP slabs was based on concrete cylinder test in Ferguson laboratory 28 days after casting. CIP topping concrete was cast when the age of the PCP was 55 days. Average relative humidity during the first month after casting was 60 %.

Each precast panel had eight 3/8 in. strands at 6 in. Initial applied prestress was 189.4 ksi per strand and the remaining prestress in the strands after the first month following casting of CIP topping was assumed as 175 ksi.

The details of top-mat reinforcement are shown in Table 4-3. This table only includes the reinforcement details in the transverse direction because to find optimized transverse top-mat reinforcement is the main focus of this test. Size and type of top-mat reinforcement in the transverse direction were varied depending on design options, but the spacing of bars in all options was 6 in. It was assumed that the values of elastic modulus of deformed bars and welded-wires were 29,000 ksi.

Longitudinal top-mat reinforcement details were the same in the Current TxDOT Standard and the Reduced Deformed-Bar Reinforcement, No. 4 bars at 9 in. The longitudinal top-mat reinforcement of the Reduced Welded-Wire Reinforcement was D 20 wire at 9 in. A D 20 wire and a No. 4 bar have the same sectional area. As stated before, longitudinal reinforcement details are not included in Table 4-3.

Table 4-3: Details of top-mat reinforcement for restraint-moment calculation

Current TxDOT Standard Reinforcement	Reduced Deformed-Bar Reinforcement	Reduced Welded- Wire Reinforcement
No. 5 bar @ 6 in.	No. 4 bar @ 6 in.	D 20 wire @ 6 in.

Using the information stated above, ultimate creep coefficients and shrinkage strains for the PCPs and the CIP slabs were calculated using ACI 209:

- i) Ultimate creep coefficient of the PCPs: 3.42
- ii) Ultimate creep coefficient of the CIP slabs: 3.40
- iii) Ultimate shrinkage strain of PCPs: 600×10^{-6}
- iv) Ultimate shrinkage strain of CIP slabs: 613×10^{-6}

Creep and shrinkage strain at time t can be obtained by multiplying ultimate values by R and the compressive strength of the CIP slabs did changed with time as shown in Section 3.2.6.3. A calculation sample of the restraint moment of the restrained-shrinkage test using the P-method is shown in Appendix C.

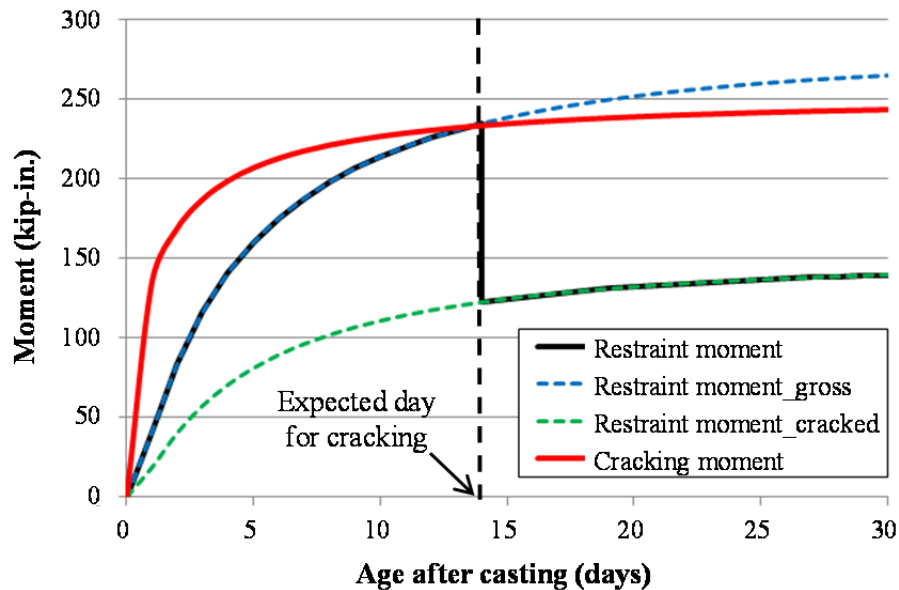


Figure 4-25: Restraint moment and cracking moment of the test frame

Figure 4-25 shows calculated restraint moments using the P-method, and calculated cracking moment using modulus of rupture of the CIP topping concrete. The top-mat reinforcement of the specimen was No. 5 bars at 6 in. In the figure, the blue dashed line represents the calculated restraint moment by P-method assuming that the specimen is not cracked. The values on this line were obtained by using the same moment of inertia for the diaphragm and main-span regions. The green dashed line represents the calculated restraint moment of the cracked section. The values on that line were obtained by using the cracked-section moment of inertia for the diaphragm region, and the gross-section moment of inertia for the main-span region.

Formation of cracks was determined by comparing the calculated restraint moment of the uncracked section (blue dashed line) to the cracking moment (red solid line). The cracking moment was calculated using the modulus of rupture of the CIP deck concrete. If the restraint moment is greater than the cracking moment, it may be concluded that cracks have been developed in the specimen.

Before cracking the restraint moment in the specimen will follow the blue dashed line; after cracking, it will drop (the black solid line) and then follow the green dashed line.

As shown in Figure 4-25, it is possible to predict that cracks will form about 2 weeks after casting. However, no crack has been observed in the test specimens. The reasons for this disparity between the test results and the predictions by P-method may be differences of geometrical and boundary conditions between specimens of this research and the specimens of Peterman and Ramirez. Moreover, in their study, the specimens were placed on the supports that consisted of plates and rollers. However, in this study, the specimen was placed over thin wooden plates, and one continuous wooden plate was used to support entire diaphragm region. Side wooden forms used in this study may have influenced the result by restraining creep and shrinkage deformation.

4.3.2 Conclusions from restrained-shrinkage test

The restrained-shrinkage test was planned to help determine optimized top-mat reinforcement in the transverse direction by comparing the performance of various top-mat reinforcement options. The restrained-shrinkage test has many advantages compared to other tests which were discussed previously in Section 2.3.2. The specimens consist of CIP slabs and precast, prestressed concrete panels (PCPs) constructed in the same manner as they would be constructed in the field. Welded-wire reinforcement, one of the test variables in this research, has been much less widely used in the field than deformed-bar reinforcement, so it is so hard to find the bridge using welded-wire reinforcement as top-mat reinforcement option.

No cracks have been observed, and all specimens have shown similar strain values. Those measured strain values are much lower than those corresponding to specified yield stress of each top-mat reinforcement. Based on the monitoring results to date, the behavior of the restrained-shrinkage specimen is consistent with that of the two bridge decks instrumented in the field.

CHAPTER 5

CONTROL OF CRACKING IN PRECAST, PRESTRESSED CONCRETE PANELS

5.1 INTRODUCTION

The objectives of the panel monitoring conducted in this study are to evaluate the effects of initial prestress and additional transverse reinforcement on the formation and propagation of collinear cracks. To this end, twenty-three precast, prestressed panels (PCPs) were fabricated at two plants, designated Plant A and Plant B. Plant A used limestone aggregate, and Plant B used river-gravel aggregate. One set of panels was fabricated using “winter” concrete mixture proportions, and the other set using “summer” concrete. Two different levels of initial prestress were used: the current TxDOT initial prestress (189.4 ksi); and a reduced initial prestress (169.4 ksi).

5.2 FABRICATION OF PANELS

In Table 5-1, panel details are presented. The panels with higher initial prestress level are designated as Current TxDOT initial prestressed panels; all were cast in winter. The panels with lower initial prestress were designated as Reduced initial prestressed panels; all were cast in summer.

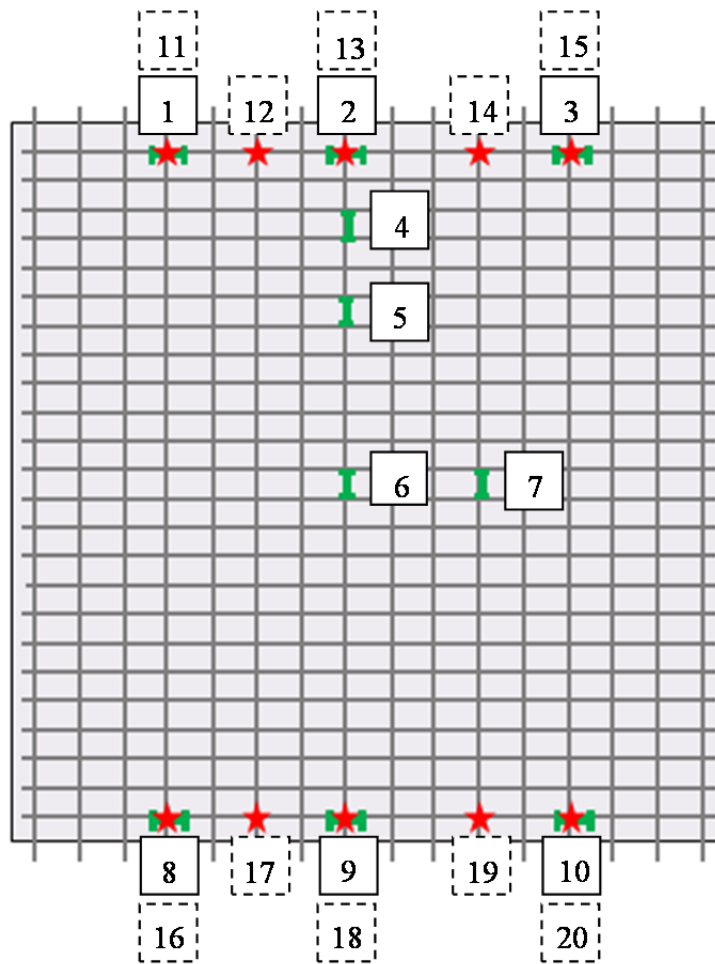
Strands were released one day after fabrication, and panels were delivered to Ferguson Lab one or two weeks later. Plant A and Plant B used the same welded-wire mats as a transverse reinforcement. However, the location of the mat differs at each plant. In Plant A, the mats were placed over the prestressed strands; in Plant B, they were placed below the strands. The specific 28-day concrete strength was 10,000 psi.

Table 5-1: Summary of fabrication of panels

	Current TxDOT		Reduced	
Plant	Plant A	Plant B	Plant A	Plant B
Coarse aggregate	Limestone	River gravel	Limestone	River gravel
Initial prestress stress	189.4 ksi per strand		169.4 ksi per strand	
Fabrication date	2/18/2009	2/18/2010	7/20/2010	9/21/2010
Releasing date	2/19/2009	2/19/2010	7/21/2010	9/22/2010
Transportation date	2/26/2009	3/1/2010	7/30/2010	10/5/2010
Reinforcement	Transverse dir.: D 7.5 wires at 4 in. Longitudinal dir.: D 3.5 wires at 18 in.			
Concrete strength	11,015 psi	10,640 psi	10,240 psi	8,810 psi

Instrumentation details are shown in Figure 5-1 to Figure 5-3. In the figures, red stars refer to the foil gages; green I shapes refer to the embedment gages; and red I shapes refer to the vibrating-wire gages. In Figure 5-1, numbers in dashed-line boxes refer to channel numbers of foil gages, and numbers in solid-lined boxes refer to the number of embedment gages. In Figure 5-2 and Figure 5-3, numbers in solid-lined boxes refer to channel number of embedment and vibrating-wire gages. Foil gages (FLA-6-350-11-8LT, Tokyo Sokki Kenkyujo Company) were 0.25-in. long. Embedment gages (PMFL-60-8L, Sokki Kenkyujo Company) had a 2.5-in. gage length. Vibrating-wire gages (VCE-4200, Geokon) had a 6-in. gage length.

The pattern of gages for the summer panels was modified based on data from the winter panels. Foil gages were not used in the summer panels because they were easily damaged during fabrication and transportation. Moreover, vibrating-wire gages (VWGs) showed stable long-term monitoring performance in the winter panels, so the number of vibrating-wire gage was increased in the summer panels. The total number of gages was reduced because it was shown that fewer gages would provide the required data based on the monitoring results of the winter. More detailed information is given in Foreman (2010) and Azimov (2012).



*Figure 5-1: Gage layout for Current TxDOT initial prestressed panel from Plant A
(Foreman 2010)*

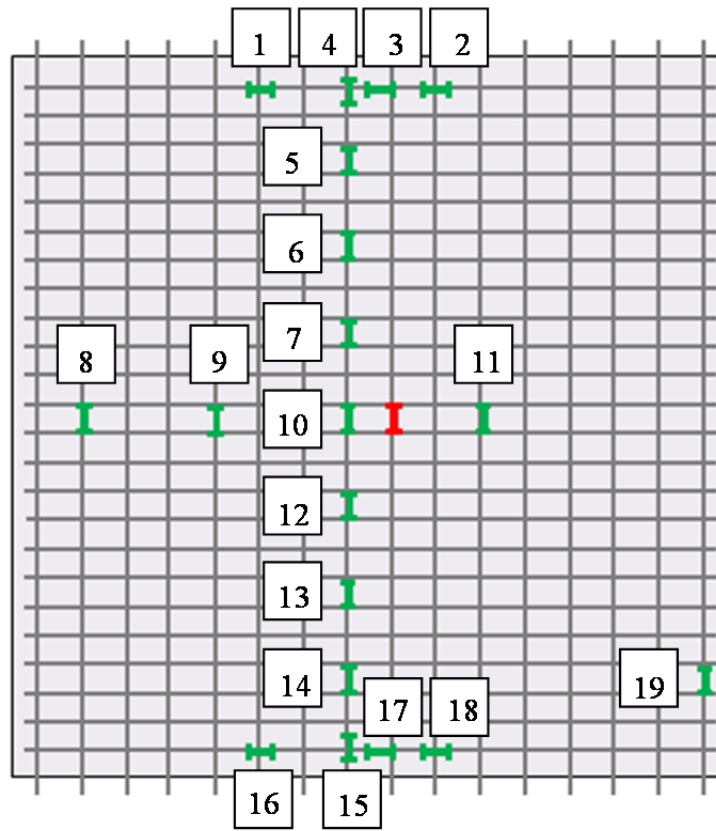


*Figure 5-2: Gage layout for Current TxDOT initial prestressed panel from Plant B
(Foreman 2010)*

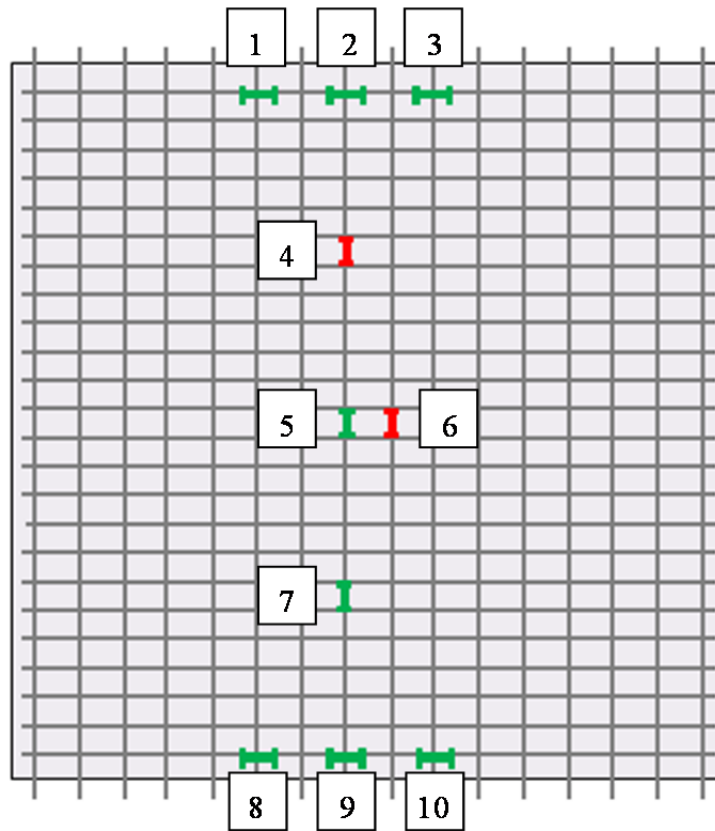


*Figure 5-3: Gage layout for Reduced initial prestressed panel from Plants A and B
(Azimov 2012)*

5.3 MONITORING OF STRAINS IN PCPS

After the panels arrived at Ferguson Laboratory, they were stacked in the same way they would be stored at a typical bridge site (Figure 5-4 and Figure 5-5). The monitoring procedures were simple. The data loggers, shown in Figure 5-6, store the data in memories allowing occasional download of the data. If the prestress losses show very slight changes, the scanning interval can be increased. The data logger was put in the steel box (Figure 5-7) and the steel box was put in orange wooden box as shown in Figure 5-8 to protect the loggers from moisture and impact. The wooden boxes were painted bright orange so that plant workers would be aware of their importance. The strains from VWGs were measured using a hand-held reader as shown in Figure 5-9.



Figure 5-4: Stacking panels at Ferguson Laboratory (Azimov 2012)



Figure 5-5: Stacked panels at Ferguson Laboratory



Figure 5-6: Campbell Scientific CR 5000 data logger



Figure 5-7: Steel box for data logger



Figure 5-8: Wooden box for data logger



Figure 5-9: Hand-held reader for VWGs (Model GK-404, Geokon)

5.4 PRESTRESS LOSS MONITORING

5.4.1 Measured prestress losses

Observed prestress losses are summarized in Table 5-2. The monitoring period is 22 to 42 months. The values in the table were obtained by calculating the average prestress losses for each set of panels with the same initial prestress level and made in the same plant. In Table 5-2, the numbers in the brackets were measured by vibrating-wire gages, and other numbers were measured by embedment gages. More detailed information about monitoring is given in Foreman (2010), and Azimov (2012).

Short-term prestress losses, which were measured during the first day after release, did not change much with initial prestress level, but did change with aggregate types. The panels with limestone (Plant A) showed larger short-term prestress losses than the panels with river-gravel aggregate (Plant B). Long-term prestress loss, which were measured during over a year, decreases as initial prestress decreases, but the difference is not significant. As with the trend of short-term prestress losses, panels with limestone aggregate showed larger long-term prestress losses than panels with river-gravel aggregate.

Table 5-2: Summary of results from prestress-loss monitoring

	Current TxDOT initial ($f_{pi}=189.4$ ksi)		Reduced initial ($f_{pi}=169.4$ ksi)	
	Plant A (limestone)	Plant B (river gravel)	Plant A (limestone)	Plant B (river gravel)
Short-term loss (ksi)	3.5	3.2 (3.1)	4.4 (4.3)	3.6 (3.1)
Long-term loss (ksi)	24.4	12.4 (11.6)	13.8 (15.3)	11.1 (11.6)

Long-term prestress losses with the current TxDOT and the Reduced initial prestressed panels are plotted in Figure 5-10 and Figure 5-11. The values in both figures were detected by the gages placed along strands. Among the gages in a panel, the gage which showed the biggest prestress loss was chosen, and its values were plotted in both figures. The gages installed at the center of the panels generally showed the biggest

prestress losses. The panels which had the same initial prestress level and were cast in the same plant showed similar patterns of prestress loss, so only one panel is presented for each group.

In both figure, red lines indicate prestress losses in the panel made in Plant A, and blue lines indicate the panels made in Plant B. Dashed lines represent a period when data logger did not function properly. Purple vertical line indicates the age at which the losses began to stabilize.

As shown in both figures, the prestress losses in the panels cast in Plant A are bigger than those in the panels cast in Plant B regardless of initial prestress level. The difference in prestress losses between two plants increases as the initial prestress increases.

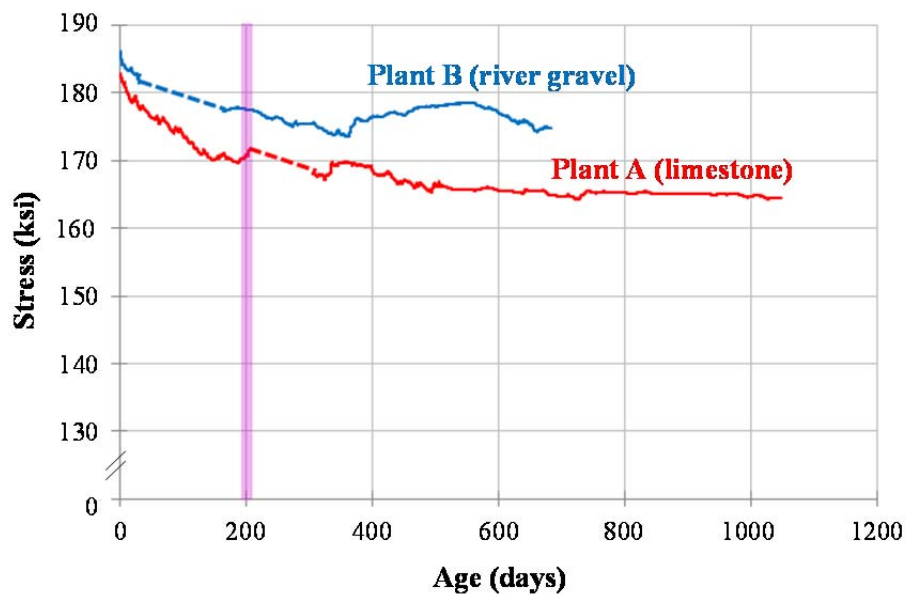


Figure 5-10: Long-term monitoring results, Current TxDOT initial prestress

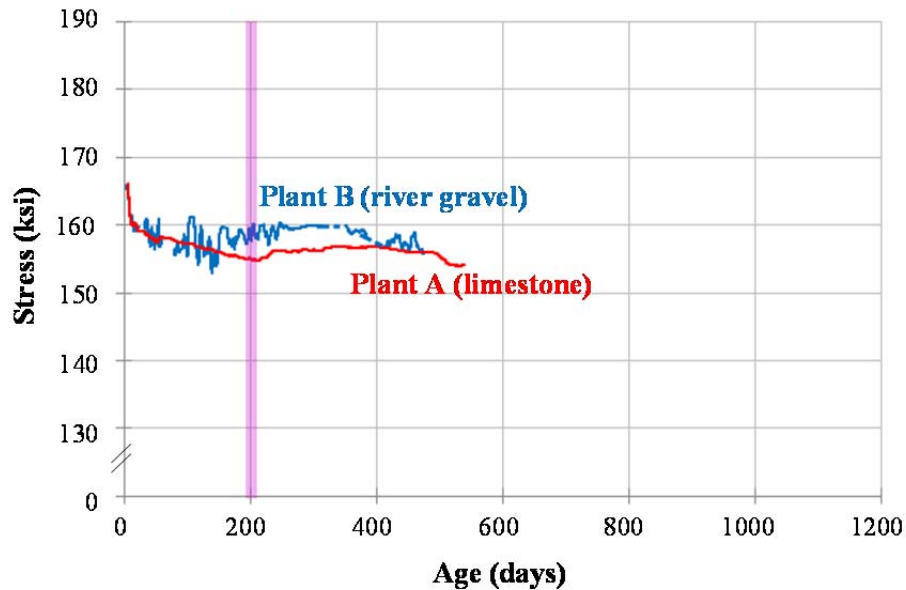


Figure 5-11: Long-term monitoring results, Reduced initial prestress

5.4.2 Effects of gage type

Figure 5-12 shows typical long-term monitoring data. The black line refers to readings from embedment gages, and red crosses refer to readings from vibrating-wire gages. The strains detected by vibrating-wire gages were occasionally measured by hand-held reader (Figure 5-9), so continuous monitoring was not conducted. For this reason, the red crosses are not connected with a line, and indicate discontinuous monitoring. The black dashed line refers to a period of time when the data logger did not work. Figure 5-12 shows the long-term monitoring data from the panels with Current TxDOT initial prestress and cast in Plant B. The data from both types of gages matched well, and the same trend is found in all panels regardless of initial prestress levels and fabrication plants. Based on this fact, it can be concluded that vibrating-wire gages can be used to back up data missing when the data logger did not work.

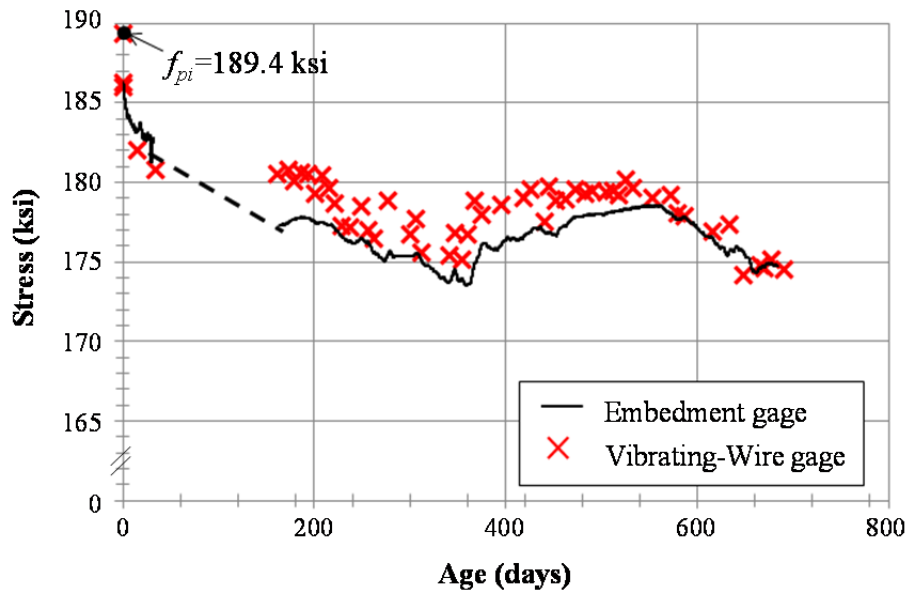


Figure 5-12: Typical long-term monitoring data

5.4.3 Effects of aggregate type and environmental conditions on prestress loss

In Table 5-3 are shown the average environmental conditions during the first month after release in both plants. The magnitude of prestress loss can vary during the entire life of panels, depending on material properties and environmental conditions. Because most prestress loss occurred within the first month, effects of material properties and environmental conditions on prestress loss can be observed by focusing on prestress loss during that time.

In this section, coarse aggregate type and three environmental factors (temperature, humidity, and wind velocity) were considered. Generally, the deformations of concrete due to creep and shrinkage increase as temperature increases, humidity decreases, and wind velocity increases. Prestress losses increase as creep and shrinkage deformations increase. After they were wet-cured, the panels were exposed to air. Therefore, the temperature of the panels can be assumed to be the same as ambient temperature after the curing period.

Under the same initial prestress level, average values of temperature and humidity in both plants were almost same, but the average wind velocity at Plant A was greater than that at Plant B (Table 5-3). Therefore, it can be expected that the creep and shrinkage deformation of the panels at Plant A may be larger than those at Plant B.

In Figure 5-13 are shown measured prestress losses for the first month after casting. The prestress loss of the panels cast at Plant B (blue lines) was less than that of panels cast at Plant A (red lines). The possible reason is that creep and shrinkage deformations of the panels from Plant B might be less than that of the panels from Plant A because of their aggregate type and environmental conditions.

Finally, it may be concluded that prestress loss during the first month can be reduced by using river-gravel aggregate instead of limestone aggregate, or by stacking the panels in a controlled environment so that shrinkage and creep can be reduced. However, prestress losses in panels from both plants were less than those currently assumed by TxDOT, and also less than those predicted by many current design provisions.

Table 5-3: Average environmental conditions of both plants during the first month after casting

	Plant	Temperature [°F]	Humidity [%]	Wind velocity [mph]
Current TxDOT (f_{pi} =189.4 ksi)	A	63	51	9
	B	59	72	7
Reduced (f_{pi} =169.4 ksi)	A	87	65	8
	B	75	64	3

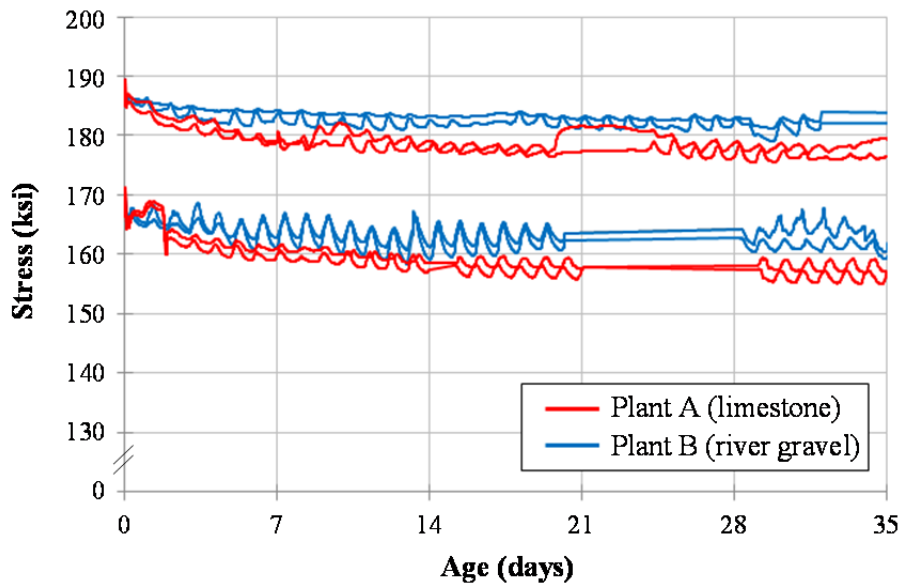


Figure 5-13: Prestress losses during first month after casting

5.4.4 Estimated prestress loss using design specification

To compare observed prestress losses with estimated losses, estimated prestresses losses were calculated using AASHTO 2004, AASHTO 2008 and TxDOT design specifications (TxDOT 2004). TxDOT uses the AASHTO 2004 specifications when bridges are designed. Therefore, the AASHTO 2004 specifications are included in this section even though they are older than AASHTO 2008.

In AASHTO 2004 and 2008, the total prestress loss is calculated by adding the followed four elements: i) elastic shortening; ii) creep; iii) shrinkage; and iv) relaxation. The prestress loss due to the elastic shortening is the short-term prestress loss, and the prestress loss due to the other three elements is the long-term prestress loss. The long-term prestress loss is time-dependent, so the age of panel at service load must be assumed to obtain the ultimate value of prestress loss at that time. The prestress loss at 100,000 days is treated as the ultimate prestress loss.

5.4.4.1 Calculated prestress losses - AASHTO 2004

For the prestress loss calculation using AASHTO 2004, the concrete strength at release was assumed to be 4,000 psi and the 28-day concrete strength was assumed as 5,000 psi. Unit concrete weight was taken as 147.5 lb/ft³. The initial jacking stress is equal to applied initial prestress (189.4 ksi for the Current TxDOT initial prestressed panels and 169.4 ksi for the Reduced initial prestressed panels).

The calculated prestress losses are listed in Table 5-4. As shown in the table, the calculation results are the same because the initial prestress is not considered in the prestress-loss calculations of AASHTO 2004.

Table 5-4: Calculated prestress losses - AASHTO 2004

	Current TxDOT	Reduced
Elastic shortening	5.1 ksi	5.1 ksi
Shrinkage	6.5 ksi	6.5 ksi
Creep	8.0 ksi	8.0 ksi
Relaxation	4.5 ksi	4.5 ksi
Total	24.1 ksi	24.1 ksi

5.4.4.2 Calculated prestress losses - AASHTO 2008

Table 5-5 shows the results of prestress losses calculations using AASHTO 2008. Concrete properties and prestressing forces are assumed the same as Section 5.4.4.1. In AASHTO 2008, prestress losses due to elastic shortening, creep, and relaxation have different values because initial prestress is considered in the calculations.

Table 5-5: Calculated prestress losses - AASHTO 2008

	Current TxDOT	Reduced
Elastic shortening	5.0 ksi	4.5 ksi
Shrinkage	15.8 ksi	15.8 ksi
Creep	10.7 ksi	9.6 ksi
Relaxation	2.6 ksi	1.4 ksi
Total	34.1 ksi	31.3 ksi

5.4.4.3 Calculated prestress losses - TxDOT design specifications

TxDOT design specifications give only a lump-sum ultimate prestress loss, equal to 45 ksi.

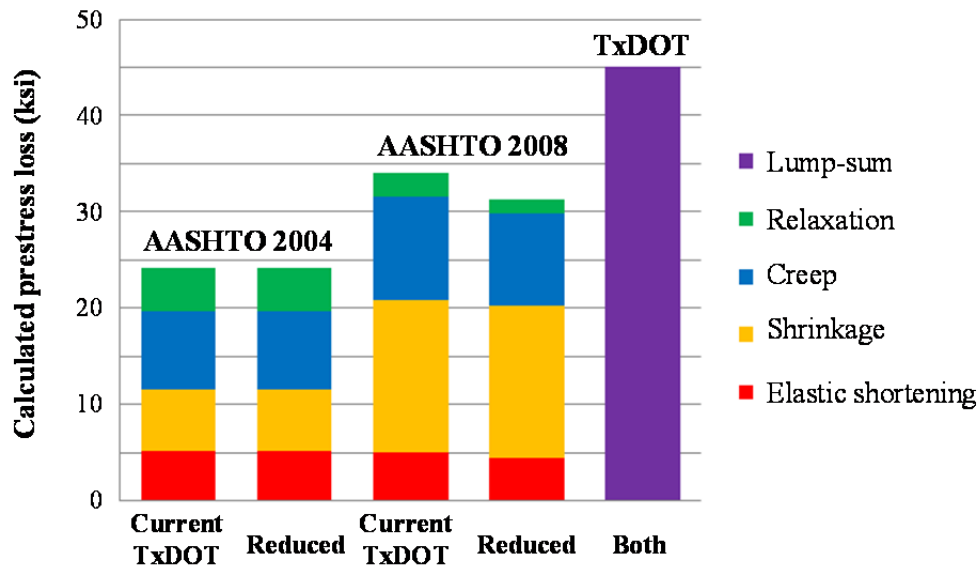


Figure 5-14: Calculations of prestress losses using AASHTO and TxDOT procedures

In Figure 5-14 are shown the calculated prestress losses using AASHTO 2004, AASHTO 2008 and TxDOT procedures. AASHTO 2004 and 2008 predict similar values of the prestress losses due to the elastic shortening. However, the predicted prestress losses due to shrinkage from AASHTO 2008 are almost twice those of AASHTO 2004.

TxDOT design specifications give only a lump-sum value, independent of the initial prestress level.

5.5 RESULTS FROM MONITORING OF PANEL STRAINS

5.5.1 Concrete tensile stress and strain during release

Three testing methods are commonly used for measuring concrete tensile strength: i) direct tensile tests; ii) splitting tensile tests; and iii) modulus of rupture tests. Upper and lower limits for the range of tensile strain values at concrete cracking are determined by empirical equations from direct tensile tests and modulus of rupture tests.

Table 5-6 shows tensile strength and the corresponding tensile strain. The tensile strength is determined by the empirical equations of direct tensile tests and modulus of rupture tests, and the equations are shown in the first column of Table 5-6. The corresponding tensile strain is calculated by dividing the tensile strength by the elastic modulus of concrete at release. The elastic modulus was taken as 4,225 ksi using Equation 5-1. In the calculation, the concrete compressive strength at release was assumed as 6,500 psi. This compressive strength at release is average value of test results from both plants.

Table 5-6: Typical tensile strengths and corresponding strains using two different tensile test methods

Test methods	Tensile strength	Tensile strain
Direct tensile strength ($4.0\sqrt{f'_c}$)	320 psi	75 $\mu\epsilon$
Modulus of rupture ($7.5\sqrt{f'_c}$)	600 psi	140 $\mu\epsilon$

$$E_c = 1265 \sqrt{f'_{ci}} + 1000$$

Equation 5-1

Where, f'_{ci} = compressive strength of concrete at release (ksi)

The measured concrete strains are shown in Figure 5-15. In the figure, “C” designates panels whose reinforcement was arranged according to TxDOT current design specification, and “M” designates panels with additional transverse bars at edges. In some panels (C01 and C07), tensile strains at release were not detected due to a malfunction of the data logger. The panels that are not included in Figure 5-15 (C03, C06, C09, C11, M06, M08 and M12) were not instrumented.

Tensile strains were in Figure 5-15 were determined by choosing the maximum strains from gages installed on the transverse reinforcement in each panel at release. Gages 1 to 3 and 8 to 10 in Figure 5-1, and Gages 1 to 3 and 16 to 18 in Figure 5-2, were used for the Current TxDOT initial prestressed panels. Gages 1 to 3 and 8 to 10 in Figure 5-3 were used for the Reduced initial prestressed panels.

The measured tensile stresses of all panels during release (Figure 5-15) are smaller than the expected tensile strengths (Table 5-6). Therefore, no cracking would be expected in the panels during release. This expectation was confirmed by field inspection before and after release. Therefore, it can be expected that additional transverse reinforcement is unnecessary to prevent collinear cracking at release. This result is consistent with the fact that reinforcement is not effective until concrete cracks, because its transformed area is generally small compared to that of the concrete.

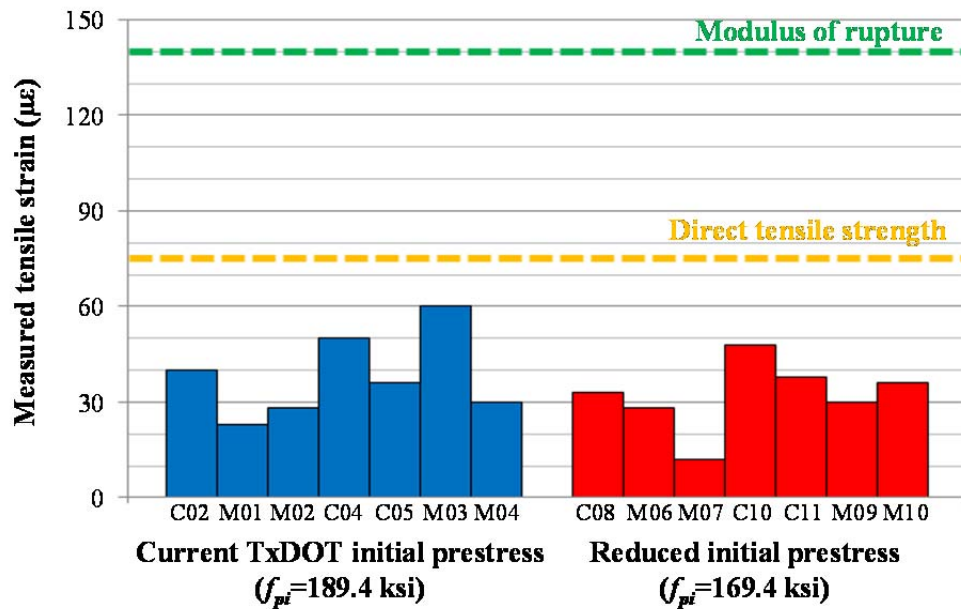


Figure 5-15: Measured tensile strains in all test panels in transverse direction (Foreman 2010, Azimov 2012)

Table 5-7 shows average tensile strains and stresses depending on initial prestress level, presence of additional transverse edge bars, and type of coarse aggregate. Stresses were calculated by multiplying measured tensile strain values by the elastic modulus of concrete used in Table 5-6.

Table 5-7: Average measured tensile strain and stress depending on existence of additional transverse edge bar and type of coarse aggregate

	Current TxDOT initial prestress $f_{pi}=189.4$ ksi				Reduced initial prestress $f_{pi}=169.4$ ksi			
	Plant A (limestone)		Plant B (river gravel)		Plant A (limestone)		Plant B (river gravel)	
	Strain [$\mu\epsilon$]	Stress [psi]	Strain [$\mu\epsilon$]	Stress [psi]	Strain [$\mu\epsilon$]	Stress [psi]	Strain [$\mu\epsilon$]	Stress [psi]
C-panels	40	184	43	198	33	152	43	198
M-panels	26	118	45	207	20	92	33	152
Average	30	140	44	202	24	112	38	175

The average tensile stress in the transverse direction for the Current TxDOT initial prestressed panels (175 psi) is higher than that for the Reduced initial prestressed panels (147 psi). The average tensile stress of the panels made using limestone aggregate (126 psi) is smaller than that of the panels made using river-gravel aggregate (188 psi).

Based on the result from Table 5-7, the transverse tensile stress in PCPs were reduced by applying reduced initial prestress, and using limestone instead of river gravel.

It is impossible to determine whether initial prestress or aggregate type is more critical in reducing collinear cracking, because this result is based on a small number of specimens and there is no specified procedure regarding the time of release or the manner in which the release is carried out.

5.5.2 Concrete tensile stress and strain during the first week after release

In Figure 5-16 and Figure 5-17 are shown the strain variation in the gages, instrumented along transverse reinforcement at edges of panels, during the first week after release. Each figure is based on the results from one panel. The yellow shaded areas in both figures refer to the strain range where cracks would be expected. The upper limit of the area is calculated tensile strain from modulus of rupture tests, and its lower limit is calculated tensile strain from direct tensile tests. The compressive strength and elastic modulus of concrete for calculating both limits had different values depending on the age of the concrete.

The range of tensile strain measured in the Current TxDOT initial prestressed panels is 150 to 200 $\mu\epsilon$, and the range measured in the Reduced initial prestressed panels is 100 to 150 $\mu\epsilon$. Peak tensile strain in the Reduced initial prestressed panels ($\approx 140 \mu\epsilon$) is 25% lower than the strain in the Current TxDOT initial prestressed panels ($\approx 180 \mu\epsilon$).

Peak tensile strain values in most panels were greater than expected cracking strains. However, only one Current TxDOT initial prestressed panel had a collinear crack. The length and the width of that crack were very small and the crack did not propagate further during the entire monitoring period. There are two possible reasons for this. The first reason is that actual concrete strength of the panels at specific time is greater than the expected strength. The second reason is that the data used for developing tensile strengths was scattered broadly.

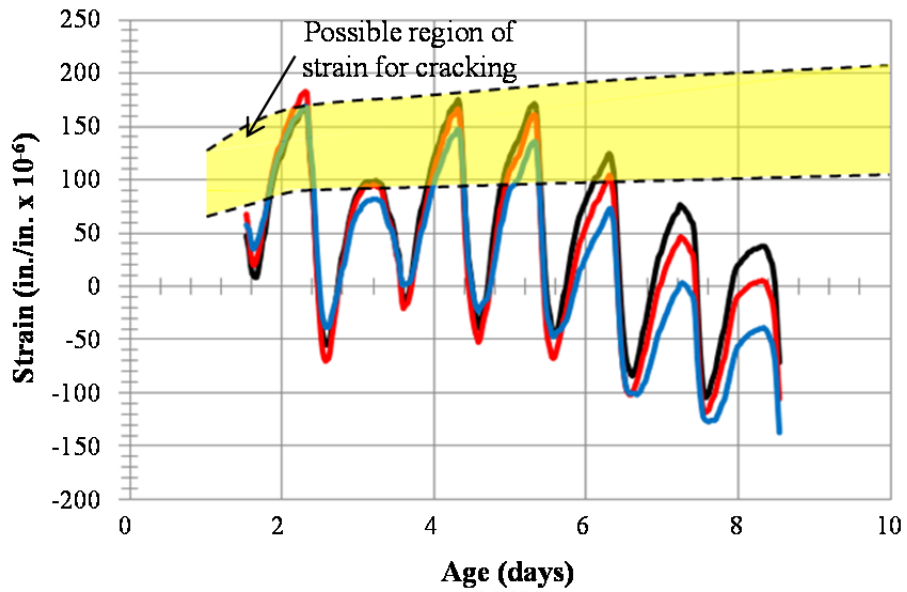


Figure 5-16: Strain variation in Current TxDOT initial prestressed panel during first week after release

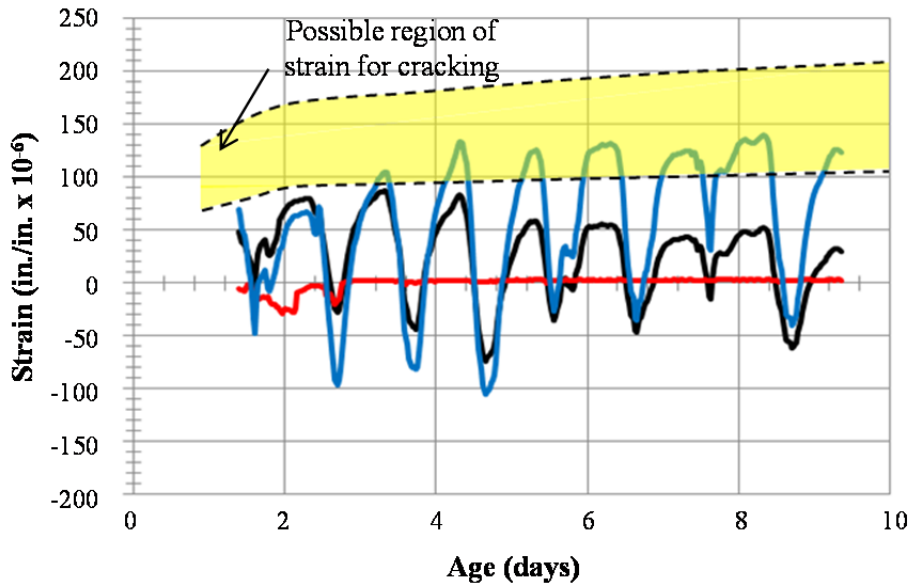


Figure 5-17: Strain variation in Reduced initial prestressed panel during first week after release

5.5.3 Measured versus predicted prestress losses

In Figure 5-18 and Figure 5-19, measured and predicted prestress are compared over time. The predicted values were calculated using AASHTO 2004, AASHTO 2008 and the TxDOT specification. Their values are shown using horizontal dashed lines. The yellow dashed line refers to AASHTO 2004, the purple dashed line refers to AASHTO 2008, and the green dashed line refers to the TxDOT specification. TxDOT design specification required consideration of the largest prestress loss (45 ksi) and AASHTO 2004 predicted smallest prestress loss (24 ksi). The measured prestress losses were smaller than the losses predicted using all three design specifications. The results indicate that initial prestress level may be reduced because the required initial prestress is determined as the prestress level required for serviceability plus expected prestress losses.

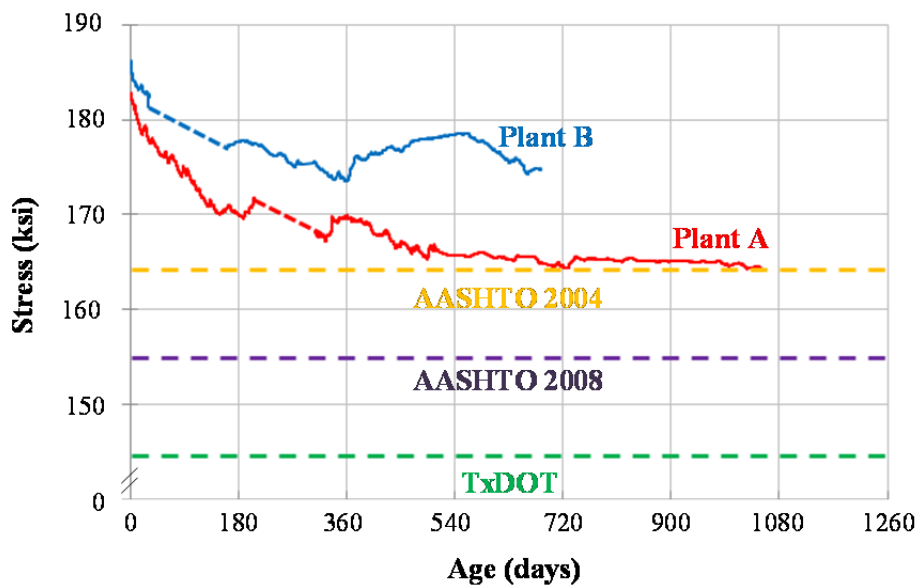


Figure 5-18: Long-term prestress in the Current TxDOT initial prestressed panels

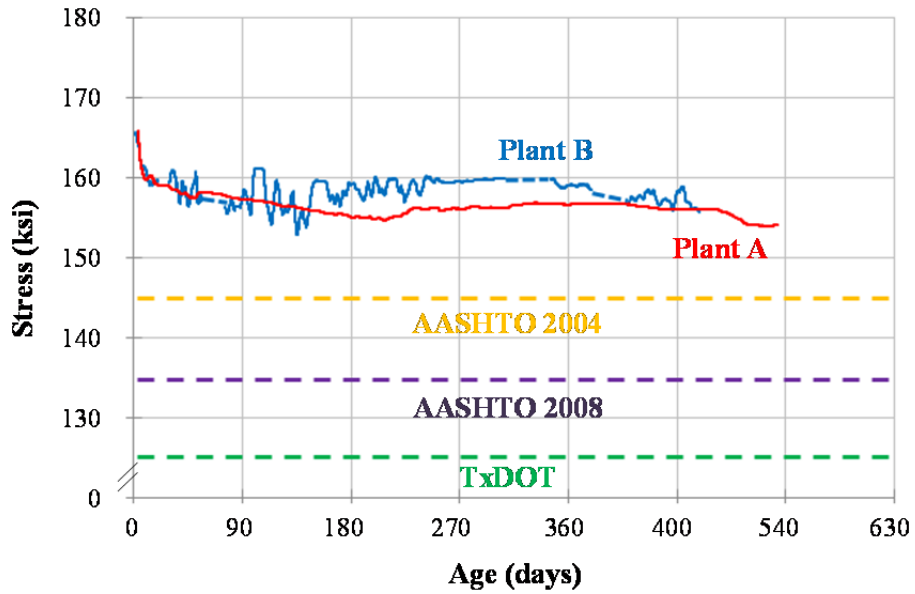


Figure 5-19: Long-term prestress losses in the Reduced initial prestressed panels

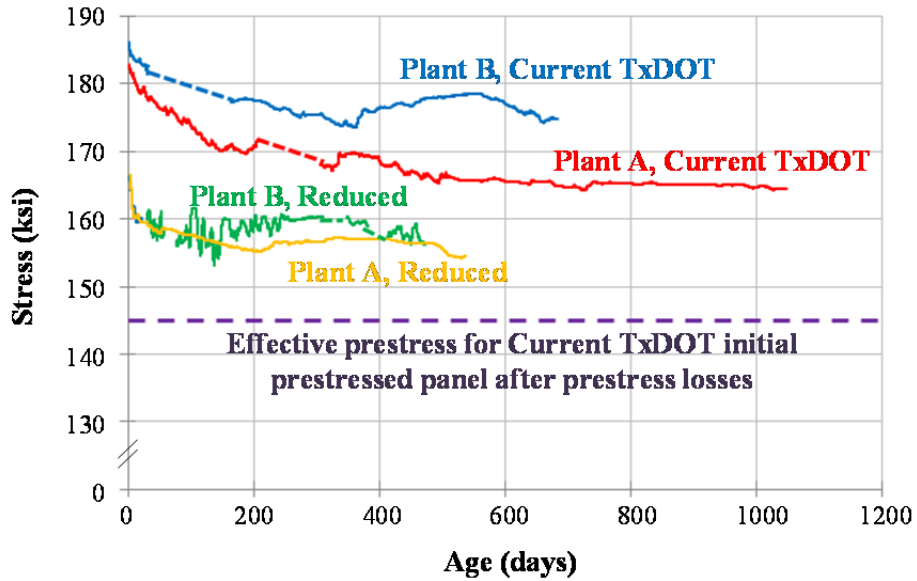


Figure 5-20: Long-term monitoring results of the Current TxDOT and the Reduced initial prestressed panels

In Figure 5-20, the monitoring results for all panels are plotted. The residual remaining prestress in the Reduced initial prestressed panels (green and yellow lines) are larger than the expected effective prestress by TxDOT specifications for the Current TxDOT initial prestressed panels (purple dashed line). The value for the purple dashed line was 149.4 ksi, calculated by subtracting lump-sum value of prestress loss in TxDOT specifications (45 ksi) from the current TxDOT initial prestress (189.4 ksi). This means that although reduced initial prestress is applied, the remaining stress is still larger than the value currently assumed by TxDOT for the panels with the current initial prestress. In other words, the serviceability requirements assumed in current TxDOT design can be satisfied even though the initial prestress is reduced.

5.6 MODEL FOR PRESTRESS LOSS IN PC PANELS

5.6.1 Introduction

Data from monitoring prestress loss in precast, prestressed concrete panels (PCPs) shows that actual prestress losses in PCPs are much smaller than the values predicted by most current models or assumed in TxDOT procedures for PCP design. Most current models overestimate prestress loss in PCPs, because those models were developed from test results of prestressed girders or beams. Prestressed girders or beams have geometric conditions (ratio of surface area to volume), initial prestress force levels, and strand profiles different than those for prestressed panels. Therefore, patterns and amounts of prestress losses in prestressed girders or beams can be different from those in prestressed panels. Some current models, such as the PCI model, can accurately predict prestress losses in PCPs, probably because they were developed based on widely scattered data. Because they also do not consider the characteristics of PCPs, they may not give consistently accurate predictions. If expected prestress loss is larger than the measured values, the initial prestressing force may be higher than required to account for losses. Increasing initial prestressing force may increase the likelihood of cracking. Therefore, a model for predicting prestress loss specifically for PCPs is proposed.

5.6.2 Current prediction models for prestress loss

5.6.2.1 AASHTO 2008

AASHTO 2008 equations for calculating prestress losses are presented in Equation 5-2 to Equation 5-15. A lump-sum prestress loss of 45 ksi is suggested as a conservative estimate.

5.6.2.1.1 Total prestress loss by AASHTO 2008

The total prestress loss can be calculated using Equation 5-2. The total prestress loss is the sum of the loss due to elastic shortening (Δf_{pES}) and the long-term loss (Δf_{pLT}). The long-term prestress loss, as shown in Equation 5-3, consists of losses due to shrinkage ($\Delta f_{pSR,id}$), creep ($\Delta f_{pCR,id}$), and relaxation ($\Delta f_{pRI,id}$). The subscript ‘*id*’ was added in all components of long-term prestress loss to indicate all components were occurred between transfer and deck placement, and this subscript was the same used in AASHTO 2008 and NCHRP Report 496. Each term for Equation 5-2 and Equation 5-3 is introduced in Sections 5.6.2.1.2 to 5.6.2.1.5.

$$\Delta f_{pT} = \Delta f_{pES} + \Delta f_{pLT} \quad \text{Equation 5-2}$$

$$\Delta f_{pLT} = (\Delta f_{pSR} + \Delta f_{pCR} + \Delta f_{pRI})_{id} \quad \text{Equation 5-3}$$

Where,	Δf_{pT}	= total loss in prestressing steel stress (ksi)
	Δf_{pES}	= loss in prestressing steel due to elastic shortening (ksi)
	Δf_{pLT}	= loss in prestressing steel due to long-term deformations (ksi)
	$\Delta f_{pSR,id}$	= prestress loss due to shrinkage between transfer and deck placement (ksi)
	$\Delta f_{pCR,id}$	= prestress loss due to creep between transfer and deck placement (ksi)
	$\Delta f_{pRI,id}$	= prestress loss due to relaxation of prestressing strands between transfer and deck placement (ksi)

5.6.2.1.2 Elastic shortening by AASHTO 2008

Prestress loss due to elastic shortening is evaluated using Equation 5-4.

$$\Delta f_{pES} = \frac{A_{ps} f_{pbt} (I_g + e_{cl}^2 A_g) - e_{cl} M_g A_g}{A_{ps} (I_g + e_{cl}^2 A_g) + \frac{A_g I_g E_{ci}}{E_p}} \quad \text{Equation 5-4}$$

(Eq. C5.9.5.2.3a-1, AASHTO 2008)

Where,	A_{ps}	= area of prestressing steel (in. ²)
	f_{pbt}	= stress in prestressing steel immediately prior to transfer (ksi)
	I_g	= moment of inertia of the gross cross section (in. ⁴)
	e_{cl}	= eccentricity of strand (in.)
	A_g	= gross area of section (in. ²)
	M_g	= maximum moment due to member self-weight (kip-in.)
	E_{ci}	= modulus of elasticity of concrete at transfer (ksi)

5.6.2.1.3 Shrinkage deformation by AASHTO 2008

Prestress loss due to shrinkage deformation is calculated using Equation 5-5. All components of the equation are deformed by equations from Eqs. 5-6 to 5-13. The values of 480×10^{-6} in Equation 5-6 and 1.9 in Equation 5-8 represent ultimate shrinkage strain and constant for creep coefficient respectively. These two constants were determined based on results reported by previous researchers (Tadoros *et al.* 2003). The tests were mostly conducted using rectangular parallelepiped concrete specimens without any reinforcement under controlled environmental conditions (constant temperature and humidity).

$$\Delta f_{pSR} = \varepsilon_{bid} E_p K_{id} \quad \text{Equation 5-5}$$

(Eq. 5.9.5.4.3a-1, AASHTO 2008)

$$\varepsilon_{bid} = k_s k_{hs} k_f k_{td} (480 \times 10^{-6}) \quad \text{Equation 5-6}$$

$$K_{id} = \frac{I}{1 + \frac{E_p A_{ps}}{E_{ci} A_g} \left(1 + \frac{A_g e c l^2}{I_g} \right) [1 + 0.7 \phi_B(t_f, t_i)]}$$

Equation 5-7
(Eq. 5.9.5.4.2a-2, AASHTO 2008)

$$\phi_B(t_f, t_i) = 1.9 k_s k_{hc} k_{td} t_i^{-0.118}$$

Equation 5-8

$$k_s = 1.45 - 0.13 \frac{V}{S}$$

Equation 5-9

$$k_{hs} = 2.00 - 0.014H$$

Equation 5-10

$$k_{hc} = 1.56 - 0.008H$$

Equation 5-11

$$k_f = \frac{5}{1 + f_{ci}'}$$

Equation 5-12

$$k_{td} = \frac{(t_f - t_i)}{61 - 4f_{ci}' + (t_f - t_i)}$$

Equation 5-13

- Where,
- ϵ_{bid} = shrinkage strain between transfer to placement of CIP deck (in./in.)
 - E_p = modulus of elasticity of prestressing steel (ksi)
 - K_{id} = transformed section age-adjusted effective modulus of elasticity factor, for adjustment between the time of transfer and deck placement
 - $\phi_B(t_f, t_i)$ = creep coefficient minus the ratio of the strain that exists t_f days after casting to the elastic strain caused when load is applied t_i days after casting
 - k_s = volume-to-surface ratio shrinkage correction factor
 - k_{hc} = humidity correction factor for creep
 - k_{td} = time-development correction factor
 - t_i = age at transfer after casting (days)
 - k_{hs} = humidity correction factor for shrinkage
 - k_f = concrete strength correction factor for creep
 - t_f = final age after casting (days)

5.6.2.1.4 Creep deformation by AASHTO 2008

The prestress loss due to creep deformation can be obtained using Equation 5-14. Equation 5-7 and Equation 5-8 can be used for obtaining K_{id} and $\phi_B(t_f, t_i)$ in Equation 5-14.

$$\Delta f_{pCR} = \frac{E_p}{E_{ci}} f_{cgp} \phi_B(t_f, t_i) K_{id} \quad \text{Equation 5-14}$$

(Eq. 5.9.5.4.2b-1, AASHTO 2008)

Where, f_{cgp} = average concrete stress at the center of gravity of the prestressing steel at time of release

5.6.2.1.5 Relaxation by AASHTO 2008

Prestress loss due to relaxation can be calculated using Equation 5-15.

$$\Delta f_{pRI} = \frac{f_{pt}}{K_L} \left(\frac{f_{pt}}{f_{py}} - 0.55 \right) \quad \text{Equation 5-15}$$

(Eq. 5.9.5.4.2c-1, AASHTO 2008)

Where, f_{pt} = stress in prestressing steel immediately after transfer (ksi)
 K_L = 30 for low relaxation steel
 f_{py} = yield strength of strands (ksi)

5.6.2.2 TxDOT 2004 Design Specification

A lump-sum value of 45 ksi is recommended for total prestress loss in PCPs designed by TxDOT 2004.

5.6.2.3 PCI Design Handbook, 6th edition

The PCI Design Handbook (PCI 2004) provides a procedure for calculating total prestress losses, presented in Eqs. 5-16 to 5-23.

5.6.2.3.1 Total prestress loss by PCI 2004

As similar with AASHTO 2008, total prestress loss in PCI design Hand book can be calculated by adding prestress losses due to elastic shortening (*ES*), shrinkage (*SH*) creep (*CR*), and relaxation (*RE*) as shown in Equation 5-16. All components of the equation are explained in Section 5.6.2.3.2 to 5.6.2.3.5.

$$TL = ES + CR + SH + RE \quad \text{Equation 5-16}$$

(Eq. 4.7.3.1, PCI 2004)

Where,

<i>TL</i>	= total prestress loss
<i>ES</i>	= loss of prestress due to elastic shortening
<i>CR</i>	= loss of prestress due to creep of concrete
<i>SH</i>	= loss of prestress due to shrinkage of concrete
<i>RE</i>	= loss of prestress due to relaxation of steel

5.6.2.3.2 Elastic shortening by PCI 2004

Prestress loss due to elastic shortening is calculated using Equation 5-17. The value of f_{cir} in the equation can be calculated using Equation 5-18.

$$ES = \frac{K_{es} E_{ps} f_{cir}}{E_{ci}} \quad \text{Equation 5-17}$$

(Eq. 4.7.3.2, PCI 2004)

$$f_{cir} = K_{cir} \left(\frac{P_i}{A_g} + \frac{P_i e^2}{I_g} \right) - \frac{M_g e}{I_g} \quad \text{Equation 5-18}$$

(Eq. 4.7.3.3, PCI 2004)

Where,

K_{es}	= 1.0 for pretensioned members
E_{ps}	= modulus of elasticity of prestressing tendons
f_{cir}	= net compressive stress in concrete at center of gravity of prestressing force immediately after the prestress has been applied to the concrete
K_{cir}	= 0.9 for pretensioned members
P_i	= initial prestress force (after anchorage seating loss)
A_g	= gross sectional area (in. ²)

e	= eccentricity of center of gravity of tendons with respect to center of gravity of concrete at the cross section considered
I_g	= moment of inertia of the gross section (in. ⁴)
M_g	= bending moment due to dead weight of prestressed member and any other permanent loads in place at time of prestressing

5.6.2.3.3 Shrinkage deformation, by PCI 2004

Prestress loss due to shrinkage deformation can be calculated using Equation 5-19.

$$SH = (8.2 \times 10^{-6}) K_{sh} E_{ps} \left(1 - 0.06 \frac{V}{S}\right) (100 - RH) \quad \text{Equation 5-19}$$

(Eq. 4.7.3.6, PCI 2004)

Where,	K_{sh}	= 1.0 for pretensioned members
	V/S	= volume to surface ratio (in.)
	RH	= average ambient relative humidity (%)

5.6.2.3.4 Creep deformation by PCI 2004

Prestress loss due to creep deformation can be evaluated using Equation 5-20. Equation 5-18 and Equation 5-21 can be used for f_{cir} and f_{cds} in Equation 5-20.

$$CR = K_{cr} \frac{E_{ps}}{E_c} (f_{cir} - f_{cds}) \quad \text{Equation 5-20}$$

(Eq. 4.7.3.4, PCI 2004)

$$f_{cds} = \frac{M_{sd} e_{cl}}{I_g} \quad \text{Equation 5-21}$$

(Eq. 4.7.3.5, PCI 2004)

Where,	K_{cr}	= 2.0 for normal weight concrete = 1.6 for light weight concrete
	E_c	= modulus of elasticity of concrete at 28 days
	M_{sd}	= moment due to all superimposed permanent dead and sustained loads applied after prestressing

5.6.2.3.5 Relaxation by PCI 2004

Prestress loss due to relaxation can be obtained using Equation 5-22 and the constant C is determined using Equation 5-23.

$$RE = [K_{re} - J(SH + CR + ES)]C \quad \text{Equation 5-22}$$

(Eq. 4.7.3.7, PCI 2004)

$$C = \frac{\left(\frac{f_{pi}}{f_{pu}}\right)}{0.21} \left[\frac{\left(\frac{f_{pi}}{f_{pu}}\right)}{0.9} - 0.55 \right] \text{ for } \left(\frac{f_{pi}}{f_{pu}}\right) \geq 0.54 \quad \text{Equation 5-23}$$

(Eq. 4.7.3.11, PCI 2004)

Where,

K_{re}	= 5,000 for 270 Grade low-relaxation strand
J	= 0.040 for 270 Grade low-relaxation strand
f_{pi}	= P_i/A_{ps}
f_{pu}	= ultimate strength of prestressing steel

5.6.3 Proposed equation for prestress loss in PC panels

Long-term prestress loss monitoring data described in Chapter 5.4, were used to develop a model for prestress loss in PC panels. Fourteen instrumented panels were used. Among the fourteen panels, six panels had an initial prestress of 189.4 ksi. Eight panels had an initial prestress of 169.4 ksi.

General conditions were used to develop a simple and user-friendly model. The model can be used to predict prestress losses from time of transfer to time of CIP slab placement, because all monitored panels used for developing the model did not have a CIP slab. CIP topping slabs change the shrinkage and creep deformations in PCPs by restraining these deformations and changing exposure conditions of PCPs. Assumed conditions used for developing the model are stated below:

- i) Concrete strength at release (f_{ci}): 4,000 psi
- ii) Concrete strength at 28 days (f_c): 5,000 psi
- iii) Volume-to-surface ratio (V/S): 1.92

- iv) Time of releasing (t_i): 1 day after casting
- v) Average ambient relative humidity (RH): 60%

The concrete strengths at release and at 28 days were determined using the values in the TxDOT design specification. The width and length of the panel are assumed to be 8 ft, and a 4-in. thickness is assumed based on dimensions of the test panels in this study. Exposed surface area is calculated adding top and bottom faces ($2 \times 8 \text{ ft} \times 8 \text{ ft}$) and two-side faces parallel to prestress strands ($2 \times 8 \text{ ft} \times 4 \text{ in.}$). The faces in which prestressing strands were projected are excluded. The date for release is set at 1 day because strands were usually cut one or two days after casting at both Plant A and Plant B. Average humidity is calculated using measured humidity data during the monitoring period.

Figure 5-21 shows the sequence for developing new model of prestress loss in PCPs, and the following sections are organized according to the sequence shown in this chart. Number and kinds of the panels used in each step were presented in the chart.

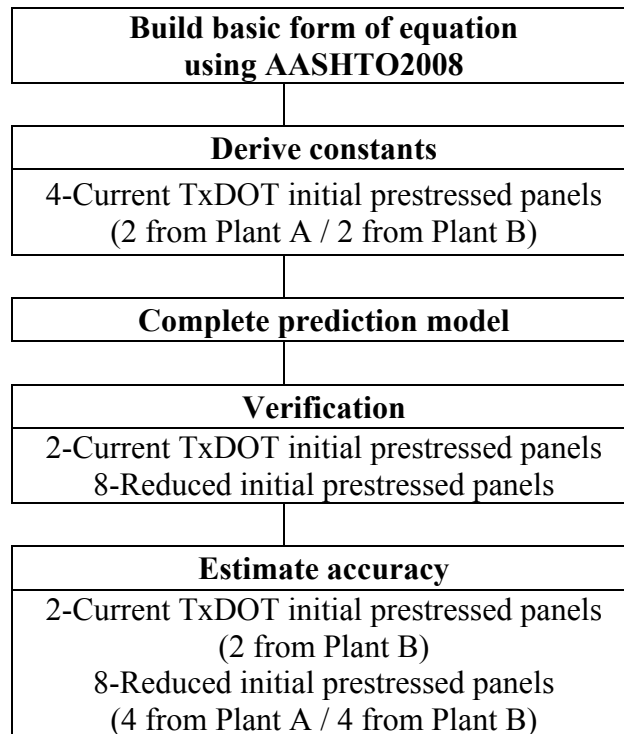


Figure 5-21: Flow chart for proposing new equation for predicting prestress loss in PCPs

5.6.3.1 Development of basic form for proposed equation

AASHTO 2008 was used for developing the basic form of the loss model. Because TxDOT design specifications give only a lump-sum value of prestress loss, TxDOT specifications were not used.

5.6.3.1.1 Elastic shortening, proposed equation

Equation 5-4 can be simplified by considering layout of strands and sectional properties of PCPs. The eccentricity of strand (e_{cl}) is zero in the panel, and the area of prestress strands (A_{ps}) is much smaller than the gross area of the section (A_g), and can be neglected in Equation 5-24. The simplified result is shown in Equation 5-24.

The prestress loss due to elastic shortening in PCPs can be calculated using Equation 5-25, whose calculated value using Equation 5-25 is 5.0 ksi for an initial prestress of 189.4 ksi, and 4.5 ksi for an initial prestress of 169.4 ksi. The calculated values are consistent with the measured values as shown in Table 5-2. By using constant values depending on initial prestress, the model can be further simplified.

$$\Delta f_{pES} = \text{Equation 5-4} = \frac{A_{ps} f_{pbt}}{A_{ps} + \frac{A_g E_{ci}}{E_p}} = \frac{E_p}{E_{ci}} \times \frac{A_{ps} f_{pbt}}{\frac{A_{ps} E_p}{E_{ci}} + A_g} \quad \text{Equation 5-24}$$

$$\Delta f'_{pES} = \frac{E_p}{E_{ci}} \times \frac{A_{ps} f_{pbt}}{A_g} \quad \text{Equation 5-25}$$

5.6.3.1.2 Shrinkage deformation, proposed equation

The prestress loss due to shrinkage deformation can be calculated using Equation 5-5. All components for that equation are obtained using Equation 5-26 to Equation 5-33, and the assumed conditions in Section 5.6.3. The prestress due to shrinkage deformation in PCPs becomes Equation 5-34.

As stated in Section 5.6.2.1.3,0 480×10^{-6} is used as ultimate shrinkage strain (C_{SH}). Based on previous research, this value is a common assumption for predicting prestress loss in prestressed girders or beams, but there is no evidence that it is also adequate for predicting prestress loss in PCPs. Therefore, ultimate shrinkage strain is left as an unknown value in Equation 5-34 and it will be derived through a numerical analysis of data. Moreover, a constant of 1.39 in Equation 5-4 was rounded to 1.50 for simplicity.

$$\Delta f_{pSR} = 1.39 \times C_{SH} \times \frac{(t_f - t_i)}{45 + (t_f - t_i)} \times E_p \times 1.00 \quad \text{Equation 5-4}$$

$$\begin{aligned}\varepsilon_{bid} &= k_s k_{hs} k_f k_{td} \times C_{SH} = 1.20 \times 1.16 \times 1.00 \times \frac{(t_f - t_i)}{45 + (t_f - t_i)} \times C_{SH} \\ &= 1.39 \times C_{SH} \times \frac{(t_f - t_i)}{45 + (t_f - t_i)}\end{aligned}\quad \text{Equation 5-26}$$

$$K_{id} = \frac{1}{1 + \frac{E_p}{E_{ci}} \frac{A_{ps}}{A_g} \left(1 + \frac{A_g e_{cl}^2}{I_g} \right) [1 + 0.7 \varphi_B(t_f, t_i)]} \cong 1.00 \quad \text{Equation 5-27}$$

$$\varphi_B(t_f, t_i) = C_{CR} \times k_s k_{hc} k_{td} t_i^{-0.118} \quad \text{Equation 5-28}$$

$$k_s = 1.45 - 0.13 \frac{V}{S} = 1.45 - 0.13 \times 1.92 = 1.20 \quad \text{Equation 5-29}$$

$$k_{hs} = 2.00 - 0.014H = 2.00 - 0.014 \times 60 = 1.16 \quad \text{Equation 5-30}$$

$$k_{hc} = 1.56 - 0.008H = 1.56 - 0.008 \times 60 = 1.08 \quad \text{Equation 5-31}$$

$$k_f = \frac{5}{1 + f_{ci}'} = \frac{5}{1 + 4} = 1.00 \quad \text{Equation 5-32}$$

$$k_{td} = \frac{(t_f - t_i)}{61 - 4f_{ci}' + (t_f - t_i)} = \frac{(t_f - t_i)}{61 - 4 \times 4 + (t_f - t_i)} = \frac{(t_f - t_i)}{45 + (t_f - t_i)} \quad \text{Equation 5-33}$$

$$\Delta f'_{pSR} = 1.50 \times C_{SH} \times \frac{(t_f - t_i)}{45 + (t_f - t_i)} \times E_p \quad \text{Equation 5-34}$$

5.6.3.1.3 Creep deformation, proposed equation

All components calculated using Equation 5-35 to Equation 5-42, and the assumed conditions in Section 5.6.3 are applied to Equation 5-14 to obtain Equation 5-43.

In AASHTO 2008, 1.9 is used as the constant (C_{CR}) for creep coefficient (φ_B). However, in Equation 5-43, the constant C_{CR} is left unknown, and will be derived

through numerical analysis of monitoring data. Moreover, a constant of 10.4 in Equation 5-13 is rounded to 10.5 in Equation 5-43 for simplicity.

$$\Delta f_{pCR} = 10.4 \times \frac{f_{pt} A_{ps}}{A_g} \times C_{CR} \times \frac{(t_f - t_i)}{45 + (t_f - t_i)} \times 1.0 \quad \text{Equation 5-13}$$

$$\frac{E_p}{E_{ci}} = \frac{2,8500}{(57,000 \sqrt{4,000}) \times 10^{-3}} \cong 8.0 \quad \text{Equation 5-35}$$

$$f_{cgp} = \frac{f_{pt} A_{ps}}{A_g} \quad \text{Equation 5-36}$$

$$\begin{aligned} \phi_B(t_f, t_i) &= C_{CR} \times k_s k_{hc} k_{td} t_i^{-0.118} \\ &= C_{CR} \times 1.20 \times 1.08 \times \frac{(t_f - t_i)}{45 + (t_f - t_i)} \times 1^{-0.118} \\ &= 1.30 \times C_{CR} \times \frac{(t_f - t_i)}{45 + (t_f - t_i)} \end{aligned} \quad \text{Equation 5-37}$$

$$k_s = 1.45 - 0.13 \frac{V}{S} = 1.45 - 0.13 \times 1.92 = 1.20 \quad \text{Equation 5-38}$$

$$\frac{V}{S} = \frac{8 \times 12 \times 4 \times 8 \times 12}{(8 \times 12 + 4) \times 2 \times 8 \times 12} = 1.92 \quad \text{Equation 5-39}$$

$$k_{hc} = 1.56 - 0.008H = 1.56 - 0.008 \times 60 = 1.08 \quad \text{Equation 5-40}$$

$$k_f = \frac{5}{1 + f_{ci}} = \frac{5}{1 + 4} = 1.00 \quad \text{Equation 5-41}$$

$$k_{td} = \frac{(t_f - t_i)}{61 - 4f_{ci} + (t_f - t_i)} = \frac{(t_f - t_i)}{61 - 4 \times 4 + (t_f - t_i)} = \frac{(t_f - t_i)}{45 + (t_f - t_i)} \quad \text{Equation 5-42}$$

$$\Delta f'_{pCR} = 10.5 \times C_{CR} \times \frac{f_{pr} A_{ps}}{A_g} \times \frac{(t_f - t_i)}{45 + (t_f - t_i)} \quad \text{Equation 5-43}$$

5.6.3.1.4 Relaxation, proposed equation

AASHTO 2008 and PCI design Handbook suggest calculating prestress loss due to relaxation by using Equation 5-15 and Equation 5-22. In these two design specifications, the loss due to relaxation is considered as constant. In the proposed equation, the prestress loss due to relaxation is ignored, because relaxation effects are generally very small and can be ignored in calculation of prestress losses. Total prestress loss, proposed equation

By combining all components explained in Section 5.6.3.1.1 to 5.6.3.1.4, the final form of an equation for predicting prestress loss in PCPs is shown in Equation 5-44. The first term refers to prestress loss due to shrinkage, and the second term refers to prestress loss due to creep. In the equation, it is assumed that the stress in strands immediately after transfer (f_{pt}) has the same value as the initial applied prestress (f_{pi}) because no change was observed in prestress value right after transfer in the tests of this study. The third term refers to prestress loss due to elastic shortening. Its value is 5.0 ksi when initial prestress is 189.4 ksi and 4.5 ksi when initial prestress is 169.4 ksi.

$$\begin{aligned} \Delta f'_{pT} &= (\Delta f'_{pSR} + \Delta f'_{pCR})_{id} + \Delta f'_{pES} \\ &= 1.50 C_{SH} \frac{(t_f - t_i)}{45 + (t_f - t_i)} E_p + 10.5 C_{CR} \frac{f_{pr} A_{ps}}{A_g} \frac{(t_f - t_i)}{45 + (t_f - t_i)} + \Delta f'_{pES} \end{aligned} \quad \text{Equation 5-44}$$

5.6.3.2 Derivation of constants, proposed equation

Values of the constants C_{SH} and C_{CR} for PCPs in Equation 5-44 were derived by numerical analysis (curve fitting), conducted using the software, IGOR Pro 6.11 (<http://www.wavemetrics.com>).

Two panels from Plant A (limestone) and two panels from Plant B (river gravel) were used to obtain constant values, C_{SH} and C_{CR} . All four panels had an initial prestress of 189.4 ksi.

Figure 5-22 and Figure 5-23 show results of curve-fitting for panels from both plants. The x-axis is based on $t/(45+t)$, and the y-axis is the prestress loss, where t equals to $t_f - t_i$, t_f is the age after casting, and t_i is the age at transfer after casting. Panels from Plant B were monitored for almost two years. However, the data were not measured from about 1 month to 5 months after casting, so the data for 1 month was used for deriving constant values C_{SH} and C_{CR} of Plant B.

Black-dashed lines in Figure 5-22 and Figure 5-23 indicate that the best curves for Panel 1 of Plants A and B. Red-dashed lines in both figures indicate the best-fit curves for Panel 2 of both plants. As shown in Figure 5-22, the best-fit curves of the panels from Plant A are almost identical. The resultant values of C_{SH} and C_{CR} for Panel are shown in the top box, and the values for Panel 2 are shown in the bottom box in both figures.

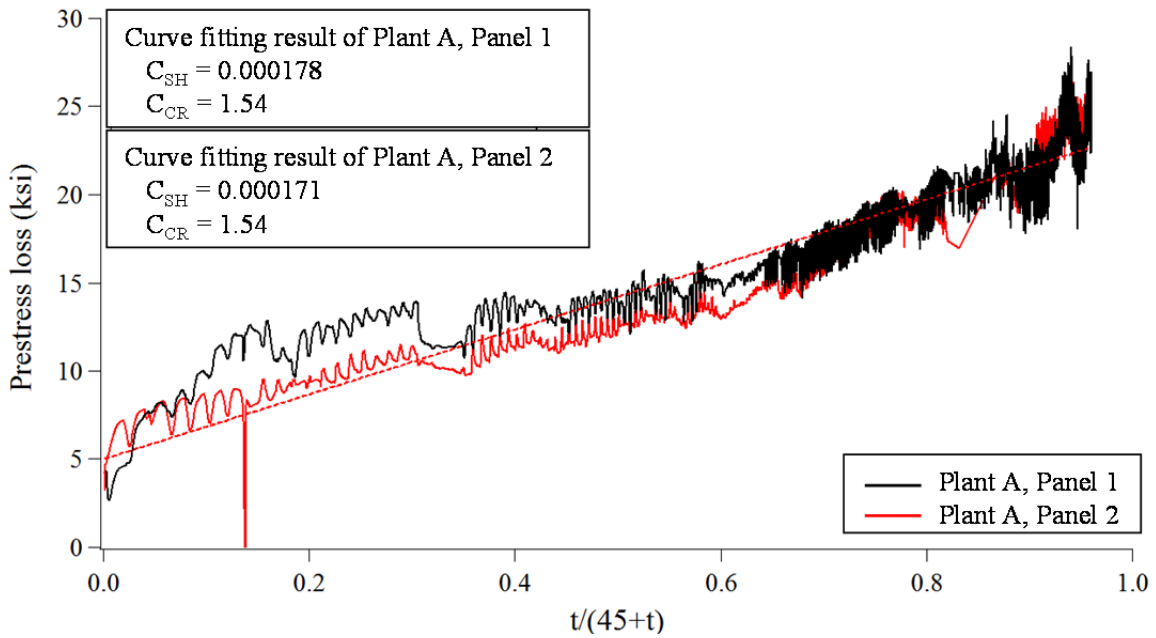


Figure 5-22: Curve fitting result for Plant A

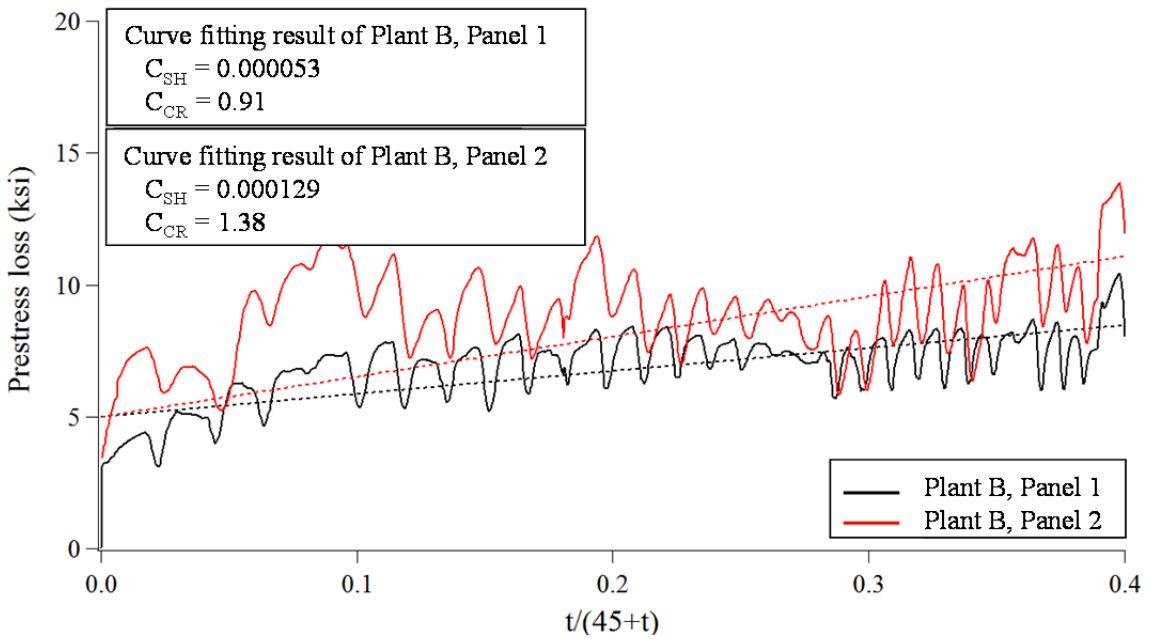


Figure 5-23: Curve fitting result for Plant B

Table 5-8: Resultant values for constants C_{SH} and C_{CR}

Constants	Values
C_{SH}	180 x 10 ⁻⁶ for limestone, Plant A 90 x 10 ⁻⁶ for river gravel, Plant B
C_{CR}	1.55 for limestone, Plant A 1.15 for river gravel, Plant B

The resultant values for the constants C_{SH} and C_{CR} are shown in Table 5-8. Those values were obtained by calculating average values of two panels from each plant. Therefore the best-fit curves for each plant using the values in Table 5-8 will be located between two dashed lines shown in Figure 5-22 and Figure 5-23.

5.6.3.3 Propose new equation for predicting prestress loss in PCPs

Based on the results from Section 5.6.3.1.1 to 5.6.3.1.4, and Section 5.6.3.2, a new equation for predicting prestress loss in PCPs is proposed. The final form for the proposed equation is shown in Equation 5-45. All constant values and parameters for the proposed equation are listed in Table 5-9.

$$\Delta f_{pT} = 1.50C_{SH} \frac{(t_f - t_i)}{45 + (t_f - t_i)} E_p + 10.5C_{CR} \frac{f_{pt} A_{ps}}{A_g} \frac{(t_f - t_i)}{45 + (t_f - t_i)} + C_{ES} \quad \text{Equation 5-45}$$

Table 5-9: Constant values and parameters for Equation 5-45

Constants & Parameters	Values & Definitions
C_{SH}	180×10^{-6} for limestone 90×10^{-6} for river gravel
C_{CR}	1.55 for limestone 1.15 for river gravel
C_{ES}	5.0 ksi for $f_{pi}=189.4$ ksi (Current TxDOT initial prestress) 4.5 ksi for $f_{pi}=169.4$ ksi (Reduced initial prestress)
t_f	final age at transfer after casting (days)
t_i	age at transfer after casting (days)
E_p	modulus of elasticity of prestressing steel (ksi)
f_{pt}	stress in prestressing steel immediately after transfer (ksi)
A_{ps}	area of prestressing steel (in. ²)
A_g	gross area of section (in. ²)

5.6.3.4 Verification of proposed equation

To verify the proposed equation, measured and predicted values were compared using four Current TxDOT initial prestressed panels and eight Reduced initial prestressed panels. All Current TxDOT initial prestressed panel from Plant A were used for derivation of C_{SH} and C_{CR} , so the same panels were used for deriving constants and for verifying the proposed equation in this case. However, the panels used for verifying the model and the panels for the derivation were different for the Current TxDOT initial prestressed panel from Plant B. Results of all twelve panels are similar; the result of one panel for each case is shown in Figure 5-24 to Figure 5-27. In those figures, the purple solid lines represent a new lump-sum prestress loss of 25 ksi as proposed by Foreman (2010). The results obtained from Figure 5-24 to Figure 5-27 are as follows:

- i) The proposed equation gives better estimates than the others.
- ii) As shown in Figure 5-24 and Figure 5-26, the PCI design code and the proposed equation give similar prediction result for the panels cast in Plant A (limestone).

- iii) The TxDOT design specifications and the AASHTO code predict prestress losses much greater than those observed in this study.
- iv) A new lump-sum value of 25 ksi is conservative for the panels with current TxDOT initial prestress (189.4 ksi) and reduced initial prestress (169.4 ksi).

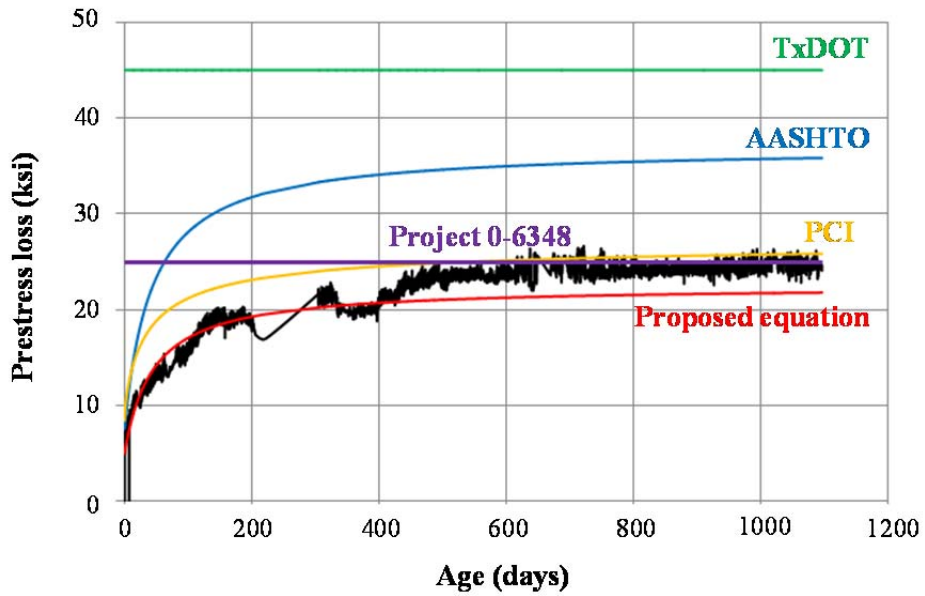


Figure 5-24: Measured and predicted prestress losses, Current TxDOT initial prestress, Plant A

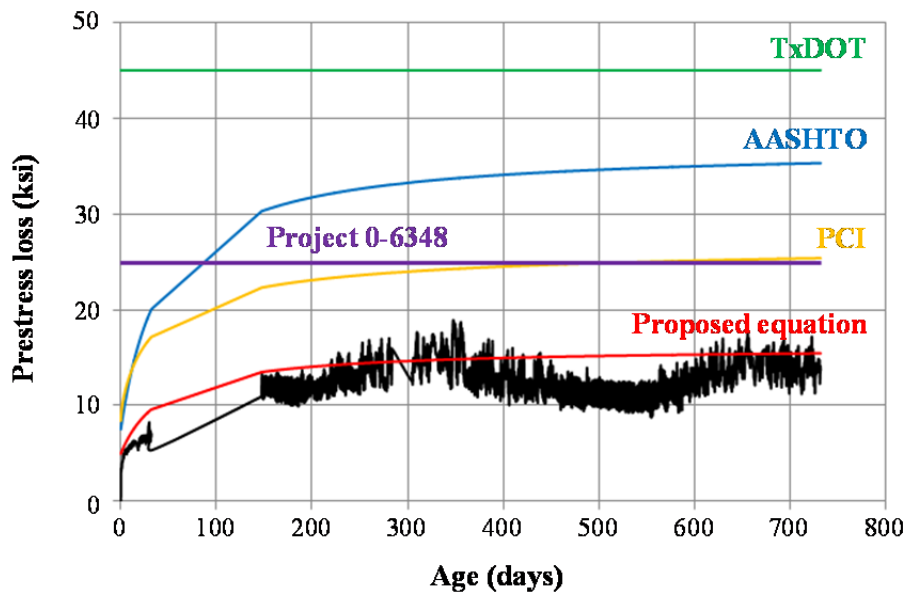


Figure 5-25: Measured and predicted prestress losses, Current TxDOT initial prestress, Plant B

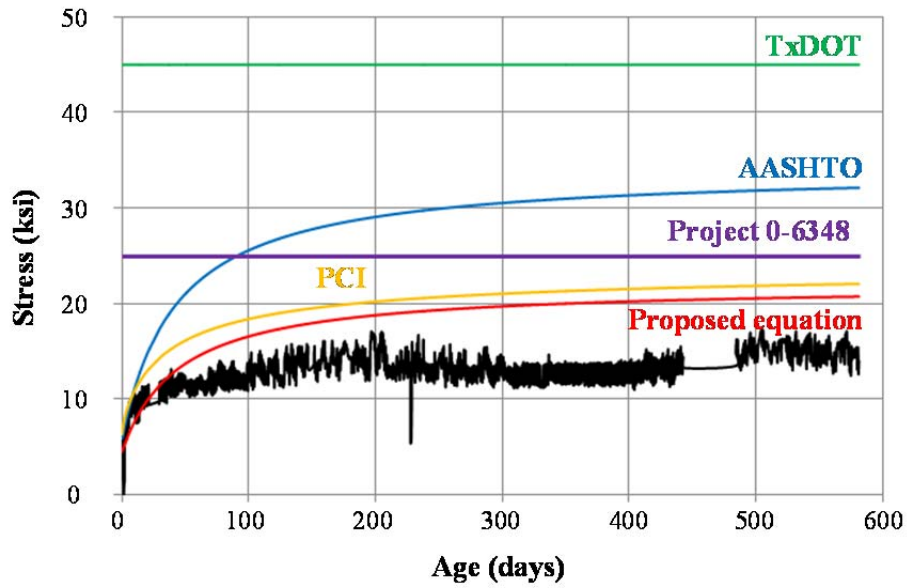


Figure 5-26: Measured and predicted prestress losses, Reduced initial prestress, Plant A

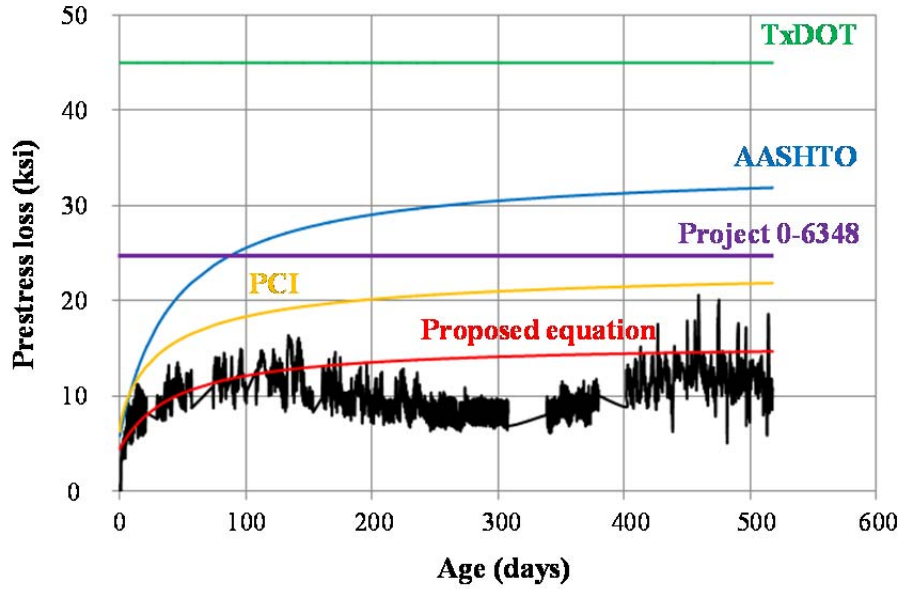


Figure 5-27: Measured and predicted prestress losses, Reduced initial prestress, Plant B

5.6.3.5 Accuracy of proposed equation

The accuracy of the proposed equation is evaluated and compared with that of the AASHTO 2008, PCI, and TxDOT methods, using four statistical methods:

- i) Residual method
- ii) CEB coefficient of variation (V_{CEB} %) method
- iii) CEB mean square error (F_{CEB} %) method
- iv) CEB mean deviation (M_{CEB}) method

5.6.3.5.1 Residual method

The residual method is one of the simplest methods for determining accuracy of a model. Residual values are calculated by subtracting predicted values from measured values. If the calculated residual values are negative, predicted values are smaller than measured values, so the model underestimates the values. If the residual values are positive, predicted values are bigger than measured values, so the model overestimates the values (Al-Manaseer and Lam 2005).

5.6.3.5.2 CEB coefficient of variation (V_{CEB} %) method

The CEB coefficient of variation method was suggested by Muller and Hilsdorf (1990). Equations for the method are stated below:

$$Y_i = \frac{\sum_{i=1}^n Y_{ij}}{n} \quad \text{Equation 5-46}$$

$$S_i = \sqrt{\frac{1}{n-1} \sum_{j=1}^n (\Delta Y_{ij})^2} \quad \text{Equation 5-47}$$

$$V_i = \frac{S_i}{Y_i} \times 100 \quad \text{Equation 5-48}$$

$$V_{CEB} = \sqrt{\frac{1}{N} \sum_{i=1}^N V_i^2}$$

Equation 5-49

Where,

n	= number of differences (data points) taken in each set, j
N	= total number of data sets considered
S_i	= standard error determined from ΔY_{ij} for experiment i
V_i	= COV of experiment i
V_{CEB}	= mean COV
Y_i	= mean value from experiment
Y_{ij}	= measured value at time j of experiment i
ΔY_{ij}	= difference between observed and predicted values at time j of experiment i

5.6.3.5.3 CEB mean square error (F_{CEB} %) method

This method was proposed by Muller and Hilsdorf (1990). Smaller values of F_{CEB} denote more accurate results. By using the following equations, F_{CEB} could be calculated.

$$f_j = \frac{(Cal X_{ij} - Obs X_{ij})}{Obs X_{ij}} \times 100$$

Equation 5-50

$$F_i = \sqrt{\frac{1}{n-1} \sum_{j=1}^n f_j^2}$$

Equation 5-51

$$F_{CEB} = \sqrt{\frac{1}{N} \sum_{i=1}^N F_i^2}$$

Equation 5-52

Where,

$Cal X_{ij}$	= predicted value of time j of experiment i
$Obs X_{ij}$	= experimental value of time j of experiment i

f_j	= percent difference between calculated and observed data point j
F_i	= mean square of residuals, %
F_{CEB}	= mean square of error, %
n	= total number of values j of experiment i considered at a fixed time
N	= total number of data sets considered

5.6.3.5.4 CEB mean deviation (M_{CEB}) method

This method was also suggested by Muller and Hilsdorf (1990). If the value of M_{CEB} is less than 1.0, the model underestimates values. If the value of M_{CEB} is bigger than 1.0, the model overestimates values.

$$M_i = \frac{1}{n} \sum_{j=1}^n \frac{Cal X_{ij}}{Obs X_{ij}} \quad \text{Equation 5-53}$$

$$M_{CEB} = \frac{\sum_{i=1}^N M_i}{N} \quad \text{Equation 5-54}$$

Where,	$Cal X_{ij}$	= predicted value of time j of experiment i
	$Obs X_{ij}$	= experimental value of time j of experiment i
	M_i	= deviation between predicted values and experimental values of experiment i
	M_{CEB}	= mean deviation
	n	= total number of values j of experiment i considered at a fixed time
	N	= total number of data sets considered

5.6.3.5.5 Results for accuracy of proposed equation

Two Current TxDOT initial prestressed panels and eight Reduced initial prestressed panels were used for estimating the accuracy of the proposed equation. Two Current TxDOT initial prestressed panels were made in Plant B. Among the eight

Reduced initial prestressed panels, four were made in Plant A, and four panels were made in Plant B. The initial prestress level of the Current TxDOT initial prestressed panel is 189.4 ksi, and that of the Reduced initial prestressed panel is 169.4 ksi. Plant A used limestone and Plant B used river gravel as coarse aggregate. All Current TxDOT initial prestressed panels made in Plant A were used in the derivation of the constants in the proposed equation, so those panels were not included in the analysis of accuracy.

Table 5-10 shows a summary of the residual method, and Table 5-11 shows a summary of other statistical analysis results including CEB coefficient of variation (V_{CEB} %), CEB mean square error (F_{CEB} %) and CEB mean deviation (M_{CEB}) method.

As shown in Table 5-11, all statistical values of the proposed equation are smaller than that of any other existing models: AASHTO, PCI and TxDOT. It means that the proposed equation has less variability and more accuracy than those other models.

Plant A shows less variability (V_{CEB} , F_{CEB} , and M_{CEB}) than Plant B. This indicates that the concrete properties of Plant A are more uniform than the properties of Plant B. This result is caused by different type of aggregate. Carrasquillo, Nilson and Slate (1981) observe that the concrete with limestone has more uniform material properties than the concrete with river gravel because of smaller micro-cracks caused by higher bond strength between aggregate and mortar.

Table 5-10: Comparative accuracy by residual method

	Plant	Specification	Range of values		Percentage of negative values	Percentage of positive values
			Min.	Max.		
Current TxDOT (189.4 ksi)	B (river gravel)	Proposed	-5.0	12.5	11.2	88.9
		PCI	0.0	22.5	0.0	100.0
		AASHTO	0.0	27.5	0.0	100.0
		TxDOT	25.0	45.0	0.0	100.0
Reduced (169.4 ksi)	A (limestone)	Proposed	-6.5	15.0	24.1	75.9
		PCI	-5.0	15.0	2.6	97.4
		AASHTO	-3.8	25.0	1.4	98.6
		TxDOT	22.5	45.0	0.0	100.0
	B (river gravel)	Proposed	-5.0	13.8	15.8	84.2
		PCI	0.0	21.3	0.0	100.0
		AASHTO	0.0	30.0	0.0	100.0
		TxDOT	26.3	45.0	0.0	100.0

Table 5-11: Summary of statistical analysis results for accuracy

Method	Specification	Current TxDOT (189.4 ksi)	Reduced (169.4 ksi)	
		Plant B (river gravel)	Plant A (limestone)	Plant B (river gravel)
V_{CEB} %	Proposed equation	30.80	32.77	56.68
	PCI	93.07	42.62	123.14
	AASHTO 2008	185.51	97.60	211.78
	TxDOT	322.61	257.07	423.26
F_{CEB} %	Proposed equation	60.10	402.80	895.71
	PCI	145.30	614.87	1382.90
	AASHTO 2008	196.64	546.49	1243.85
	TxDOT	144606.32	3660.45	8576.78
M_{CEB}	Proposed equation	1.28	1.00	1.56
	PCI	2.16	1.46	2.36
	AASHTO 2008	2.80	1.90	3.23
	TxDOT	4.78	4.31	6.13

5.7 CONCLUSIONS OF STUDY ON CONTROL OF CRACKING IN PCPS

Long-term monitoring of prestress loss in precast, prestressed concrete panels (PCPs) was conducted to determine if collinear cracking in PCPs could be controlled. The variables that could be controlled were the coarse aggregate used in concrete, the season of fabrication, and initial prestress. It was observed that the current TxDOT design procedure overestimates prestress loss in PCPs. Moreover, although initial prestress was reduced from current initial prestress of 189.4 ksi to 169.4 ksi, the remaining prestress after stabilization was greater than the currently assumed prestress level after losses are considered (144.4 ksi).

The lump-sum prestress loss assumed in TxDOT procedure (45 ksi) is much larger than that observed. Therefore, a new lump-sum value of 25 ksi is proposed for prestress loss in PCPs. This value gives conservative results for the panels with the current TxDOT initial prestress (189.4 ksi) and the reduced initial prestress (169.4 ksi).

Using the measured losses in PCPs in this research, a new equation for prestress loss in the panels was developed. AASHTO 2008 was used as the basic form of the model. Terms in the AASHTO model were simplified using new constants that were introduced. The constants were derived through numerical analysis of the monitoring data. The constants have different values depending on types of aggregates. The proposed equation includes effects of aggregate types on prestress loss.

Prestress losses due to relaxation were not included in the proposed equation because they are very small for low-relaxation tendons which were used in this research. Total prestress loss predicted by the proposed equation is smaller than that by current design codes. As a result, the level of initial prestressing force could be reduced, and the occurrence of collinear cracking in the PCPs would be reduced as well by using the proposed equation in design of PCPs.

However, the proposed equation has several limitations. Since the data are limited to the project reported here, the testing method, equipment, material properties and geometrical properties do not vary. Therefore, the proposed equation needs to be verified by different research groups. Moreover, the number of the panels which were

used in this research is not sufficient and composite action between PCPs and the CIP slab is not considered. To overcome these limitations and develop a more general prediction model, additional tests by different research groups would be very useful.

CHAPTER 6

SUMMARY AND CONCLUSIONS

6.1 SUMMARY

Bridge decks composed of precast, prestressed panels (PCPs) overlain by cast-in-place (CIP) are popular in many states of the US, including Texas. Because PCPs placed between adjacent girders serve as stay-in-place formwork for CIP slabs, construction cost and time can be saved. Moreover, the system uses precast panels as the bottom portion of the deck, so it is much easier to control quality of the bridge deck than when full-depth CIP concrete decks are used. The following requirements to current TxDOT designs were studied in this project.

- i) Ways to reduce top-mat reinforcement; and
- ii) Ways to reduce the rejection rate of PCPs in the field due to cracking after fabrication and transportation to the site.

Foster (2010), who worked in the same project, suggested possible top-mat reinforcement options based on crack-width calculations, and conducted laboratory tests, including bending tests and direct tensile tests. Based on his study, three conclusions were obtained:

- i) Longitudinal top-mat reinforcement specified by TxDOT (No. 4 bars at 9-in. spacing) could not be reduced.
- ii) To find optimized top-mat reinforcement in the transverse direction, field conditions (CIP-PCP interaction, boundary conditions) should be simulated as closely as possible.
- iii) Large test specimens were too complex to test in the laboratory.

To overcome the limitations noted in previous exploratory studies by Foster (2010), two sets of field applications and large-scale restrained-shrinkage test were conducted in this study. Moreover, the optimization of transverse reinforcement was the focus of this study because the longitudinal reinforcement is already optimized.

Transverse reinforcement controls longitudinal cracks. Cracks are the result of creep deformation of PCPs and shrinkage deformation of the CIP deck. Therefore, it is important to simulate proper CIP-PCP interactions and boundary conditions in evaluating the performance of various top-mat reinforcement options in the transverse direction. A large-scale restrained-shrinkage test and field instrumentation of two bridges (Wharton-Weems Overpass and Lampasas River Bridge) under construction were carried out. Current TxDOT design for the transverse reinforcement is No. 5 bars at 6-in. spacing. Two alternatives were considered: reducing bar size (No. 4 bars at 6-in. spacing) and welded-wire reinforcement (D 20 wires at 6-in. spacing) which would provide the same area as No. 4 bars at 6-in. spacing. Use of No. 4 bars or D 20 wire results in a 30% reduction in the transverse steel, and represents a significant cost saving considering the area of bridge deck constructed annually in Texas.

To control collinear cracking in PCPs, two approaches were considered: placing additional transverse bars at ends of the panel; and reducing initial prestressing force.

To evaluate the effects of additional transverse bars on control crack width, knife-edge test was conducted by Foreman (2010). In the test, collinear cracks were made by applying negative moment along strands. Through the test, it was observed that width and spacing of collinear cracks can be reduced by placing additional transverse reinforcement near the edge of the panel, and strands did not slip although the crack was quite wide. However, his tests did not simulate load and boundary conditions of real bridges, so it is still unclear whether the additional bars help control cracks under real field conditions.

Based on long-term monitoring of prestress loss in PCPs, Foreman (2010) and Azimov (2012) propose reducing initial prestressing force. They also suggest that prestress loss in PCPs be estimated using a lump-sum value of 25 ksi. They report the

necessity of developing new model for predicting prestress losses in PCP accurately. Most existing models, including those used by TxDOT, cannot accurately predict prestress losses in PCPs, because they were developed based on test results of prestressed girders and beams, which have different shrinkage and creep characteristics than PCPs, and also different values of effective prestress. In this study, all long-term monitoring results were summarized and a model for prestress loss in PCPs was proposed to overcome limitations of existing models.

Table 6-1 shows the current status and limitations of this study, and outlines future studies needed.

Table 6-1: Current status, limitations and future studies of this research

	Current status	Limitations and Future studies needed
Field applications	<u>Wharton-Weems Overpass (Houston, TX)</u> <ul style="list-style-type: none"> • Monitoring period: 1 year after casting • Top-mat options: <ul style="list-style-type: none"> ○ Current TxDOT Standard Reinforcement ○ Reduced Deformed-Bar Reinforcement • The bridge was opened to the traffic 9 months after casting • The bridge has only transverse cracks over its joints. No longitudinal cracks have been observed 	<ul style="list-style-type: none"> • Traffic has only been monitored for a short period after opening the bridge to traffic • No longitudinal cracks have been observed, so optimized top-mat reinforcement details in the transverse direction cannot be fully evaluated • Longer period monitoring and additional monitoring data of various bridges are needed
	<u>Lampasas River Bridge (Belton, TX)</u> <ul style="list-style-type: none"> • Monitoring period: 2 months after casting • Top-mat options: <ul style="list-style-type: none"> ○ Current TxDOT Standard Reinforcement ○ Reduced Deformed-Bar Reinforcement ○ Reduced Welded-Wire Reinforcement • The bride has not been opened to traffic 	
Restrained-shrinkage test	<ul style="list-style-type: none"> • Monitoring period: 8 months after casting • Top-mat options: <ul style="list-style-type: none"> ○ Current TxDOT Standard Reinforcement ○ Reduced Deformed-Bar Reinforcement ○ Reduced Welded-Wire Reinforcement • No cracks have been observed and all design options show similar strain values 	<ul style="list-style-type: none"> • The test does not simulate boundary conditions of real bridge. • Additional tests with following modifications are needed to confirm optimized top-mat reinforcement: <ul style="list-style-type: none"> ○ Applying higher restraining force ○ Adjusting concrete mix proportion to have larger shrinkage and creep strains

Table 6-1: Current status, limitations and future studies of this research (continued)

	Current status	Limitations and Future studies needed
Long-term monitoring of prestress loss in PCPs	<ul style="list-style-type: none"> • Fourteen PCPs which had different initial prestress levels and coarse aggregate have been monitored • Monitoring period ranges from 22 months to 42 months • Prestress loss prediction model for PCPs was developed based on the monitoring results 	<ul style="list-style-type: none"> • Most monitoring data was used for developing the model • Limited numbers of panels were used to verify the model • All monitoring results come from the same research group, so tests conducted by other labs and using different materials would be useful so that the model can be applied generally

6.2 CONCLUSIONS

Through the tests and data analyses of this study, the following conclusions were derived:

- i) Field applications and restrained-shrinkage test
 - a. Current longitudinal reinforcement (No. 4 @ 9 in.) is already optimized.
 - b. Current transverse reinforcement (No. 5 @ 6 in.) can be reduced by using a smaller bar (No. 4 @ 6 in.) or welded-wire reinforcement (D 20 @ 6 in.).
- ii) Long-term monitoring of prestress loss in PCPs
 - a. Initial applied prestress level can be adjusted from current TxDOT specified value (189.4 ksi) to a reduced value (169.4 ksi). By reducing the level of initial prestress, the possibility of cracking in panels can be reduced, and the panels will still meet the serviceability criteria implied by current TxDOT specifications.
 - b. The lump-sum prestress losses assumed in current TxDOT specifications of 45 ksi can be decreased to 25 ksi. That new lump-sum value (25 ksi) gives conservative result for the panels with Current TxDOT initial prestress (189.4 ksi) and Reduced initial prestress (169.4 ksi).
 - c. A new equation for predicting prestress loss in PCP was proposed that takes into account the types of aggregate and the levels of initial prestress.

APPENDIX A

Development Length Calculation

In this appendix, the detailed calculation procedures for the development length for Chapter 3 are introduced. For considering worst case, it is assumed that rebar and wire are coated with epoxy. Development length in the section where two different types of reinforcement used, longer one is governed. Some sections have the same development length, so representative cases are only shown in here. Following things were assumed for calculating development length in Chapter 3:

- Specified concrete strength = 4,000 psi
- Specified yield strength of deformed bar = 60,000 psi
- Specified yield strength of welded wire = 75,000 psi

A.1 SECTION A-A (NO. 4 BAR AT 9 IN.)

Equation 3-1 can be transformed as follow

$$l_d = \left[\frac{3}{40} \times \frac{f_y}{\lambda \times \sqrt{f'_c}} \times \frac{\psi_t \times \psi_e \times \psi_s}{\left(\frac{c_b + K_{tr}}{d_b} \right)} \right] \times d_b$$

where,

$$d_b = \frac{4}{8} \text{ in.}$$

$$f_y = 60,000 \text{ psi}$$

$$f'_c = 4,000 \text{ psi}$$

$$\psi_t = 1.0 \text{ (for less than 12 in. of concrete is cast below the rebar)}$$

$$\psi_e = 1.5 \text{ (for epoxy coated bar)}$$

$$\psi_s = 0.8 \text{ (for No. 6 and smaller bar)}$$

$$\lambda = 1.0 \text{ (for normal weight concrete)}$$

$$c_b = \left[\begin{array}{l} 2 + \frac{14}{28} = 2.5 \\ \frac{1}{2} \times 9 = 4.5 \end{array} \right]_{\min.} = 2.25$$

$$K_{tr} = 0$$

$$\frac{c_b + K_{tr}}{d_b} = \frac{2.25 + 0}{4/8} = 4.5 \geq 2.5 \rightarrow \text{Use } 2.5$$

Therefore,

$$l_d = \left(\frac{3}{40} \frac{6,000}{1.0 \times \sqrt{4,000}} \frac{1.0 \times 1.5 \times 0.8}{2.5} \right) \times \frac{4}{8} = 17.1 \text{ in.} \geq 12.0$$

→ Required development length = **17.1 in.**

→ Actual development length = **18.0 in.**

A.2 SECTION E-E (D 20 WIRE AT 9 IN.)

Equation 3-2 can be transformed as follow

$$l_d = \left[\psi_w \times \frac{3}{40} \frac{f_y}{\lambda \times \sqrt{f_c'}} \frac{\psi_t \times \psi_e \times \psi_s}{\left(\frac{c_b + K_{tr}}{d_b} \right)} \right] \times d_b$$

where,

$$\psi_w = \left[\begin{array}{l} \frac{f_y - 35,000}{f_y} = \frac{75,000 - 35,000}{75,000} = 0.53 \\ \frac{5d_b}{s} = \frac{5 \times 0.504}{9} = 0.28 \end{array} \right]_{\max.} = 0.53 \leq 1.0 \rightarrow \text{Use } 0.53$$

$$s = 9 \text{ in.}$$

$$d_b = 0.504 \text{ in.}$$

$$f_y = 75,000 \text{ psi}$$

$$\lambda = 1.0$$

$$f_c' = 4,000 \text{ psi}$$

$$\psi_t = 1.0$$

$$\psi_e = 1.0 \text{ (for epoxy coated welded wire reinforcement)}$$

$$\psi_s = 0.8$$

$$\frac{c_b + K_{tr}}{d_b} = \frac{2.252 + 0}{0.504} = 4.683 \geq 2.5 \rightarrow \text{Use } 2.5$$

Therefore,

$$l_d = \left[0.53 \times \frac{3}{40} \frac{75,000}{1.0 \times \sqrt{4,000}} \frac{1.0 \times 1.0 \times 0.8}{2.5} \right] \times 0.504 = 7.6 \leq 8.0$$

→ Required development length = **8.0 in.**

→ Actual development length = **16.0 in.**

A.3 SECTION M-M (NO. 5 BAR AT 6 IN.)

$$l_d = \left[\frac{3}{40} \frac{f_y}{\lambda \times \sqrt{f'_c}} \frac{\psi_t \times \psi_e \times \psi_s}{\left(\frac{c_b + K_{tr}}{d_b} \right)} \right] \times d_b$$

where,

$$d_b = \frac{5}{8} \text{ in.}$$

$$f_y = 6,000 \text{ psi}$$

$$f'_c = 4,000 \text{ psi}$$

$$\psi_t = 1.0$$

$$\psi_e = 1.5$$

$$\psi_s = 0.8$$

$$\lambda = 1.0$$

$$c_b = \left[\begin{array}{l} 2 + \frac{1.5}{2.8} = 2.3125 \\ \frac{1}{2} \times 9 = 4.5 \end{array} \right]_{\min.} = 2.3125$$

$$K_{tr} = 0$$

$$\frac{c_b + K_{tr}}{d_b} = \frac{2.3125 + 0}{5/8} = 3.7 \geq 2.5 \rightarrow \text{Use } 2.5$$

Therefore,

$$l_d = \left(\frac{3}{40} \frac{6,000}{1.0 \times \sqrt{4,000}} \frac{1.0 \times 1.5 \times 0.8}{2.5} \right) \times \frac{5}{8} = 21.3 \text{ in.} \geq 12.0$$

→ Required development length = **21.3 in.**

→ Actual development length = **24.0 in.**

A.4 SECTION O-O (D 20 WIRE AT 6 IN.)

$$l_d = \left[\psi_w \times \frac{3}{40} \frac{f_y}{\lambda \times \sqrt{f'_c}} \frac{\psi_t \times \psi_e \times \psi_s}{\left(\frac{c_b + K_{tr}}{d_b} \right)} \right] \times d_b$$

where,

$$\psi_w = \left[\begin{array}{l} \frac{f_y - 3,500}{f_y} = \frac{75,000 - 35,000}{75,000} = 0.53 \\ \frac{5d_b}{s} = \frac{5 \times 0.504}{6} = 0.42 \end{array} \right]_{\text{max.}} = 0.53 \leq 4.0 \rightarrow \text{Use } 0.53$$

$$s = 6 \text{ in.}$$

$$d_b = 0.504 \text{ in.}$$

$$f_y = 75,000 \text{ psi}$$

$$\lambda = 1.0$$

$$f'_c = 4,000 \text{ psi}$$

$$\psi_t = 1.0$$

$$\psi_e = 1.0 \text{ (for epoxy coated welded wire reinforcement)}$$

$$\psi_s = 0.8$$

$$\frac{c_b + K_{tr}}{d_b} = \frac{2.252 + 0}{0.504} = 4.683 \geq 2.5 \rightarrow \text{Use } 2.5$$

Therefore,

$$l_d = \left[0.53 \times \frac{3}{40} \frac{75,000}{1.0 \times \sqrt{4,000}} \frac{1.0 \times 1.0 \times 0.8}{2.5} \right] \times 0.504 = 7.6 \leq 8.0$$

→ Required development length = **8.0 in.**

→ Actual development length = **16.0 in.**

A.5 SECTION R-R (NO. 4 BAR AT 6 IN.)

$$l_d = \left[\frac{3}{40} \frac{f_y}{\lambda \times \sqrt{f'_c}} \frac{\psi_t \times \psi_e \times \psi_s}{\left(\frac{c_b + K_{tr}}{d_b} \right)} \right] \times d_b$$

where,

$$d_b = \frac{4}{8} \text{ in.}$$

$$f_y = 6,000 \text{ psi}$$

$$f'_c = 4,000 \text{ psi}$$

$$\psi_t = 1.0$$

$$\psi_e = 1.5$$

$$\psi_s = 0.8$$

$$\lambda = 1.0$$

$$c_b = \left[\begin{array}{l} 2 + \frac{14}{28} = 2.25 \\ \frac{1}{2} \times 9 = 4.5 \end{array} \right]_{\min.} = 2.25$$

$$K_{tr} = 0$$

$$\frac{c_b + K_{tr}}{d_b} = \frac{2.25 + 0}{4/8} = 4.5 \geq 2.5 \rightarrow \text{Use } 2.5$$

Therefore,

$$l_d = \left(\frac{3}{40} \frac{6,000}{1.0 \times \sqrt{4,000}} \frac{1.0 \times 1.5 \times 0.8}{2.5} \right) \times \frac{4}{8} = 17.1 \text{ in.} \geq 12.0$$

→ Required development length = **17.1 in.**

→ Actual development length = **18.0 in.**

APPENDIX B

Sample Restraint Moment Calculation using P-method Wharton-Weems Overpass

The restraint moments of the Wharton-Weems overpass in both directions were calculated using Excel and the results were shown in Chapter 3. This appendix shows the detailed calculation procedure of the restraint moment in the Wharton-Weems Overpass 14 days after casting of the CIP topping slabs. In the calculation, following conditions and assumptions are used:

B.1 CONDITIONS AND ASSUMPTIONS FOR CALCULATION

Precast concrete panels:

Design strength (f_c')_{precast}: 9000 psi

Elastic modulus of strand (E_s): 29000 ksi

Unit weight concrete (w_c): 150 lb/ft³

Use eight 3/8 in. low-relaxation strand per panel

Strands are located 2 in. from top of precast panel

Remaining prestress during a month after CIP concrete casting: 175 ksi.

Ultimate shrinkage strain of PCPs: 600×10^{-6}

Ultimate creep coefficient of the PCPs: 3.42

CIP concrete slabs:

Design strength (f_c')_{CIP}: 4000 psi

Compressive strength at 14 days after casting using Equation 4-5:

$$f_c(14) = 4000 \times \frac{14}{2.3 + (0.92 \times 14)} = 3689 \text{ psi}$$

Elastic modulus of top-mat reinforcement (E_s): 29000 ksi

Current TxDOT standard reinforcement was used:

No. 5 bar at 6 in (transverse dir.) / No. 4 bar at 6 in (longitudinal dir.)

Unit weight concrete (w_c): 150 lb/ft³

CIP concrete was cast when the precast panels was 55 days old

Ultimate shrinkage strain of CIP slabs: 613×10^{-6}

Ultimate creep coefficient of the CIP slabs: 3.40

B.2 CALCULATIONS OF COMPONENTS FOR LONGITUDINAL RESTRAINT MOMENT

Dimension of specimen:

Width: 111.6 in. (=9.3 ft)

Length of main span (L_m): 600 in. (=50 ft)

Length of diaphragm (L_d): 1 in.

Thickness: 8 in. (4 in. precast panel and 4 in. CIP topping)

Composite section properties:

$$y_b = 3.56 \text{ in.}$$

$$y_t = 4.44 \text{ in.}$$

$$I_g = 5879.4 \text{ in.}^4$$

$$I_{cr} = 371.0 \text{ in.}^4$$

Calculate the moment due to eccentric prestressing, M_p :

$$M_p = f_p \times A_p \times (y_b - 2) = 175 \times 0 \times (3.54 - 2) = 0 \text{ kip-in.}$$

$$f_p = 175 \text{ kips}$$

$$A_p = 0 \text{ in.}^2$$

$$y_b = 3.56 \text{ in.}$$

Calculate the dead load moment, $(M_d)_{\text{precast}}$, $(M_d)_{\text{CIP}}$:

$$(M_d)_{\text{precast}} = \frac{wl^2}{8} = \frac{4 \times 111.6}{144} \times 150 \times \frac{50^2}{8} \times 10^{-3} \times 12 = 1743.8 \text{ kip-in.}$$

$$(M_d)_{\text{CIP}} = \frac{wl^2}{8} = \frac{4 \times 111.6}{144} \times 150 \times \frac{50^2}{8} \times 10^{-3} \times 12 = 1743.8 \text{ kip-in.}$$

Calculate the uniform shrinkage moment, M_s :

$$M_s = \varepsilon_s E_d A_d \left(e_s - \frac{h}{2} \right) \left(\frac{1}{1 + \frac{E_p A_p}{E_d A_d}} \right) \left(\frac{1}{1 + \frac{E_s A_s}{E_d A_d}} \right)$$

$$E_d = 57\sqrt{3689} = 3462 \text{ ksi}$$

$$E_p = 57\sqrt{9000} = 5408 \text{ ksi}$$

$$E_s = 29000 \text{ ksi}$$

$$A_d = A_p = 111.6 \times 4 = 446.4 \text{ in.}^2$$

$$A_s = 12.4 \times 0.2 = 2.48 \text{ in.}^2 \text{ (No. 4 bar at 9 in. in 111.6 in. width deck)}$$

$$e_c = y_t = 4.44 \text{ in.}$$

$$h = 4 \text{ in.}$$

Therefore,

$$M_s = \varepsilon_s \times 3462 \times 192 \left(4.44 - \frac{4}{2} \right) \left(\frac{1}{1 + \frac{5408 \times 446.4}{3462 \times 446.4}} \right) \left(\frac{1}{1 + \frac{29000 \times 2.48}{3462 \times 446.8}} \right)$$

$$= 3,711,346.5 \times \varepsilon_s \text{ kips-in.}$$

Shrinkage strains in precast panels and CIP concrete slabs for calculating M_s :

Precast concrete panels

Shrinkage strain in the panels at time t using Equation 4-4

$$\varepsilon_{sh,precast}(t) = 600 \times 10^{-6} \times 0.13 \times \ln(t+1)$$

Shrinkage in the panels when the CIP topping is cast ($t=55$ days)

$$\varepsilon_{sh,precast}(55) = 600 \times 10^{-6} \times 0.13 \times \ln(55+1) = 314 \times 10^{-6}$$

Shrinkage in the panels when CIP topping is 14 days old ($t=55+14=69$ days)

$$\varepsilon_{sh,precast}(69) = 600 \times 10^{-6} \times 0.13 \times \ln(55+14+1) = 331 \times 10^{-6}$$

Shrinkage strain in precast panel during 14 days after CIP topping is cast

$$\varepsilon_{sh,precast} = (331 \times 10^{-6}) - (314 \times 10^{-6}) = 17 \times 10^{-6}$$

CIP concrete slabs

Shrinkage strain in CIP concrete slabs at time t

$$\varepsilon_{sh,CIP}(t)=613 \times 10^{-6} \times 0.13 \times \ln(t+1)$$

Shrinkage in CIP topping during the first 14 days ($t=14$ days)

$$\varepsilon_{sh,CIP}(14)=613 \times 10^{-6} \times 0.13 \times \ln(14+1)=216 \times 10^{-6}$$

Differential shrinkage between precast concrete panels and CIP slabs

$$\varepsilon_{sh}=(216 \times 10^{-6})-(17 \times 10^{-6})=199 \times 10^{-6}$$

Therefore

$$M_s=3,711,346.5 \times (199 \times 10^{-6})=736.3 \text{ kip-in.}$$

Creep effects on M_p and $(M_d)_{precast}$:

$$[\Delta(1-e^{-\varphi_1})]=(1-e^{-1.889})-(1-e^{-1.790})=0.01577$$

$$(\varphi_1)_{\text{initial}}=3.42 \times 0.13 \times \ln(55+1)=1.790$$

$$(\varphi_1)_{14 \text{ days}}=3.42 \times 0.13 \times \ln(55+14+1)=1.889$$

Creep effects on $(M_d)_{CIP}$ and M_s :

$$\varphi_2=3.40 \times 0.13 \times \ln(14+1)=1.197$$

$$(1-e^{-\varphi_2})=(1-e^{-1.197})=0.698$$

$$\frac{(1-e^{-\varphi_2})}{\varphi_2}=\frac{(1-e^{-1.197})}{1.197}=0.583$$

B.3 CALCULATE LONGITUDINAL RESTRAINT MOMENT

α can be calculated using moment distribution method, and it is assumed that the specimen has not been cracked ($I_d=I_m=I_g$). Resultant restraint moments due to fixed-ends moment M_s and M_d are shown in Figure B-1 and Figure B-2.

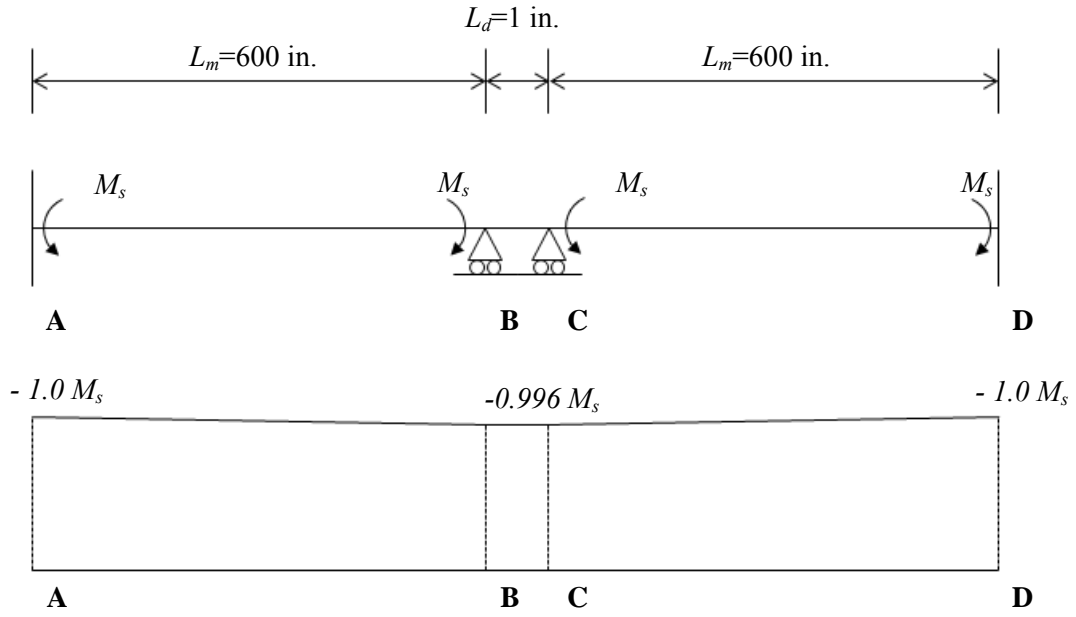


Figure B-1: Longitudinal restraint moment due to M_s

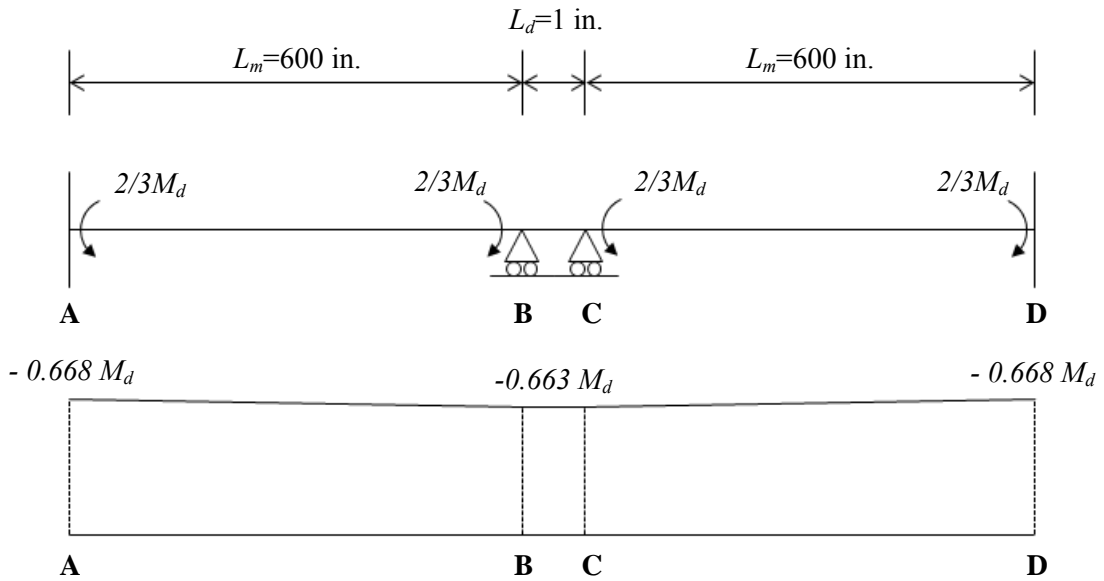


Figure B-2: Longitudinal restraint moment due to M_d

Therefore

$$\begin{aligned}
 M_r &= \text{Equation 3-2} \\
 &= [\alpha M_p - \alpha (M_d)_{\text{precast}}] [\Delta (1 - e^{-\phi_1})] - \alpha (M_d)_{\text{CIP}} (1 - e^{-\phi_2}) - \alpha M_s \left(\frac{1 - e^{-\phi_2}}{\phi_2} \right) \\
 &= [(0.996 \times 0 - 0.663 \times 1743.75) \times 0.01577] - (0.663 \times 1743.75 \times 0.698) \\
 &\quad - (0.996 \times 736.3 \times 0.583) \\
 &= -1253.9 \text{ kip-in.}
 \end{aligned}$$

Cracking moment at 14 days after CIP topping is cast

$$M_{cr} = -\frac{7.5\sqrt{3689}}{1000} \times \frac{111.6 \times 8^2}{6} = -542.3 \text{ kip-in.}$$

The restraint moment is greater than the cracking moment ($|M_r| > |M_{cr}|$), so it can be concluded that cracks are formed in the specimen.

B.4 CALCULATIONS OF COMPONENTS FOR TRANSVERSE RESTRAINT MOMENT

Dimension of specimen:

Width: 1,200 in. (=100 ft)

Length of main span (L_m): 92 in. (=7.67 ft)

Length of diaphragm (L_d): 36 in.

Thickness: 8 in. (4 in. precast panel and 4 in. CIP topping)

Composite section properties:

$$y_b = 3.56 \text{ in.}$$

$$y_t = 4.44 \text{ in.}$$

$$I_g = 63219.0 \text{ in.}^4$$

$$I_{cr} = 8118.4 \text{ in.}^4$$

Calculate the moment due to eccentric prestressing, M_p :

$$M_p = f_p \times A_p \times (y_b - 2) = 175 \times 16 \times (3.56 - 2) = 4371.7 \text{ kip-in.}$$

$$f_p = 175 \text{ kips}$$

$$A_p = 200 \times 0.08 = 16 \text{ in.}^2$$

$$y_b = 3.56 \text{ in.}$$

Calculate the dead load moment, $(M_d)_{\text{precast}}$ $(M_d)_{\text{CIP}}$:

$$(M_d)_{\text{precast}} = \frac{wl^2}{8} = \frac{4 \times 1200}{144} \times 150 \times \frac{7.67^2}{8} \times 10^{-3} \times 12 = 440.8 \text{ kip-in.}$$

$$(M_d)_{\text{CIP}} = \frac{wl^2}{8} = \frac{4 \times 1200}{144} \times 150 \times \frac{7.67^2}{8} \times 10^{-3} \times 12 = 440.8 \text{ kip-in.}$$

Calculate the uniform shrinkage moment, M_s :

$$M_s = \varepsilon_s E_d A_d \left(e_s - \frac{h}{2} \right) \left(\frac{1}{1 + \frac{E_p A_p}{E_d A_d}} \right) \left(\frac{1}{1 + \frac{E_s A_s}{E_d A_d}} \right)$$

$$E_d = 57 \sqrt{3689} = 3462 \text{ ksi}$$

$$E_p = 57 \sqrt{9000} = 5408 \text{ ksi}$$

$$E_s = 29000 \text{ ksi}$$

$$A_d = A_p = 1200 \times 4 = 4800 \text{ in.}^2$$

$$A_s = 200 \times 0.31 = 62 \text{ in.}^2 \text{ (No. 5 bar at 6 in. in 1200 in. width deck)}$$

$$e_c = y_t = 4.44 \text{ in.}$$

$$h = 4 \text{ in.}$$

Therefore,

$$\begin{aligned} M_s &= \varepsilon_s \times 3462 \times 192 \left(4.44 - \frac{4}{2} \right) \left(\frac{1}{1 + \frac{5408 \times 4800}{3462 \times 4800}} \right) \left(\frac{1}{1 + \frac{29000 \times 62}{3462 \times 4800}} \right) \\ &= 37,686,507.5 \times \varepsilon_s \text{ kips-in.} \end{aligned}$$

Shrinkage strains in precast panels and CIP concrete slabs for calculating M_s :

Precast concrete panels

Shrinkage strain in the panels at time t using Equation 4-4

$$\varepsilon_{sh,precast}(t)=600 \times 10^{-6} \times 0.13 \times \ln(t+1)$$

Shrinkage in the panels when the CIP topping is cast ($t=55$ days)

$$\varepsilon_{sh,precast}(55)=600 \times 10^{-6} \times 0.13 \times \ln(55+1)=314 \times 10^{-6}$$

Shrinkage in the panels when CIP topping is 14 days old ($t=55+14=69$ days)

$$\varepsilon_{sh,precast}(69)=600 \times 10^{-6} \times 0.13 \times \ln(55+14+1)=331 \times 10^{-6}$$

Shrinkage strain in precast panel during 14 days after CIP topping is cast

$$\varepsilon_{sh,precast}=(331 \times 10^{-6})-(314 \times 10^{-6})=17 \times 10^{-6}$$

CIP concrete slabs

Shrinkage strain in CIP concrete slabs at time t

$$\varepsilon_{sh,CIP}(t)=613 \times 10^{-6} \times 0.13 \times \ln(t+1)$$

Shrinkage in CIP topping during the first 14 days ($t=14$ days)

$$\varepsilon_{sh,CIP}(14)=613 \times 10^{-6} \times 0.13 \times \ln(14+1)=216 \times 10^{-6}$$

Differential shrinkage between precast concrete panels and CIP slabs

$$\varepsilon_{sh}=(216 \times 10^{-6})-(17 \times 10^{-6})=199 \times 10^{-6}$$

Therefore

$$M_s=37,686,507.5 \times (199 \times 10^{-6})=7477.0 \text{ kip-in.}$$

Creep effects on M_p and $(M_d)_{precast}$:

$$[\Delta(1-e^{-\phi_1})]=(1-e^{-1.889})-(1-e^{-1.790})=0.01577$$

$$(\phi_1)_{\text{initial}}=3.42 \times 0.13 \times \ln(55+1)=1.790$$

$$(\phi_1)_{14 \text{ days}}=3.42 \times 0.13 \times \ln(55+14+1)=1.889$$

Creep effects on $(M_d)_{CIP}$ and M_s :

$$\varphi_2 = 3.40 \times 0.13 \times \ln(14+1) = 1.197$$

$$(1 - e^{-\varphi_2}) = (1 - e^{-1.197}) = 0.698$$

$$\frac{(1 - e^{-\varphi_2})}{\varphi_2} = \frac{(1 - e^{-1.197})}{1.197} = 0.583$$

B.5 CALCULATE TRANSVERSE RESTRAINT MOMENT

α can be calculated using moment distribution method, and it is assumed that the specimen has not been cracked ($I_d = I_m = I_g$). Resultant restraint moments due to fixed-ends moment M_p , M_s and M_d are shown in Figure B-3 to Figure B-5.

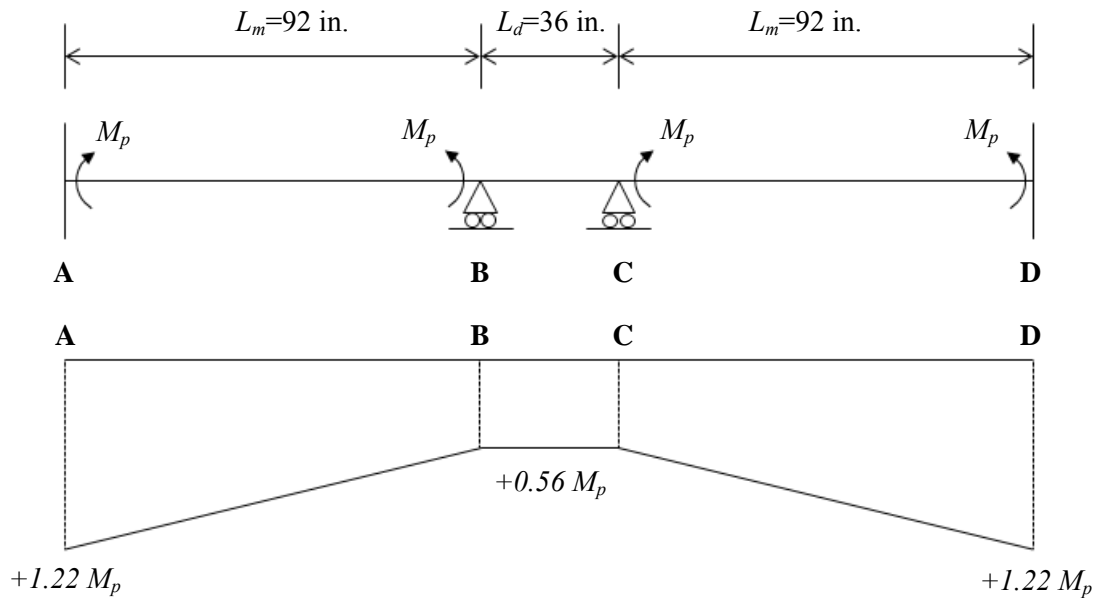


Figure B-3: Transverse restraint moment due to M_p

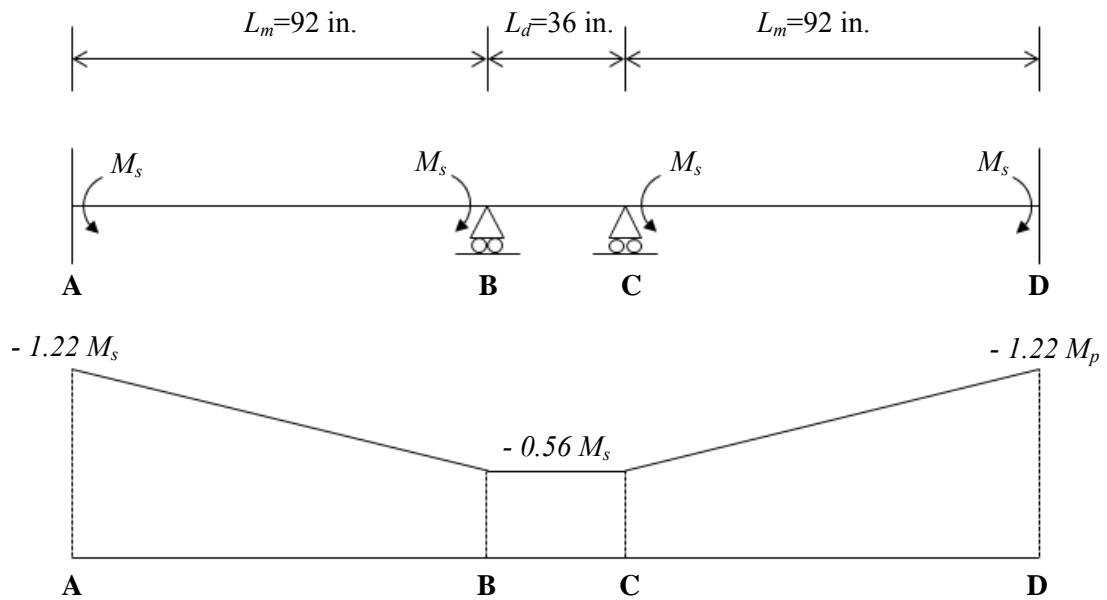


Figure B-4: Transverse restraint moment due to M_s

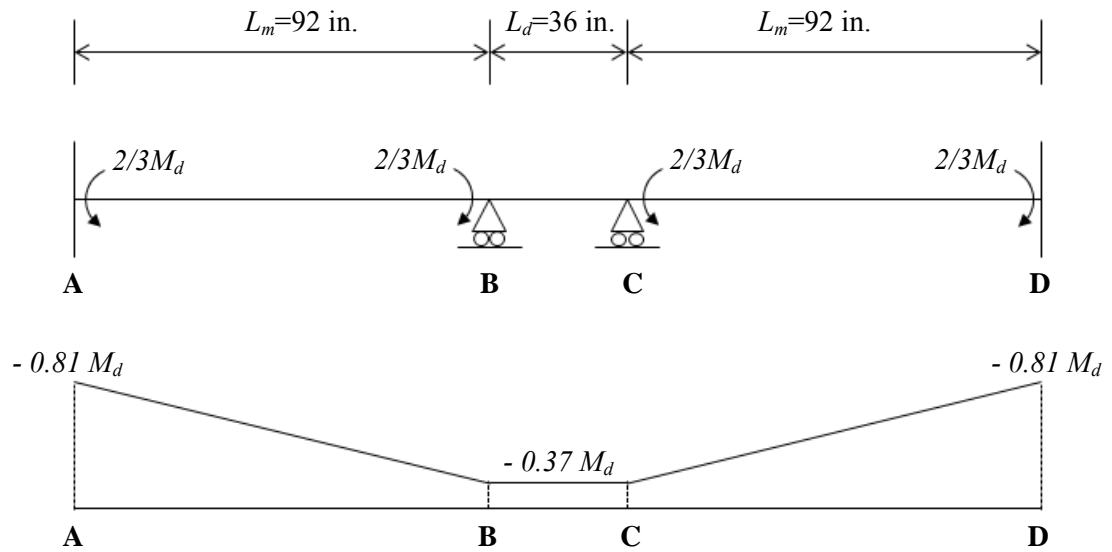


Figure B-5: Transverse restraint moment due to M_d

Therefore

$M_r = \text{Equation 3-2}$

$$\begin{aligned} &= [\alpha M_p - \alpha (M_d)_{\text{precast}}] [\Delta (1 - e^{-\phi_1})] - \alpha (M_d)_{\text{CIP}} (1 - e^{-\phi_2}) - \alpha M_s \left(\frac{1 - e^{-\phi_2}}{\phi_2} \right) \\ &= [(0.56 \times 4371.7 - 0.37 \times 440.8) \times 0.01577] - (0.37 \times 440.8 \times 0.698) \\ &\quad - (0.56 \times 7477.0 \times 0.583) \\ &= -2519.1 \text{ kip-in.} \end{aligned}$$

Cracking moment at 14 days after CIP topping is cast

$$M_{cr} = -\frac{7.5\sqrt{3689}}{1000} \times \frac{1200 \times 8^2}{6} = -5830.8 \text{ kip-in.}$$

The restraint moment is greater than the cracking moment ($|M_r| < |M_{cr}|$), so it can be concluded that cracks are not formed in the specimen.

APPENDIX C

Sample Restraint Moment Calculation using P-method Restrained Shrinkage Test

The restraint moment of the test specimen was calculated using P-method in Chapter 4, and the results were shown in Figure 4-25. This appendix shows the detailed calculation procedure of the restraint moment in the specimen 14 days after casting of the CIP topping slabs. In the calculation, following conditions and assumptions are used:

C.1 CONDITIONS AND ASSUMPTIONS FOR CALCULATION

Precast concrete panels:

Design strength (f_c')_{precast}: 9000 psi

Elastic modulus of strand (E_s): 29000 ksi

Unit weight concrete (w_c): 150 lb/ft³

Use eight 3/8 in. low-relaxation strand per panel

Strands are located 2 in. from top of precast panel

Remaining prestress during a month after CIP concrete casting: 175 ksi.

Ultimate shrinkage strain of PCPs: 600×10^{-6}

Ultimate creep coefficient of the PCPs: 3.42

CIP concrete slabs:

Design strength (f_c')_{CIP}: 4000 psi

Compressive strength at 14 days after casting using Equation 4-5:

$$f_c(14) = 4000 \times \frac{14}{2.3 + (0.92 \times 14)} = 3689 \text{ psi}$$

Elastic modulus of top-mat reinforcement (E_s): 29000 ksi

Current TxDOT standard reinforcement was used: No. 5 at 6 in.

Unit weight concrete (w_c): 150 lb/ft³

CIP concrete was cast when the precast panels was 55 days old

Ultimate shrinkage strain of CIP slabs: 613×10^{-6}

Ultimate creep coefficient of the CIP slabs: 3.40

Dimension of specimen:

Width: 48 in.

Length of main span (L_m): 8 ft

Length of diaphragm (L_d): 10 in.

Thickness: 8 in. (4 in. precast panel and 4 in. CIP topping)

Composite section properties:

$$y_b = 3.56 \text{ in.}$$

$$y_t = 4.44 \text{ in.}$$

$$I_g = 2528.8 \text{ in.}^4$$

$$I_{cr} = 324.7 \text{ in.}^4$$

C.2 CALCULATIONS OF EACH COMPONENT FOR CALCULATING RESTRAINT MOMENT

Calculate the moment due to eccentric prestressing, M_p :

$$M_p = f_p \times A_p \times (y_b - 2) = 175 \times 0.64 \times (3.56 - 2) = 174.7 \text{ kip-in.}$$

$$f_p = 175 \text{ kips}$$

$$A_p = 8 \times 0.08 = 0.64 \text{ in.}^2$$

$$y_b = 3.56 \text{ in.}$$

Calculate the dead load moment, $(M_d)_{\text{precast}}$, $(M_d)_{\text{CIP}}$:

$$(M_d)_{\text{precast}} = \frac{wl^2}{8} = \frac{4 \times 48}{144} \times 150 \times \frac{8^2}{8} \times 10^{-3} \times 12 = 19.2 \text{ kip-in.}$$

$$(M_d)_{\text{CIP}} = \frac{wl^2}{8} = \frac{4 \times 48}{144} \times 150 \times \frac{8^2}{8} \times 10^{-3} \times 12 = 19.2 \text{ kip-in.}$$

Calculate the uniform shrinkage moment, M_s :

$$M_s = \epsilon_s E_d A_d \left(e_s - \frac{h}{2} \right) \left(\frac{1}{1 + \frac{E_p A_p}{E_d A_d}} \right) \left(\frac{1}{1 + \frac{E_s A_s}{E_d A_d}} \right)$$

$$E_d = 57 \sqrt{3689} = 3462 \text{ ksi}$$

$$E_p = 57\sqrt{9000} = 5408 \text{ ksi}$$

$$E_s = 29000 \text{ ksi}$$

$$A_d = A_p = 48 \times 4 = 192 \text{ in.}^2$$

$$A_s = 8 \times 0.31 = 2.48 \text{ in.}^2$$

$$e_c = y_t = 4.44 \text{ in.}$$

$$h = 4 \text{ in.}$$

Therefore,

$$M_s = \epsilon_s \times 3462 \times 192 \left(4.44 - \frac{4}{2} \right) \left(\frac{1}{1 + \frac{5408 \times 192}{3462 \times 192}} \right) \left(\frac{1}{1 + \frac{29000 \times 2.48}{3462 \times 192}} \right)$$

$$= 1,507,460.3 \times \epsilon_s \text{ kips-in.}$$

Shrinkage strains in precast panels and CIP concrete slabs for calculating M_s :

Precast concrete panels

Shrinkage strain in the panels at time t using Equation 4-4

$$\epsilon_{sh,precast}(t) = 600 \times 10^{-6} \times 0.13 \times \ln(t+1)$$

Shrinkage in the panels when the CIP topping is cast ($t=55$ days)

$$\epsilon_{sh,precast}(55) = 600 \times 10^{-6} \times 0.13 \times \ln(55+1) = 314 \times 10^{-6}$$

Shrinkage in the panels when CIP topping is 14 days old ($t=55+14=69$ days)

$$\epsilon_{sh,precast}(69) = 600 \times 10^{-6} \times 0.13 \times \ln(55+14+1) = 331 \times 10^{-6}$$

Shrinkage strain in precast panel during 14 days after CIP topping is cast

$$\epsilon_{sh,precast} = (331 \times 10^{-6}) - (314 \times 10^{-6}) = 17 \times 10^{-6}$$

CIP concrete slabs

Shrinkage strain in CIP concrete slabs at time t

$$\epsilon_{sh,CIP}(t) = 613 \times 10^{-6} \times 0.13 \times \ln(t+1)$$

Shrinkage in CIP topping during the first 14 days ($t=14$ days)

$$\epsilon_{sh,CIP}(14) = 613 \times 10^{-6} \times 0.13 \times \ln(14+1) = 216 \times 10^{-6}$$

Differential shrinkage between precast concrete panels and CIP slabs

$$\varepsilon_{sh}=(216 \times 10^{-6})-(17 \times 10^{-6})=199 \times 10^{-6}$$

Therefore

$$M_s=1,507,460.3 \times (199 \times 10^{-6})=300 \text{ kip-in.}$$

Creep effects on M_p and $(M_d)_{\text{precast}}$:

$$[\Delta(1-e^{-\varphi_1})]=(1-e^{-1.889})-(1-e^{-1.790})=0.01577$$

$$(\varphi_1)_{\text{initial}}=3.42 \times 0.13 \times \ln(55+1)=1.790$$

$$(\varphi_1)_{14 \text{ days}}=3.42 \times 0.13 \times \ln(55+14+1)=1.889$$

Creep effects on $(M_d)_{\text{CIP}}$ and M_s :

$$\varphi_2=3.40 \times 0.13 \times \ln(14+1)=1.197$$

$$(1-e^{-\varphi_2})=(1-e^{-1.197})=0.698$$

$$\frac{(1-e^{-\varphi_2})}{\varphi_2}=\frac{(1-e^{-1.197})}{1.197}=0.583$$

C.3 CALCULATE RESTRAINT MOMENT

Assume that the specimen has not been cracked ($I_d=I_m=I_g$)

$$\alpha=\frac{\frac{2I_d}{L_d}}{\frac{2I_d}{L_d}+\frac{3I_m}{L_m}}=\frac{\frac{2I_g}{L_d}}{\frac{2I_g}{L_d}+\frac{3I_g}{L_m}}=\frac{\frac{2 \times 2528.8}{10/12}}{\frac{2 \times 2528.8}{10/12}+\frac{3 \times 2528.8}{8}}=0.865$$

Therefore

M_r = Equation 3-2

$$\begin{aligned} &= \left[\frac{3}{2} \alpha M_p - \alpha (M_d)_{\text{precast}} \right] [\Delta(1-e^{-\varphi_1})] - \alpha (M_d)_{\text{CIP}} (1-e^{-\varphi_2}) - \frac{3}{2} \alpha M_s \left(\frac{1-e^{-\varphi_2}}{\varphi_2} \right) \\ &= \left[\left(\frac{3}{2} \times 0.865 \times 174.72 - 0.865 \times 19.2 \right) \times 0.01577 \right] - (0.865 \times 19.2 \times 0.698) \\ &\quad - \left(\frac{3}{2} \times 0.865 \times 300 \times 0.583 \right) \\ &= -234.80 \text{ kip-in.} \end{aligned}$$

Cracking moment at 14 days after CIP topping is cast

$$M_{cr} = -\frac{7.5\sqrt{3689}}{1000} \times \frac{48 \times 8^2}{6} = -233.23 \text{ kip-in.}$$

The restraint moment is greater than the cracking moment ($|M_r| > |M_{cr}|$), so it can be concluded that cracks are formed in the specimen. The restraint moment should be re-calculated considering reduction of stiffness in diaphragm region ($I_d = I_{cr}$). The stiffness of main span is not changed ($I_m = I_g$).

$$\alpha = \frac{\frac{2I_d}{L_d}}{\frac{2I_d}{L_d} + \frac{3I_m}{L_m}} = \frac{\frac{2I_{cr}}{L_d}}{\frac{2I_{cr}}{L_d} + \frac{3I_g}{L_m}} = \frac{\frac{2 \times 324.7}{10/12}}{\frac{2 \times 324.7}{10/12} + \frac{3 \times 2528.8}{8}} = 0.451$$

Then

$$\begin{aligned} M_r &= \left[\left(\frac{3}{2} \times 0.451 \times 174.72 - 0.451 \times 19.2 \right) \times 0.01577 \right] - (0.451 \times 19.2 \times 0.698) \\ &\quad - \left(\frac{3}{2} \times 0.451 \times 300 \times 0.583 \right) \\ &= -122.64 \text{ kip-in.} \end{aligned}$$

REFERENCE

- AASHTO (2004). *LRFD Design Specifications*, 3rd Edition, American Association of State Highway and Transportation Officials, Washington, D.C.
- AASHTO (2008). *LRFD Design Specifications*, 4th Edition, American Association of State Highway and Transportation Officials, Washington, D.C.
- ACI 318 (2008). *Building Code Requirements for Structural Concrete (ACI 318-08) and Commentary (ACI 318R-08)*, American Concrete Institute, Farmington Hills, MI.
- ACI 318 (2011). *Building Code Requirements for Structural Concrete (ACI 318-11) and Commentary (ACI 318R-11)*, Farmington Hills, MI.
- Al-Manaseer, A. & J.-P. Lam (2005). "Statistical Evaluation of Shrinkage and Creep models," *ACI Materials Journal*, 102, 170-176.
- Ayyub, B. M., P. C. Chang & N. A. Al-Mutairi (1994). "Welded wire fabric for bridges. I: ultimate strength and ductility," *ASCE Journal of Structural Engineering*, 120, 1866-1881.
- Azimov, U. (2012). "Controlling Cracking in Precast Prestressed Concrete Panels," Masters Thesis, The University of Texas at Austin.
- Barker, J. M. (1975). "Research, Application, and Experience with Precast Prestressed Bridge Deck Panels," *PCI Journal*, 20, 66-85.
- Batchelor, B. D. & B. E. Hewitt (1976). "Tests of model composite bridge decks," *ACI Journal*, 73, 340-343.
- Bazant, Z. P. (1972). "Prediction of Concrete Creep Effects Using Age-Adjusted Effective Modulus Method," *ACI Journal*, 69, 212-217.
- Bernold, L., P. Chang & B. M. Ayyub. (1989). "Feasibility of Using Welded Steel Mesh in Bridge Decks," *Report No. FHWA/MD-89/14*, Maryland Department of Transportation.
- Buth, E., H. L. Furr & H. L. Jones (1972). "Evaluation of a Prestressed Panel, Cast-in-Place Concrete Bridge," *Research Report 145-3*, Texas Transportation Institute, College Station, Texas.

- Carrasquillo, R. L., A. H. Nilson & F. Slate (1981). "Microcracking and Behavior of High Strength Concrete Subject to Short-Term Loading," *ACI Journal*, 78, 179-186.
- Collins, M. P. & D. Mitchell (1991). *Prestressed Concrete Structures*, Prentice-Hall, New Jersey.
- Coselli, C. J. (2004). "Behavior of Bridge Deck with Precast Panels at Expansion Joints," Master Thesis, The University of Texas at Austin, Austin, TX.
- Coselli, C. J., E. M. Griffith, J. L. Ryan, O. Bayrak, J. O. Jirsa & J. E. Breen. (2006). "Bridge Slab Behavior at Expansion Joints," *Research Report 0-4418-1*, Center for Transportation Research, The University of Texas at Austin.
- Corley, W. & M. Sozen (1966). "Time Dependent Deflection of Reinforced Concrete Beams," *ACI Journal*, 63, 373-386.
- Dilger, W. H. (1982). "Creep Analysis of Prestressed Concrete Structures using Creep Transformed Section Properties," *PCI Journal*, 27, 89-117.
- Fang, I.-K., J. Worley, R. E. Klingner & N. H. Burns (1986). "Behavior of Ontario-Type Bridge Decks on Steel Girders," *Report 350-1*, Center for Transportation Research, The University of Texas at Austin.
- Fang, I.-K., J. Worley, R. E. Klingner & N. H. Burns (1990). "Behavior of Isotropic Concrete Bridge Decks on Steel Girders," *ASCE Structures Journal*, 116, 659-679.
- Fang, I.-K., C. K.-T. Tsui, N. H. Burns & R. E. Klingner (1990). "Fatigue Behavior of Cast-in-Place and Precast Panel Bridge Decks with Isotropic Reinforcement," *PCI Journal*, 35, 28-39.
- Folliard, K., C. Smith, G. Sellers, M. _Brown & J. E. Breen. (2003). "Evaluation of Alternative Materials to Control Drying-Shrinkage Cracking in Concrete Bridge Decks," *Report 0-4098-4*, Center for Transportation Research, The University of Texas at Austin.
- Foreman, J. M. (2010). "Controlling Cracking in Prestressed Concrete Panels," Master Thesis, The University of Texas at Austin.

- Foster, S. W. (2010). "Reducing Top Mat Reinforcement in Bridge Decks," Master Thesis, The University of Texas at Austin.
- Gilbert, R. I. & Z. I. Sakka (2007). "Effect of Reinforcement Type on the Ductility of Suspended Reinforced Concrete Slabs," *ASCE Journal of Structural Engineering*, 133, 834-843.
- Goldberg, D. (1987). "Precast Prestressed Concrete Bridge Deck Panels," *PCI Journal*, 32, 26-45.
- Graddy, J. C., N. H. Burns & R. E. Klingner (1995). "Factors Affecting the Design Thickness of Bridge Slabs," *Report 0-1305-3F*, Center for Transportation Research, The University of Texas at Austin.
- Graddy, J. C., J. Kim, J. H. Whitt, N. H. Burns & R. E. Klingner (2002). "Punching-Shear Behavior of Bridge Decks under Fatigue Loading," *ACI Structures Journal*, 99, 257-266.
- Kim, J., N. H. Burns & R. E. Klingner (1994). "Factors Affecting the Design Thickness of Bridge Slabs: Results of Static and Fatigue Tests," *Report 1305-2*, Center for Transportation Research, The University of Texas at Austin.
- Klingner, R. E., I.-K. Fang, C. K.-T. Tsui & N. H. Burns (1990). "Load Capacity of Isotropically Reinforced, Cast-in-Place and Precast Panel Bridge Decks," *PCI Journal*, 35, 104-114
- Krauss, P. D. & E. A. Rogalla. (1996). "Transverse Cracking in Newly Constructed Bridge Decks," *NCHRP Report 380*, Transportation Research Board, Washington, D.C.
- Krishnamurthy, D. (1971). "A Method of Determining the Tensile Stresses in the End Zones of Pre-tensioned Beams," *The Indian Concrete Journal*, 45, 286-297.
- Krishnamurthy, D. (1973). "Design of End Zone Reinforcement to Control Horizontal Cracking in Pre-Tensioned Concrete Members at Transfer," *The Indian Concrete Journal*, 47, 346-349.

- Lukefahr, E. & L. Du (2010). "Coefficients of Thermal Expansion of Concrete with Different Coarse Aggregates-Texas Data," *Journal of Testing and Evaluation*, 38, 1-8.
- Merrill, B. D. (2002). "Texas' Use of Precast Concrete Stay-In-Place Forms for Bridge Decks," *Proceedings*, Concrete Bridge Conference, National Concrete Bridge Council, Skokie, IL.
- Muller, H. S. & H. K. Hilsdorf (1990). "Evaluation of the Time-Dependent Behavior of Concrete," *CEB Bulletin d'Information*, 199.
- Neville, A. M., W. H. Dilger & J. J. Brooks. (1983). *Creep of Plain and Structural Concrete*. Construction Press, London and New York.
- PCI (2004). *Manual for the Evaluation and Repair of Precast, Prestressed Concrete Bridge Products*, Precast/Prestressed Concrete Institute, Chicago, IL.
- Peterman, R. J. & J. A. Ramirez (1998). "Restraint moments in Bridges with Full-Span Prestressed Concrete Panels," *PCI Journal*, January-February, 54-73.
- Riding, K. A., J. L. Poole, A. K. Schindler, M. C. G. Juenger & K. J. Folliard (2009). "Effects of Construction Time and Coarse Aggregate on Bridge Deck Cracking," *ACI Materials Journal*, 106, 448-454.
- Robert, C. L., J. E. Breen & M. E. Kreger. (1993). "Measurement based Revisions for Segmental Bridge Design and Construction Criteria," *Report 1234-3F*, Center for Transportation Research, The University of Texas at Austin.
- Russo, S. (1999). "Structural Behavior of Double-T Prestressed Slabs with High Quality Welded Wire Mesh," *ACI Structural Journal*, 96, 972-980.
- Shrestha, K. M. & B. Chen (2011). "Aging Coefficient, Creep Coefficient and Extrapolating Aging Coefficient from Short Term Test for Sealed Concrete," *Journal of Wuhan University of Technology-Mater*, 26, 154-159.
- Sneed, L., A. Belarbi & Y. M. You. (2010). "Spalling Solution of Precast-Prestressed Bridge Deck Panels," *Report TRyy0912*, Missouri Department of Transportation.
- Soltani, M., X. An & K. Maekawa (2004). "Cracking response and local stress characteristics of RC membrane elements reinforced with welded wire mesh.

- Cement and Concrete Composites,” *Cement and Concrete Composites*, 26, 389-404.
- Sprinkel, M. M. (1985). “Prefabricated Bridge Elements and Systems,” *NCHRP Synthesis of Highway Practice 119*, Transportation Research Board, Washington D.C.
- Tadros, M. K., A. Ghali & W. H. Dilger (1975). “Time-Dependent Prestress Loss and Deflection in Prestressed Concrete Members,” *PCI Journal*, 20, 86-98.
- Tadoros, M. K., A. Nabil, A. J. Seguirant, & J. G Gallt (2003). “Prestress Losses in Pretensioned High-Strength Concrete Bridge Girders,” *NCHRP Report 496*, Transportation Research Board, Washington, D.C.
- TxDOT (2004). *Standard Specifications for Construction and Maintenance of Highways, Streets, and Bridges*, Texas Department of Transportation, Austin, TX.
- TxDOT (2008). *Standard Specifications for Construction and Maintenance of Highways, Streets, and Bridges*, Texas Department of Transportation, Austin, TX.
- Uygunoğlu, T. & İ. B. Topçu (2009). “Thermal expansion of self-consolidating normal and lightweight aggregate concrete at elevated temperature,” *Construction and Building Materials*, 23, 3063-3069.

VITA

Ki Yeon Kwon was born in Seoul, Republic of Korea on August 10, 1983, the daughter of Chun Tack Kwon and Weol Soon Wang. In February of 2002, she graduated from Shinmok High School, Seoul, Korea. She entered The Korea University in Seoul, Korea to study civil engineering. She received the degree of Bachelor of Engineering from The Korea University in August of 2005. In March of 2006, she entered the graduate school at The Korea University, and she received her Master of Engineering degree in February of 2008. She started work on her Ph.D. under the supervision of James O. Jirsa and Richard E. Klingner. She graduated with the degree of Doctor of Philosophy in December of 2012 at The University of Texas at Austin.

Permanent Address:

522-dong 104-ho, Mokdong Apt. 5 Danji,
Mok 5-dong, Yangcheon-gu,
Seoul, 158-755, Republic of Korea

This dissertation was typed by the author.